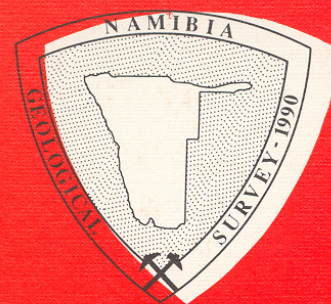


GEOLOGICAL SURVEY OF NAMIBIA

MINISTRY OF MINES AND ENERGY



**STRONTIUM ISOTOPE HETEROGENEITIES IN AMPHIBOLITE  
FACIES, BANDED METASEDIMENTS - A CASE STUDY FROM THE  
LATE PROTEROZOIC KUISEB FORMATION OF THE SOUTHERN  
DAMARA OROGEN, CENTRAL NAMIBIA**

by

**CHRISTINE KUKLA**



**MEMOIR 15**

**1993**

**Front cover:** Photograph of anatectic Kuiseb Formation metapelite KB103, which was used for Rb-Sr small-domain analyses (base of photograph is 17 cm). Migmatization of the Kuiseb Formation occurs locally within the northern Khomas Trough, in the vicinity of the Donkerhuk Granite (sample locality: Davetsaub river, farm Davetsaub 29)

**MINISTRY OF MINES AND ENERGY**

**GEOLOGICAL SURVEY OF NAMIBIA**

Director: B. G. Hoal

**MEMOIR 15**

**Strontium isotope heterogeneities in amphibolite facies, banded metasediments - a case study from the Late Proterozoic Kuiseb Formation of the southern Damara Orogen, central Namibia**

by

**Christine Kukla**

Editor: Clare Kennedy Galloway

Obtainable from the Geological Survey  
P.O. Box 2168, Windhoek, Namibia

	Price
Local	(+GST) R20.00
Abroad (Post Free)	R25.00

ISBN 0-86976-263-X

*Copyright reserved*  
**1993**



---

## ABSTRACT

The study investigates small-scale Rb-Sr isotope characteristics of banded metasediments from the Late-Proterozoic/Early Palaeozoic Kuiseb Formation (Damara Sequence) of the Khomas Trough, Damara Orogen, central Namibia.

The Kuiseb Formation, exposed in the western Khomas Trough, comprises a several-thousand-metres-thick sequence of predominantly pelitic and psammitic metasediments with subordinate calc-silicate rocks, graphite schists, scapolite schists and amphibolites (Matchless Member) which were metamorphosed under amphibolite facies conditions. Primary sedimentary structures, turbidite facies and facies associations, the cyclicity of the sequence and the great lateral extent of sedimentary units suggests that the sedimentary protoliths were deposited on an elongate submarine fan system. The structural overprint is characterised by four phases of ductile deformation, three of which are coaxial with folds verging consistently to the southeast. The overall structural pattern shows that deformation within the Khomas Trough is characterised by contemporaneous folding and thrusting which led to the development of extensive, northward-steepening slices within an overall imbricate fan geometry, with probably repeated sedimentary sequences.

Micro-textural relationships show that the thermal peak of metamorphism outlasted the main regional deformation. The physical conditions of metamorphism are estimated to range between 530-590°C/4-9.5 kb (southern Khomas Trough) and maximum temperatures of about 700°C at 4-5 kb (northern Khomas Trough). Structural criteria suggest that the formation of trondhjemitic partial melts within the Kuiseb Formation in the northernmost Khomas Trough occurred prior to the intrusion of the Donkerhuk Granite. With regard to the overall tectonic setting of the Khomas Trough and the apparent absence of a high-pressure metamorphism, the metamorphic overprint of the Kuiseb Formation within the Khomas Trough is interpreted to be related to crustal thickening through the collision of the Congo and the Kalahari Cratons during late Pan-African times.

To constrain the absolute timing of metamorphism, U-Pb monazite analyses were carried out on migmatite samples, a pelite sample from the Kuiseb Formation as well as on samples of the Donkerhuk Granite and associated granitic rocks. The data imply that the intrusion of the Donkerhuk Granite and the other investigated granitic rocks occurred after 510 Ma. A concordant age of 505± 4 Ma was obtained from the Donkerhuk Granite. The emplacement of the granitic rocks at the same time terminates the temperature peak of metamorphism and the main deformation in the Khomas Trough. Although the data points are slightly discordant, the U-Pb monazite data from the migmatites and the pelite sample form one cluster in the concordia diagram with  $^{207}\text{Pb}/^{235}\text{U}$  apparent ages ranging between 514 and 525 Ma. These data are interpreted to mark the temperature peak of regional metamorphism in the investigated area.

Within the framework of these data, Rb-Sr small-domain isotope analyses were carried out on banded metasediments of the Kuiseb Formation, 1) to investigate the applicability of the method to the dating of metamorphic processes, and 2) to study the isotopic homogeneity of these metasediments. Six samples (KB167, KB117, KB307, KB421, KB115, KB103) were selected which are characterised by a compositional layering of either sedimentary or metamorphic origin. The samples differ in their structural overprint as well as in their metamorphic grade. Rock profiles between 4 and 16 cm long were cut perpendicular to the banding of the samples and subsequently divided into mm-thick slabs. Apart from whole-rock analyses of each slab, mineral fractions (biotites, muscovites, plagioclase-quartz fractions, apatites) were analysed from individual slabs.

The obtained element distribution patterns of Rb and Sr within the metamorphically banded samples show a characteristic positive correlation of Rb and Sr both within the phyllosilicate-rich (P-) and quartz-rich (Q-) domains of the banding, which suggests that quartz has been removed from the P-domains during prograde metamorphism.

Put into isochron diagrams, the isotope data of all six rock profiles align along straight lines (MSWD 0.5-3.2). The corresponding whole-rock age data range from 449± 20 Ma (KB117) to 509 ± 17 Ma (KB307). In contrast, the investigated biotite fractions show a more limited range of mineral-whole-rock ages (485 ± 10 to 498 ± 10 Ma), despite the composite

character of the fractions and the structurally and metamorphically different history of the samples. Plagioclase-whole-rock pairs yielded between  $476 \pm 15$  and  $497 \pm 14$  Ma. K-Ar and  $^{40}\text{Ar}$ - $^{39}\text{Ar}$  data obtained from selected biotite and muscovite fractions are consistent with the respective Rb-Sr data. Compared to the U-Pb monazite ages, all of the Rb-Sr and the K-Ar/ $^{40}\text{Ar}$ - $^{39}\text{Ar}$  mineral data clearly fall below the supposed peak of metamorphism. The pronounced uniformity of the mineral data (from the metasediments as well as Rb-Sr data for mineral fractions from the Donkerhuk Granite) points towards a regional event or regionally significant processes responsible for the isotopic equilibration of the minerals after the peak of regional metamorphism. The resetting of the isotopic systems is attributed either to the temperature-induced self diffusion, which continues during regional cooling of the rocks, or to a late deformational and/or high temperature retrograde event which led to a partial recrystallisation of the minerals.

With regard to the relation between the mineral and whole-rock isotope data, the rock profiles KB117 and KB115 appear to be most important for an evaluation of the significance of the apparent whole-rock ages. In these samples, the regression of the whole-rock data from individual slabs of the rock profiles revealed younger ages ( $449 \pm 20$  Ma, MSWD 0.5;  $479 \pm 11$  Ma, MSWD 0.7) than the mineral-whole-rock pairs from individual slabs. The significance of the calculated whole-rock ages is discussed by means of profile diagrams which illustrate the spatial and the computed temporal development of the  $^{87}\text{Sr}/^{86}\text{Sr}$  for individual slabs. This form of diagram thus allows a geometrical control over the isotope distribution within the rock profiles.

The most striking feature of the spatial distribution and the computed temporal development of the  $^{87}\text{Sr}/^{86}\text{Sr}$  isotope ratios is that for most rock profiles, no homogeneous distributions of the  $^{87}\text{Sr}/^{86}\text{Sr}$  isotope ratios can be calculated for the time of the apparent whole-rock ages. Instead, the isotope distribution patterns are characterised by isotopic heterogeneities. It is important that the isotopic heterogeneities within the distribution patterns could not have evolved from an undisturbed, previously equilibrated isotope distribution. However, partial isotope equilibria apparently exist within the rock profiles. In accordance with previous studies, the isotope distribution patterns which show the least variation of the isotope ratios, might be interpreted as representing a metamorphic event leading to a partial equilibration of the isotope ratios although the regression lines do not represent true isochrons. This dating by means of disequilibrium distributions might be applied to the samples KB167, KB307, KB421 and KB103.

The two rock profiles KB117 and KB115 show comparatively homogeneous distribution patterns of their  $^{87}\text{Sr}/^{86}\text{Sr}$  ratios for the time of the calculated whole-rock ages. In both samples, plagioclase-quartz concentrates were analysed which demonstrate that there is no homogeneity of isotopes between the plagioclases and the respective whole rocks at the time of the apparent whole-rock equilibrium. In three slabs of the rock profile KB115, the analysed plagioclase-quartz fractions rather have a homogeneous isotope distribution with the respective whole rock at the calculated biotite-whole-rock ages. Furthermore, it could be shown for the rock profile KB115 that the homogenisation of the plagioclases with their respective whole rocks occurred discontinuously within different slabs. These apparent isotope heterogeneities strongly suggest that apparent whole-rock ages obtained from the two samples do not denote the timing of whole-rock isotope homogenisation, since the major constituents of the rocks were not in isotope equilibrium with their respective whole rocks at that time.

Two theories are discussed to explain the quite uncommon relationship between the mineral and whole-rock ages within the two rock profiles. The first model is based on the assumption that no isotope exchange occurred between the whole rocks of individual slabs, but between the minerals within individual slabs. It seems unlikely, however, that no isotope exchange at all occurred between the mm- to cm-thick slabs of the investigated amphibolite facies metasediments. The second model is based on the assumption that an equilibration only between the plagioclases continued, whereas the homogenisation of the plagioclases with the respective biotites and whole rocks within and between contiguous slabs ceased at an earlier time. This model would imply that plagioclase closes at a later stage than biotite which, however, has not yet been observed in other

---

studies. Thus neither of these models seems to be compelling for the interpretation of the isotope systematics of the two rock profiles. A third possible explanation would encounter an open system behaviour of the whole rocks. It might be assumed that the interaction of the rock with fluid phases, for example by an addition of Sr in an interstitial phase, could alter either the whole-rock isotopic composition or the concentrations of the elements. The minerals would remain closed systems. In practice, there are arguments for and against an open system behaviour of the rocks. The occurrence of certain retrograde mineral phases confirms the presence of a fluid phase in the late stages of metamorphism. Although the genesis of the apparent “isochrons” is not yet clear, it can undoubtedly be shown that they do not bear geologic relevance. This study shows that apparent “isochron” ages derived from Rb-Sr whole-rock small-domain analyses of metasedimentary rocks can lead to geologically meaningless ages which casts doubt on the applicability of the Rb-Sr small-domain method as a tool in dating metamorphic events, and on the significance of previous Rb-Sr whole-rock data from metamorphic rocks.

The evolution of the Rb-Sr isotopic systems most likely is governed by a combination of processes which operate in a contrary way. The different Rb-Sr ratios will permanently enforce the development of gradients within the  $^{87}\text{Sr}/^{86}\text{Sr}$  isotopic compositions between compositionally different rock volumes. The homogenisation of strontium isotopes, on the other hand, may be inferred to result from a continuous temperature-induced self diffusion, and more episodically, increases in the rate and extent of isotope exchange due to deformational processes and metamorphic reactions with a net transport of Rb and Sr. It is also assumed that the changes in the physical conditions of metamorphism and the mineralogy of the rocks will result in changing rates and mechanisms of isotope homogenisation. Self diffusion may become the most important process of isotope exchange when the main deformation as well as metamorphic reactions have ceased. The existence of the strontium isotope heterogeneities within the isotope distribution patterns of the investigated microprofiles suggests that the extent of strontium diffusion during the final stages of the Pan-African metamorphism did not exceed a few centimetres.



## TABLE OF CONTENTS

<b>1. INTRODUCTION AND GEOLOGICAL SETTING</b>	
1.1 OBJECTIVES OF STUDY.....	1
1.2 PREVIOUS WORK.....	1
1.3 GEOLOGICAL SETTING .....	1
1.3.1 Regional framework.....	1
1.3.2 Geological setting and tectonic evolution of the Khomas Trough .....	3
1.4 GEOCHRONOLOGY OF THE DAMARA OROGEN.....	4
1.5 LOCATION OF STUDY AREA.....	5
1.6 ACKNOWLEDGEMENTS .....	5
 <b>2. GEOLOGY OF THE KUISEB FORMATION IN THE KHOMAS HOCHLAND AREA</b>	
2.1 INTRODUCTION .....	7
2.2 LITHOTYPES OF THE KUISEB FORMATION.....	7
2.2.1 Lithotypes of the Kuiseb Formation metasediments.....	7
2.2.2 Heavy mineral spectra .....	8
2.2.3 The Matchless Member .....	8
2.3 SEDIMENTOLOGY AND PALAEO-ENVIRONMENTAL INTERPRETATION .....	8
2.3.1 Sedimentary structures .....	8
2.3.2 Sedimentary facies and facies associations .....	9
2.3.3 Palaeoenvironmental setting.....	9
2.4 STRUCTURE .....	9
2.4.1 Structural domains.....	10
2.4.2 Heterogeneous strain and thrusting in the Khomas Trough.....	13
2.4.3 Time sequence of deformational events .....	13
2.4.4 Structural evolution of the Khomas Trough.....	14
2.5 METAMORPHISM .....	14
2.5.1 Mineral textures.....	14
2.5.2 Metamorphic mineral assemblages .....	17
2.5.3 Aspects of metamorphic banding formation.....	20
2.5.4 Mineral chemistry.....	21
2.5.5 P-T conditions of metamorphism .....	23
 <b>3. THE RELATIONSHIP OF GRANITES AND MIGMATITES ALONG THE NORTHERN MARGIN OF THE KHOMAS TROUGH AND ITS BEARING ON THE TIMING OF METAMORPHISM</b>	
3.1 INTRODUCTION .....	29
3.2 THE DONKERHUK GRANITE AND ASSOCIATED GRANITIC ROCKS .....	29
3.2.1 Distribution of granitic rocks .....	29
3.2.2. Timing of intrusion.....	30
3.3 THE MIGMATITE ZONE OF DAVETSAUB .....	31
3.3.1 Regional extent.....	31
3.3.2 Conditions of migmatite generation.....	31
3.4 MIGMATITE FORMATION IN THE DAVETSAUB AREA: EXPRESSION OF CONTACT OR REGIONAL METAMORPHISM? .....	33
 <b>4. ISOTOPE STUDIES - OBJECTIVES AND PRINCIPLES</b>	
4.1 INTRODUCTION .....	35
4.2 RB-SR INVESTIGATIONS .....	35
4.2.1 Objectives .....	35
4.2.2 Principles .....	35
4.2.3 The Rb-Sr small-domain method .....	36
4.3 U-PB ANALYSES .....	37
4.3.1 Objectives .....	37
4.3.2 Significance of U-Pb zircon and monazite data.....	37
4.4 K-AR ANALYSES - OBJECTIVES AND PRINCIPLES .....	38
 <b>5. RB-SR SMALL-DOMAIN INVESTIGATIONS OF WHOLE ROCKS AND MINERALS FROM THE KUISEB FORMATION METASEDIMENTS</b>	
5.1 INTRODUCTION .....	39
5.2 ROCK PROFILE KB167 .....	39
5.2.1 Character of sample .....	39
5.2.2 Analytical results.....	39
5.3 ROCK PROFILE KB117.....	42
5.3.1 Character of sample .....	42
5.3.2 Analytical results.....	44



# 1. INTRODUCTION AND GEOLOGICAL SETTING

## 1.1 OBJECTIVES OF STUDY

This work forms part of a joint research project on the Late Proterozoic Kuiseb Formation in the southern Damara Orogen of central Namibia. The project was designed to study the tectonic setting of the Kuiseb Formation and the evolution of the Khomas Trough which plays an important role in the Damaran orogenic cycle.

The aim of this study is to put age constraints on the protoliths and prospective source areas of the Kuiseb Formation metasediments in the Khomas Trough as well as to delineate the timing of metamorphic processes within the southern Damara Orogen by means of radiometric dating techniques.

Apart from the scope of dating regional events, isotope studies of the Kuiseb Formation essentially were aimed at the application of Rb-Sr small-domain analyses as a tool in controlling the degree of isotope homogeneity within metamorphic rocks. Knowledge of the extent of isotopic equilibrium is essential for the dating of geological events, in particular for isochron modelling.

## 1.2 PREVIOUS WORK

Pioneering studies on the geology of the southern Damara Orogen have been undertaken by Gevers (1963) and Martin (1965). The stratigraphic terminology used is based on the South African Committee for Stratigraphy (SACS, 1980), Hoffmann (1983) and Miller (1983a). Structural aspects of the southern Damara Orogen have previously been dealt with by a number of authors (Gevers, 1963; Smith, 1965; Hälbich, 1977; Kasch, 1983a, 1983b; Miller, 1979, 1983a; Sawyer, 1981, 1983; Preussinger, 1987, 1990), but there has been little research so far on the sedimentology of the Kuiseb Formation, although primary sedimentary structures have been reported (Miller, 1979; Miller *et al.*, 1983; Downing, 1983; Preussinger *et al.*, 1987). The thermal evolution has been studied by Hoffer (1977, 1983), Hartmann *et al.* (1983), Behr *et al.* (1983), Sawyer (1981), Kasch (1983b, 1987) and Preussinger (1990). Geochemical studies on Kuiseb Formation metasediments and amphibolites were undertaken by Miller *et al.* (1983), Schneider (1983), Schmidt and Wedepohl (1983), Phillips *et al.* (1989) and Preussinger (1990). Killick (1983), Klemd *et al.* (1987, 1989), Breitkopf and Maiden (1988), Preussinger (1990) and Klemd and Okrusch (1990) dealt with genetic aspects of the Matchless Belt and its associated massive sulphide deposits.

## 1.3 GEOLOGICAL SETTING

### 1.3.1 Regional framework

The Damara Orogen of Namibia forms part of the Late Proterozoic Pan-African mobile belt system which surrounds and transects large parts of the African continent. A pre- to synorogenic succession deformed in this orogen is referred to as the Damara Sequence. The Damara Orogen consists

of two branches forming a triple junction. The north-northwest-trending coastal branch approximately parallels the present Namibian coastline and connects southwards with the Gariiep and Malmesbury Belts in southern Namibia and South Africa, respectively. The northeast-trending, approximately 400-km-wide inland branch extends between the Congo and the Kalahari Cratons and is considered to join with the Zambezi and Mozambique Belts further to the east (Clifford, 1967; Martin and Porada, 1977). Porada (1979) suggested that the Ribeira Orogen in Brazil could represent the western most counterpart of the Damara Orogen. Most geological work so far has focused on the inland branch of the Damara Orogen. Results of geological studies of the last decade are published in two compilation volumes edited by Miller (1983b) and Martin and Erler (1983).

On the basis of stratigraphy, structure, grade of metamorphism, types of plutonic rocks and radiometric data, the Damara Orogen has been subdivided into different tectonostratigraphic zones (Fig. 1.1) which are from north to south: Kaoko Zone (KZ), Northern Platform (NP), Northern Zone (NZ), Central Zone (CZ), Okahandja Lineament Zone (OLZ), Southern Zone (SZ), Southern Margin Zone (SMZ) and Southern Foreland (SF). The Southern Zone and the Okahandja Lineament Zone together are referred to as the Khomas Trough, a term which will be used in this study. The SMZ has been termed Southern Margin Thrust Belt by Hoffmann (1983). Most zone boundaries form major linear features and are either thrusts, lineaments or stratigraphic boundaries.

The Damara Sequence (SACS, 1980) consists of four major stratigraphic units (Fig. 1.2) comprising predominantly metamorphosed sediments. These developed from basal arkosic arenites with local volcanics and evaporites (Nosib Group) through a middle carbonate sequence with variable amounts of clastics (lower Swakop Group, Otavi Group), an upper clastic sequence including metavolcanic rocks (upper Swakop Group) and finally molasse sediments in the northern and southern forelands (Mulden and Nama Groups). The distribution of rock types and stratigraphic units across the Damara Orogen shows distinct asymmetries. Some of the sequences are unconformity-bound (Fig. 1.2).

The structure across the Damara Orogen is also markedly heterogeneous. Generally, the intensity of deformation increases southwards within the orogen. Fold styles change from gentle open, upright on the Northern Platform to tight, northward-verging in the Northern Zone (Miller, 1983a). In the Central Zone tight upright to locally recumbent folds interfere with northeast-trending dome structures. The southern boundary of the Central Zone is the Okahandja Lineament (Miller, 1979), a huge, monocline-like downfold of the entire Damara succession. This lineament is a fundamental and deep-penetrating zone of weakness in the crust which has repeatedly been active and which had a major influence throughout the depositional and tectonic history of the orogen (Miller, 1983a). Folds are tight to isoclinal and upright in the Okahandja Lineament Zone but become southeast-

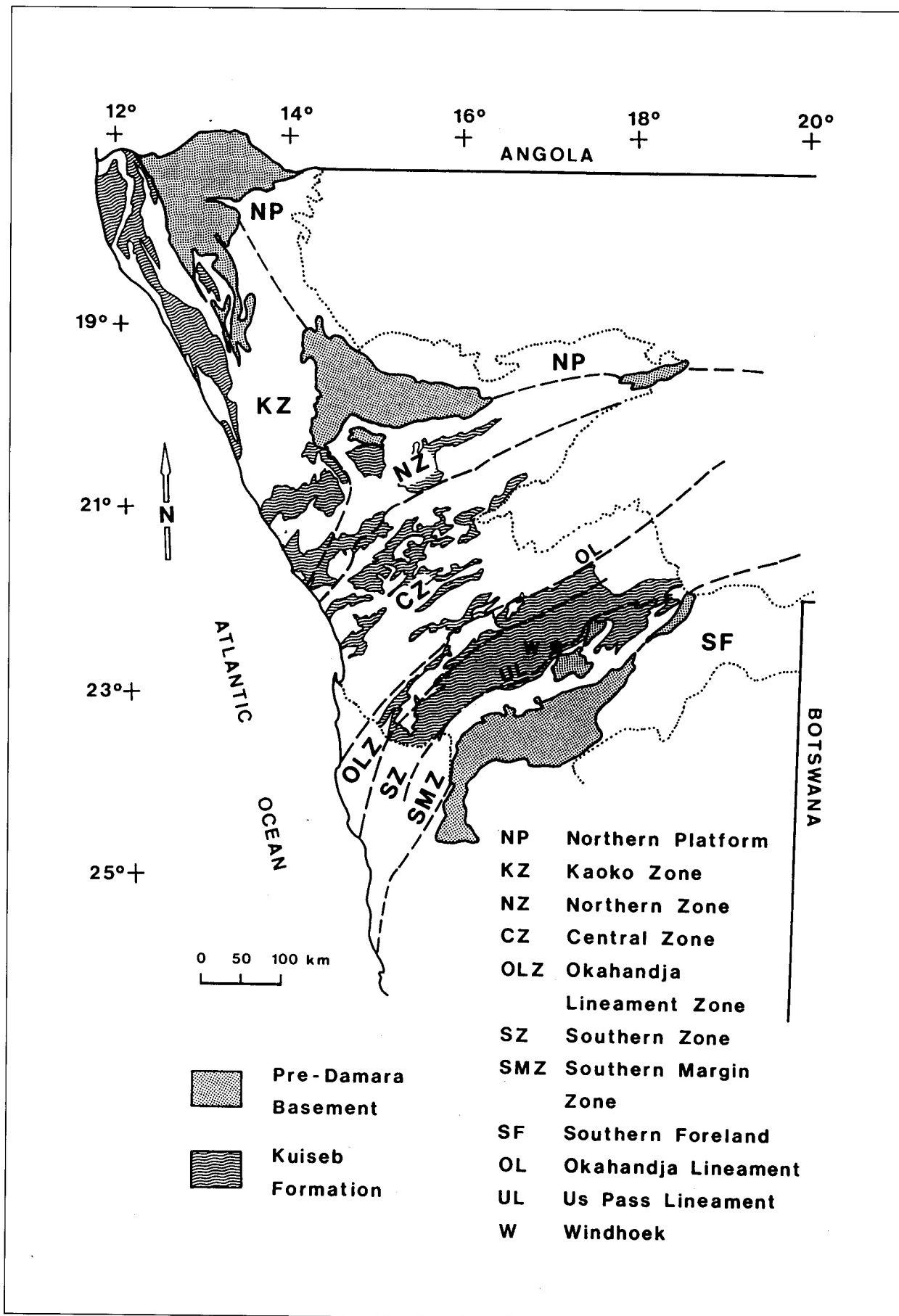


Figure 1.1: Tectonostratigraphic zones of the Damara Orogen (after Miller, 1983a)

NORTH				CENTRE				SOUTH						
GROUP	SUBGROUP	FORMATION	LITHOLOGY (MAX. THICKNESS)	GROUP	SUBGROUP	FORMATION	LITHOLOGY (MAX. THICKNESS)	GROUP	SUBGROUP	FORMATION	LITHOLOGY (MAX. THICKNESS)			
MULDEN		OWAMBO	Shale, marl, siltstone, sandstone (1000 m)											
		KOMBAT	Shale dolomite lenses											
		TSCHUDI	Quartzite, conglomerate, arkose, argillite (3000 m)											
UNCONFORMITY IN NW														
OTAVI	TSUMEB	HÜTTENBERG	Dolomite with chert shale, limestone, stromatolites, oolites (900 m)	SWAKOP	KHOMAS	KUISEB	Quartz-biotite schist, biotite-gamet-cordierite schist, amphibole schist, quartzite, marble, calcisilicate rock (3000 m)	SWAKOP	KHOMAS	KUISEB	Biotite schist, biotite quartzite, graphitic schist, calcisilicate rock, amphibolite (matchless member) (10000 m)			
		ELANDS-HOEK	Dolomite with chert stromatolites (1100 m)			KARIBIB	Marble, biotite schist, quartz schist, calcisilicate rock (700 m)			AUAS	Quartzite, schist, marble, amphibolite, itabirite (1800 m)			
		MAIEBERG	Dolomite, limestone, slump breccia (950 m)			CHUOS	Mixtite, marble, quartzite (700 m)			CHUOS	Pebbles schist, mixtite, quartzite, schist, itabirite, amphibolite, calcisilicate rock (1650 m)			
		CHUOS	Mixtite, dolomite, limestone, sandstone, itabirite, oolite chert (700 m)			LOCAL DISCORDANCE				LOCAL DISCORDANCE				
	LOCAL DISCORDANCE													
	ABENAB	AUROS	Dolomite, limestone, marl, shale (450 m) stromatolites		UGAB	RÖSSING			Marble, quartzite, conglomerate, biotite schist, biotite-hornblende schist, calcisilicate rock (700 m)	KUDIS	BLAU-KRANS	Graphite schist, quartzite, quartz-mica schist, conglomerate, itabirite (1700 m)		
		GAUSS	Dolomite, limestone, oolitic chert, sandstone (750 m)				?		HAKOS		Quartzite schist (2000 m)			
		BERG AUKAS	Dolomite, limestone, stromatolites, arkose, greywacke (525 m)				CORONA		Dolomite schist, conglomerate (400 m)					
	LOCAL DISCORDANCE													
	NOSIB	VARIANTO	Mixtite, tuff, itabirite		NOSIB		KHAN		Calcisilicate rock, amphibole-pyroxene gneiss and quartzite (1100 m)	NOSIB		DURU-CHAUS	Phyllite, quartzite, conglomerate, limestone (5000 m)	
ASKEVOLD NAALWPOORT		Rhyolite, tuff, agglomerate, andesite, epidote, bostonite (6000 m)	KAMTAS	Quartzite, arkose, conglomerate schist, rhyolite (3500 m)										
NABIS		Quartzite, arkose, conglomerate		Quartzite, arkose, conglomerate (6700 m)										
LOCAL DISCORDANCE														

Figure 1.2: Lithostratigraphy of the Damara Sequence (from Martin, 1983; based on SACS, 1980)

ward-vergent, open to isoclinal in the Southern Zone. The intensity of folding as well as thrusting increases towards the southern edge of the Southern Zone. The Southern Margin Zone is dominated by thrust piles and nappe systems incorporating basement inliers and ultramafic bodies (Hoffmann, 1983b). The Schlesien-Amerongen Line (Hartnady, 1978), also termed Us Pass Lineament (Hoffmann, 1983), forms the boundary between the Southern and Southern Margin Zones and is also considered to represent a major tectonic boundary within the Damara Orogen. Deformation has affected the northern part of the Southern Foreland resulting in open to tight folds but dies out further to the south.

The metamorphic grade within the Damara Orogen increases both from north and south towards the Central Zone where the conditions of partial melting have been reached. Hoffer (1977) established a reaction isograd scheme with isograds describing a concentric pattern around the area of Swakopmund.

A number of geodynamic models on the evolution of the Damara Orogen have previously been published. All models assume that the coastal branch of the Damara Orogen had developed into a Pan-African South Atlantic Ocean (Adamastor Ocean; Hartnady *et al.*, 1985) during rifting of the inland branch. The crucial point to all models, however, was the question whether oceanic crust had formed in the inland branch. Martin and Porada (1977), Kröner (1982) and

Porada (1983) proposed ensialic (aulacogen-related) models for the development of the latter. Watters (1976) first suggested a Wilson cycle model for the Damara Orogen. Blaine (1977), Hartnady (1978), Kasch (1983a), Barnes and Sawyer (1980), Downing and Coward (1981) and Miller (1983a) demonstrated that models incorporating the development of oceanic crust, northwestward subduction, ocean closure and final continental collision could account for the major features observed in the orogen.

### 1.3.2 Geological setting and tectonic evolution of the Khomas Trough

The Kuiseb Formation represents the uppermost unit of the Swakop Group and is the only formal stratigraphic unit present in the Khomas Trough. The Kuiseb Formation forms a mostly clastic sequence comprising meta-greywackes and metapelites with intercalated graphite schists, scapolite schists, calc-silicate rocks as well as the mafic magmatic rocks of the Matchless Member (SACS, 1980). The thickness has been estimated to reach about 10 000 m in the Khomas Trough (Martin, 1965). Facies relationships with the platform sequence (Karibib Formation) and slope facies (Tinkas Formation) equivalents of the Central Zone have largely been obliterated by the late-tectonic Donkerhuk Granite which intruded into the Okahandja Lineament Zone over a length of

more than 200 km, but interfingering of the Kuiseb and Tinkas Formations has been established by Porada and Wittig (1983). At the southern border of the Khomas Trough, rocks of the Kuiseb Formation have been thrust upon stratigraphic units of the Southern Margin Zone (Vaalgras Subgroup). Hoffmann (1983) has interpreted the latter stratigraphic units as representing slope and ocean basin deposits. The contact to the overlying Kuiseb Formation of the Khomas Trough is structural. The provenance of the Kuiseb Formation sedimentary sequence in the Khomas Trough has been discussed by a number of authors (Martin, 1983; Miller *et al.*, 1983) who have postulated a sediment source situated to the northeast.

The Matchless Member forms a narrow, between 1- and 3-km-thick sequence of metamorphosed mafic volcanics, mafic intrusives and intercalated metasediments. It may be traced along strike for about 350 km. Massive sulphide deposits as well as ultramafic bodies are in places associated with the Matchless Member. The Matchless Member amphibolites have been geochemically characterised as tholeiitic mid-ocean ridge basalts (Finnemore, 1978).

The structure within the Khomas Trough is characterised by a multiple-phase deformation and an amphibolite facies metamorphic overprint.

Very little geological data have so far been available from the Khomas Trough in order to constrain models on its geodynamic evolution within the framework of the evolution of the Damara Orogen as a whole. Most of the previous models introduced above are therefore not based on primary data in the case of the Khomas Trough. Blaine (1977) has summarised his structural studies in the eastern Khomas Trough by proposing a fore-arc basin model for this area. Miller *et al.* (1983) suggested, on the basis of geochemical studies, that spreading-phase deposits are preserved south of the Matchless Member and younger subduction-phase deposits to the north of this unit. Breitkopf and Maiden (1987) proposed a limited ocean basin model comprising the development of subbasins on both oceanic and continental crust. Downing and Coward (1981) and Hoffmann (1983) have speculated upon a possible accretionary prism setting for the Khomas Trough.

A tectono sedimentary model for the geotectonic evolution of the Khomas Trough was recently proposed by P. Kukla (1990) and P. Kukla and Stanistreet (1991). This model suggests the evolution of an accretionary prism within a convergent continental margin setting. According to the latter author, rifting in the Khomas Trough was initiated along pre-existing tectonic lines. During continental divergence (spreading phase), a gulf-type oceanic basin, termed the Khomas Sea, was underlain by oceanic crust and is assumed to have extended for a minimum of hundreds of kilometres between the Congo and the Kalahari Cratons. Subsequent convergence led to northwestward subduction of the oceanic crust (now represented by the Matchless Member) beneath the Congo Craton and to the development of an oceanic trench which was filled with a southwestward-prograding, elongated submarine fan. The accretionary prism evolved in this model through the off scraping of the trench sediments together with some pelagics from the descending slab. Early folding and thrusting occurred during accretion of the sediments against the Congo Craton. Continental collision

produced a northerly steepening thrust pile with southeastward-directed thrusting and folding. Strike-slip dislocations occurred at a late stage at the Okahandja Lineament which is assumed to represent the former backstop of the accretionary prism. The Matchless Member is interpreted as having been emplaced into the sedimentary succession during abduction of the accretionary prism onto the Kalahari Craton. Crustal thickening and thermal relaxation following subduction resulted in amphibolite facies metamorphism which reached its thermal peak after the main deformation had ceased.

#### 1.4 GEOCHRONOLOGY OF THE DAMARA OROGEN

The Damara Sequence unconformably overlies a mostly granitic pre-Damaran basement which is exposed to the north and south of the orogen as well as in small inliers in its centre. U-Pb zircon ages between 1730 and 1870 Ma have been reported for the basement outcropping in the north (Burger *et al.*, 1976) and ages up to 1955 Ma in the centre of the Damara Orogen (Jacob, *et al.* 1978, Briquieu *et al.*, 1980; Tegtmeier and Kröner, 1985). A major magmatic phase in the southern basement has been dated at 1200 to 1000 Ma (Malling, 1978; Seifert, 1986; Reid *et al.*, 1988). Thus it has been suggested that the Damara Orogen is underlain by a 1.7 to 2.0 Ga old basement which has been overprinted by volcanic activity and granitic intrusions in the southern part between 1000 and 1200 Ma during the Kibaran orogeny (Haack and Martin, 1983).

U-Pb zircon data of  $728 \pm 40$  Ma and  $750 \pm 65$  Ma (Miller and Burger, 1983a) for quartz-feldspar porphyry lavas of the Nosib Group in the Northern Zone have been interpreted by Miller (1983a) to mark the initiation of intra-continental rifting. An age of 840 Ma (Kröner, 1982) for a syenite complex intruding Nosib Group sediments has been disqualified as unreliable (Miller, 1983a) and thus the end of Nosib/beginning of Swakop Group sedimentation is inferred at about 750 Ma. Hawkesworth *et al.* (1981) reported a Rb-Sr whole-rock age of  $765 \pm 37$  Ma for the Matchless Member amphibolites which they interpreted as a minimum age of sedimentation in the Khomas Trough.

There are few constraints on the following depositional history of the Damara Sequence. Most radiometric data available are based on Rb-Sr whole-rock analyses of syn- and post-tectonic granites and granitoids which were used to put age constraints on the deformational evolution. The granitic intrusives may be differentiated into syn- to post-orogenic Salem type and red granites and post-tectonic leucogranites and alaskites. The Donkerhuk Granite which intruded into the Okahandja Lineament Zone, is typical of the Damaran leucogranites. Most of the plutonic rocks were emplaced between 650 and 460 Ma (Kröner, 1982; Hawkesworth *et al.* 1983a, 1983b; Miller, 1983a). The intrusions appear to have occurred in three pulses at about 650, 550 and 500 Ma, as suggested by the frequency distribution of the radiometric data (Miller, 1983a). The onset of regional deformation in the Central Zone is bracketed by granodiorite complexes which have been dated at  $651 \pm 20$  Ma (Kröner, 1982) and  $553 \pm 22$  Ma (Haack *et al.*, 1980). It has been stated that pre-

560 Ma intrusives comprise syenites, carbonatites and diorites. Only late syn- $F_1$  and younger intrusions are of granitic composition. Apparently, the transition from an extensional to a compressive regime in the development of the orogen is marked by the change in type, source and intensity of magmatism (Haack and Martin, 1983).

The peak of metamorphism has been inferred to have culminated between 520 and 530 Ma (Haack, 1983) and was associated with a major phase of magmatism according to Haack and Martin (1983). An upper intercept of  $534 \pm 7$  Ma for zircons from a (S-type) red granite is considered to mark the peak of metamorphism (Briqueu *et al.*, 1980). K-Ar ages for detrital and authigenic white micas of 570 to 670 Ma and 500 to 530 Ma, respectively, from the Nama Group of the Southern Foreland were taken to constrain the timing of metamorphism within the orogen (Ahrendt *et al.*, 1978; Horstmann, 1987). Rb-Sr whole-rock ages of  $521 \pm 15$  and  $523 \pm 8$  Ma for the post-metamorphic Donkerhuk Granite were considered to terminate the peak of regional metamorphism (Blaxland *et al.*, 1979). The timing of post-metamorphic alaskitic intrusions is constrained through concordant monazite ages of  $508 \pm 2$  and  $509 \pm 1$  Ma (Briqueu *et al.*, 1980) and a Rb-Sr whole-rock  $458 \pm 68$  Ma (Kröner and Hawkesworth, 1977; Hawkesworth *et al.*, 1983).

The cooling history of the Damara Orogen has been investigated by Haack (1983) through Rb-Sr, K-Ar and fission track studies. He concluded that rapid uplift of the southern relative to the central orogen occurred between 530 and 520 Ma and that cooling proceeded fast in the Khomas Trough. In contrast, temperatures remained high in the Central Zone. K-Ar ages ranging between 520 and 420 Ma (Clifford, 1967; Haack and Hoffer, 1976; Clauer and Kröner, 1979; Ahrendt *et al.*, 1983; Hawkesworth *et al.*, 1983) were interpreted to reflect cooling below a  $300^\circ\text{C}$  isotherm (Haack, 1983). A certain diachronism is indicated from the distribution of

the mineral ages which tend to be younger in the centre of the orogen than those at the margins (Hawkesworth, 1983; Haack, 1983).

## 1.5 LOCATION OF STUDY AREA

The study area is located about 120 km west of Windhoek in the area of the Great Escarpment which borders the Khomas Hochland against the Namib desert in the west. On grounds of excellent exposure of the Kuiseb Formation along the ephemeral Khomaskaan, Amsas and Koam rivers, a north-south-trending study traverse was chosen across the Khomas Trough in the Khomas Hochland between the Otjimbingwe reservate 104 and the farm Usambara 304 at the confluence of the Koam and the Kuiseb rivers (Fig. 1.3)

## 1.6 ACKNOWLEDGEMENTS

This study forms part of a joint research project on the Kuiseb Formation of the southern Damara Orogen, in which the Geological Survey of Namibia, the Department of Geology of the University of the Witwatersrand, Johannesburg and the Mineralogisches Institut, Universität Würzburg participated. The study was funded by the Deutsche Forschungsgemeinschaft (DFG) which is gratefully acknowledged.

I am grateful to my supervisor Prof. Dr M. Okrusch who initiated the study, for his great encouragement and his great support. I want to thank Prof. Dr B. Grauert, Zentrallabor für Geochronologie, Universität Münster for his interest in the project, for many discussions during my stay at the laboratory and for reading the manuscript. Special thanks are extended to Dr U. Kramm, Zentrallabor für Geochronologie, Universität Münster for supervising the isotope techniques, for many useful discussions and for reviewing the manuscript.

Special thanks are extended to Dr I.G. Stanistreet and Dr

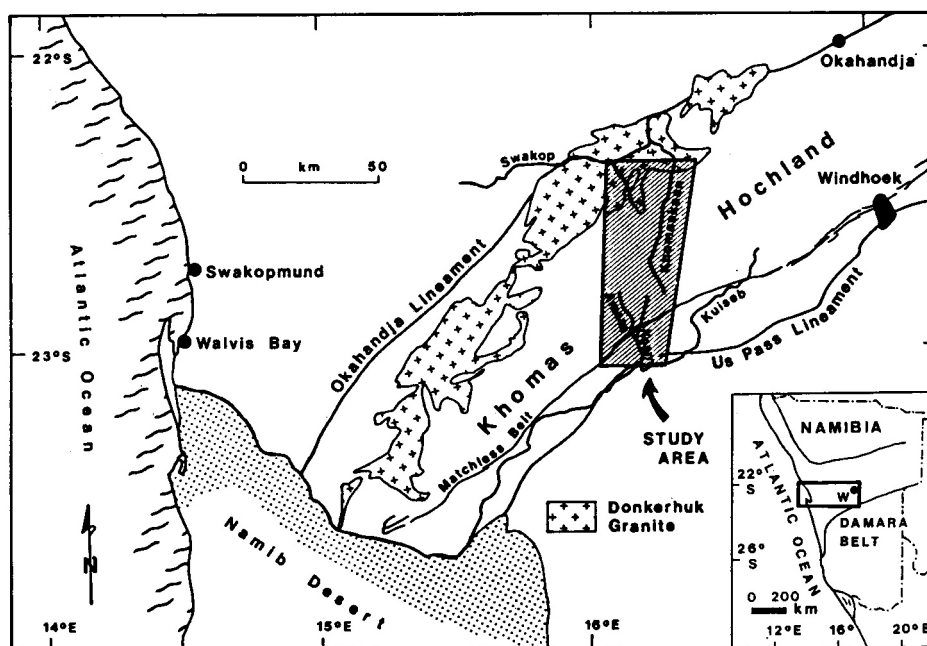


Figure 1.3: Location of the study area

E.G. Charlesworth, University of the Witwatersrand, Johannesburg, for their encouragement and useful discussions during field work and during my visits to their department. I want to thank Dr R. McG. Miller from the Geological Survey of Namibia for his interest in the project. He and the Survey staff are thanked for logistical and technical support during field work.

Dr H. Kreuzer from the Bundesanstalt für Geowissenschaften und Rohstoffe, Hannover and his technical staff are thanked for carrying out of K-Ar and Ar-Ar isotope analyses and for their support during my visit to the Bundesanstalt, Hannover.

I want to thank the personnel and the colleagues from the Zentrallabor für Geochronologie, Universität Münster for useful discussions and practical help, in particular Ms H. Baier, Dr A. Baumann, Dr A. Deutsch, Dr B. Hansen, Dr J. v. Hogen, Dr A. Kalt, Ms A. Lark and Mr S. Rochnowski.

The project benefited much from discussions with the personnel and colleagues from the Mineralogisches Institut, Universität Würzburg, in particular Dr B. Bühn, Dr L. Franz, Dr

H. Häussinger and Prof. P. Richter. Dr U. Schüssler is thanked for advice during the microprobe analyses. Dr H. Häußinger and Dr L. Franz are thanked for providing computer programmes which helped to process microprobe data; Mrs R. Baur is thanked for assistance during geochemical analyses. Mr P. Späthe and Mr P. Kelber are thanked for the preparation of polished and thin sections and for photographic work. I want to thank Mrs A. Kirchner for her always friendly administrative help.

Special thanks go to the farmers in the Khomas Hochland whose hospitality and support were magnificent. In particular Hardus and Anita Myburgh (Okasume), Mrs Johnston (Kaan), Mr and Mrs Jacob (Kaan Dam), Mr Langner (Keises) and Mr and Mrs Spath (Davetsaub) are thanked for their friendly help.

Last but not least I want to thank my husband and colleague Peter for his encouragement and support during this project, for reading through the manuscript and for a magnificent time in Namibia.

## 2. GEOLOGY OF THE KUISEB FORMATION IN THE KHOMAS HOCHLAND AREA

### 2.1 INTRODUCTION

With regard to an interpretation of the isotopic evolution of the metasediments in the Khomas Trough, it is important to give an introduction to the geology of this area. It is therefore the aim of this chapter to present an overview of the sedimentological, structural and metamorphic development of the Kuseb Formation within the western Khomas Trough. The metamorphic evolution, especially, is particularly of importance regarding the isotopic evolution of the metasediments.

The fieldwork on which this study is based, was carried out in cooperation with P. Kukla as part of a joint project on the geological situation of the Kuseb Formation in the Khomas Hochland area. Selected aspects of the geology and the geotectonic evolution of this area were published by P. Kukla *et al.* (1988, 1989, 1990) and P. Kukla and Stanistreet (1991). A detailed documentation of the geology of the Kuseb Formation in the Khomas Hochland area has been presented by P. Kukla (1990).

### 2.2 LITHOTYPES OF THE KUISEB FORMATION

#### 2.2.1 Lithotypes of the Kuseb Formation metasediments

The Kuseb Formation exposed in the southern Damara Orogen has previously been described as a monotonous sequence of pelitic and psammitic rocks (e.g. Miller, 1983a). Major and minor lithotypes occurring within the Kuseb Formation, some of which form discrete marker horizons, will be introduced in this section.

The following lithological classification of the Kuseb Formation metasediments will make use of the terms "pelite" and "psammite" which should be understood according to the following definitions. "Pelite" is used in the sense of Bayly (1968): "As commonly used, a pelite means an aluminous sediment metamorphosed, but if used systematically, it means a fine-grained sediment metamorphosed." The present study refers to the former definition. A comparable definition is given for the term "psammite" which is understood as a metamorphic derivative of an arenite. The term "semi-pelitic" is introduced to indicate a certain variation in the mica content within pelitic rocks.

#### *Psammites/quartz-plagioclase-mica schists*

Psammitic rocks constitute major portions of the Kuseb Formation in the Khomas Trough and occur in layers between 5 cm and several metres thick. The mineralogical composition of the quartz-plagioclase-mica schists is uniform with differences occurring in the amounts of the individual mineral species. Although most of the psammites show a schistose foliation, the term "schist" is not appropriate in all cases,

since the amount of micas does not reach 50 % of the total rock which is required by the definition of the term (Bates and Jackson, 1987). The grain size is fine to medium grained (below 0.5 mm). Quartz and plagioclase are commonly well recrystallised forming polygonal grain boundaries. Further constituents are biotite, chlorite (in the southern part of the study area), muscovite, and the accessory phases apatite, tourmaline, titanite, opaque phases, graphite, epidote and zircon. Scapolite may be present in association with calc-silicate rocks. Aluminium silicates rarely occur or are totally absent in psammitic rocks. Sedimentary precursors of psammitic rocks are greywackes.

#### *Pelites/Mica-quartz-plagioclase schists*

Pelites form the second major rock type of the Kuseb Formation. Major constituents are biotite, muscovite, chlorite (in the southern part of the study area), quartz and plagioclase, forming the matrix of the rocks. Depending on the metamorphic grade and the bulk rock composition, the following minerals may occur in varying quantities: garnet, staurolite, kyanite, andalusite or sillimanite. Accessory phases are apatite, tourmaline (which may reach considerable quantities), opaque phases, titanite, epidote, graphite, monazite and zircon. Pelites occur in layers of mostly one to tens of centimetres thick, but units of predominantly pelitic composition may reach thicknesses of several tens of metres. Sedimentary precursors are muds and mudstones, but silty deposits have also been transformed to more quartz-rich pelitic rocks termed semi-pelites.

#### *Graphitic schists*

Graphitic schists which occur in discrete units in the central and the southern part of the Khomas Trough, are graphite-bearing pelites containing quartz and plagioclase, micas and in most cases pyrite grains. The amount of graphite is in the order of tens of percent of the total rock. The most prominent graphite schist unit is exposed in the central Khomas Trough on the farm Kaan 309 where it reaches a total thickness of about 60 m. The graphite content of these pelitic schists most likely originates from organic carbon, which conclusion may be supported by stable isotope data (P. Kukla, 1990).

#### *Calc-silicate rocks*

Calc-silicate rocks occur throughout the sequence as intercalated layers or small bodies of various shapes (spindles, nodules or diffusive masses) and compositions. The following constituents may be present: quartz, plagioclase, garnet, chlorite, hornblende, biotite, muscovite, calcite, diopside, zoisite, clinozoisite, epidote, titanite, scapolite, apatite and tourmaline. Some of the so-called calc-silicate spindles occurring in thick-bedded psammite horizons consist of quartz and plagioclase only with minor amounts of garnet and biotite. The calc-silicates are thought to have been derived from impure carbonates of clastic origin intercalated with the siliciclastic sediments.

*Marble and tremolite schist*

An approximately 1-m-thick horizon consisting mainly of tremolite with minor amounts of quartz and biotite is exposed at the footwall of the major graphite schist unit in the centre of the Khomas Trough. The horizon is heavily weathered and could not be mapped laterally.

A 2-m-thick marble horizon is intercalated in the pelite-dominated sequence in the hanging wall of the Matchless Member and can be traced laterally for some kilometres. The marble horizon is composed mainly of fine-grained dolomite and calcite with minor amounts of quartz and muscovite.

*Scapolite schists*

Scapolite schists occur in two predominantly pelitic units in the northern Khomas Trough. The sequences act as major marker horizons of great lateral extent. The host rocks are rich in intercalated calc-silicate rocks, and massive scapolitisation has replaced all of the previously present plagioclase. The scapolites form poikiloblastic porphyroblasts of cm dimensions which enclose all other mineral phases. The scapolitisation as a whole is stratabound, but apparently discordant on a smaller scale, where scapolite formation is intimately associated with fractures. Scapolite formation is attributed to a metasomatic reaction of carbonate-bearing psammites and pelites with circulating brines.

## 2.2.2 Heavy mineral spectra

To determine sedimentary provenance, heavy mineral studies were carried out on 25 psammites as well as some pelite samples from different parts of the study traverse. Initial results revealed that there is apparently no large variation in the heavy mineral spectra throughout the investigated samples. Most abundant in psammitic samples is tourmaline, followed by apatite, opaque phases and zircon.

The latter is the only mineral which can undoubtedly be recognised as detrital in origin; all other minerals are of metamorphic origin or have recrystallised during metamorphism. The detrital nature of the zircons can be detected by the pitted surfaces of the crystals (cf. Chapter 6). The zircons can be grouped into a number of fractions on the basis of their colour and morphology; characteristic fractions can be traced throughout different samples. From the various zircon morphologies, either mixing of detritus from different source areas or a heterogeneous sediment source can be inferred. The varying degrees of corrosion of the zircon crystals can be interpreted to indicate differing transport distances and amount of reworking before final sedimentation.

Mineral phases dominating the heavy mineral spectra of pelitic rocks are the  $Al_2SiO_5$  polymorphs, staurolite and garnet as well as tourmaline, apatite and opaques. Less frequent are titanite and epidote. The occurrence of these mineral phases, however, is solely dependent on the bulk rock composition and the metamorphic grade of the samples.

## 2.2.3 The Matchless Member

The Matchless Member has long been recognised as an important stratigraphic marker in the Khomas Trough. In the present study area, the Matchless Member is exposed on the farms Kobos 305, Okasume 304 and Bergkrans 370. The sequence consists of two major bands of amphibolite separated by about 20 m of pelitic and psammitic schists occasionally containing graded units. Three types of amphibolite may be distinguished within the sequence: a) a banded, carbonate-rich type, b) a more massive, dark-green type, rich in epidote and c) bodies of coarse-grained amphibolite which are referred to as metagabbros (Häußinger, 1990). In type b) amphibolites, breccias and structures interpreted as former pillows are exposed. The mineralogy of the amphibolites is characterised by the mineral phases plagioclase, hornblende, calcite, biotite, quartz, scapolite and epidote.

## 2.3 SEDIMENTOLOGY AND PALAEOENVIRONMENTAL INTERPRETATION

Prior to this project no detailed sedimentological work had been carried out on the Kuseb Formation exposed in the Khomas Trough. Some sedimentary structures were previously reported by Miller *et al.* (1983) and Preussinger *et al.* (1987). During the present study, delicate sedimentary structures could be mapped and sedimentary facies defined in the multiply deformed and metamorphosed series (P. Kukla *et al.*, 1990). Because of the character of deformation, primary sedimentary structures are best preserved in the central to northern Khomas Trough, although metamorphism reached the upper amphibolite facies in this area. This section will aim to provide an overview of sedimentological features and to outline depositional palaeoenvironments.

## 2.3.1 Sedimentary structures

The most widespread primary sedimentary feature preserved in large parts of the study area is sedimentary layering. Its primary nature is confirmed by sharp bases and tops of the individual layers as well as various erosional features.

Graded bedding is frequent and is present as compositional grading from a quartz-plagioclase-rich base to a mica-rich top (Fig. 2.1a). From the recognition of graded layering, previous authors have inferred a turbiditic origin for the Kuseb Formation metasediments (Miller, 1983a; Preussinger *et al.*, 1987). Erosional structures are present as small-scale scours and channels. In some cases, the undersides of massive psammitic layers show bilaterally symmetrical flute casts (Fig. 2.1 b). Common sedimentary features throughout the study traverse are load casts on the undersides of massive psammites (Fig. 2.1c, d). In some layers, the loads became detached from the

**Right: Figure 2.1:** Sedimentary structures preserved within the Kuseb Formation metasediments

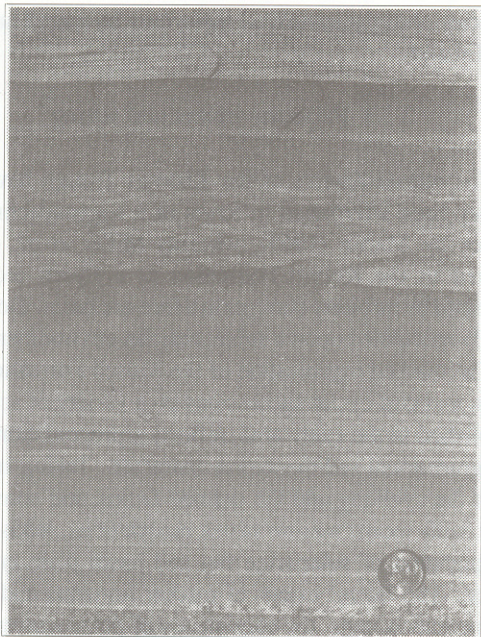


**Figure 2.1a:** Graded layering (coin is 2.5 cm in diameter); farm Tsawisis 308



**Figure 2.1b:** Flute casts and trough cross-lamination (Bouma C division; pocket knife is 8.5 cm long); farm Dagbreek 365



**Figure 2.1c:** Load casts, indicated by arrows (lens cap is 4.9 cm in diameter); farm Dagbreek 365



**Figure 2.1d:** Overturned load structures; farm Kaan 309



**Figure 2.1e:** Dewatering structures, flame structures and ball-and-pillow structures; farm Dagbreek 365

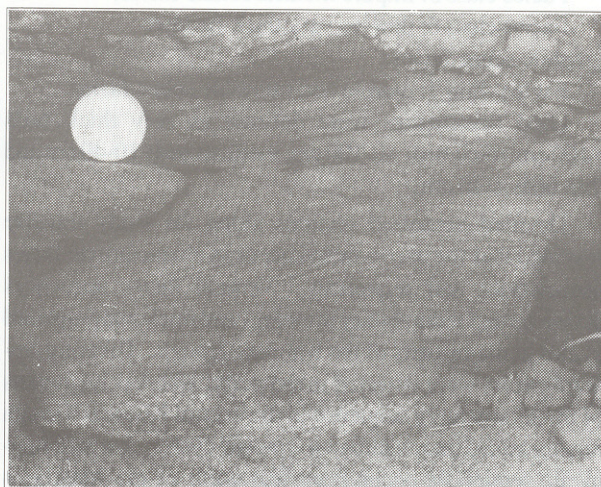


**Figure 2.1f:** Trough cross-lamination (Bouma C division); farm Dagbreek 365

original sediments to form load balls and ball-and-pillow structures (Fig. 2.1 e). Flame structures are also present. Pelitic rip-up clasts were found at the base of psammitic layers.

Individual psammite layers may be either massive and structureless, or show an internal organisation which may involve plane or cross-lamination. Small-scale trough cross-lamination (Fig. 2.1b, f) has been recognised in several beds and occurs mostly on top of massive, structureless psammites thus representing Bouma T<sub>AC</sub> divisions (cf. Kukla *et al.*, 1990).

The presence of sedimentary structures within graded units shows that parts of the Kuiseb Formation are organised in classical Bouma sequences (Bouma, 1962). Their presence confirms that the deposition of the precursor sediments was governed by turbidity currents. Based on measurements of flute casts and sets of trough cross-laminae, palaeocurrent directions were determined indicating a current flow along the basin axis from east-northeast to west-southwest (230° - 250°).

### 2.3.2 Sedimentary facies and facies associations

Although the metasediments have undergone severe deformation and metamorphism, sedimentary facies may be defined on the basis of bedding style, vertical bed thickness distribution, variations in psammite/pelite ratio and sedimentary structures. On the basis of these features and by comparison with common turbidite classification schemes (Mutti and Ricci Lucchi, 1975; Pickering *et al.*, 1986), the following seven facies classes, representing both turbidite and pelagic facies were defined by P. Kukla (1990; extending the facies classification scheme of P. Kukla *et al.*, 1988):

Facies class 1: medium- to very thick-bedded psammite facies, (comprising massive, structureless psammites; massive, organised psammites; parallel-stratified psammites, and cross-stratified psammites);

Facies class 2: very thick- to thin-bedded graded psammite/pelite facies;

Facies class 3: thin-laminated meta-siltstone facies;

Facies class 4: very thick- to thin-bedded pelite facies;

Facies class 5: impure metacarbonate facies;

Facies class 6: thin- to very thick-bedded graphite schist facies;

Facies class 7: marble and tremolite schist facies. (Bed thicknesses were defined as very thick beds > 100 cm, thick beds 40-100 cm, medium beds 10-40 cm and thin beds 1-10 cm.)

Detailed measured sections along the study traverse revealed that the above facies occur in characteristic facies associations and sequences. Vertical facies sequences define nested sedimentary thinning - and thickening-upward cycles in major parts of the Khomas Trough. Thinning-upward cycles were detected in the north, whereas large parts of the sedimentary sequence in the central Khomas Trough are organised into thickening-upward cycles. Largely non-cyclic sequences occur from just north of the Matchless Member to the southern margin of the trough (P. Kukla *et al.*, 1988). Cycles range in scale from metres to kilometres. Despite internal folding within these cycles, sequential lithofacies

changes occur and these may be traced laterally on all scales.

### 2.3.3 Palaeoenvironmental setting

The metasediments of the Khomas Trough have previously been interpreted in terms of a eugeosynclinal sequence by Martin (1965), whereas Miller *et al.* (1983) referred to the Kuiseb Formation as a flysch sequence deposited by turbidity currents in a fore-arc basin. Downing (1983) speculated upon a submarine fan environment.

The marked organisation of the Kuiseb Formation into cyclic and non-cyclic successions on a variety of scales as established in the study area, reflects a progradational and retrogradational sedimentation character. Taking into account the cyclicity and the defined facies, and comparing these with recent marine facies associations, leads to the interpretation of submarine fan and basin plain environments. The lateral extent of marker horizons and major sedimentation units, the consistency of palaeocurrents, the size of sedimentary cycles, the uniformity of lithologies and the lack of coarse-grained material, strongly suggest a mixed-sediment elongate fan system as defined by Nelson and Nilsen (1984). The distribution of facies, the vertical organisation of facies associations and the cyclic patterns indicate middle and outer fan associations in the northern and central Khomas Trough. The southern Khomas Trough, which is characterised by a lack of cyclicity, high pelite contents and reduced bed thicknesses, is interpreted to represent predominantly basin plain depositional environments (P. Kukla *et al.* 1988).

According to P. Kukla (1990), clastic sedimentation in the Khomas Trough commenced during divergent plate movements in the southern Damara Orogen. The lithofacies and facies associations indicate turbiditic sedimentation of clastic material on an elongate submarine fan within the Khomas Sea which developed between the Congo and the Kalahari Cratons. The sediment was transported laterally parallel to the margins of the basin from the northeast to the southwest. Palaeocurrent data confirm that a major sediment source was located at the northeastern end of the Khomas Trough. Minor amounts of calcareous material were shed off the northerly adjoining carbonate shelf. The mass-flow processes were accompanied by contemporaneous pelagic and hemipelagic sedimentation represented by the graphite schists and some of the pelites within the sequence. Reworking of pelagic material also occurred.

## 2.4 STRUCTURE

Previous work on the structure of the Khomas Trough was undertaken by Gevers (1963) and Smith (1965), Hiil-bich (1977), Blaine (1977), Sawyer (1981, 1983), Miller (1979, 1983a), Kasch (1983b), Preussinger (1987, 1990) and Preussinger *et al.* (1987).

In the study area, four phases of ductile deformation associated with cleavage development were discerned, three of which are coaxial with fold axes paralleling the general northeasterly regional trend. The recognition of structural elements is facilitated by nearly continuous outcrop and by



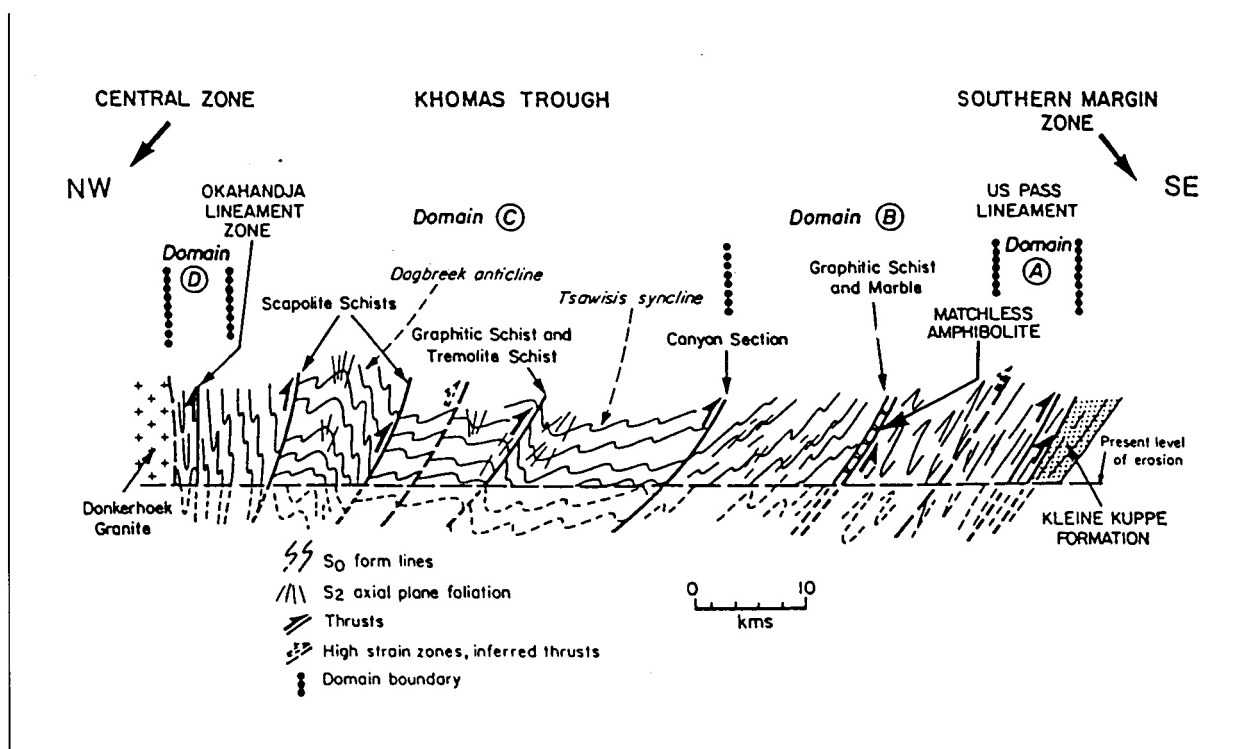


**Figure 2.3:** Structural profile across the Khomas Trough showing the style of major  $D_2$  folds and the position of major structural discontinuities (after P.Kukla, 1990)

folds. A third fabric ( $S_3$ ), developed preferentially in narrow shear zones and is mostly present as a penetrative biotite fabric. The orientation of  $S_3$  is similar to that of  $S_2$ . An  $S_4$  crenulation cleavage occurs in pelitic lithologies. The orientation of this fabric is variable, describing a clockwise rotation in strike from  $010^\circ$  to  $060^\circ$  northwards.

Folding during  $D_2$  has produced isoclinal  $F_2$  folds with wavelengths of up to 250 m, but mostly at a 10-20 m scale. Axial surfaces dip to the northwest and fold axes are sub-horizontal. In the Koam canyon section (farm Annerlie 412), downward-facing  $F_2$  folds could be discerned which were generated by refolding and thrusting of overturned  $F_1$  fold limbs (P. Kukla *et al.*, 1989). Small-scale, tight to isoclinal  $F_3$  folds developed in narrow shear zones with fold axes plunging moderately to the northeast and axial planes dipping to the northwest.

#### Domain C

In domain C only  $D_2$  and  $D_3$  structural elements were observed. Bedding is defined by sedimentary structures. The first planar structural element is considered to correspond to the  $S_2$  cleavage of the other domains. The fabric is mostly developed as a strong, pervasive metamorphic banding cleavage which is axial planar to  $F_2$  folds. The  $S_3$  fabric is restricted to narrow shear zones in the southern part of the domain, but becomes more prominent towards the north.

Major  $F_2$  folds could be mapped in this domain as indicated in Figure 2.3. Minor  $D_2$  folding produced folds with wavelengths of 5 to 50 m. The style of folding is pronouncedly asymmetric in most parts of the domain, with folds showing a northerly, steep to upright limb and a southerly, shallow-

dipping limb. Axial surfaces generally dip to the northwest. Fold axes are subhorizontal except in high-strain zones where fold axes plunge at low angles to the northeast.  $F_3$  folds at a m-scale occur mainly in high-strain zones. They are most prominent in the two scapolite schist sequences on the farms Kaan 309/Dagbreek 365 and Keises 312. Axial planes dip to the northwest and fold axes plunge at shallow angles to the northeast.

#### Domain D

This domain represents the northernmost part of the Khomas Trough up to the Donkerhoek Granite and is characterised by the occurrence of an  $S_4$  crenulation cleavage and steeply plunging fold axes. In addition, a clockwise rotation of fabric elements and fold structures occurred in that area.

Bedding is defined by sedimentary structures, and the first structural fabric recognised is the  $S_2$  cleavage which occurs as a strong, pervasive biotite fabric or metamorphic banding cleavage folded by  $D_3$  in shear zones. An  $S_4$  crenulation cleavage occurs in pelitic units.

$F_2$  folds are open to tight in the southern part of the domain and tighten towards the north to become strongly isoclinal with a wavelength decreasing to about 5 m. Minor folds indicate that the domain is situated on the overturned limb of a major  $D_2$  anticlinal structure. Axial planes of  $F_2$  folds dip towards the north and fold axes plunge at  $10^\circ - 40^\circ$  to the east in contrast with the usually horizontal to subhorizontal trend in other domains.  $F_3$  folds with wavelengths of about 5 m are developed in shear zones. Small-scale  $F_4$  folds were observed locally in the northern part of the domain.

### 2.4.2 Heterogeneous strain and thrusting in the Khomas Trough

Deformation within the study traverse is characterised by a highly heterogeneous distribution of strain on all scales. On a large scale, high-strain zones several hundreds of metres wide alternate with km-wide low-strain zones. Major high-strain zones are located on the southern margin of the Khomas Trough, within the Matchless Member sequence, the Koam canyon section on the farm Annerlie 412, within the central graphite schist unit on the farm Kaan 309, and within the two scapolite schist sequences on the farms Dagbreek 365 and Keises 312 (Fig. 2.3). The following characteristics are common to most of the high-strain zones: (1) the zones represent structural discontinuities where thrusting has been observed through the displacement of fold limbs which have been sheared out mainly during the  $D_2$  and  $D_3$  phases of deformation. There is evidence, however, that thrusting has already occurred during  $D_1$ ; (2) discontinuities are zones of major shear which is confirmed most markedly by deflected foliations; (3) discrete and abrupt changes of fold styles with respect to the  $D_2$  phase of deformation occur across the discontinuities (Fig. 2.3); (4) in high-strain zones there is a pronounced increase in the intensity of the  $D_3$  deformation which is comparatively weak in low-strain zones, indicating that major thrusting was associated with the  $D_3$  phase of deformation; (5) downward-facing  $D_2$  and  $D_3$  fold structures are confined to the high-strain zones, and (6) pervasive, post- $D_3$  scapolite formation within two of the major high-strain zones indicates fluid movements along the thrust zones.

In conclusion, the high-strain zones described are interpreted as major shear and thrust zones which are situated in pelitic sequences. The positions of major thrusts are shown in Figure 2.2. The structural features observed confirm that folding, cleavage formation and thrusting took place contemporaneously.

### 2.4.3 Time sequence of deformational events

The correlation of structural elements along the study traverse is based on the  $S_2$  fabric which is the most prominent planar structural element throughout the study traverse. It is always a recognisable metamorphic banding cleavage which is axial planar to  $F_2$  folds. Although the following time sequence of deformation is proposed in terms of various deformational phases inferred from successive cleavage and fold generations, the structural evolution through time must rather be seen as a continuous process.

#### *The $D_1$ phase of deformation*

The  $D_1$  phase of deformation is represented by an early biotite fabric which in most places is intensely transposed and refolded by subsequent stages of deformation. Relics of an  $S_1$  fabric can be observed in the structural domains A and B. In the southern portion of the Khomas Trough (domain A), the  $S_1$  cleavage forms part of the composite  $S_{0,1,2,3}$  fabric. North of the Matchless Member (domain B), the  $S_1$  fabric in places is still present as a distinct metamorphic banding cleavage in

$F_2$  fold hinges. Because of the later overprint, however, there is no consistency in orientation. The intense overprint could account for the lack of small-scale  $F_1$  fold hinges.  $F_1$  folds of regional scale can be inferred from downward-facing  $F_2$  structures which originated from the refolding of overturned  $F_1$  fold limbs as discussed by P. Kukla *et al.* (1989). Silicified and brecciated zones are cut by  $S_2$  demonstrating that thrusting had already begun during  $D_1$ . The structural style and the character of the  $S_1$  cleavage indicate an overall compressive regime.

#### *The $D_2$ phase of deformation*

The  $D_2$  phase of deformation is of regional importance and represents the only deformation with consistent characteristics throughout the Khomas Trough. The  $S_2$  fabric is the most prominent planar element that can be traced continuously across the Khomas Trough. It is therefore used to correlate other fabrics. Folding associated with  $D_2$  resulted in medium- to large-scale fold structures.

The major feature of the  $D_2$  deformational event is the strong, northwest-dipping  $S_2$  fabric which frequently developed as a metamorphic banding cleavage in psammitic rocks and as a penetrative, slaty cleavage in pelitic lithologies. In the southern part of the Khomas Trough, it forms part of the composite  $S_{0,1,2,3}$  fabric. The  $S_2$  cleavage is axial planar to  $F_2$  folds of various fold styles. Folds are tight to isoclinal in the southern part of the Khomas Trough (domain B) with wavelengths in the order of 10 m, with northwesterly dipping axial planes and with shallow northeasterly and southwesterly plunging fold axes. On the farm Bergkrans 370, there is strong evidence for downward-facing  $D_2$  folds as described by P. Kukla *et al.* (1989). Further north, in the central portion of the Khomas Trough (domain C), the style of folding changes to medium- to large-scale, open asymmetric folds which build major synformal and antiformal structures. This style of folding prevails to the very north of the study area (domain D), where strongly isoclinal folding occurred on a 5-10 m scale. In contrast to the other structural domains, fold axes here are steeply plunging to the east-southeast. Downward-facing of fold structures is also indicated in this domain. The style of major thrust-bound  $D_2$  fold structures across the Khomas Trough is shown in the schematic cross-section in Figure 2.3.

The consistent southeasterly vergence, the subhorizontal fold axes and the corresponding axial planar cleavage are indicative of a compressive stress regime. The development of open, asymmetric folds in low-strain zones in the central Khomas Trough might be attributed to southeast-directed translation during fold development (P. Kukla, 1990).

A major phase of thrusting is associated with this deformational event. The thrust zones are evident as high-strain zones within major pelitic units. Simple shear plays a major role as can be seen from non-coaxial deformation. The main thrusting phase occurred contemporaneous with folding at the culmination of the  $D_2$  deformational event.

#### *The $D_3$ phase of deformation*

Structural elements which characterise the  $D_3$  deformational event developed preferentially within high-strain zones. The  $S_3$  biotite fabric occurs as a penetrative spaced

cleavage and  $F_3$  folds occur mostly within these zones of high strain. The style and scale of folding, which includes plunging  $F_3$  fold axes, is indicative of shear processes that played a major role during  $D_3$ . In the northern Khomas Trough, the participation of fluid phases during deformation in high-strain zones is evident from a large-scale scapolitisation of metasediments. The  $D_3$  structural patterns indicate a compressive stress regime during deformation.

#### The $D_4$ phase of deformation

$S_4$  crenulation cleavages occur both in the southern and in the northern Khomas Trough. Locally, associated small-scale  $F_4$  folds developed. The appearance of the crenulation cleavages is restricted to pelitic lithologies where earlier planar fabrics are overprinted. The  $D_4$  deformation still affected some apophyses of the Donkerhuk Granite and an early generation of pegmatites which are also associated with the granite.

#### The $D_5$ phase of deformation

In the southern Khomas Trough, up to the Matchless Member, asymmetric and monoclinical kink folds occur which overprint the  $S_4$  crenulation of the area and thus are designated as  $D_5$  structures (Table 2.1). Axial planes generally dip southward.

	Planar elements				Folds				
Domain A	$S_{0,1,2,3}$			$S_4$				$F_4$	$F_5$
Domain B	$S_1$	$S_2$	$S_3$	$S_4$	$F_1$	$F_2$	$F_3$	$F_4$	
Domain C		$S_2$	$S_3$			$F_2$	$F_3$		
Domain D		$S_2$	$S_3$	$S_4$		$F_2$	$F_3$	$F_4$	

**Table 2.1a:** Summary of planar fabrics and folds encountered in structural domains A-D, after P. Kukla (1990)

Domain	E	D	C		B	A	Kukla et al. (1988)
Domain	D	C		B	A	Kukla (1990)	

**Table 2.1b:** Comparison of structural domains after P. Kukla et al. (1988) and P. Kukla (1990)

#### Strike-slip displacement along the northern margin of the Khomas Trough

As has been pointed out above, structural elements are rotated clockwise in the northernmost part of the Khomas Trough. This rotation has previously been explained as being related to the intrusion of the Donkerhuk Granite (Faupe, 1974) or by strike-slip movements along the Okahandja Lineament (Gevers, 1963; Blaine, 1977; Miller, 1979; Downing and Coward, 1981). P. Kukla (1990) inferred that the clockwise rotation occurred post- $D_4$  within a right-lateral transpressional strike-slip regime possibly contemporaneous with the intrusion of the Donkerhuk Granite.

#### 2.4.4 Structural evolution of the Khomas Trough

The structural evolution of the Khomas Trough is characterised by an early deformation ( $D_1$ ) associated with folding and fabric development as well as thrusting. The main regional deformation ( $D_2$ ) resulted in open and tight to isoclinal folding of strata with the development of a pervasive axial planar cleavage and contemporaneous thrusting. The direction of major compression was to the northwest and elongation occurred parallel to the  $D_2$  axes in a northeasterly direction. The  $D_3$  deformation was strongest in high-strain zones with the formation of a spaced cleavage and folds, accompanied by thrusting and pronounced shear. It can be concluded that deformation was progressive from  $D_1$  to  $D_3$ . Late deformation resulted in local crenulation cleavages, kink folds and a final right-lateral strike-slip displacement along the northern margin of the Khomas Trough which might have been contemporaneous with the emplacement of the Donkerhuk Granite.

The overall structural pattern shows that deformation within the Khomas Trough is characterised by contemporaneous folding and thrusting which led to the development of laterally extensive, northward-steepening thrust slices within an overall imbricate fan geometry with probably repeated sedimentary sequences.

## 2.5 METAMORPHISM

Previous work on the metamorphism in the Khomas Trough was undertaken by Hoffer (1977, 1978b, 1983) as part of a project on the thermal evolution of the entire Damara Orogen. Puhon and Hoffer (1973) investigated calc-silicate assemblages, Hoernes and Hoffer (1979) worked on stable isotopes and Behr et al. (1983) studied fluid inclusions within the Damara Orogen. Kasch (1983c, 1987) studied the metamorphism in the eastern Khomas Trough; Barnes and Sawyer (1980), Sawyer (1981), Preussinger (1987), and Häußinger (1990) worked in the western Khomas Trough.

The question of a polymetamorphic evolution of the Damara Orogen has long been a matter of discussion. It has been debated whether there was one long prograde, perhaps fluctuating phase of metamorphism which accompanied the whole tectonic development, or whether there were two or three discrete metamorphic peaks separated by a drop in temperature. Petrologic investigations on metapelites (Jacob, 1974; Hoffer, 1977, 1983) and siliceous carbonates (Puhon and Hoffer, 1973; Puhon, 1976, 1983) as well as oxygen-isotope studies (Hoernes and Hoffer, 1979) so far have only proved one prograde metamorphic phase. A polymetamorphic evolution was proposed by Kasch (1983c), Kröner et al. (1978) and Kröner (1982) based on micro-textural observations (e.g. different generations of critical mineral phases, discontinuously zoned garnet porphyroblasts) as well as geochronological data.

This section will a) outline critical mineral assemblages

and mineral textures along the study traverse and b) delineate the metamorphic development and the P-T conditions of metamorphism particularly for those samples which were selected for systematic Rb-Sr isotope analyses. These studies will provide a basis for the interpretation of the isotope data. Since only a limited number of samples was investigated, it is not possible to present a comprehensive petrographic description of the Kuiseb Formation along the entire study traverse. For more details the reader is therefore referred to Hoffer (1977) and P. Kukla (1990).

Petrographic investigations in the present study concentrate mainly on 6 composite samples selected for Rb-Sr small-domain analyses. The samples comprise different lithologies and show metamorphic grades from lower amphibolite facies up to partial melting. Additional pelite samples from crucial locations were investigated for a better documentation of mineral assemblages and reaction textures in the area.

Abbreviations used in the text and in figures are as follows: Qz = quartz, Pl = plagioclase, Ab = albite, An = anorthite, Kf = K-feldspar, Ch = chlorite, Ms = muscovite, Bi = biotite, Ga = garnet, St = staurolite, Cd = cordierite, Ky = kyanite, Ad = andalusite, Si = sillimanite, Hb = hornblende, Ep = epidote, Cc = calcite, V = vapour. The terms  $X_{Fe}$  and  $X_{Mg}$  represent the Fe/(Fe+Mg) and Mg/(Fe+Mg) ratios, respectively.

### 2.5.1 Mineral textures

Textural relationships of metamorphic mineral assemblages were investigated to delineate the relative timing of mineral formation with regard to deformation phases  $D_1$  to  $D_4$ . Due to their Al-rich bulk rock composition, the pelitic rocks provide a much greater variety of mineral assemblages compared to the rather monotonous psammites. The common mineral phases of pelitic as well as calc-silicate-bearing rocks of the Kuiseb Formation metasediments will be characterised as follows:

#### *Quartz*

Quartz forms a major constituent in the matrix of basically all metasedimentary rocks throughout the study traverse. It occurs in various grain sizes from fine- to coarse-grained and is generally well recrystallised. Only few samples were observed showing highly strained quartz crystals with undulous extinction and subgrain development.

#### *Plagioclase*

Plagioclase also occurs as a common constituent in psammitic and pelitic rock types with the exception of the scapolite schists where plagioclase has been replaced. Plagioclases are commonly fine- to medium-grained and occur as xenoblastic grains together with quartz forming the matrix of the rocks. The crystals are mostly untwinned with high-angle grain boundaries and may be weakly sericitised.

#### *K-feldspar*

K-feldspar was found only in one of the investigated samples from the immediate contact between the Kuiseb Formation metasediments and the Donkerhuk Granite. The psam-

mitic material of this sample is coarsely recrystallised and contains both microcline and muscovite. The latter, however, might be of retrograde origin.

#### *Biotite*

Biotite occurs in almost all rock types throughout the study traverse and forms a major constituent of pelitic rocks. Biotite crystallised at various stages throughout the metamorphic P-T evolution, and several synkinematic as well as post-kinematic generations were found. Synkinematic biotites which essentially define the different planar and linear fabrics occur as flakes and lath-shaped crystals aligned within the cleavage domains. Post-kinematic biotites generally form platy, unoriented crystals overgrowing all previous structural features. These late biotites may reach grain sizes of several millimetres. The biotites are mostly brown to red-brown in colour which accounts for all individual biotite generations present within one sample. Green-brown biotites are less frequent, but do occur in the southern part of the Khomas Trough. Small zircon crystals form frequent inclusions in the biotites causing abundant pleochroic haloes.

#### *White mica*

White mica occurs throughout the study traverse in syn- and post-kinematic generations. Synkinematic white micas generally occur as small (mostly below 0.5 mm) crystals oriented within the structural fabrics (composite fabric in the southern Khomas Trough or  $S_2$  in the northern part). These early white micas are associated with prograde chlorites to form the matrix of pelitic rocks, but they also occur together with biotite throughout the study traverse. Two generations of retrograde white mica can be identified. 1) Late crosscutting, platy white micas formed after sillimanite/fibrolite often with relic inclusions of the latter phases. The grains may also appear as ragged crystals intergrown with quartz and may reach grain sizes of several millimetres. The crystallisation of this generation partly predates the  $S_4$  crenulation cleavage observed in the northern Khomas Trough, but the muscovites were also found overprinting the  $S_4$  crenulation cleavage. 2) Late sericitisation of the  $Al_2SiO_5$  polymorphs and staurolite is frequent and can lead to a replacement of those minerals.

#### *Chlorite*

Chlorite occurs as prograde, synkinematic as well as post-kinematic, retrograde phase. Prograde chlorite is restricted to the southern half of the study traverse where it occurs as fine-grained flakes or laths oriented in the composite structural fabric or, further north, in the  $S_1$  and  $S_2$  cleavages. A post-kinematic generation of coarse-grained chlorite overgrows the regional  $S_4$  crenulation and occurs as laths or platy porphyroblasts up to several millimetres in grain size. Additionally retrograde chloritisation of biotite and garnet occurs.

#### *Garnet*

Three generations of garnets can be distinguished on the basis of their textural relationships. Garnets of generation I are generally anhedral, intimately intergrown with quartz

and elongated parallel to the composite fabric in the southern Khomas Trough. Length/width ratios may reach 10:1. The timing of crystallisation is uncertain, but could be pre-D<sub>2</sub>. Garnet porphyroblasts of generation II are subhedral to euhedral and bear snowball inclusion trails of opaque phases which correspond to the composite fabric of the rock. This type of garnet occurs rarely in the investigated samples; a syn-D<sub>2</sub> growth was inferred for this generation (P. Kukla, 1990). The garnets of generation III developed mostly as euhedral to subhedral porphyroblasts which overgrow all structural fabrics up to the S<sub>3</sub>-cleavage thus post-dating D<sub>3</sub>. The different generations of garnets were observed to occur within the same samples. Garnets occurring in the neosomes of the investigated migmatite sample are anhedral and appear fragmented. There is no textural evidence on the timing of garnet growth in the migmatites, but a pre-migmatitic crystallisation may be inferred.

#### Staurolite

Staurolite is a common phase in pelitic rocks throughout most of the study traverse. In the investigated samples it occurs as subhedral to euhedral porphyroblasts commonly up to 5 mm grains, occasionally reaching cm-size. The post-D<sub>3</sub> crystallisation of the staurolite is inferred from the overgrowth on the composite fabric in the southern Khomas Trough and the S<sub>3</sub> cleavage in the north. In one sample, remnants of largely sericitised, poikiloblastic staurolites were observed which indicate also earlier generations of staurolite.

#### The Al<sub>2</sub>SiO<sub>5</sub> polymorphs

Kyanite was found in quartz segregations in the field, which are similar features to those described by Kerrick (1988) for the Lepontine Alps. Kyanite was not observed, however, in the investigated samples, but has been described by Hoffer (1977) and P. Kukla (1990) to occur in paragenesis with garnet.

Andalusite has a rather limited occurrence in the central Khomas Trough. The mineral forms mostly large, up to 10-cm-long, randomly oriented porphyroblasts which crosscut the S<sub>2</sub> and S<sub>3</sub> fabrics, indicating a post-S<sub>3</sub> age of crystallisation. Most andalusite porphyroblasts are largely replaced by muscovite. In the investigated samples, relics of largely sericitised andalusite were found in samples KB307 and CO418. The relics possibly put constraints on an earlier crystallisation phase of the mineral.

Sillimanite occurs nearly exclusively as fibrolite together with biotite forming nodular aggregates. The fibrolite nodules are frequently elongated parallel to the S<sub>2</sub> and S<sub>3</sub> cleavages, but are deformed by the S<sub>4</sub> crenulation. In places, the fibrolite nodules are largely replaced by platy muscovites which may be intergrown with quartz. Most of the muscovites still contain some fibrolitic and rarely prismatic sillimanite.

#### Graphite

Graphite occurs as small flakes mainly in pelitic rocks. It may become a major component in some horizons, especially in the graphite schists.

#### Calcite

Calcite is a common constituent of all calc-silicate rocks which are intercalated with the more siliceous rock types.

#### Epidote group

Epidote or clinozoisite and/or zoisite are frequent in calc-silicate assemblages and calc-silicate-bearing rocks of the Kuiseb Formation.

#### Amphiboles

When present, green hornblende may be a major constituent of calc-silicate rocks. The timing of calc-silicate formation can best be inferred from textural relationships of hornblendes. In well defined bodies of calc-silicate material, an early generation of hornblendes was found both aligned parallel to the S<sub>2</sub> foliation of the surrounding rocks as well as partly overgrowing the fabric. A second generation of hornblendes is deformed by small-scale D<sub>3</sub> folds, but also overgrows these structures. Judging from these relationships, the hornblendes must have crystallised syn- to post-kinematically with regard to both the D<sub>2</sub> and D<sub>3</sub> deformation phases.

#### Titanite

Titanite occurs as accessory phase in pelitic rocks, but may reach considerable quantities in calc-silicate rocks. In the latter rocks titanite forms massive aggregates of anhedral grains and is mostly associated with biotite and calcite.

#### Scapolite

Scapolite occurs as a major constituent in two largely scapolitised sequences in the northern Khomas Trough. It appears in minor quantities in calc-silicate nodules where it is either concentrated in the centre or forms a reaction rim around the calc-silicate material. Scapolite forms generally large (up to 2 cm), poikiloblastic and unoriented porphyroblasts which overgrow S<sub>2</sub> and S<sub>3</sub> textures, thus indicating a post-D<sub>3</sub> age of crystallisation. With the exception of plagioclase which was quantitatively replaced, the poikiloblasts enclose all other mineral phases present in the rocks.

The relative timing of mineral growth with regard to deformational events is summarised in Figure 2.4. Only little is known about the pre-D<sub>2</sub> mineral growth. Kyanite was omitted in the diagram, since the mineral is only scarcely occurring.

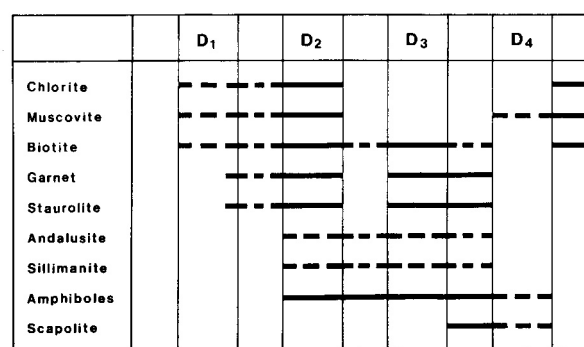
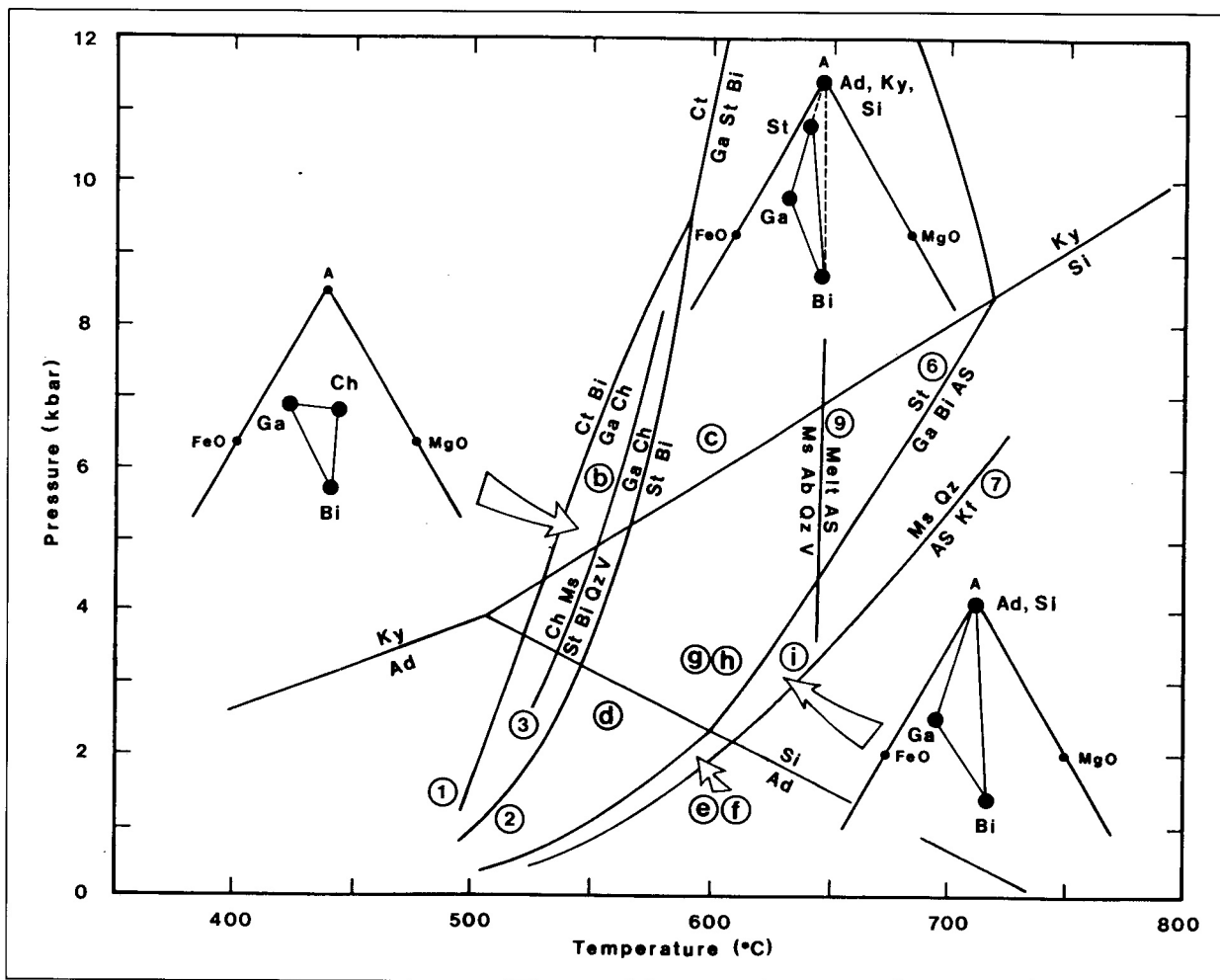


Figure 2.4: Digram showing the relative timing of mineral growth with respect to deformational events in the central Khomas Trough. Dashed lines stand for uncertain crystallisation

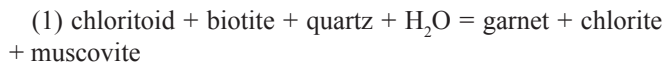




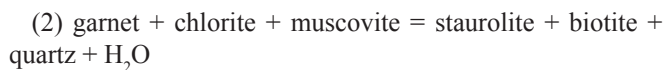
**Figure 2.6:** Partial petrogenic grid for the KFMASH system after Spear and Cheney 1989) showing the stability fields of the mineral assemblages (AFM projections) occurring in the metapelites of the study area. Circled letters refer to metamorphic assemblages (a) - (i), circled numbers refer to reactions discussed in the text. Reactions (1), (2), (6) after Spear and Cheney (1989); (3) after Hoschek (1969); (7) after Chatterjee and Johannes (1974); (9) after Storre (1973). Stability fields of aluminium silicates after Holdaway (1971)

quently be observed from an interlayering of horizons comprising garnet-chlorite and staurolite-biotite assemblages. Prograde chlorite was not found north of the farm Kaan Dam 411 as indicated in Figure 2.5.

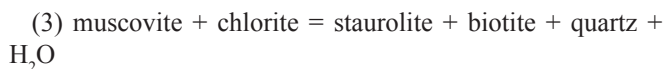
The absence of chloritoid may indicate that chlorite formed according to the reaction



after Spear and Cheney (1989). Staurolite formation may be attributed to the reactions



as determined by Thompson (1976) and



experimentally determined by Hoschek (1969). The reac-

tions terminate the occurrence of prograde chlorite in the presence of muscovite.

*Assemblage zone 2*

This assemblage zone is characterised by the presence of andalusite. The occurrence of the latter extends geographically from the footwall of the central graphite schist unit on the farm Kaan 309 to the southern border of the farm Davetsaub 365, where relics of andalusite were found in the investigated samples KB307 and CO418. The division of the assemblage zone into two sub zones according to P. Kukla (1990) has therefore been revised. The critical assemblages are

d) andalusite + staurolite + biotite + muscovite + plagioclase + quartz garnet,

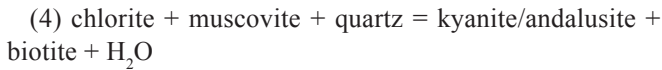
e) andalusite + biotite + muscovite + plagioclase + quartz garnet,

but the andalusite-free assemblage

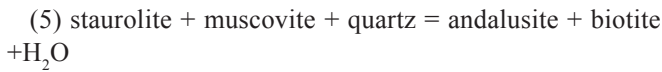
f) staurolite + garnet + biotite + muscovite + plagioclase + quartz

is the most common paragenesis occurring in the pelitic rocks of the area. Andalusite formation has been inferred by

Hoffer (1977) through the reaction



described by Carmichael (1970) and through the decomposition of staurolite according to the reaction



experimentally determined by Hoschek (1969) at  $575 \pm 15^\circ\text{C}$  at 2 kb and  $675 \pm 15^\circ\text{C}$  at 5.5 kb. In the northern part of the assemblage zone, however, both andalusite and staurolite occur as largely sericitised relics which do not allow to draw conclusions on their relative timing of formation.

#### *Assemblage zone 3*

Assemblage zone 3 is bordered to the south by the first appearance of sillimanite and towards the north by the last occurrence of staurolite. Critical assemblages are

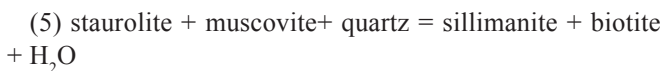
g) sillimanite + staurolite + garnet + biotite + muscovite + plagioclase + quartz and

h) sillimanite + staurolite + biotite + muscovite + plagioclase + quartz.

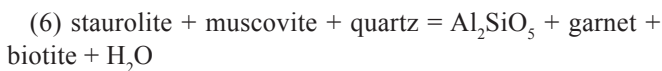
Staurolite, however, successively decreases towards the north and most of the investigated samples of this assemblage zone are already dominated by the paragenesis

i) sillimanite + biotite + muscovite + plagioclase + quartz.

Sillimanite occurs mainly in form of nodules consisting of fibrolite + biotite. Although no staurolite was observed in these nodules, the conspicuous aggregates may have formed according to the reaction



experimentally determined by Hoschek (1969). The garnet-bearing assemblage g) may have formed according to the reaction



described by Guidotti (1970) and calculated by Spear and Cheney (1989).

#### *Assemblage zone 4*

The southern border of assemblage zone 4 is defined by the last occurrence of staurolite on the farm Keises 312, about 5 km south of the Donkerhuk Granite. The main paragenesis occurring in this zone is

i) sillimanite + biotite + muscovite + plagioclase + quartz which may be ascribed to the decomposition of staurolite according to reaction (5).

K-Feldspar (microcline) was only found in one pelitic sample from the immediate contact of the Kuiseb Formation and the Donkerhuk Granite. The microcline could have

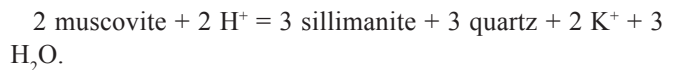
formed according to the reaction



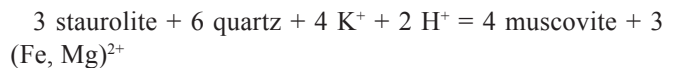
determined by Chatterjee and Johannes (1974), although muscovite is present within the sample. The muscovite, however, might be of retrograde origin. In the Khomaska section of the study traverse, the metamorphic assemblage i) is regarded as representing the highest metamorphic conditions attained during metamorphism.

#### *Retrograde mineral reactions*

Retrograde mineral reactions occurred throughout the study area. Post-kinematic formation of large platy porphyroblasts of chlorite, muscovite and biotite is frequent, but apparently occurred close to the temperature peak of metamorphism and has to be distinguished from later sericitisation and chloritisation of minerals. The breakdown of the  $\text{Al}_2\text{SiO}_5$  polymorphs and staurolite to muscovite is a common feature. Very similar observations have been made by Wickham (1987) who claims a high temperature, retrogressive hydration of the rocks responsible for the formation of the late muscovites. Eugster (1970) ascribed the muscovitisation of sillimanite to the reaction



The replacement of staurolite by muscovite may have occurred according to the reaction



after Carmichael (1969) who reports this reaction to be common near the upper limit of the staurolite zone. The formation of this late muscovite generation therefore requires reasonably high temperatures. Within the study area, the formation of late muscovites is most probably contemporaneous with the  $D_4$  phase of deformation in the northern Khomas Trough.

#### *The migmatite zone of Davetsaub*

In contrast, further west in the Davetsaub river section of the study area, partial melting of the Kuiseb Formation metasediments has occurred (Fig. 2.5). The genesis of these migmatites, however, has been discussed rather controversially in terms of contact or regional metamorphism. Since the migmatites bear a key role in delineating the timing of metamorphism and magmatism along the northern margin of the Khomas Trough, their relationships to the non-migmatitic metasediments of the Kuiseb Formation and to the Donkerhuk Granite will be presented in more detail in an own chapter (Chapter 3). Disregarding genetic discussions, phase relations within the migmatites will be discussed in this chapter. Solidus relations in the system  $\text{Na}_2\text{O-K}_2\text{O-CaO-Al}_2\text{O}_3\text{-SiO}_2\text{-H}_2\text{O}$  are presented in Figure 2.7.

The migmatites occurring in the Davetsaub area have previously been described to comprise different (compositional and genetic) types of leucosomes (Nieberding, 1976). This

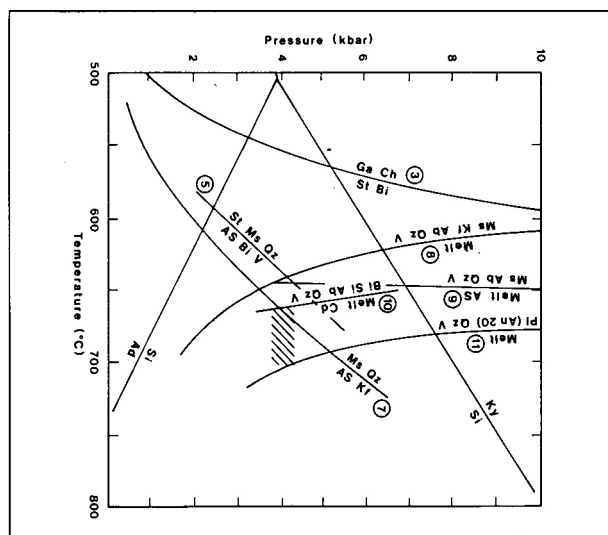


**Figure 2.7:** Solidus phase relations for the system  $\text{Na}_2\text{O}-\text{K}_2\text{O}-\text{CaO}-\text{Al}_2\text{O}_3-\text{SiO}_2-\text{H}_2\text{O}$  and partial petrogenic grid for the KFMASH system. Reactions (1) and (2) after Spear and Cheney (1989); (5) after Hoschek (1969); (7) after Chatterjee and Johannes (1974); (8) after Thompson and Algor (1977); (9) after Storre (1973); (10) after Hoffer (1978); (11) after Johannes (1978, 1985). Stability fields of aluminium silicates after Holdaway (1971). Hatched area indicates the range of experimentally determined solidus temperatures for Kuiseb Formation pelites and migmatites (after Hoffmann, 1976)

study is mainly interested in the *in situ* generated leucosomes showing trondhjemitic composition. In this type of leucosome as well as the palaeosomes K-feldspar is absent which is a typical feature of the Kuiseb Formation in general. Some K-feldspar may have formed through the decomposition of muscovite prior to the onset of partial melting. In this case the granite minimum melting according to the reaction

(8) muscovite + K-feldspar + albite + quartz +  $\text{H}_2\text{O}$  = melt

(Thompson and Algor, 1977) could fairly describe the phase relations encountered during partial melting. Thompson and Tracy (1979) have shown that subsolidus and melting reactions involving calcic plagioclase in pelitic assemblages in the K-Na-Ca model system occur at higher temperatures than in Na-K model systems. The above granite minimum melting curve can thus provide at least minimum temperature estimates for partial melting in the study area. Melting in the absence of K-feldspar could have occurred according to the reaction

(9) muscovite + albite + quartz +  $\text{H}_2\text{O}$  = kyanite/sillimanite + melt

as determined by Storre (1973) at about  $650^\circ\text{C}$  in the pressure range between 3.5 and 11 kb (provided  $P_{\text{tot}} = P_{\text{H}_2\text{O}}$ ). Hartmann *et al.* (1983) described the sporadic appearance of anatexites in the immediate vicinity of the Donkerhuk Granite and favoured the above reaction for their genesis. In the study area, however, sillimanite appears to be restricted

to the restates in form of deformed fibrolite nodules. Hoffer (1978a) investigated the stability limits for the assemblage biotite + sillimanite + quartz in the presence of albite along the cordierite-forming reaction

(10) biotite + albite + sillimanite + quartz +  $\text{H}_2\text{O}$  = melt + cordierite.

Cordierite, however, was neither found in the migmatites nor in the non-migmatitic Kuiseb Formation metasediments. Some rare pinitic aggregates might indicate the former presence of the mineral. Johannes (1978, 1985) experimentally investigated the melting behaviour in the tonalite system Qz-Ab-An- $\text{H}_2\text{O}$  with changing Ab/An ratios. The solidus relations for the reaction

(11) plagioclase (An 20) + quartz +  $\text{H}_2\text{O}$  = melt

were determined at about  $700^\circ\text{C}/5$  kb (Fig. 2.7). Plagioclase compositions determined from the investigated migmatite sample show 27-31 % An content. The reaction, however, does not account for the presence of Fe- and Mg-silicates and may thus also be rather an approximation of the true solidus relations.

Neither of the above phase equilibria satisfactorily accounts for the paragenesis found in the neosomes and palaeosomes of the migmatites. But certainly they provide a rough estimation of the P-T conditions of partial melting in the aluminous pelites of the Kuiseb Formation. Furthermore, all of the above considerations are based on the assumption that  $P_{\text{H}_2\text{O}}$  equals  $P_{\text{tot}}$ . If  $P_{\text{H}_2\text{O}} < P_{\text{tot}}$ , the melting reaction curves will be shifted towards higher temperatures as was shown for the granite solidus by Kerrick (1972). The discussed melting reactions thus provide minimum estimates for the P-T conditions of partial melting in the Kuiseb Formation.

### 2.5.3 Aspects of metamorphic banding formation

The  $S_2$  metamorphic banding cleavage which is axial planar to  $F_2$  folds is a prominent feature in meta-greywacke layers throughout the study traverse. The development of metamorphic banding cleavages reflects the intimate connection of deformation and metamorphism. With regard to the metamorphic processes which bear an important role in the evolution of isotope systems and the extent of isotopic equilibration (cf. Chapter 5), some of the mechanisms of metamorphic banding formation shall be discussed briefly in the following. The term "metamorphic banding" used in this context is comparable to what Hobbs *et al.* (1976) referred to as "differentiated layering", i.e. a layering which has clearly formed by some differentiation process during deformation and metamorphism. Such a process may be inferred in cases, as in the study area, where original bedding is preserved.

The banding is characterised by an alternation of phyllosilicate-rich and quartz-plagioclase-rich domains, termed P- and Q-domains, respectively (Williams, 1972; Stephens *et al.*, 1979; Beach, 1979). Spacing of the cleavage domains occurs on a mm- to cm-scale (Fig. 2.8). In P-domains an en-

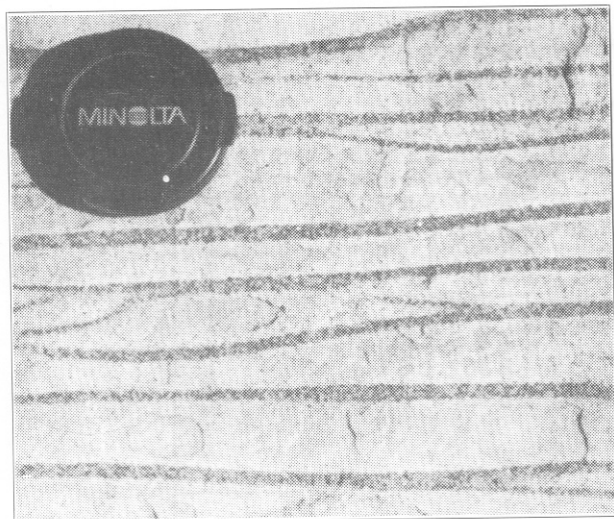


**Figure 2.8a (above):** Typical appearance of spaced metamorphic banding cleavage in a psammitic rock (lens cap is 4.9 cm in diameter); farm Keises 312

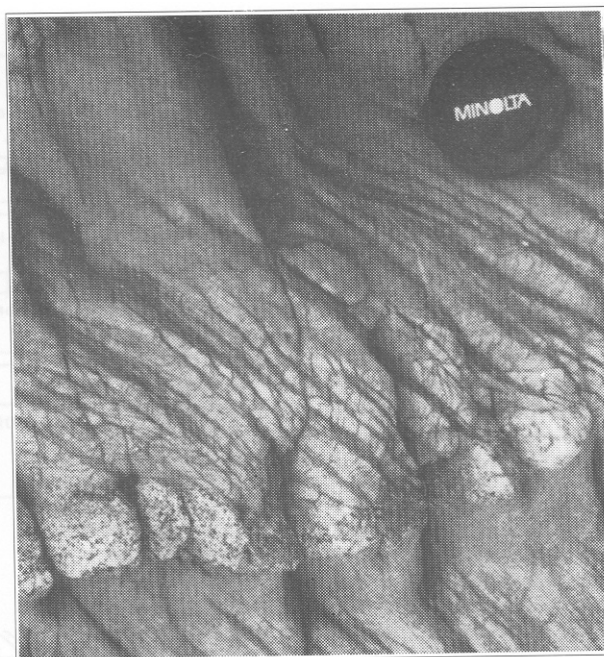


**Figure 2.8b (right):** Metamorphic banding cleavage which developed selectively in the psammitic base of a graded layer; farm Dagbreek 365

richment of tourmaline has been observed, the boron content of which may be derived from detrital clay minerals (Behr *et al.*, 1983).

Metamorphic layering has frequently been described from metamorphic greywackes. The formation of metamorphic banding cleavages generally is assumed to occur during low-grade metamorphism at shallow depth (6-8 km; Engelder and Marshak, 1985). The genesis of metamorphic differentiation, however, has been discussed rather controversially. Essentially, two hypotheses have been proposed. One theory concentrates on pressure solution predominantly of quartz and its removal by solute transfer as the driving force of the metamorphic differentiation (Williams, 1972; Beach, 1917, 1979, 1982; Gray, 1979a, 1979b; Wright and Platt, 1982). Beach (1979) proposed reactions for the decomposition of detrital minerals (K-feldspar, detrital micas) and the formation of phyllosilicates during the development of a metamorphic banding. The reactions are characterised mainly by the mobility of  $K^+$  and  $H^+$  ions. Stephens *et al.* (1979) demonstrated chemical mobilities for elements other than Si, in particular Na, Mn, Ca, P, Fe and Mg.

The transfer distance of solute has considerable implications for the nature of fluid behaviour in metamorphic terranes, i.e. the closed or open system behaviour of deformation and the degree of volume loss (Waldron and Sandiford, 1988). The latter authors suggest that P-Q fabrics develop in response to plain-strain deformation dominated by solute transfer at cm-scale via diffusion in a stationary fluid rather than large-scale advective fluid transport as proposed by Etheridge *et al.* (1983, 1984). The second hypothesis relates the formation of P-Q fabrics to dewatering mechanisms during the pre-lithification stage of the sediments. The enrichment in phyllosilicates is interpreted to be the result of clay mineral concentration caused by settling effects in dewatering channels (Behr *et al.*, 1983).

An application of these theories to the study area has to

consider that the  $S_2$  metamorphic banding cleavage shows oblique angles to bedding  $S_0$ . Furthermore the fanning of the cleavage around  $D_2$  fold structures strongly suggests that the P-Q-domains originated from processes during the  $D_2$  phase of deformation and the associated thermal regime.

#### 2.5.4 Mineral chemistry

Mineral compositions were analysed by microprobe 1) to investigate the compositional variation of the composite mineral concentrates used for isotope analyses and 2) to apply quantitative geothermobarometry for an evaluation of the metamorphic P-T path. The investigated samples are a pelite from the southern border of the study area (CO138) and six composite, psammite- as well as pelite- and calc-silicate-bearing samples chosen for Rb-Sr isotope analyses (KB167, CO117, KB307, KB421, KB115 and KB103). Sample localities are shown in Figure 2.9. With regard to the composite nature of the mineral fractions (micas) used for the isotope analyses (cf. Chapter 5), most mineral data were averaged if there was no systematic or significant variation in mineral compositions found within lithologically homogeneous units of the composite samples. Analytical conditions and analytical data are provided in the Appendix (Tables A.1-A.6).

#### Plagioclase

Microprobe analyses yield a range in the An-content between 13 and 31% for the samples CO138, KB167, KB117, KB307, KB115 and KB103 (Table A.1; Fig. 2.10). A variation of plagioclase compositions within the composite samples of up to 10% (e.g. sample KB167) is controlled by the bulk rock composition of lithologically different parts of the respective samples. The plagioclases in the calc-silicate-bearing sample KB421 vary between about 40 and 60% An-component (Fig. 2.10). All of the investigated plagioclase grains are apparently unzoned.

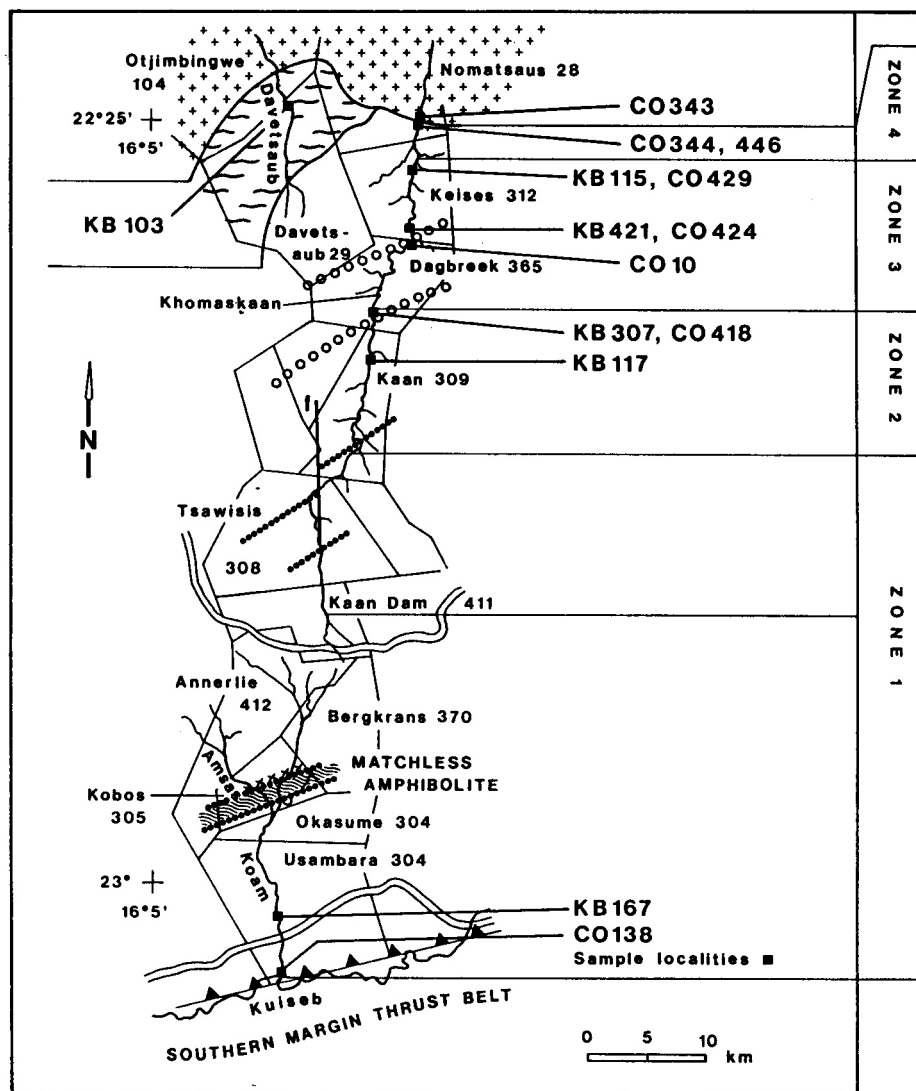


Figure 2.9: Sketch map of the study traverse showing sample localities and metamorphic assemblage zones 1 - 4. For key to symbols see Figure 2.2

### Biotite

Biotites were analysed from all seven samples and from different generations within these samples. No systematic internal variation in the chemical composition of the biotites with regard to different generations was found within the individual samples. In general, the biotites are dominated by the end members (after Holdaway *et al.*, 1988) phlogopite-annite (30-57%) and eastonite-siderophyllite (24-38%), Ti-biotite makes up 7-20% (Table A.2). From south to north of the study area, an increase in the  $Al^{IV}$  concentration from about 2.4 to 2.6 is indicated with the exception of the calc-silicate-bearing sample KB421, showing an  $Al^{IV}$  value of about 2.35 (Table A.2).

### White Mica

Microprobe analyses of white micas were carried out from the samples CO138, CO117, KB307, KB115 and KB103. Cations were calculated on the basis of 22; end members were calculated following Holdaway *et al.* (1988). The composition of the analysed white micas is generally muscovite-dominated with up to 9% celadonite component. The percentage of paragonite in solid solution ranges between 5 and 18%. The

measured Si values range from 6.0 to 6.3 (Table A.3). The analyses of different generations of white micas, synkinematic as well as post-kinematic (e.g. in sample KB307), showed that the late muscovite porphyroblasts apparently have lower Si values than matrix muscovites from the same sample. Due to their chemical composition close to pure muscovite, white micas will be referred to as muscovites in the following text. Paragonite was not found in any of the investigated samples.

### Chlorite

Chlorites were analysed in the samples CO138 and KB167 from the southern Khomas Trough. Prograde chlorites from sample KB167 have an  $X_{Mg}$  of 0.60, those from sample CO138 show a value of 0.58 (Table A.4) which is well in agreement with the analytical data of Hoffer (1977). Retrograde chlorites (CO138) can be shown to have a significantly lower  $X_{Mg}$  of 0.37 (Table A.4).

### Hornblende

Hornblendes were analysed only from the calc-silicate-rich sample KB421 from the northern scapolite schist unit (Table

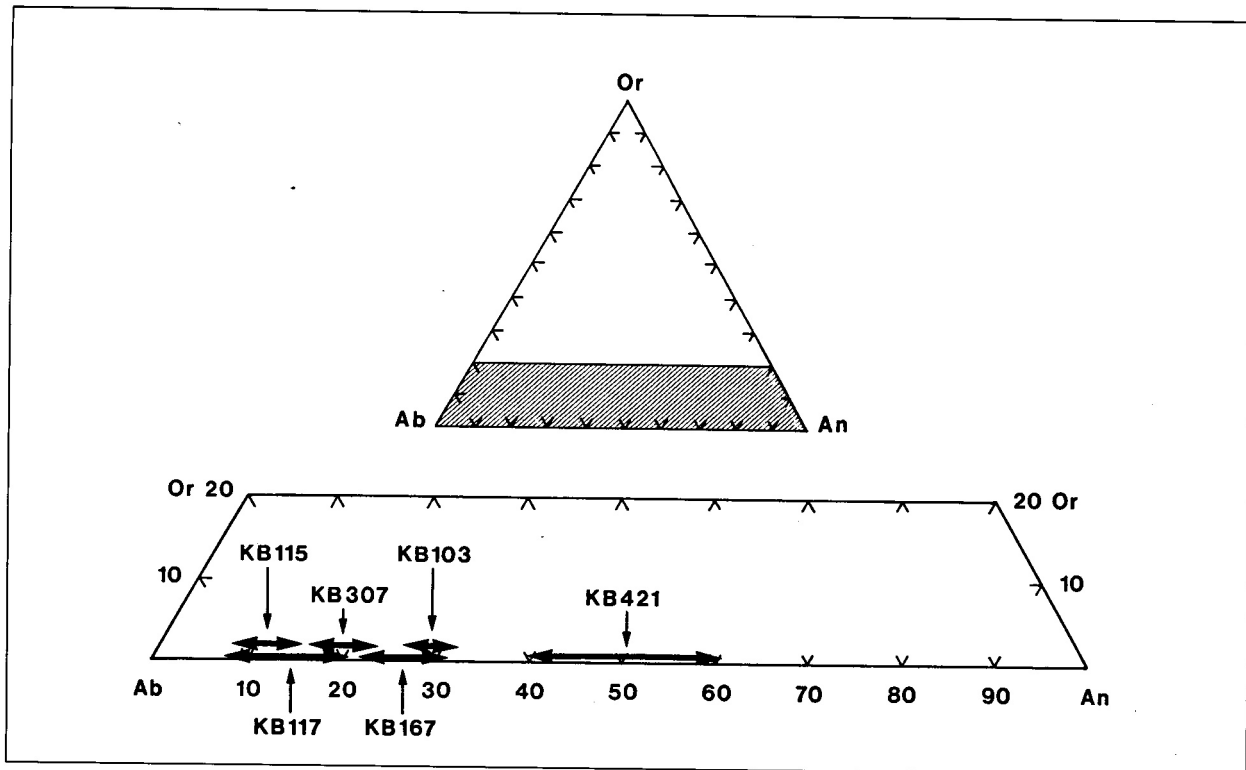


Figure 2.10: Plagioclase compositions of the investigated microprofiles shown in system Ab-An-Or

A.5). Using the nomenclature of Leake (1978), the chemical composition is that of magnesio-hornblendes of the group of calcic amphiboles.

#### Garnet

Microprobe analyses were carried out on garnets of generations I and III (Table A.6). Representative analyses of garnets from the samples CO138, KB167, KB307 and KB103 are illustrated as end member concentration profiles in Figure 2.11. The garnets from assemblage zone I (samples CO138, KB167) show a well-developed zonation expressed by an increase in both almandine and pyrope components at the expense of spessartine from the core to the rim of the crystals (Fig. 2.11a, b). For sample CO138, an inversion of the distribution curves is indicated for the outermost rim of the garnet which may be attributed to a diffusional cation exchange in the outer rim during the retrograde P-T path. Assemblage zone 2 garnets (sample KB307) seem less distinctly zoned, but show end member distribution profiles which are comparable to the above samples (Fig. 2.11 c, d). Unlike the garnets from the assemblage zone I and 2, the garnets from the migmatized meta-sediments of the northern Khomas Trough do not show any prograde zonation. A retrograde element distribution pattern is instead indicated by an increase in Mn at the expense of Mg for the outer rim of the crystals (Fig. 2.11 e, f). The absence of a prograde zonation probably reflects its elimination by cation diffusion during/after the temperature peak of metamorphism (Dempster, 1985). Yardley (1977) assumed the homogenisation of garnet zonations to start above temperatures of about 640°C.

#### 2.5.5 P-T conditions of metamorphism

Critical mineral assemblages and the application of geothermo-barometers were used for qualitative and quantitative estimation of the pressure and temperature conditions encountered during metamorphism. Relevant experimentally determined and calculated equilibrium curves which were discussed above (Figs 2.6 and 2.7) are referred to in the following. P-T estimations were made on the assumption  $P_{\text{tot}}$  equals  $P_{\text{H}_2\text{O}}$ .

##### Qualitative P-T estimations

Pelites in assemblage zone I are characterised by the presence of prograde chlorite + muscovite and biotite-staurolite-garnet assemblages in the absence of chloritoid. A lower temperature and pressure limit of about 530°C/4 kb is given by reaction (1) calculated by Spear and Cheney (1989). For the southern part of assemblage zone I, an upper temperature/pressure limit of 590°C/9.5 kb is given by the stability limit of chlorite + muscovite (3) experimentally determined by Hoeschek (1969) at 540±15°C at 4 kb and 565±15°C at 7 kb.

The transformation of kyanite into andalusite which was mapped as an isograd by Hoffer (1977), suggests a discontinuity within the metamorphic series in the central Khomas Trough. If andalusite and kyanite had formed according to the same reaction, a distinct drop in metamorphic pressure is indicated for the transition between assemblage zones I and 2 (Fig. 2.6).

For assemblage zone 2, a maximum pressure of 3 kb and a maximum temperature of about 610°C can be inferred from

Sample	CO138	KB167	CO117	KB307	KB115	KB103
(estimated pressure)	(6 kb)	(6 kb)	(3 kb)	(3 kb)	(4 kb)	(4 kb)
<b>Garnet-biotite thermometry</b>						
F & S (1978)	591-643°C	516-532°C		563-609°C		544-614°C
H (1986)	645-709°C	577-603°C		584-634°C		570-646°C
I & M (1985)	573-631°C	526-570°C		587-635°C		553-612°C
P & L (1983)	591-615°C	548-557°C		582-607°C		563-607°C
K <sub>D</sub>	0.18-0.21	0.14-0.15		0.16-0.20		0.16-0.19
<b>Muscovite-biotite thermometry</b>						
Hoisch (1989)	543-578°C		565-653°C	440-526°C	493-567°C	508-530°C
Abbreviations: F & S (1978) = Ferry and Spear (1978); H (1986) = Hoinkes (1986); I & M (1985) = Indares and Martignole (1985); P & L (1983) = Perchuk and Lavrent'eva (1983). K <sub>D</sub> = (Fe/Mg) <sub>Biotite</sub> / (Fe/Mg) <sub>Garnet</sub>						

Table 2.2: Summary of thermometric data

the presence of andalusite in paragenesis with staurolite and biotite and/or with garnet. The respective P-T field is framed by the andalusite-sillimanite equilibrium curve after Holdaway (1971), by reaction 7 curve (2) and by the upper stability of muscovite according to the reaction curve (7) determined by Chatterjee and Johannes (1974).

The P-T conditions in assemblage zone 3 are bracketed by the Al<sub>2</sub>SiO<sub>5</sub> phase transitions andalusite-sillimanite and sillimanite-kyanite, by the upper thermal stability of muscovite according to reaction (7) and the absence of partial melting. The equilibrium curves allow for a possible range in P-T conditions of about 2-7.5 kb and 540-700°C if referring for the maximum conditions to melting curve (11) after Johannes (1978, 1985; Figs 2.6 and 2.7).

A more precise estimate may be obtained for assemblage zone 4. A lower temperature/pressure limit of 590°C/2.5 kb is given by staurolite decomposition according to reaction (5). In the absence of migmatitic structures in the Khomaska river section, the maximum temperature attained in assemblage zone 4 is estimated from K-feldspar-free melting reactions (9), (10) and (11). Reactions (5), (7) and (11) define maximum P-T conditions of 680°C/5.5 kb and 700°C/4.5 kb.

The same solidus relations may serve to estimate minimum temperatures reached during partial melting of the Kuiseb Formation in the study area. Pressures may range between 3.5 kb, inferred from the reactions (7) and (8) and about 7 kb

which is the intersection of the sillimanite-kyanite boundary and reaction (11) in Figure 2.7.

#### Quantitative P-T estimations

For quantitative P-T estimations, geothermobarometric calculations can be applied to garnet-biotite and muscovite-biotite assemblages which both are common to all metamorphic zones within the Khomas Trough. Garnet-biotite thermometry was employed using the data of Ferry and Spear (1978), Perchuk and Lavrent'eva (1983), Indares and Martignole (1985) and Hoinkes (1986). Muscovite-biotite geothermometry was employed according to Hoisch (1986). The phengite-barometer after Masonne and Schreyer (1987) was used for an estimate of minimum pressure conditions. Garnet-biotite geothermometry was applied to the samples CO138, KB167, KB307 and KB103. In all cases the relation of garnet rims to coexisting biotites could be investigated, but no biotite inclusions could be measured within the analysed garnets. Calculated thermometric data are summarised in Table 2.2. The employed garnet-biotite geothermometers are based on different assumptions. Ferry and Spear (1978) experimentally calibrated their garnet-biotite thermometer based on experiments in systems with X<sub>Fe</sub> at 0.9. The authors state a maximum resolution of the thermometer of 50°C. Perchuk and Lavrent'eva's (1983) experimental calibration uses systems with X<sub>Fe</sub> at 0.6. Indares and Martignole (1985) combined the

**Right: Figure 2.11a - f:** Garnet end member zonation profiles.

a - Sample CO138, garnet III; b - Sample KB167, garnet I; c and d - Sample KB307, garnet III; e and f - Sample KB103, garnet III. Key to symbols: squares = almandine; open circles = pyrope; filled circles = spessartine; triangles = grossular

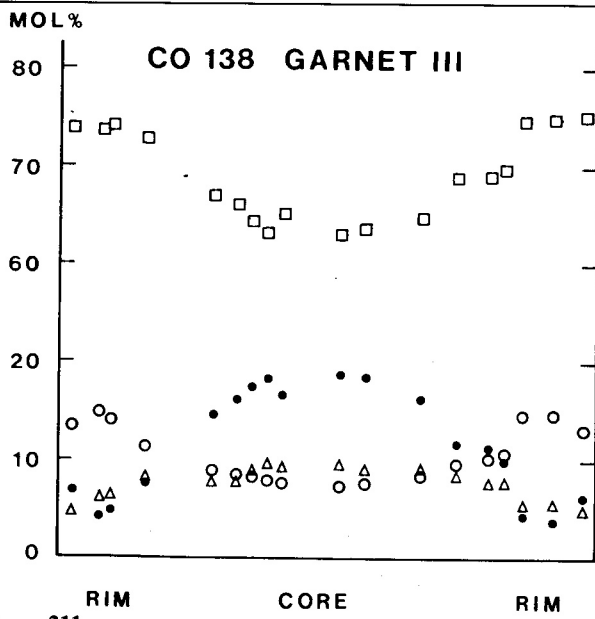


Figure 2.11a 0.5 mm

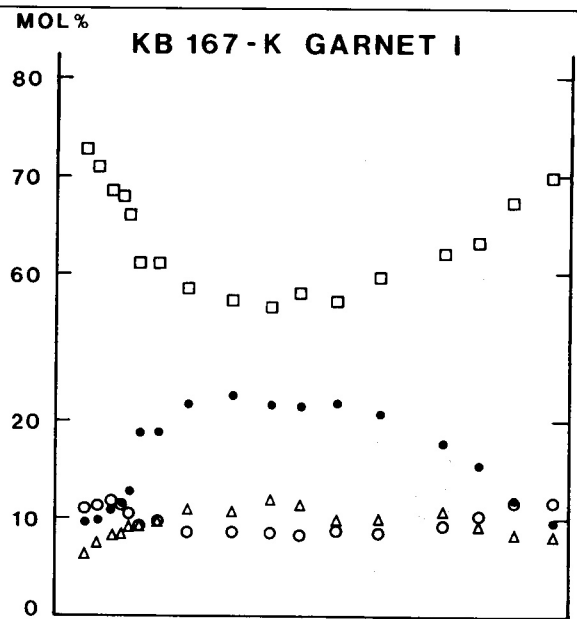


Figure 2.11b 0.5 mm

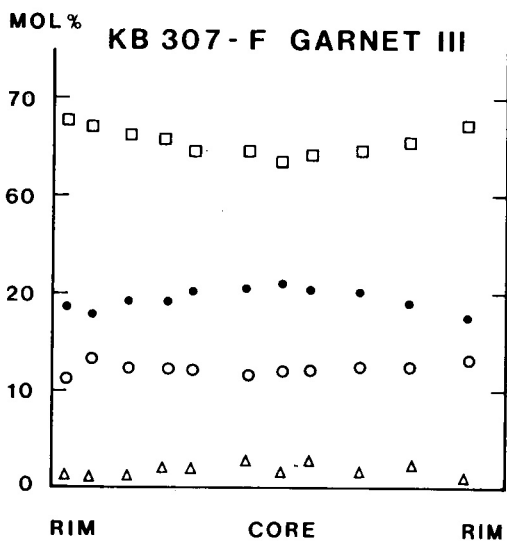


Figure 2.11c 0.5 mm

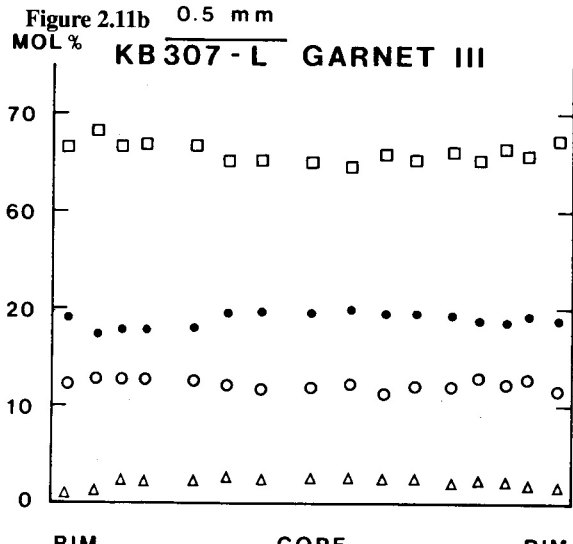


Figure 2.11d 0.5 mm

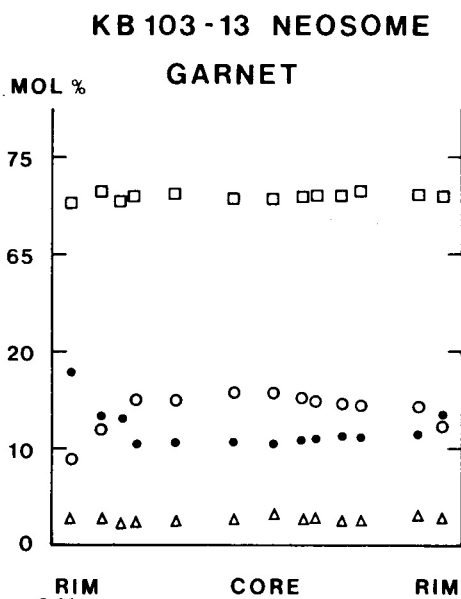


Figure 2.11e 0.5 mm

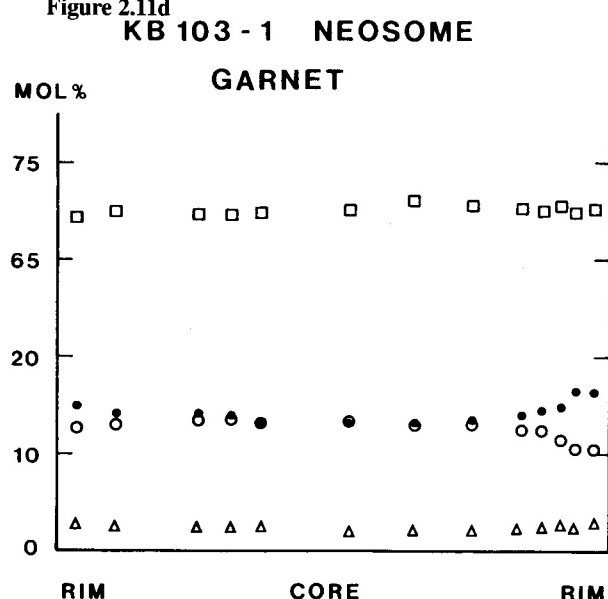
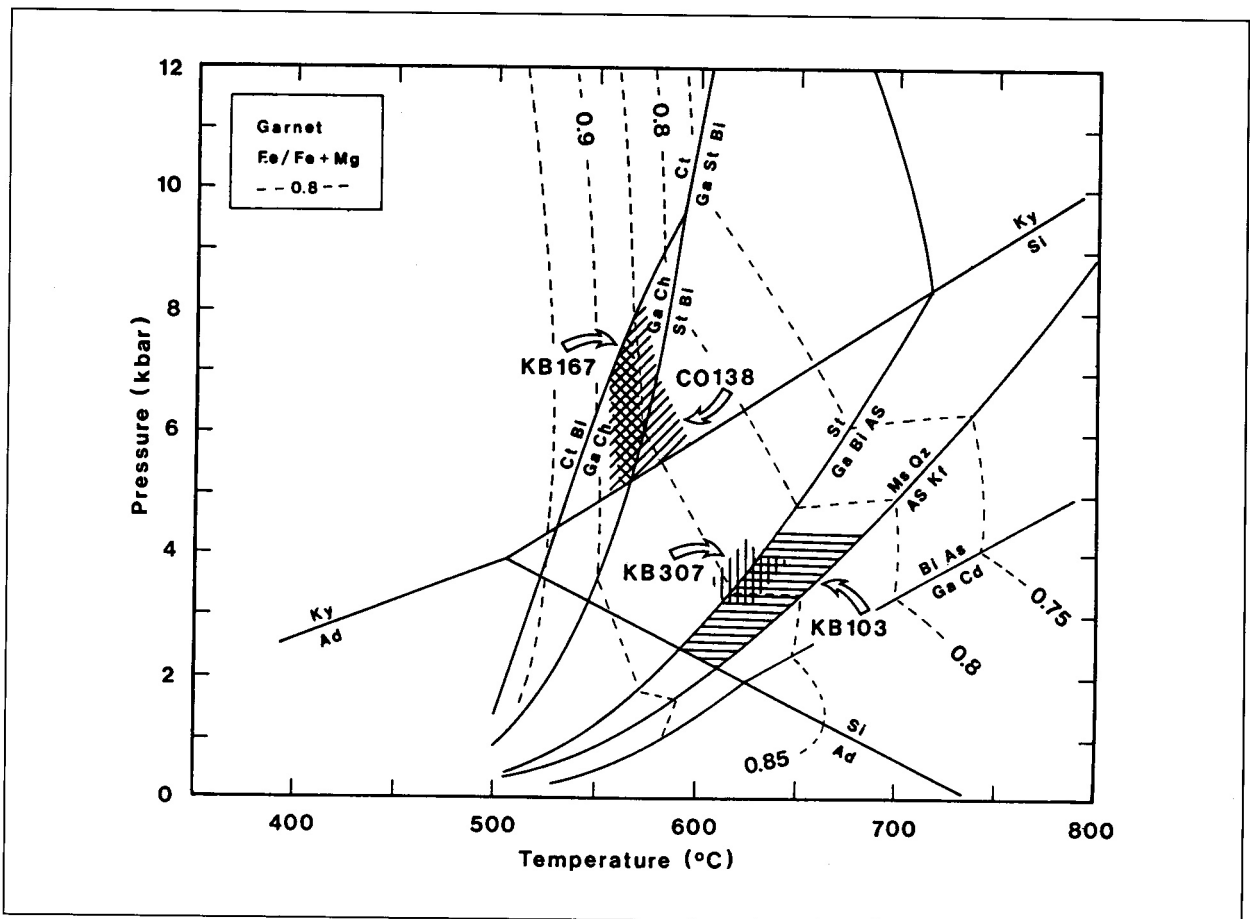


Figure 2.11f 0.5 mm



**Figure 2.12:** Partail petrogenetic grid for KFMASH system contoured with isopleths of  $X_{Mg}$  in garnet in assemblages which contain garnet + biotite, after Spear and Cheney, 1989. Hatched areas correspond to the range in  $X_{Fe}$  values measured for garnets of the samples indicated by arrows

experimental data of Ferry and Spear (1978) with data from natural garnet-biotite occurrences to derive an empirical thermometer which is corrected for diluents in both biotite and garnet. Hoinkes (1986) investigated the effect of Ca contents in garnet on the Mg-Fe exchange between garnet and biotite in staurolite-grade metapelites. With the exception of garnet I from sample KB167, all of the investigated garnets belong to the garnet generation III. The range of data for individual samples resulted from the analyses of different garnet-biotite pairs per sample.

The range of thermometric data calculated from garnet-biotite pairs clearly reflects the diversity of the various calibrations used. However, the application of quantitative thermometry does not improve the precision of previous estimates for peak metamorphic conditions derived from the stability fields of assemblages. For the samples CO138 and KB167 metamorphic temperatures were estimated from chlorite + muscovite stability at about 560°C. Calculated data apparently are too high for CO138, but reasonable results may be obtained for KB167 from the calibrations of Indares and Martignole (1985) and Perchuk and Lavrent'eva (1983). For sample KB307, temperatures are obtained from all four calibrations which are well in the range of previously estimated maximum P-T conditions of 610°C/3 kb (considering a maximum resolution of about 50°C). For the migmatite sample KB103 thermometric data apparently are too low compared to minimum metamorphic temperatures established at 650°C from various

melting reactions. However, the analysed garnets show retrograde re-equilibration of the garnet rims which accounts for the comparatively low temperatures calculated.

Apart from the thermometers discussed above, P-T estimates can be also derived from the  $X_{Fe}$  in garnets from low-Al, garnet-biotite-bearing assemblages according to Spear and Cheney (1989) who contoured their petrogenetic grid with  $Fe/(Fe+Mg)$  isopleths. Garnets were analysed from four of the investigated samples and the measured  $Fe/(Fe+Mg)$  ratios were plotted into the petrogenetic grid (Fig. 2.12). The range of the ratios which corresponds to the zoning of the crystals and the variation in composition of different garnet individuals, is indicated by the hatched areas in Figure 2.12. Inferred P-T conditions are in the range of 550-600°C/5-8 kb for the sample CO138, 550-570°C/5-8 kb for KB167, 600-640°C/3-4 kb for KB307 and 590-680°C/2-4.5 kb for KB103. The rather wide range of data for KB103 is largely due to a certain heterogeneity in the  $X_{Fe}$  of the analysed garnets. In the sample KB307, however, significantly lower P-T conditions were inferred from the presence of andalusite which might indicate that the andalusite persists metastable in the sample. Except for KB307, thermometric data derived from the  $X_{Fe}$  in garnet agree quite well with P-T estimates from the stability limits of metamorphic assemblages. In contrast, the thermometric data calculated from different garnet-biotite pairs given in Table 2.2 yielded too low T-estimates except for sample KB307. In the present study the calibration based

solely on the  $X_{\text{Fe}}$  in garnets yielded more consistent results than other calibrations.

A geothermometer based on the exchange of Mg Tschermak's component between muscovite and biotite was empirically calibrated by Hoisch (1989). The author interpreted systematic compositional variations within biotite and muscovite to be a function of metamorphic grade. The application to the present study is facilitated by the compositional range of the micas as well as the range of P-T conditions which is similar to that of Hoisch's data set. The paragenesis muscovite-biotite is common to all psammites and pelites occurring in the study area. The application of the geothermometer revealed the following temperatures (Table 2.2): assemblage zone 1 (sample CO138) muscovite-biotite pairs gave 543-578°C at 6 kb; assemblage zone 2 muscovite-biotite pairs yielded 565-653°C at 3 kb for sample CO117 and 440-526°C at 3 kb for sample KB307; sample KB115 from assemblage zone 3 gave 493-567°C at 4 kb and the migmatite sample (KB103) 508-530°C at 4 kb. Compared to the data derived from phase equilibria, the temperatures obtained for samples KB307, KB115 and KB103 apparently are too low to represent peak conditions, although formal requirements for the application of the geothermometer are met. The temperatures calculated for sample CO138 agree quite well with metamorphic temperatures of about 560°C estimated from the chlorite + muscovite stability.

The experimental work of Velde (1965, 1967) and Masonne and Schreyer (1987) has revealed a pressure dependence of the phengite composition, i.e. the substitution of the celadonite component within K-bearing white micas in the critical paragenesis phengite-biotite-K-feldspar-quartz. In the absence of K-feldspar, like in the investigated samples, only minimum pressures may be obtained from the phengite composition. Muscovite compositions were analysed in four samples. Si values range between 6.03 and 6.26 (Table A.2), showing a slight decrease from south to north within the study area. In the samples CO138 and CO117 both syn-kinematic, prograde muscovites were analysed showing an average Si of 6.23 for CO138 and a range from 6.24 to 6.26 Si per formula unit for sample CO117. Corresponding pressures may be inferred after Masonne and Schreyer (1987) at about 4 kb at an estimated temperature of 560°C (Fig. 2.13). Both samples, however, are located in the kyanite zone of the study traverse, indicating a minimum pressure of about 5 kb for the above temperature (Fig. 2.6). In sample KB307, both syn- as well as post-kinematic muscovites were analysed which yielded Si values between 6.10 and 6.27 corresponding to pressures below 3 kb for estimated temperatures below 610°C. This pressure agrees well with pressures inferred from the upper stability of andalusite (after Holdaway, 1971) present in the sample. From the late muscovites of sample KB115 with Si values ranging between 6.03 and 6.19, corresponding pressures below 3 kb were obtained for estimated temperatures between 600 and 650°C (Fig. 2.13). The estimates, however, have to be considered to represent minimum pressures only.

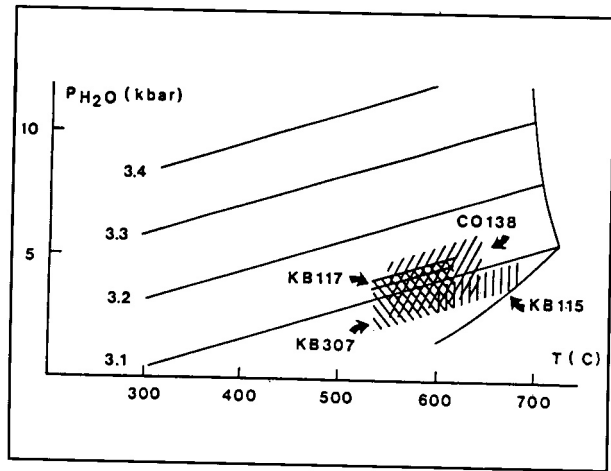


**Figure 2.13:** Pressure—temperature plot with Si isopleths for phengite Si contents per formula unit in the limiting assemblage with K-feldspar, quartz and phlogopite, after Masonne and Schreyer (1987). Solid curves at high temperatures mark the border of the stability range of the limiting assemblage. Hatched areas correspond to the range of Si values measured for white micas for the samples indicated by arrows

#### Summary of P-T conditions and conclusions

The Khomas Trough exposes from south to north a series of lower to upper amphibolite facies metamorphic rocks. Anatectic rocks occur at its northern margin. The change in mineralogy from south to north was mapped by Hoffer (1977) as a continuous and progressive sequence of reaction isograds. The present study investigated microtextural relations, mineral assemblages and mineral chemistry of selected samples. In summary, the following conclusions can be drawn:

a) micro-textural relationships clearly show that the thermal peak of metamorphism outlasted the main regional deformation which includes the  $D_1$  to  $D_3$  deformational events.

b) P-T conditions are estimated from the stability fields of metamorphic assemblages based on experimentally and calculated reaction curves and from the application of quantitative geothermometry. The P-T conditions for the rocks of the southern most part of the study traverse (assemblage zone 1) were estimated at about 530-590°C/4-9.5 kb. In assemblage zone 2, maximum temperatures and pressures of 610°C at 3 kb were inferred from the presence of andalusite. The northern part of the study area experienced P-T conditions which can be bracketed between a minimum of 590°C/2.5 kb and a maximum of 680-700°C/4.5-5.5 kb. These phase-petrological data suggest different P-T regimes along the present outcrop surface and thus oppose Hoffer's (1977) interpretation of a coherent isograd pattern in the Khomas Trough. The most marked expression of this incoherent pattern is the distinct low-pressure zone in the central Khomas Trough.

c) Estimates of the P-T conditions for the anatexis of the metasediments in the northernmost Khomas Trough can be derived from solidus relations in the system  $\text{Na}_2\text{O}-\text{K}_2\text{O}$ -

CaO-Al<sub>2</sub>O<sub>3</sub>-SiO<sub>2</sub>-H<sub>2</sub>O. A minimum temperature of 650°C is inferred from the wet granite solidus after Storre (1973) and a minimum pressure of 3.5 kb from the stability of muscovite + quartz within the migmatites.

d) A high temperature retrograde event is evident from coarse, syn- to post-D<sub>4</sub> muscovites. A late, coarse-grained generation of both biotite and chlorite is most likely related to this event as well.

Based on fluid inclusion work, Behr *et al.* (1983) concluded that the P-T path of the northern Khomas Trough branches off from that of the southern part. The authors proposed a tectonic

boundary, possibly marking a former suture which developed due to subduction or subfluence, between the northern and southern Khomas Trough south of the Matchless Member. In contrast, the present study concludes that an abrupt change in P-T conditions occurs south of the main graphite schist unit in the central Khomas Trough, marked by the first appearance of andalusite. This pattern, however, is interpreted to be related to late- to post-Pan-African differential uplift affecting the Khomas Trough, leading to the exposure of formerly different crustal levels.

### 3. THE RELATIONSHIP OF GRANITES AND MIGMATITES ALONG THE NORTHERN MARGIN OF THE KHOMAS TROUGH AND ITS BEARING ON THE TIMING OF METAMORPHISM

#### 3.1 INTRODUCTION

The Khomas Trough is bordered towards the north, against the Central Zone of the Damara Orogen, by the late-tectonic Donkerhuk Granite which intruded into the Okahandja Lineament Zone (Fig. 1.3). In the course of this study in the Khomas Trough, some emphasis was put on the contact relationships along its northern margin between the sillimanite-grade metasediments of the Kuiseb Formation, locally occurring migmatites and the Donkerhuk Granite. In this chapter, geological evidence will be presented in order to put constraints on the chronology of deformation, metamorphism - with special regard to the anatectic event - and magmatism in the northwestern Khomas Trough during the final stages of the Damaran orogeny. In Chapter 6, radiometric data will be presented supporting the field relationships.

#### 3.2 THE DONKERHUK GRANITE AND ASSOCIATED GRANITIC ROCKS

##### 3.2.1 Distribution of granitic rocks

The Donkerhuk Granite forms a more than 200-km-long, and 10- to 30-km-wide, composite batholith which intruded into the Okahandja Lineament Zone. A number of authors have previously reflected upon the structural relationships between the Donkerhuk Granite and its country rocks and the timing of granite emplacement (Gevers, 1963; Martin, 1965; Smith, 1965; Jacob, 1974; Sawyer, 1983). Detailed investigations on the Donkerhuk Granite in the western Khomas Trough were carried out by Faupel (1974).

Within the study area, rocks of the Donkerhuk Granite are exposed on the farms Nomatsaus 28, Davetsaub 29 and on Otjimbingwe 104 (Fig. 3.1). All outcrops investigated belong to marginal portions of the granite. Faupel (1974) characterised the Donkerhuk Granite as "light grey, medium grained, homogeneous biotite-muscovite monzogranite" and reported coarser-grained varieties with porphyritic K-feldspars restricted to marginal areas of the pluton. In the study area, varieties differing in colour and grain size were found. Near the southern border of the farm Nomatsaus 28, a white granite with porphyritic, zoned K-feldspar phenocrysts crops out. Further constituents are quartz, plagioclase (which is frequently zoned), biotite, primary muscovite and accessory phases (apatite, tourmaline, zircon, monazite and opaque phases). Secondary sericitisation and chloritisation occur. Further north, in the Swakop river gorge (farm Nomatsaus 28), an even-grained, partly foliated pink variety of the granite is exposed.

A number of small granite bodies occur within the country rocks along the contact of the granite batholith. Some small bodies, mainly dykes, are exposed in the migmatite area on the farm Davetsaub 29 (Fig. 3.1). The dykes vary

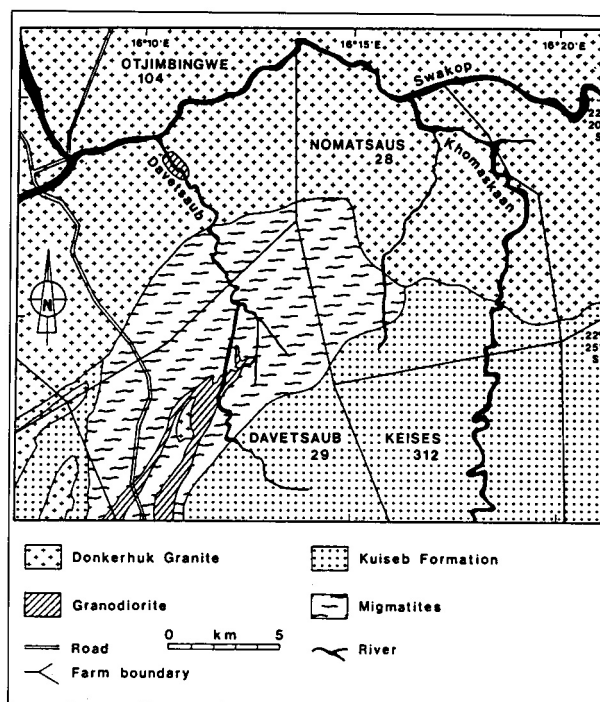


**Figure 3.1:** Geological sketch map showing the distribution of the Donkerhuk Granite, the associated granodiorite and the Kuiseb Formation migmatites in the study area (in parts after Nieberding, 1976)

in their lithology from fine-grained, light-coloured granites, to coarse-grained pegmatites with large K-feldspar phenocrysts; leucocratic, garnet-bearing rocks have also been found. Structural relationships are generally discordant to the country rocks. Further rocks which are at least spatially associated with the Donkerhuk Granite in the study area are pegmatites and a more biotite-rich, foliated granodiorite (Fig. 3.2a).

On the farm Keises 312, pegmatite veins intruded parallel to subparallel to the regional structural fabric into the country rocks. These veins were found up to a distance of several kilometres from the granite contact. The frequency and thickness of the pegmatites increases when approaching the Donkerhuk Granite.

On Otjimbingwe 104, foliated granodioritic rocks crop out along the lower course of the Davetsaub river (Fig. 3.2a). The rocks are characterised by a higher biotite content than the Donkerhuk Granite, faint nebulitic or schlieren structures and the lack of porphyritic feldspars. Near the confluence of the Davetsaub and the Swakop rivers on Otjimbingwe 104, the granodiorite was found to be enclosed within the Donkerhuk Granite. Nieberding (1976) mapped similar granodioritic rocks in the Davetsaub river. The relationship of the granodiorite with regard to the Donkerhuk Granite could not be clarified.

Thermal effects induced by the intrusion of the granite are restricted to a comparatively narrow zone. The most prominent feature is a zone of coarse recrystallisation developed

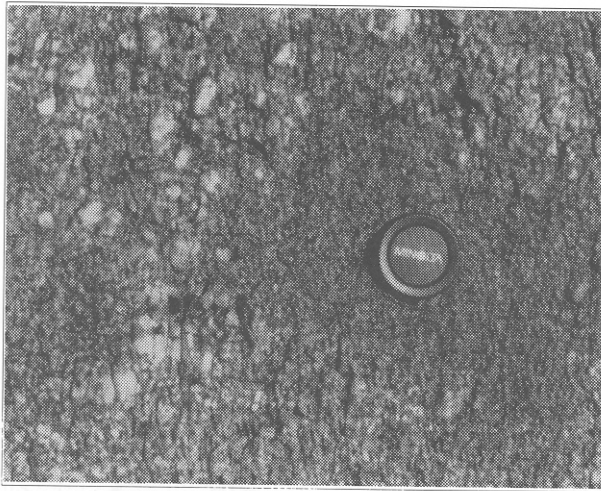


Figure 3.2a

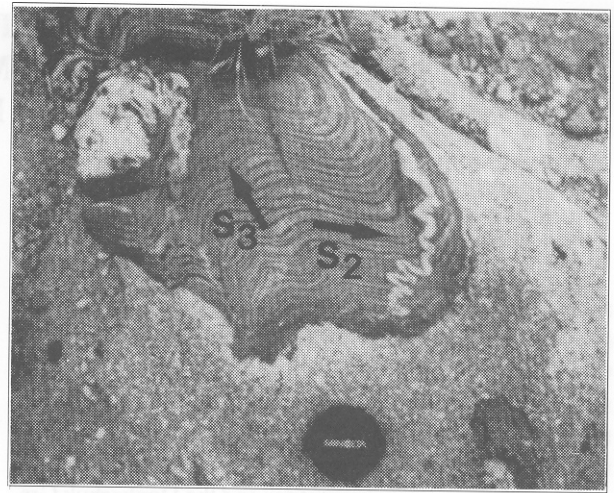


Figure 3.2b

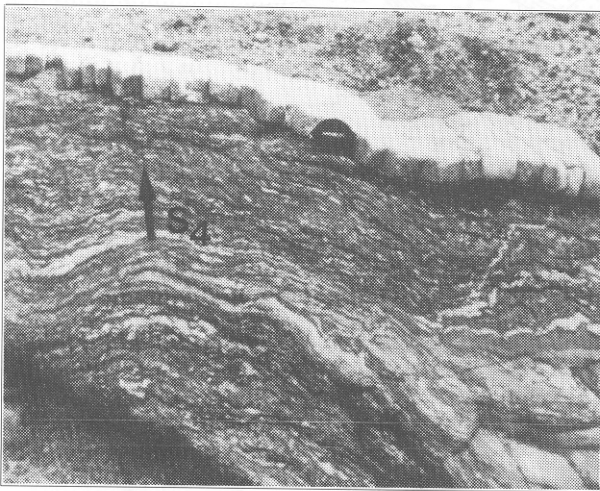


Figure 3.2c

**Figure 3.2:** The Donkerhuk Granite and its associated rocks:

- a - Foliated granodioritic rock (lens cap is 4.9 cm in diameter); farm Otjimbingwe 104
- b - Xenolith of Kuiseb Formation psammite displaying the regional  $S_2$  and  $S_3$  fabrics within white, phphyritic Donkerhuk Granite; farm Davetsaub 29
- c - Granitic veinlet in migmatized Kuiseb Formation metasediments, deformed by  $D_4$ ; farm Davetsaub 29

in the sillimanite-muscovite-bearing metasediments in the Khomaskaan river on the farm Nomatsaus 28. This zone extends some hundred metres southward from the contact of the Donkerhuk Granite with the metasediments. At the immediate contact, late hornblendes were found overgrowing the  $S_4$  crenulation cleavage in a pelite sample. This unique feature for Kuiseb pelites is most probably related to a thermal and/or metasomatic imprint of the granite. The formation of K-feldspar which was observed in a pelite sample from this zone might as well be related to the intruding melts. There are no migmatitic structures or signs of initial partial melting in the surrounding schists in this part of the study area.

In contrast, an intense migmatization of the country rocks occurred in an area several square kilometres in size, mostly situated on the farm Davetsaub 29 (Fig. 3.1). The migmatites in this area have been interpreted as products of a contact metamorphism by most previous authors (Nieberding, 1976; Hoffer, 1977; Miller, 1983a). The migmatites will be discussed in more detail below.

Some work has already been undertaken to determine the conditions of granite intrusion such as the temperature of the intruding melts and the level of intrusion. The P-T conditions were estimated from melting experiments on rock samples from the Donkerhuk Granite by Hoffmann and Winkler

(1973) and Winkler (1983). The experiments yielded solidus temperatures of  $648^\circ\text{C}$  at  $P_{\text{H}_2\text{O}} = 4 \text{ kb}$ , and  $640$  and  $646^\circ\text{C}$  at  $P_{\text{H}_2\text{O}} = 5 \text{ kb}$ , respectively, which provide a lower limit for the temperature of the intruding melts. The stability range of primary muscovite led to P-T estimates of a 3.5 kb minimum and a maximum of  $675^\circ\text{C}$  for the emplacement of the two-mica granite (Faupel, 1974). Hoffmann (1976) obtained a solidus temperature of  $659^\circ\text{C}$  at  $P_{\text{H}_2\text{O}} = 4 \text{ kb}$  for a light-coloured granitic vein from Davetsaub 29. Barnes and Sawyer (1980) inferred P-T estimates of  $700 \pm 20^\circ\text{C}$  and  $4.6 \pm 1.0 \text{ kb}$  from a roof pendant to the granite in the western Khomas Trough.

### 3.2.2 Timing of intrusion

Geological evidence on the relative timing of granite intrusion shows that the emplacement clearly postdates the main regional deformation. Xenoliths of Kuiseb Formation psammites within the granite display the regional  $S_2$  and  $S_3$  fabric (Fig. 3.2b). Some granitic veinlets are deformed together with the metasediments by  $D_4$  (Fig. 3.2c) thus indicating a syn- to post- $D_4$  emplacement.

Geochronological constraints on the granite intrusion were provided by Blaxland *et al.* (1979). The authors obtained Rb-Sr whole-rock ages of  $521 \pm 15 \text{ Ma}$  and  $52 \pm 8 \text{ Ma}$  for

the Donkerhuk Granite which they interpreted as the age of granite emplacement. Rb-Sr mineral ages between 505 and 485 Ma obtained for the Donkerhuk Granite and one migmatite sample were interpreted by the authors as subsequent cooling stages. Haack *et al.* (1988) presented further constraints on the emplacement of the Donkerhuk Granite by a Rb-Sr hornblende-WR age of  $524 \pm 7$  Ma (1) for the Otjimbingwe syenite, which was emplaced pre- to syn-S<sub>2</sub> and was subsequently intruded by the Donkerhuk Granite. The authors interpreted the above age as the resetting of the Rb-Sr system during intrusion of the granite.

### 3.3 THE MIGMATITE ZONE OF DAVETSAUB

#### 3.3.1 Regional extent

The metamorphic grade, i.e. the temperature of metamorphism, increases within the Damara Orogen towards the western Central Zone. Metamorphic isograds define a concentric pattern with a local temperature high reaching the conditions of partial melting in the area of Swakopmund (Hoffer, 1977; Hartmann *et al.*, 1983). A second complex of migmatites crops out along the southern margin of the Donkerhuk Granite in the area southwest and southeast of the Otjimbingwe settlement (Figs 3.1 and 3.3a). The migmatites have been described by Smith (1965), Hoffer (1977) and Miller (1983a); Nieberding (1976) mapped the spatial distribution of the migmatites and discussed the genetic relationships between the granitic rocks of the Donkerhuk Granite and the metasediments of the Kuiseb Formation in the area southeast and southwest of Otjimbingwe.

The terminology used to describe the macroscopic features of the migmatites follows the definitions of Mehnert (1968) and Ashworth (1985). Their terminology will be utilised in a nongenetic, descriptive sense.

The migmatites exposed in the study area can be followed to the east up to the Chaibib river in the western part of the farm Nomatsaus 28 (Fig. 3.1). Generally, the migmatites do not follow the margin of the granite intrusion, but rather occur in an irregular manner as is indicated in Figure 3.1. The eastern border of the migmatites is discordant to the regional strike of the surrounding metasedimentary series. The contact of the migmatites with the metasediments in this area appears to be gradational, although the relationships could not be investigated in great detail because of incoherent exposure. The same is also valid for the southern contact between the migmatites and the metasediments.

In the Davetsaub area at least two generations of leucosomes can be distinguished macroscopically. One generation of thin leucosome bands parallels the main regional fabric of the rocks (Fig. 3.3b) and is interpreted to have formed *in situ*. A second generation of more massive leucosomes

discordantly cuts the earlier structures (Fig. 3.3c). Nieberding (1976) distinguished between granitic, granodioritic and trondhjemitic leucosomes. The latter correspond to the thin, fabric-parallel leucosomes described above which were found to be free of K-feldspar in contrast to the other, microcline-bearing types of leucosome.

Proceeding northward from Davetsaub to Otjimbingwe, the regional fabric preserved in the palaeosomes of the migmatites gets progressively disintegrated while the amount of newly formed melt increases (Figs 3.3d and e). Nieberding (1976) used the terms "Nomatsaus type" and "Davetsaub type" to characterise the different appearance of the migmatites.

#### 3.3.2 Conditions of migmatite generation

Trondhjemitic leucosomes, if assumed to have formed *in situ* from partial melting of the Kuiseb Formation, may be explained as being generated at P-T conditions within the stability range of muscovite. Below a pressure of about 3.5 kb, K-feldspar would have formed at the expense of muscovite which is a stable phase within the migmatites. Granodioritic rocks may have evolved from melting of metasedimentary rocks at deeper crustal levels. Indicative of this process are the observed schlieren structures and the small, marginally disintegrated rafts of mica schists.

P-T estimates for the anatexis of the metasediments are largely based on melting experiments on samples from the migmatite zone of Davetsaub and on samples from the Kuiseb Formation of this area carried out by Hoffmann (1976). He determined similar solidus temperatures for a neosome/palaeosome pair of 683/685°C at  $P_{H_2O} = 4$  kb and explained the different megascopic appearance of the migmatites as originating from different rates of melt generation within small temperature intervals. Nieberding (1976) reported melting experiments on a pelite sample from the Kuiseb Formation which yielded a solidus temperature of 695°C (4 kb), while a granitic leucosome gave only 667°C (4 kb). Three samples of trondhjemitic, K-feldspar-free leucosomes gave solidus temperatures between 659 and 700°C at 4 kb, indicating the onset of partial melting at a minimum temperature of about 660°C. The experimental data of Hoffmann (1976) are indicated by the hatched area in Figure 2.7.

Solidus relations in the tonalite system as well as other melting reactions were discussed in Chapter 2.5; solidus phase relations in the system Na<sub>2</sub>O- K<sub>2</sub>O-CaO-Al<sub>2</sub>O<sub>3</sub>-SiO<sub>2</sub>-H<sub>2</sub>O were shown in Figure 2.7. From various melting reactions which, however, can only approximate true phase relations, temperatures between 650 and 700°C at pressures ( $P_{tot} = P_{H_2O}$ ) of 3.5 to 5.5 kb may be estimated for the onset of partial melting in the Davetsaub area which is consistent with experimental data derived from the melting experiments.

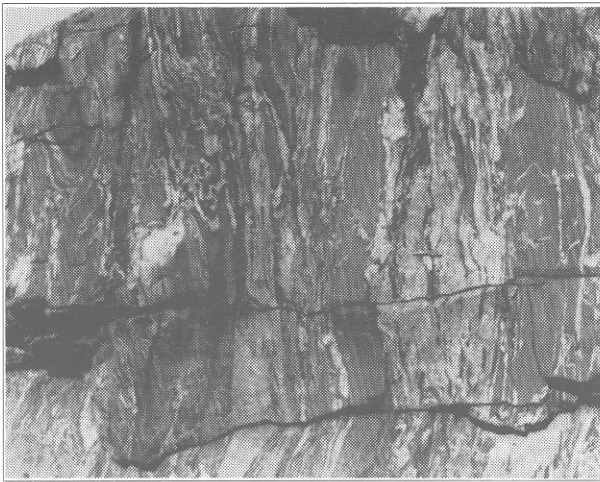


Figure 3.3a

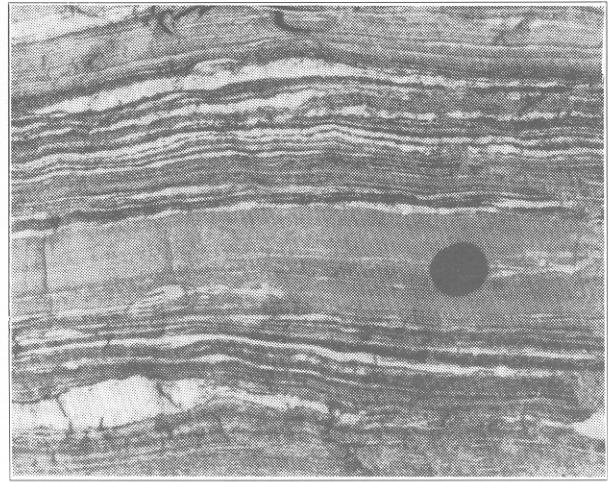


Figure 3.3b

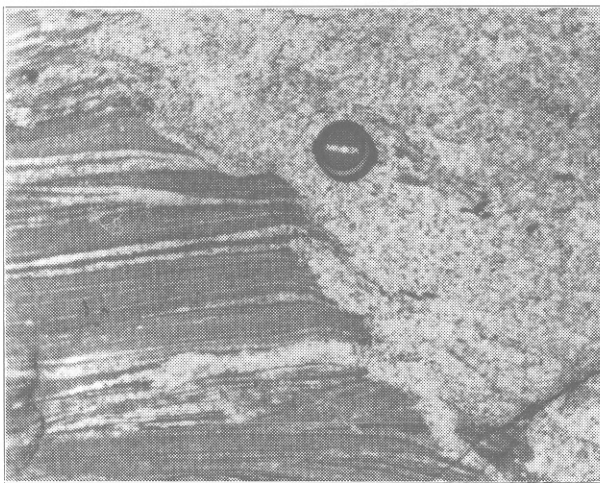


Figure 3.3c

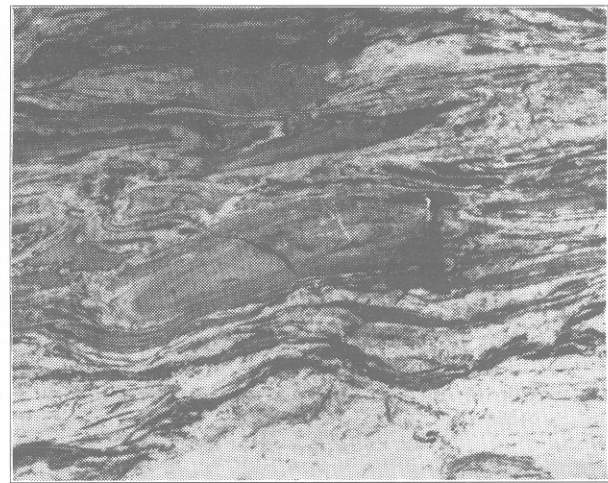


Figure 3.3d

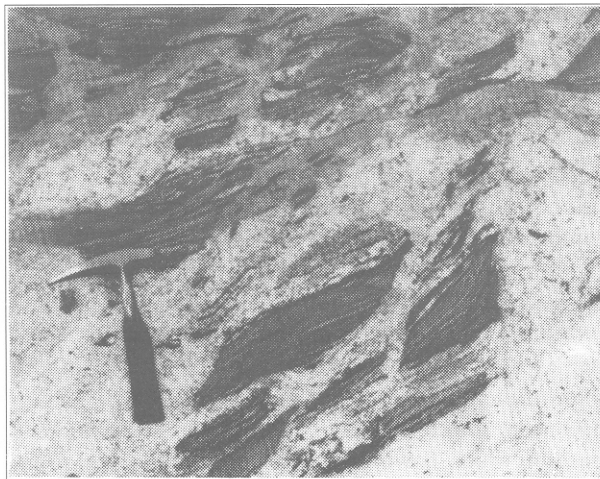


Figure 3.3e

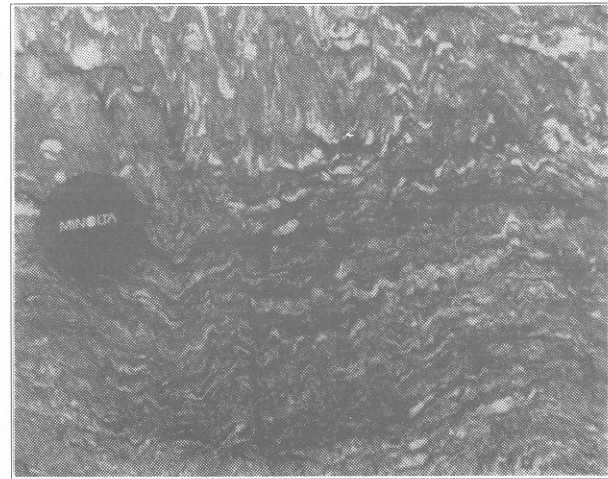


Figure 3.3f

- Figure 3.3:** Features of the Kuiseb Formation migmatites:
- a - Typical migmatite outcrop in the Davetsaub river (hammer for scale); farm Davetsaub 29.
  - b - Thin trondhjemitic leucosomes paralleling the regional structural fabric (lens cap is 4.9 cm in diameter); farm Davetsaub 29
  - c - In situ leucosomes discordantly cut by a massive, granitic type of leucosome; farm Davetsaub 29
  - d - "Nomatsaus type" migmatites showing largely disintegrated structural fabrics, a high percentage of newly formed melt and relict calc-silicate boudins; Otjimbingwe 104
  - e - Rafts of migmatized mica schists and schlieren structures in granitic melt; Otjimbingwe 104
  - f - Migmatized pelitic schist crenulated by D4; farm Davetsaub 29

### 3.4 MIGMATITE FORMATION IN THE DAVETSAUB AREA:

#### EXPRESSION OF CONTACT OR REGIONAL MET AMORPHISM?

The distribution and the spatial association of the migmatites with granitic rocks of the Donkerhuk pluton has led most previous authors to the assumption that the formation of the migmatites resulted from thermal effects of the granite intrusion (Nieberding, 1976; Hoffer, 1977; Sawyer, 1981). Hoffer (1977) and Sawyer (1981, 1983) even attributed the growth of sillimanite, at least in parts, to a thermal overprint in a contact aureole.

In this author's opinion, however, arguments can be found which cast doubts on an entire contact metamorphic origin of the migmatites, if the term "contact metamorphism" is solely related to thermal effects associated with the Donkerhuk Granite as it is presently exposed. According to the investigations in the Davetsaub river area, at least two different stages of migmatization can be distinguished. A first generation of thin, fabric-parallel leucosome bands is discordantly cut by a second generation of massive leucosomes. Structural relationships observed in the study area are as follows: (1) xenoliths of metasediment within the two-mica granite display the regional  $S_2$  and  $S_3$  cleavages and partly an  $S_4$  crenulation cleavage; (2) thin granite apophyses are folded by the  $S_4$  crenulation cleavage; (3) anatectic structures in a migmatized pelite are overprinted together with a small granitic veinlet by the  $S_4$  crenulation; (4) granites and pegmatites show intrusive contacts with the migmatites and crosscut the migmatitic structures with rather sharp contacts; (5) migmatites do not follow the granite border, but occur in an irregular fashion, and (6) the eastern border of the Davetsaub migmatite complex is discordant with respect to the regional strike of lithological units.

The melting experiments by Hoffmann (1976) have revealed lower solidus temperatures for the Donkerhuk Granite and a granitic type of leucosome compared with the solidus temperatures obtained from the migmatites and metasediments. These findings might favour an interpretation of an independent thermal phase leading to the formation of the migmatites.

The following conclusions are drawn from the above observations. The magmatic rocks associated with the Donkerhuk Granite clearly postdate the main regional deformations ( $D_2$  and  $D_3$  phases of deformation) as well as the temperature peak of metamorphism. It has been shown for the study area, however, that the granite did not produce an extensive thermal aureole. This is an indication that the melts must have intruded into a still hot environment as suggested also by Faupel (1974). A close genetic relation between regional and contact metamorphic processes has therefore to be considered. Furthermore, observations (1) and (2) confirm that the late  $S_4$  crenulation cleavage is contemporaneous with the granite intrusion. Observations (3) and (4) confirm that at least one leucosome generation predates  $S_4$  and that these leucosomes were already crystallised before the intrusion of the granitic melts. This indicates that an anatectic event occurred post- $S_3$  but pre- $S_4$  thus predating the intrusion of the Donkerhuk Granite.

However, it can also be argued that the different generations of leucosomes correspond to different stages of migmatite generation. The first generation of leucosomes may have formed *in situ* corresponding to the temperature peak of regional metamorphism. The discordant, massive leucosomes either were injected at a later stage as Donkerhuk - derived melts and/or they were emplaced as partial melts mobilised from deeper crustal levels. The migmatites might therefore have evolved both from a regional metamorphic temperature high as well as from a subsequent intrusion of granitic melts of the Donkerhuk Granite.



## 4. ISOTOPE STUDIES - OBJECTIVES AND PRINCIPLES

### 4.1 INTRODUCTION

The successful dating of metamorphic rocks requires knowledge of the volume of isotope homogeneity which particularly applies to studies on the Rb-Sr isotope system. The extent of isotope equilibrium, however, is commonly unknown, and thus dating of whole rocks by the Rb-Sr method frequently concentrates on unmetamorphosed, magmatic rocks which are expected to have experienced large-scale isotope homogenisation during magma ascent and emplacement. In the Damara Orogen, accordingly, most geochronological data so far available are Rb-Sr whole-rock data obtained from the widespread pre-, syn- and post-tectonic intrusives which only indirectly constrain the timing of deformational and metamorphic events. The data were in most cases interpreted as reflecting the time of emplacement (approximately between 760 and 460 Ma; cf. Chapter 1), but only rarely has a metamorphic re-equilibration of the isotopic system been recorded (e.g. Hawkesworth *et al.*, 1983). The climax of metamorphism associated with the Pan-African orogeny has been estimated from radiometric data of post-tectonic granites at 530 Ma in the central and southern Damara Orogen (e.g. Blaxland *et al.*, 1979). Few attempts have been made so far directly to date the widely distributed, medium- to high-grade metasediments.

Due to the described problems surrounding isotope homogeneity, this study attempts to put constraints on the apparent P-T path undergone by the Kuiseb Formation of the Khomas Trough during Pan-African metamorphism, as well as to constrain the age of the protoliths of the metasediments. This will be approached by means of Rb-Sr whole rock and mineral analyses of the banded metasediments, combined with K-Ar analyses of selected mineral fractions, as well as U-Pb monazite analyses of magmatic and metamorphic monazites and detrital zircons. It is the aim of this chapter to introduce the objectives, principles and methods of the isotope analyses employed during this study. Analytical results and interpretations will be presented in Chapters 5 and 6.

Rb-Sr and U-Pb isotope analyses were carried out at the Sentrallabor für Geochronologie, Universität Münster. K-Ar and Ar-Ar analyses were provided by Dr H. Kreuser from the Bundesanstalt für Geowissenschaften und Rohstoffe, Hannover. Details of analytical techniques and parameters of age calculations are discussed in Appendices III and V.

### 4.2 RB-SR INVESTIGATIONS

#### 4.2.1 Objectives

The behaviour of the Rb-Sr system particularly within minerals is considered effectively to be controlled by changes in metamorphic temperature. This makes Rb-Sr analyses well suited to date the temperature-dominated part of a P-T loop, i.e. the temperature peak of metamorphism and subsequent retrograde stages of the P-T loop until the blocking temperatures of individual mineral species are reached, provided that no other factor will cause partial or total resetting

of the isotope system. Since a quantity of data is available contributing to the understanding of the cooling history of the Damara Orogen, the dating of peak metamorphic conditions through small-scale Rb-Sr whole-rock analyses was concentrated on as one of the aims of the study. Dating of prograde metamorphic stages is possible, if a volume of rock had been isotopically homogenised during prograde metamorphism, but remained closed during subsequent temperature increase. An important feature in this context is the  $S_2$  metamorphic banding cleavage as described in Chapter 2.5. In this study, an attempt is therefore made to constrain the timing of metamorphic banding cleavage formation which is clearly a prograde feature within the metasediments.

Apart from the regional interest in the isotope systematics of the Kuiseb Formation, the main object of the study was to investigate the applicability of the Rb-Sr small-domain method to the dating of metamorphic processes. The banded metasediments of the Kuiseb Formation appear particularly suitable for an application of the Rb-Sr small-domain technique due to the frequent occurrence of a distinct metamorphic banding cleavage in the metagreywackes. The alternation of mica-rich pelitic and psammitic rocks as well as the distinct metamorphic banding causes a high variation of Rb-Sr ratios on a mm to cm scale which is one of the prerequisites for this type of analysis. In contrast to most rocks investigated by the Rb-Sr small-domain method previously, the rocks of the Kuiseb Formation most probably have not undergone polymetamorphic development, but are characterised by one phase of prograde metamorphism (cf. Chapter 2.5).

With regard to the problem of isotope homogeneity in metasediments, it is the primary aim of the Rb-Sr small-domain method applied in this study to delineate the extent of isotope equilibrium between the individual slabs of the rock profiles and between minerals and the respective bulk rock.

#### 4.2.2 Principles

Relevant information about the principles of the Rb-Sr method and isochron modelling was compiled by Faure and Powell (1972), Jäger (1979) and Faure (1986). The concept of blocking temperatures as presented by Purdy and Jäger (1976), Jäger (1979) and Dodson (1973, 1979) is most commonly applied to the interpretation of Rb-Sr and K-Ar mineral data. The problem of closure temperatures was more recently discussed by Von Blanckenburg *et al.* (1989) and Seitler (1989). Closure temperatures for the Rb-Sr system in biotites were estimated at  $300 \pm 50^\circ\text{C}$  by Purdy and Jäger (1976) and at temperatures above  $400^\circ\text{C}$  by Verschure *et al.* (1980) and Del Moro *et al.* (1982). The closure temperature for radiogenic strontium in muscovite is considered to be  $500 \pm 50^\circ\text{C}$  (Purdy and Jäger 1976). Haack (1983), Van Breemen and Dallmeyer (1984) and Peucat and Martin (1985) obtained blocking temperatures of 660 and  $600^\circ\text{C}$ , respectively, for the cm-scale isotope exchange in Rb-Sr whole-rock systems.

## 4.2.3 The Rb-Sr small-domain method

The question of isotope homogeneity is essential to the choice of the sample size for whole-rock investigations. The Rb-Sr small-domain method tries to find an alternative to whole-rock analyses of large, isotopically non-equilibrated volumes of rock and pure mineral analyses. Its application particularly to metamorphically banded gneisses and anatectic rocks is based on the small-scale variation in Rb-Sr ratios which results from the fractionation of the Rb-Sr ratios during metamorphic processes. The principle procedure of the method is the analysis of a rock profile which is cut perpendicular to any existing lithological or metamorphic banding or heterogeneity. The profile is then split parallel to the layering into contiguous slabs of contrasting composition. To obtain an isochron, however, the small-domain method has to follow the condition of isotopic homogeneity within the studied volume of rock, i.e. the minimum distance of isotopic equilibrium must exceed the extent of the rock profile, usually by a few centimetres. The size of the rock profile and the thickness of its individual slabs is largely determined by the type of banding and the geological objectives of the respective study.

Attempts to date metamorphic events with this method have been undertaken in a number of studies (Pidgeon and Compston, 1965; Krogh *et al.*, 1968; Krogh and Davis, 1969, 1971, 1973; Hofmann, 1972; Hofmann and Grauert, 1973; Grauert, 1974; Grauert and Hall, 1974; Montgomery and Hur-

ley, 1978; Aftalion and Van Breemen, 1980; Bachmann und Grauert, 1986; Peucat and Martin, 1985; Buhl, 1987). In most cases, the application of the Rb-Sr small-domain method was designed to study local variations in the whole-rock  $^{87}\text{Sr}/^{86}\text{Sr}$  ratios predominantly in polymetamorphic rocks to achieve a better resolution of metamorphic events. Peucat and Martin (1985) showed that the application of the small-domain method may lead to geologically meaningless data. The scale of isotopic equilibrium was found to extend over distances of only several centimetres in medium- to high-grade metamorphic rocks (e.g. Montgomery and Hurley, 1978; Aftalion and Van Breemen, 1980). Critical arguments have been raised on the applicability of the small-domain method to the dating of metamorphic events by qualifying the calculated ages as cooling of that mineral phase which dominates the respective part of a rock profile (Hoffmann, 1979; Peucat and Martin, 1985).

In contrast to conventional Rb-Sr analyses, the application of the small-domain method gives a geometric control over the measured isotope characteristics, provided that a rock profile has completely been analysed. The method in particular allows control over the extent of isotope homogeneity/isotope heterogeneities within an investigated volume of rock. To resolve the spatial distribution of isotope signatures,  $^{87}\text{Sr}/^{86}\text{Sr}$  ratios are plotted against a geometrical parameter (e.g. the position of the slab within the rock profile) in a so called "profile diagram" (Bachmann and Grauert, 1986). The principles of the method will briefly be outlined with the help of a fictitious

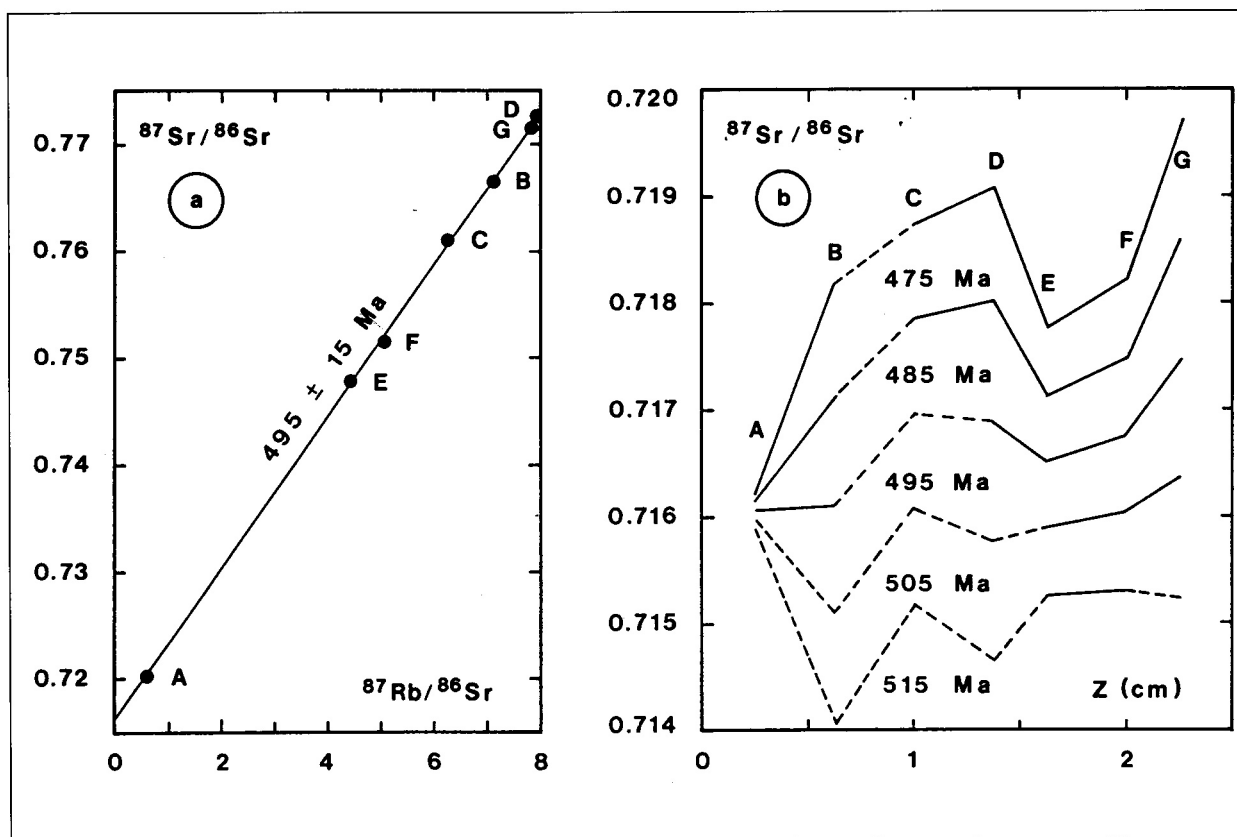


**Figure 4:** a - Rb-Sr isochron diagram showing the whole rock data for a rock profile consisting of 7 contiguous slabs A-G. b -  $^{87}\text{Sr}/^{86}\text{Sr}$  profile diagram showing the distribution of  $^{87}\text{Sr}/^{86}\text{Sr}$  ratios of the individual slabs calculated for  $t = 515, 505, 495, 485$  and  $475 \text{ Ma}$  plotted against the position of the centre of each slab within the profile. The dashed lines mark unlikely isotope distribution patterns, the other curves represent possible distribution patterns (for explanation see text)

rock profile consisting of 7 contiguous slabs (Fig. 4.1).

Put into an isochron diagram (Fig. 4.1a), the Rb-Sr whole-rock data for the individual slabs of the profile align along a regression line, the slope of which corresponds to an age of  $495 \pm 15$  Ma. In Figure 4.1 b the variation in and the development of the  $^{87}\text{Sr}/^{86}\text{Sr}$  ratios of the individual slabs is illustrated. The  $^{87}\text{Sr}/^{86}\text{Sr}$  ratios were calculated for  $t = 515$  Ma, 505 Ma, 495 Ma (which corresponds to the "isochron age"), 485 Ma and 475 Ma. The dashed lines represent unlikely distribution patterns, since slabs having higher  $^{87}\text{Rb}/^{86}\text{Sr}$  ratios (e.g. slabs B or D), show lower  $^{87}\text{Sr}/^{86}\text{Sr}$  ratios with respect to their neighbouring slabs (e.g. slabs A and C, C and E). These patterns cannot evolve from a natural and previously homogeneous, undisturbed isotope system. All other distribution curves represent hypothetical patterns. Although the data points show scatter beyond the analytical errors in the isochron diagram, an equilibrated isotope distribution is not obtained for any specific time. Hence the age value of  $495 \pm 15$  Ma obtained from the regression of the whole-rock data may not be interpreted as an isochron age. According to Bachmann und Grauert (1986), a geological relevance nevertheless may be assigned to an incomplete equilibration of the  $^{87}\text{Sr}/^{86}\text{Sr}$  ratios among the whole-rock samples. In the present example, the  $^{87}\text{Sr}/^{86}\text{Sr}$  ratios show the least variation at 495 Ma for the slabs C-G. This time would be interpreted as the time of a metamorphic overprint leading to a partial homogenisation of the strontium isotopes.

It has to be emphasized, however, that the  $^{87}\text{Sr}/^{86}\text{Sr}$  isotope ratios are hypothetical values, in that the above considerations are based on a closed system behaviour of the minerals and whole rocks.

### 4.3 U-Pb ANALYSES

#### 4.3.1 Objectives

One of the problems in delineating the palaeoenvironmental setting of the Kuiseb Formation was to deduce prospective source areas for the vast amounts of detritus supplied into the Khomas Trough sedimentary basin. Studies of the heavy mineral spectra of meta-greywacke layers along the study traverse combined with radiometric dating of detrital zircons were regarded as a reasonable tool in delineating the nature and age of the sediment sources and thus setting an upper limit on the depositional age of the sediments.

The heavy mineral spectra obtained from various meta-greywacke layers have been discussed in Chapter 2. Zircon apparently is the only mineral of undoubtedly detrital origin.

During this study, U-Pb analyses of detrital zircons as well as metamorphic and magmatic monazites were carried out. U-Pb analyses of detrital zircons from the Kuiseb Formation were expected to give an insight into the age spectrum of its sediment sources which, at the same time, would give an upper limit for the deposition in the Khomas Trough. A northeasterly location of major sediment sources could be inferred from palaeocurrent measurements (cf. Chapter 2.3). Monazite analyses from granitic as well as metamorphic

rocks were expected to provide a reliable approximation for the intrusion of the late- to post-tectonic Donkerhuk Granite and the temperature peak of metamorphism in the northern Khomas Trough.

Principles of the U-Pb method of dating were compiled by Gebauer and Grünenfelder (1979) and Faure (1986). Pioneering studies on the U-Pb system, the systematics of lead diffusion in zircon and monazite and the interpretation of U-Pb data in the concordia diagram were undertaken by Wetherill (1956, 1963), Nicolaysen (1957), Tilton (1969), Wasserburg (1963) and Allégre *et al.* (1974).

#### 4.3.2 Significance of U-Pb zircon and monazite data

A brief review of the current knowledge of zircon and monazite stability with particular reference to the behaviour of these minerals during metamorphism as well as the characteristics of their U-Pb systems will be given.

#### Zircon

Zircon is a common accessory mineral in felsic plutonic rocks and, due to its mechanical and chemical resistivity, a common detrital mineral in clastic sediments. The morphology of zircon crystals is largely controlled by the petrogenesis of its host rock. The length-width ratios of zircon crystals are indicative for a metamorphic or a magmatic crystallisation of the minerals (Poldervaart, 1950). Metamorphic zircons commonly are less elongated than magmatic crystals, having length-width ratios  $< 2$  (magmatic zircons  $> 2$ ). In addition, the crystal shape of magmatic zircons is strongly dependent on temperature and composition of the parent magma and these have thus been used for granite classification (Pupin, 1980). Silver and Deutsch (1963) first described a correlation of grain size with uranium content, magnetic susceptibility and apparent ages of zircons.

Zircons frequently exhibit discordant U-Pb data. Intercept ages may be of geological relevance in the case of a simple two-stage development (model of episodic lead loss, Wetherill, 1956). The upper intercept is commonly interpreted as crystallisation age of the zircon, whereas the lower intercept corresponds to a phase of lead loss (metamorphic overprint, weathering). Lower intercept ages may become meaningless in the case of multi-episodic lead loss in polymetamorphic rocks (Wetherill, 1963; Allégre *et al.*, 1974) or continuous lead loss (Nicolaysen, 1957; Tilton, 1960; Wasserburg, 1963). The phenomenon of recent lead loss (Black, 1987; Hansen and Friderichsen, 1989) may also lead to geologically meaningless intercept ages.

#### Monazite

Monazite is a lanthanide phosphate occurring as a widespread accessory phase in leucocratic rocks and as a minor accessory in medium- to high-grade metamorphic rocks. It has a strong preference for LREE and can accommodate several percent  $\text{ThO}_2$  and  $\text{UO}_2$  (Overstreet, 1967; Nash, 1984).

Regarding the metamorphic environment, monazite becomes unstable under low-grade metamorphic conditions

and is newly formed under upper amphibolite facies conditions (Overstreet, 1967). According to Smith and Barreiro (1990), monazite forms in pelitic schists at or near the P-T conditions of the staurolite isograd. The latter authors observed a breakdown of monazite to allanite in biotite-grade rocks and thus assumed a minimum temperature of  $525 \pm 25^\circ\text{C}$  (3 kb) for monazite formation. Kingsbury *et al.* (1990) estimated a temperature of  $500^\circ\text{C}$  necessary for monazite formation. Experiments on monazite solubility by Montel (1986) and Rapp and Watson (1986) constrained a thermal stability up to  $700\text{--}800^\circ\text{C}$  in granitic melts. The U-Pb system in monazite was reported to remain closed under greenschist facies conditions (monazites from the Palung Granite, Himalaya; Schärer and Allègre, 1983) and even amphibolite facies conditions (polymetamorphic Alpine rocks; Köppel *et al.*, 1980). In contrast, Kingsbury *et al.* (1990) reported a 5-10% loss of radiogenic Pb from monazites which experienced  $400^\circ\text{C}$  and 60% loss of radiogenic Pb after  $680^\circ\text{C}$ . Further examples of discordant monazite data were described by Black *et al.* (1984), Copeland *et al.* (1988), Teufel (1988) and Kingsbury *et al.* (1990). Black *et al.* (1984) investigated the internal structure of discordant monazites from polymetamorphic rocks from Antarctica. The authors could show that the monazite grains are composed of crystalline domains, disoriented with respect to each other by confused boundary regions.

Nevertheless, U-Pb monazite analyses in most cases reveal concordant age data (e.g. Grauert, 1974; Köppel and Grünenfelder, 1975; Aftalion and Van Breemen, 1980; Köppel *et al.*, 1980; Van Breemen *et al.*, 1982; Teufel, 1988; Smith and Barreiro, 1990). In igneous rocks, U-Pb monazite data are commonly interpreted as time of crystallisation or emplacement (Schärer and Allègre, 1983; Schärer, 1984; Corfu, 1987; Copeland *et al.*, 1988). In metamorphic rocks, concordant U-Pb monazite data are believed to represent either the peak of a metamorphic overprint as assumed by a number of authors (Grauert *et al.*, 1974; Köppel and Grünenfelder, 1975; Köppel *et al.*, 1980; Aftalion and Van Breemen, 1980), or the closure of the mineral with respect to radiogenic Pb. Blocking temperatures were estimated at  $530^\circ\text{C}$  by Wagner *et al.* (1977). Copeland *et al.* (1988) found significantly higher closure temperatures of  $720\text{--}750^\circ\text{C}$ .

In any case, U-Pb monazite data may be correlated with high temperatures, either dating a metamorphic event or the cooling thereafter. The retentivity of monazites with respect to U and Pb is limited almost by the stability of the mineral itself. Grauert *et al.* (1990) investigated concordant monazites from anatectic gneisses of the Moldanubicum. By comparison of different isotopic systems, they were able to show that the U-Pb system reflects the anatectic event; the Sm-Nd system

of the monazites, however, indicates an earlier crystallisation and thus a total loss of radiogenic Pb during the anatexis. The authors concluded that concordant monazite ages in metamorphic rocks do not necessarily reflect the crystallisation of the minerals.

#### 4.4 K-Ar ANALYSES - OBJECTIVES AND PRINCIPLES

K-Ar analyses on micas from the Kuiseb Formation meta-sediments were intended as complementary investigations to the Rb-Sr small-domain whole-rock and mineral analyses. In contrast to the latter, age calculation from K-Ar data does not involve the regression of data from different mineral phases or mineral-whole-rock pairs which do not always meet the essential prerequisite of being cogenetic. Conventional K-Ar and/or  $^{40}\text{Ar}\text{--}^{39}\text{Ar}$  analyses were carried out on selected mica fractions from the investigated rock-profiles identical to those investigated with the Rb-Sr method.

K-Ar and  $^{39}\text{Ar}/^{40}\text{Ar}$  analyses were carried out by Dr H. Kreuser from the BGR, Hannover, and his co-workers who are thanked for their efforts. For details of analytical techniques and principles of the methods the reader is referred to Merrihue and Turner (1966), Dalrymple and Lanphere (1971, 1974), McDougall (1974), Dallmeyer (1979) and Faure (1986).

The interpretation of K-Ar dates is traditionally based on the concept of blocking temperatures (Purdy and Jäger, 1976; Dodson, 1979). Blocking temperatures were estimated by Purdy and Jäger (1976) for biotites at  $300 \pm 50^\circ\text{C}$  which is considered to be the same for radiogenic strontium and argon, and for muscovites at  $350 \pm 50^\circ\text{C}$ . Other authors (Verschure *et al.*, 1980; Del Moro *et al.*, 1982) assumed the blocking temperatures for biotites to lie above  $400^\circ\text{C}$ .

However, arguments have been raised against the general application of the concept of blocking temperatures. The concept of blocking temperatures exclusively relates Rb-Sr and K-Ar mineral data to the cooling of the host rock to that temperature, below which the quasi-quantitative retention of the radiogenic daughter isotope in the mineral is started. Examples which question the general applicability of the concept of blocking temperatures, were reported by Deutsch and Steiger (1985) and Chopin and Maluski (1980), amongst others. The latter authors concluded that chemical reactivity, starting mineralogy and primarily a pervasive deformation and the related fluid behaviour may be the effective controls on the opening of the isotopic system.

## 5. Rb-Sr SMALL-DOMAIN INVESTIGATIONS OF WHOLE ROCKS AND MINERALS FROM THE KUISEB FORMATION METASEDIMENTS

### 5.1 INTRODUCTION

For the purpose of Rb-Sr small-domain investigations, six samples of banded metasediments were collected along the study traverse in the Khomas Trough. The samples differ in their metamorphic grade, the intensity and style of their structural overprint and the nature of their banding. Five out of the six samples were selected from the northern central and northern Khomas Trough (CO117, KB307, KB421, KB115, KB103) where metamorphism was temperature-dominated but deformation was less intense than in the southern part (cf. Chapter 2.4). Three of the samples show a distinct metamorphic banding cleavage (CO117, KB421, KB103), the other three exhibit a type of banding which clearly can be attributed to sedimentary layering (KB167, KB307, KB115). Sample localities are shown in Figure 2.8.

In the following, each sample will be characterised according to its structure (type and number of fabrics) and petrography (mineral textures and metamorphic assemblages). Mineral compositions were determined by microprobe analyses and are listed in Appendix I (Tables A1-A6). Analytical data were averaged for individual layers or slabs of the rock profiles, if there was no significant and systematic variation within the data of the respective units. Apart from the application of geothermo-barometers, mineral analyses were designed to study the chemical composition of different generations of minerals, in particular micas. The samples will be dealt with in geographical order from south to north. This order is also representative of increasing metamorphic temperatures across the Khomas Trough. The rock profiles are generally about 2 by 2 cm in cross-section and between 3 and 16 cm long.

Analytical results of the Rb-Sr small-domain whole-rock and mineral analyses will be presented in the form of con-

ventional isochron diagrams as well as profile diagrams. Analytical data as well as the calculated apparent age data are listed in Appendix IV (Tables A.8-A13, A.15). The profile diagrams show the spatial distribution and the computed temporal development of the  $^{87}\text{Sr}/^{86}\text{Sr}$  ratios for the individual slabs which provides a geometric control over isotopic heterogeneities within the rock profiles. This form of diagram only allows for the evaluation of the geological significance of the isotope data.

### 5.2 ROCK PROFILE KB167

#### 5.2.1 Character of sample

##### *Geological situation*

Sample KB167 was collected in the southern part the study traverse on the farm Usambara 304, about 2 km north of the Us Pass road. The Kuiseb Formation in this area is dominated by thin-bedded, mainly pelitic and minor psammitic lithologies. The structural overprint is characterised by intense isoclinal folding and thrusting. The rocks display a composite  $S_{0,1,2,3}$  fabric; locally an  $S_4$  crenulation cleavage is developed. Bedding can be inferred on outcrop scale by major lithological changes. The sample locality lies approximately on the boundary between the structural domains A and B in Figure 2.8.

##### *Outline of the rock profile*

A rock profile 2 by 2 by 5.2 cm in size was cut perpendicular to the lithological layering and subsequently split into 12 layer-parallel slabs termed A to L. The extent of the rock profile and the position of the individual slabs with regard to the lithological layering are outlined in Figure 5.1.

The sample is characterised by a lithological layering on a cm-scale consisting of 6 compositionally different layers

on a cm-scale consisting of 6 compositionally different layers

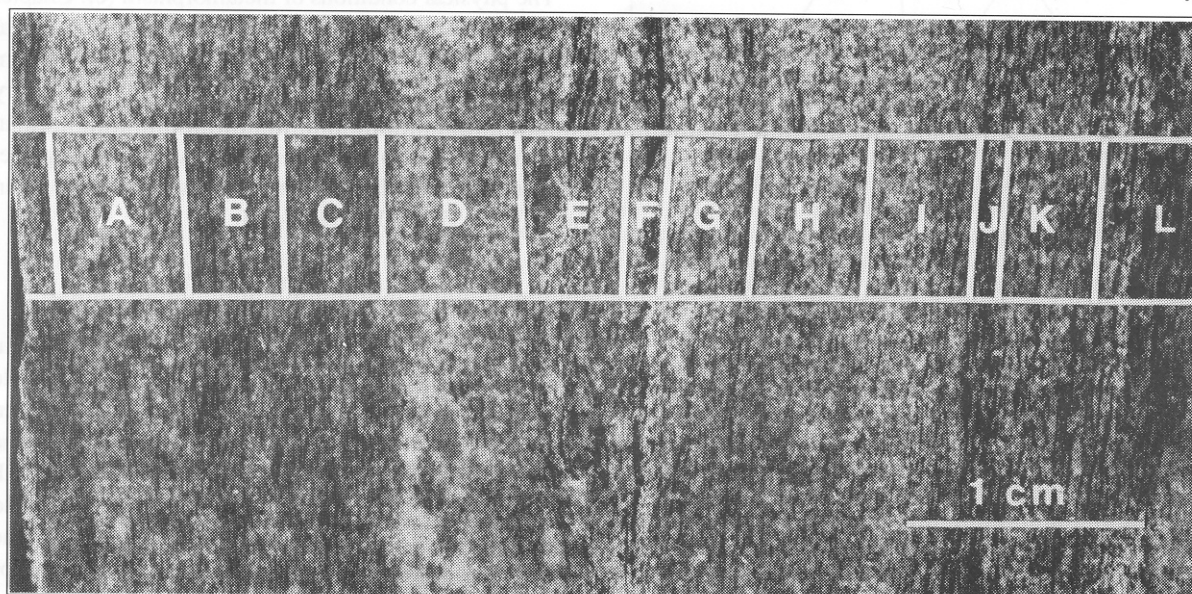


Figure 5.1: Sample KB167: Photograph of the sample and sketch of the rock profile with position of individual slabs indicated

(from left to right in Fig. 5.1):

- a psammitic layer (slab A),
- a more pelitic, biotite-rich layer (slabs B and C),
- a light-coloured psammitic, plagioclase- and garnet-rich (calc-silicate) layer (slabs D and E),
- a pelitic zone containing a partly sheared and crenulated chlorite-rich layer (slabs F and G),
- a psammitic, more plagioclase-quartz rich layer (slabs H and I),
- a biotite-chlorite rich pelitic layer including sheared lenses of quartz (slabs J, K and L).

The lithological changes within the sample certainly originate from sedimentary layering although bedding planes are obliterated by the composite  $S_{0,1,2,3}$  fabric.

Rb-Sr whole-rock analyses were carried out from the 11 contiguous slabs A-K. In addition, biotite fractions from the slabs B and C, each 60 to 180  $\mu\text{m}$  in grain size, were analysed for their Rb-Sr systematics.

#### Petrography

The pelitic and psammitic layers of the sample show the parageneses biotite + muscovite  $\pm$  garnet + plagioclase + quartz and chlorite + muscovite  $\pm$  garnet + plagioclase + quartz which are characteristic for the southern part of assemblage zone I (Fig. 2.5). Accessory phases are opaque minerals, tourmaline, titanite, apatite and zircon. The assemblages and the respective mineral compositions are illustrated in the AFM projection in Figure 5.2.

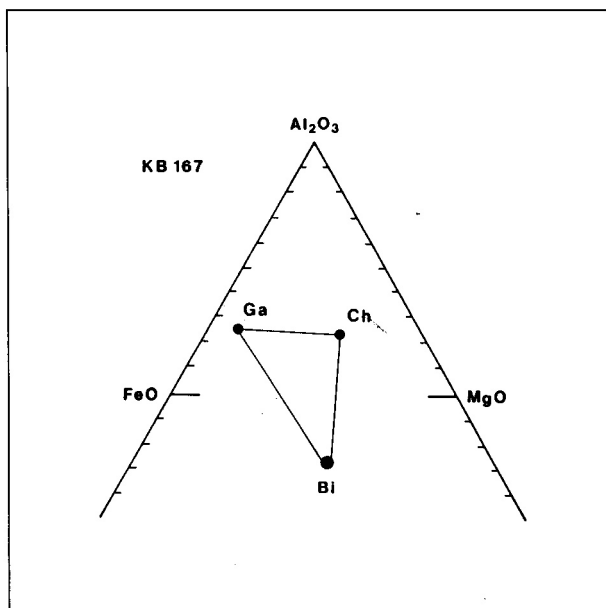


**Figure 5.2:** Sample KB167: AFM projection from theoretical muscovite showing the assemblage biotite + chlorite + garnet and the respective mineral compositions

Quartz occurs as xenomorphic grains in the matrix of the rock. The grain size is smaller in pelitic than in psammitic layers, but is generally heterogeneous ranging from fine- to medium-grained (up to 400  $\mu\text{m}$ ). Elongated crystals are frequent, but no undulous extinction or subgrain development were found.

Plagioclase is also a major constituent in the matrix of the rock. The crystals are generally untwinned with grain sizes <

100  $\mu\text{m}$ . The composition of the plagioclases varies depending on the bulk rock composition of lithologically different units of the rock profile. The An contents range from 22% for slab K to 31 % for slab D (Table A.1).

Biotite is green-brown and is mostly oriented in the main structural fabric of the sample. Two generations of biotite can be distinguished: an early generation which is oriented within the composite  $S_{0,1,2,3}$  fabric of the rock, and a second generation which crystallised post- $S_4$  as late, cross-cutting individuals (Fig. 5.3a). Both generations mostly show grain sizes of a few hundred micrometres, but may reach millimetre size. Microprobe analyses revealed no systematic variation in composition for the two biotite generations, although a general variability was found in the range of a few percent of the end-member concentrations (Table A2).

Muscovite occurs as fine-grained flakes in the matrix of the rock and is oriented within the  $S_{0,1,2,3}$  composite fabric. Muscovite coexists with primary chlorite and biotite, but is mainly confined to the chlorite-rich layer in the central portion of the rock profile.

Chlorite occurs both as a primary and a secondary phase. Primary chlorite is mainly confined to a distinct, partly sheared and crenulated layer in the central portion of the profile (slab F<sub>1</sub>, but occurs together with muscovite forming the matrix of the sample and is elongated in the  $S_{0,1,2,3}$  composite fabric. Late chlorite individuals crystallised post- $S_4$  overgrowing crenulated matrix chlorites (Fig. 5.3b). Secondary chlorite formed at the expense of biotite and garnet. Microprobe analyses of prograde chlorites revealed an average  $X_{\text{Mg}}$  of 0.59 (Table A4).

Garnet occurs in the sample as anhedral, lobate grains which are elongated parallel to the composite fabric of the rock and reach grain sizes up to 5  $\mu\text{m}$  (Fig. 5.3c). All garnets belong to garnet generation I (cf. Chapter 2.5). Inclusions in the garnets consist mainly of quartz and opaque phases. Microprobe analyses revealed a well-developed zoning pattern with a distinct increase in almandine and pyrope components and a decrease of spessartine and grossular from the core towards the rim of the crystals (Fig. 2.8; Table A.6).

The physical conditions of metamorphism (cf. Chapter 2.5) were estimated from the stability fields of mineral assemblages at temperatures of 530-590°C for a maximum pressure range of 4-9.5 kb. Garnet-biotite thermometry yielded T-estimates ranging from 516°C to 603°C at an estimated pressure of 6 kb; P-T estimates based on garnet compositions according to Spear and Cheney (1989) are in the range of 550-570°C and 5-8 kb.

#### 5.2.2 Analytical results

Results of the Rb-Sr whole-rock analyses are shown in Figures 5.4 and 5.5. The individual slabs of the rock profile display a total range in Rb and Sr concentrations between 56 and 168 ppm and 91 and 140 ppm, respectively. The element distribution curves (Fig. 5.4) show highest Rb concentrations for the pelitic slabs B, C, G, J and K, but do not reveal a correlation of Rb and Sr within the sample. The eleven slabs display a total spread in their  $^{87}\text{Rb}/^{86}\text{Sr}$  ratios of about 1.5 to 4.5.

Put into an isochron diagram (Fig. 5.5), the data scatter

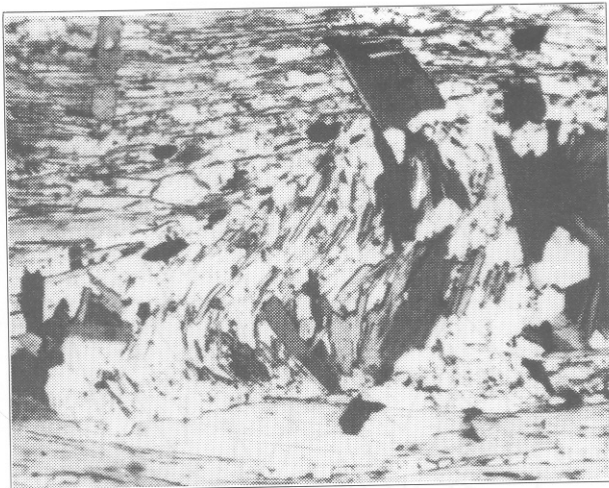


Figure 5.3a

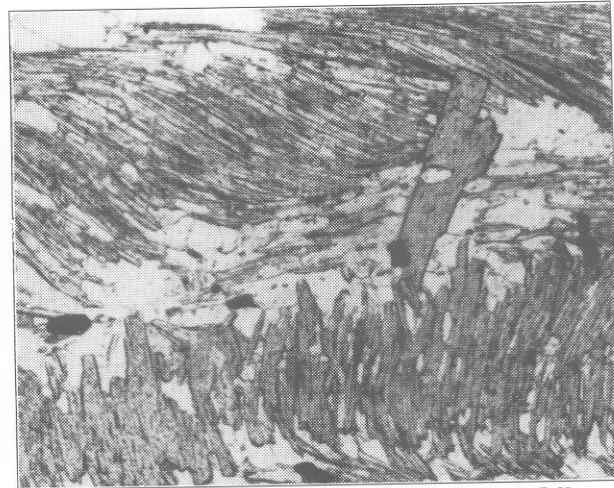


Figure 5.3b

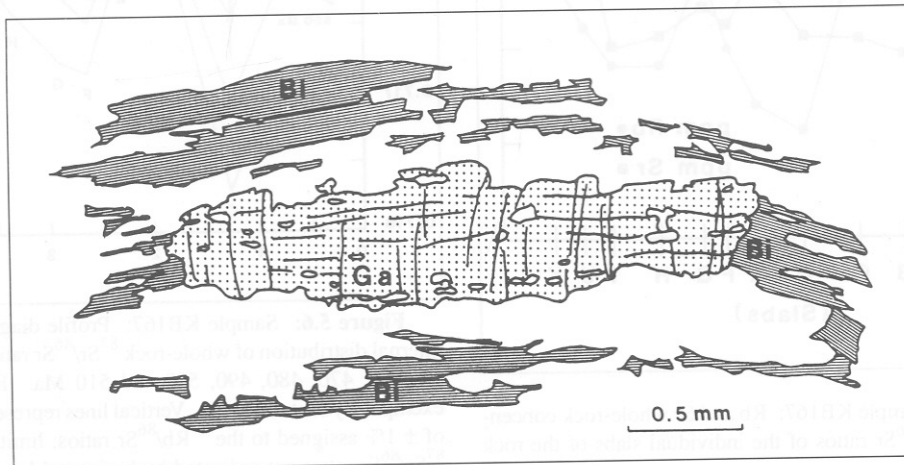


Figure 5.3c

**Figure 5.3:** Sample KB167: Thin section photographs showing a) biotites deformed by the  $S_4$  crenulation cleavage and overgrown by post- $D_4$  biotite (length of photograph is 2.0 mm). b) Chlorites deformed by  $D_4$  and overgrown by a late, crosscutting chlorite flake (length of photograph is 1.4 mm). c) Tracing from thin section showing elongated garnet I

around a regression line, the gradient of which corresponds to an age of  $488 \pm 13$  Ma. An initial  $^{87}\text{Sr}/^{86}\text{Sr}$  ratio of  $0.71841 \pm 0.00049$  was calculated. Not all of the data points, however, fall within limits of error onto the regression line as is evident from an MSWD value of 1.7.

Age calculations from biotite-whole-rock pairs yield  $491 \pm 10$  Ma for slab B and  $483 \pm 10$  Ma for slab C. The calculated age data for the whole rocks and both biotite-whole-rock pairs overlap within limits of error.

The spatial distribution and the computed temporal development of the  $^{87}\text{Sr}/^{86}\text{Sr}$  ratios from the individual slabs is illustrated in the profile diagram in Figure 5.6.  $^{87}\text{Sr}/^{86}\text{Sr}$  ratios were calculated corresponding to 460, 470, 480, 490, 500 and 510 Ma before present. Errors are shown exemplarily for the isotope ratios at 490 Ma. The length of the vertical error bars represents an uncertainty of 1% which is assigned to the  $^{87}\text{Rb}/^{86}\text{Sr}$  ratios. For the  $^{87}\text{Sr}/^{86}\text{Sr}$  ratios, errors are given as the analytical errors of the measured  $^{87}\text{Sr}/^{86}\text{Sr}$  ratios. In the case of repeated analyses, which are marked by asterisks in the profile diagram, the uncertainty obtained from the deviation of the repeated analyses (if exceeding the analytical error of the individual data) is given instead of the analytical errors of the individual  $^{87}\text{Sr}/^{86}\text{Sr}$  ratios. The range of the error of the  $^{87}\text{Sr}/^{86}\text{Sr}$  ratios is limited by horizontal bars (cf. age calculation and error evaluation in Appendix III). The same applies to the profile diagrams computed for

the other five rock profiles.

The most striking feature of the isotope distribution curves is that for no time can a homogeneous  $^{87}\text{Sr}/^{86}\text{Sr}$  ratio for all slabs be calculated. This, however, is in accordance with the slight scatter of the whole-rock data as shown in Figure 5.5. It has to be emphasised that the calculated isotope ratios show unlikely distribution patterns for the slabs C-D, E-F and I-J-K prior to 470 Ma and for the slabs B-C throughout all of the curves. Despite higher Rb concentrations, the slabs C, F and J have lower  $^{87}\text{Sr}/^{86}\text{Sr}$  ratios with respect to the adjacent portions of the rock. This kind of pattern cannot have evolved from an undisturbed, equilibrated isotope system. The isotope ratios at 470 and 460 Ma represent possible distribution patterns with regard to the measured Rb and Sr concentrations of the individual whole rocks. Partial equilibria in the isotope distribution pattern exist for the slabs C-F at 470 Ma and G-H at 480 Ma. Slabs D and E, which share similar isotope characteristics, were both cut from the same psammitic layer.

Because no homogeneous  $^{87}\text{Sr}/^{86}\text{Sr}$  isotope distribution can be calculated for the rock profile, it can be concluded that either no equilibrium distribution of Sr isotopes was reached during final metamorphism, or the Sr isotope equilibrium has subsequently been disturbed.

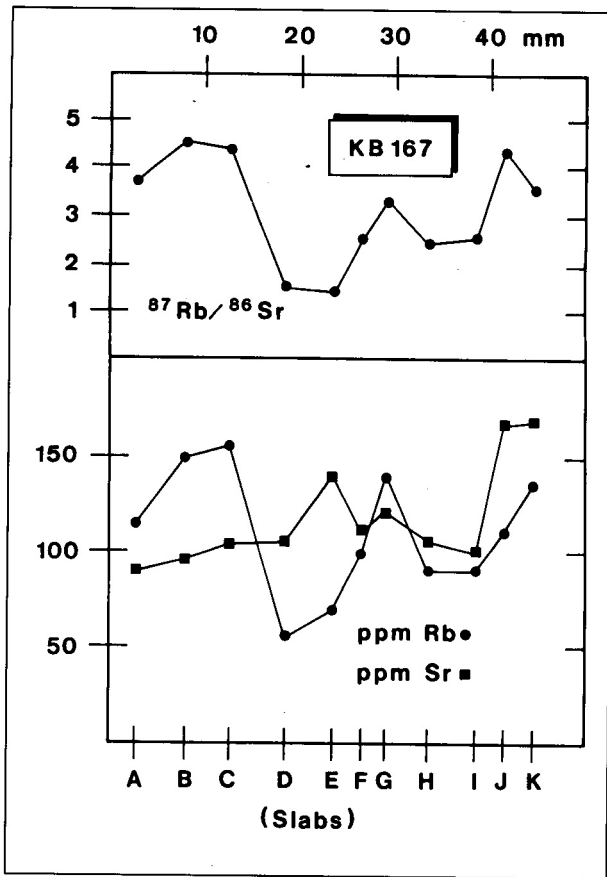


Figure 5.4: Sample KB167: Rb and Sr whole-rock concentrations and  $^{87}\text{Rb}/^{86}\text{Sr}$  ratios of the individual slabs of the rock profile

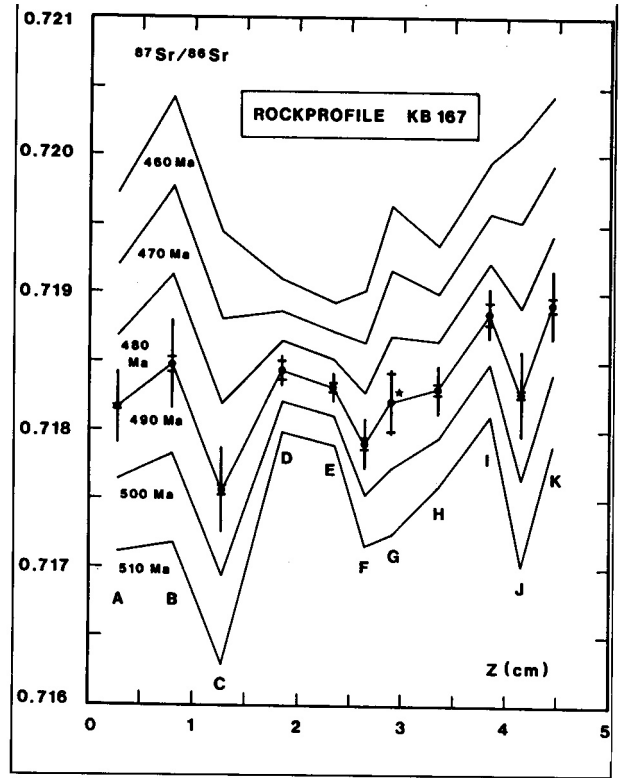


Figure 5.6: Sample KB167: Profile diagram showing the internal distribution of whole-rock  $^{87}\text{Sr}/^{86}\text{Sr}$  ratios, calculated for  $t = 460, 470, 480, 490, 500$  and  $510$  Ma. Errors are shown exemplarily for  $t = 490$  Ma. Vertical lines represent an uncertainty of  $\pm 1\%$  assigned to the  $^{87}\text{Rb}/^{86}\text{Sr}$  ratios; limits of error for the  $^{87}\text{Sr}/^{86}\text{Sr}$  ratios are indicated by horizontal bars. Repeated analyses are marked by asterisks

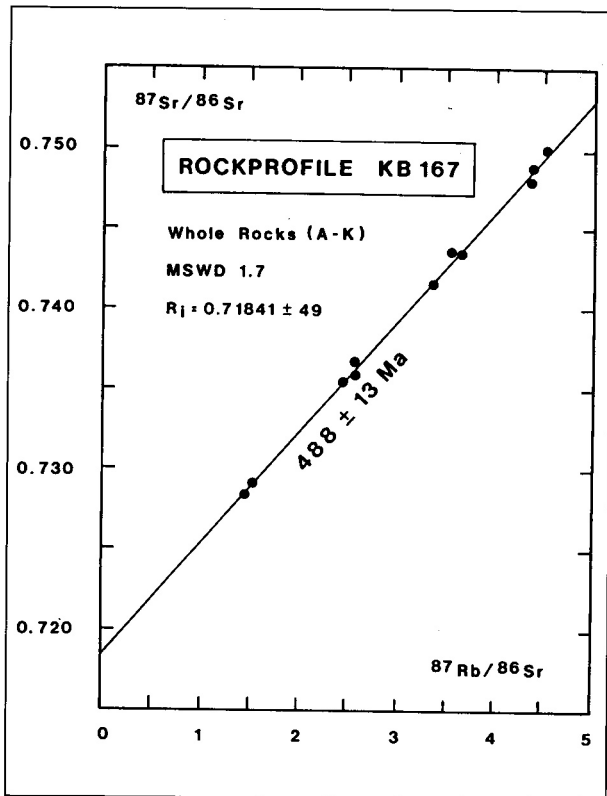


Figure 5.5: Sample KB167: Isochron diagram

### 5.3 ROCK PROFILE KB117

#### 5.3.1 Character of sample

##### Geological situation

Rock profile KB117 was taken from the 150 kg sample CO117 which was collected in the central part of the Khomas Trough (farm Kaan 309) from a 3-m-thick meta-greywacke layer for the purpose of zircon separation. The psammitic material displays a strong metamorphic banding correlated with the regional  $S_2$  fabric. The striped appearance is due to an alternation of biotite-rich P- and biotite-poor Q-domains; spacing is on a mm scale. In pelitic and semi-pelitic layers in the hanging wall and footwall of the horizon, the  $S_2$  cleavage developed as a schistose type of fabric. Bedding can clearly be distinguished from the metamorphic layering by sedimentary structures within the outcrop. The  $S_2$  fabric is axial planar to an upright, open  $F_2$  syncline. During the  $D_3$  deformational event, the  $S_2$  fabric was overprinted by  $S_3$  at an oblique angle. Figure 5.7 is a photograph of the sample material.

##### Outline of the rock profile

For Rb-Sr small-domain investigations, a rock profile was cut perpendicular to the metamorphic banding of the sample. The profile was split into 13 contiguous slabs of contrasting composition which in most cases correspond to the P- and Q-domains of the rock. The profile has a total length of 3.9

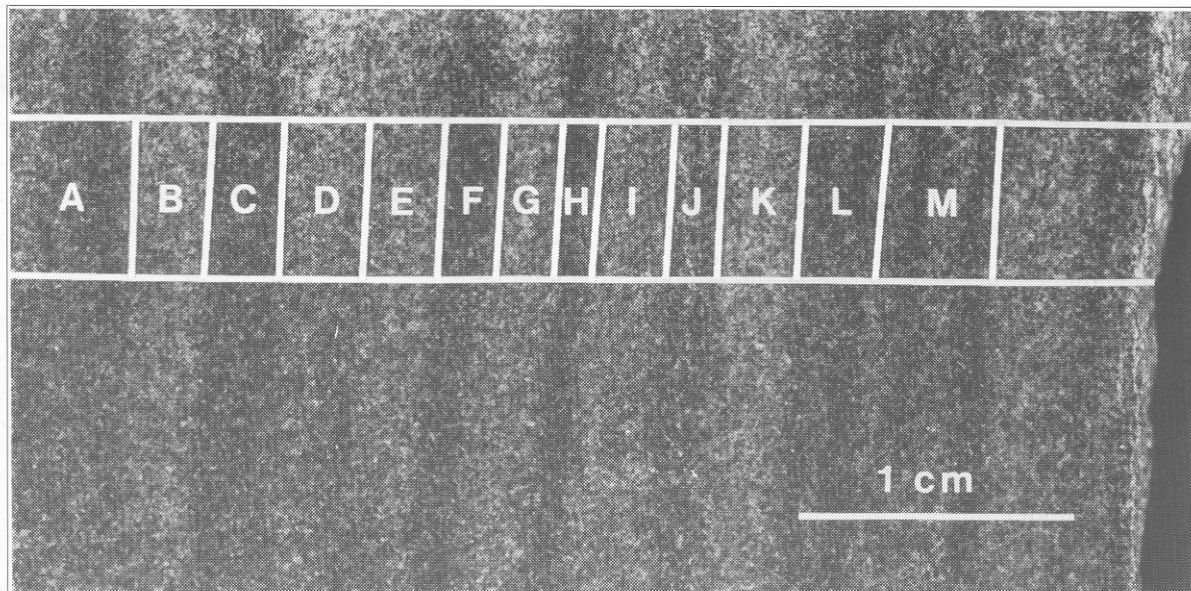


Figure 5.7: Sample KB117: Photograph of sample and sketch of the rock profile with the position of the individual slabs indicated

cm, the individual slabs ranging from 1 to 4 mm thick. The extent of the rock profile and the position of the individual slabs are outlined in Figure 5.7.

Rb-Sr whole-rock analyses were carried out on the 12 contiguous slabs B-M of the rock profile. In addition, one biotite fraction (60-180  $\mu\text{m}$ ) and one quartz-plagioclase concentrate (< 60  $\mu\text{m}$ ) from slab B was analysed. Besides the small-domain investigations of the rock profile, Rb-Sr analyses were also carried out on a representative split of the large-scale sample CO117 (total weight about 150 kg) including analyses of the whole-rock composition and one fraction each of biotite (60-180  $\mu\text{m}$ ), muscovite (60100  $\mu\text{m}$ ) and apatite (60-100  $\mu\text{m}$ ).

#### Petrography

The metamorphic assemblage observed in the psammite material is biotite + muscovite + plagioclase + quartz with local secondary chlorite. Accessory minerals are apatite, tourmaline, zircon and opaque phases. Two bedding-parallel, each about 10-cm-thick calc-silicate horizons comprising the paragenesis calcite + clinozoisite + plagioclase + garnet + green hornblende + titanite  $\pm$  biotite are intercalated within the meta-greywacke. Pelitic and semi-pelitic horizons below and above the psammite are characterised by the assemblage staurolite  $\pm$  andalusite + garnet + biotite + muscovite + plagioclase + quartz. From the stability fields of mineral assemblages and the presence of andalusite, maximum P-T conditions of 610°C and 3 kb were inferred in Chapter 2.5 to have been reached during metamorphism.

Due to the small size of the investigated rock profile, microprobe analyses were carried out using another specimen from the same sample.

Quartz and plagioclase occur as xenomorphic grains in the matrix of the rock. The grain size is mostly fine-grained (< 100  $\mu\text{m}$ ), but may reach about 200  $\mu\text{m}$ . The size of matrix minerals is reduced in P-domains compared to Q-domains. Quartz apparently recrystallised under stress-free condi-

tions. Plagioclase crystals are generally untwinned. Microprobe analyses revealed a range in plagioclase compositions of 13 to 19% An; the variation is about the same within and between the P- and Q-domains (Table A.1).

Biotite is concentrated in P-domains where it constitutes between 30 and 60% of the rock. In Q-domains biotites make up about 20% of the rock, but the domains are not strictly defined and the transitions between the domains are continuous. Three generations of biotite can be distinguished on the basis of their orientation. The first generation is oriented within the  $S_2$  metamorphic banding of the rock. A second biotite generation corresponds to the regional  $S_3$  fabric (Fig. 5.8). A third generation of biotites consists of late, cross-cutting and non-oriented individuals. Grain sizes are similar for all three generations (mostly < 200  $\mu\text{m}$ , up to 300  $\mu\text{m}$ ). Microprobe analyses revealed no systematic differences in the composition of biotites from different generations; the average composition of  $S_2$  biotites is equivalent to the total

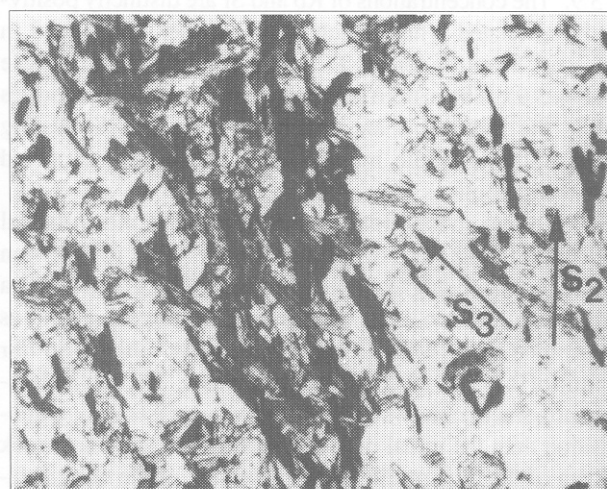


Figure 5.8: Sample CO117: P-Q-fabric in thin section showing P-domain in the centre of the photograph with  $S_2$  and  $S_3$  biotites (length of photograph is 1.4 mm)

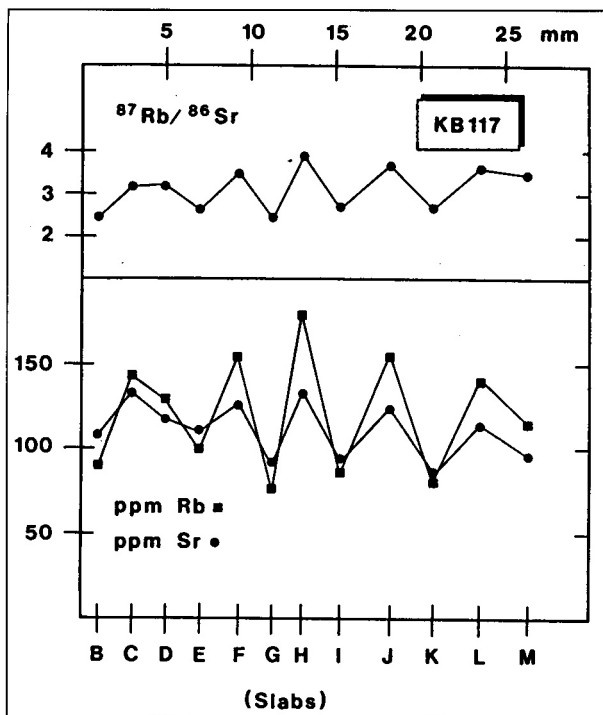


Figure 5.9: Sample KB117: Rb and Sr concentrations and Rb-Sr ratios of individual slabs of the rock profile

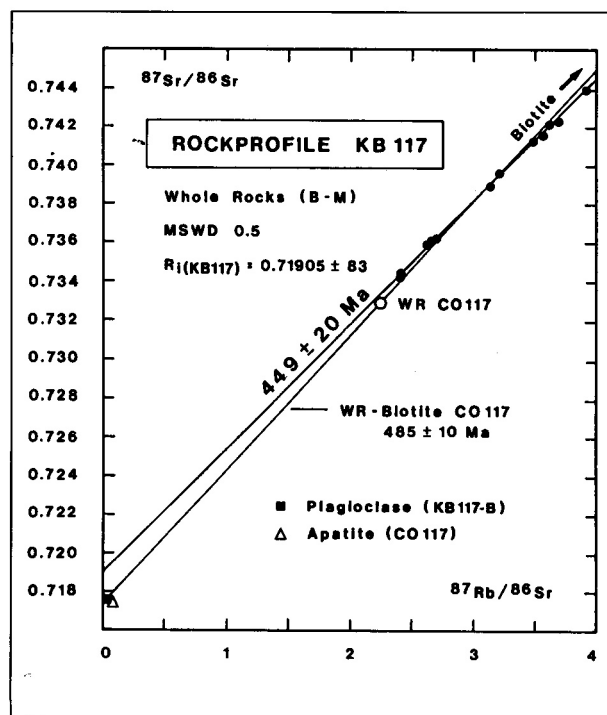


Figure 5.10: Sample KB117: Isochron diagram

average (Table A.2).

Muscovite occurs as network-like oriented small grains (mostly < 100  $\mu\text{m}$ , rarely > 200  $\mu\text{m}$ ) in the matrix of both the P- and Q-domains. As far as can be estimated from the number of analytical data, there is no significant variation in the chemical composition of the muscovites. Si values range from 6.24 to 6.26 (Table A.3).

### 5.3.2 Analytical results

Analytical results are illustrated in Figures 5.9 and 5.10. The Rb and Sr concentrations of the individual slabs of the rock profile vary between 81 and 179 ppm and 87 and 133 ppm, respectively. Rb-Sr ratios range between 2.4 and 3.9. The concentrations of Rb and Sr are distinctly positively correlated which results in the rather low spread in  $^{87}\text{Rb}/^{86}\text{Sr}$  ratios for the P- and Q-domains of the sample (Fig. 5.9). The pattern of the element distribution indicates that the P-domains are enriched in Rb- and Sr-bearing minerals, i.e. biotite, muscovite and plagioclase, compared to the Q-domains.

Put into an isochron diagram (Fig. 5.10), the analytical data for the 12 slabs of the rock profile define a regression line corresponding to an age of  $449 \pm 20$  Ma. All of the data points fall, within limits of error, onto the regression line, as recorded by an MSWD value of 0.5. An initial  $^{87}\text{Sr}/^{86}\text{Sr}$  ratio of  $0.71905 \pm 0.00083$  was calculated. The plagioclase-quartz fraction shows a significantly lower isotopic composition than the initial ratio calculated from the whole-rock data of the rock profile. The regression of the quartz-plagioclase and whole-rock data of slab B yields  $491 \pm 15$  Ma. The biotite fraction of the same slab gave a biotite whole-rock age of  $472 \pm 10$  Ma.

The mineral fractions from the composite sample CO117 re-

vealed the following data:  $485 \pm 10$  Ma for biotite whole-rock,  $500 \pm 22$  Ma for apatite whole-rock and  $546 \pm 17$  Ma for the muscovite whole-rock pair. The isotopic composition of the plagioclase fraction from slab B of the rock profile falls, within limits of error, onto the two-point regression line of whole rock and biotite from CO117; the data point for the apatite fraction of CO117 even falls below the latter regression line (Fig. 5.10).

The most striking feature of this sample is the fact that the regression of the whole-rock data from the rock profile yields a lower age than the biotite and plagioclase fractions from one of the slabs, although both minerals form the major constituents and the major Rb- and Sr-bearing mineral phases of the rock. Thus a resetting of the whole-rock isotopic system without an opening of the isotopic systems within the two minerals seems unlikely.

The spatial distribution and the computed temporal development of the  $^{87}\text{Sr}/^{86}\text{Sr}$  ratios of the individual slabs is illustrated in the profile diagram in Figure 5.11.  $^{87}\text{Sr}/^{86}\text{Sr}$  ratios were calculated corresponding to 430, 440, 449, 460, 470 and 491 Ma before present. Errors are shown exemplarily for the whole-rock isotope ratios at 449 and 491 Ma. The plagioclase fraction of slab B is shown as point P.  $^{87}\text{Sr}/^{86}\text{Sr}$  ratios for the plagioclase fractions were calculated for a time interval between 400 and 600 Ma represented by the vertical extent of the symbol. The errors in the  $^{87}\text{Sr}/^{86}\text{Sr}$  and  $^{87}\text{Rb}/^{86}\text{Sr}$  ratios do not exceed the given range of the isotope ratios for the time interval.

In accordance with the good fit of data in the isochron diagram, isotope ratios show, within limits of error, a homogeneous distribution pattern for  $t = 449$  Ma. Towards lower and higher ages, the whole-rock isotope signatures become increasingly heterogeneous. At the time of the biotite-whole-rock isotope equilibrium ( $472 \pm 10$  Ma and  $485 \pm 10$  Ma), apparently no

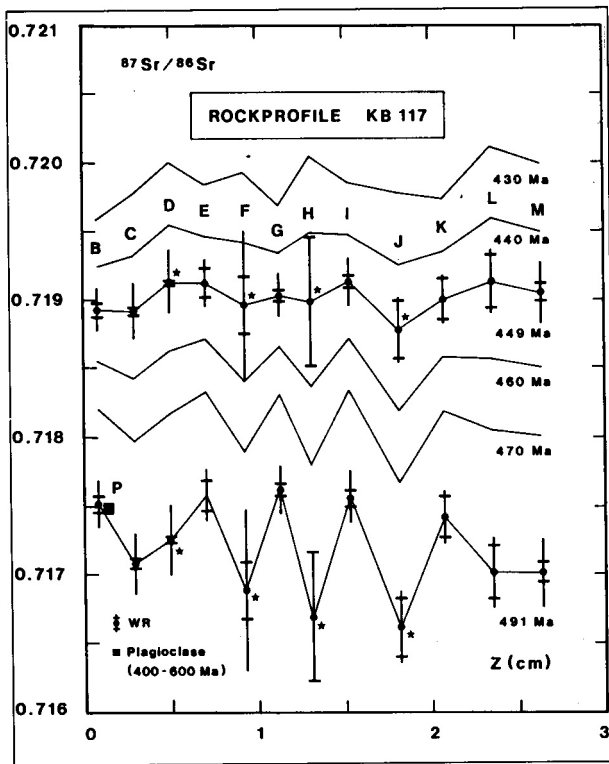


**Figure 5.11:** Sample KB117: Profile diagram showing the computed internal distribution of whole-rock  $^{87}\text{Sr}/^{86}\text{Sr}$  ratios, calculated for  $t = 430, 440, 449, 460, 470$  and  $491$  Ma. Errors are shown exemplarily for  $t = 449$  and  $491$  Ma. Vertical lines represent an uncertainty of  $\pm 1\%$  assigned to the  $^{87}\text{Rb}/^{86}\text{Sr}$  ratios; limits of error for the  $^{87}\text{Sr}/^{86}\text{Sr}$  ratios are indicated by horizontal bars. Repeated analyses are marked by asterisks

equilibrium conditions existed between the individual slabs of the rock profile. The plagioclase fraction from slab B which has an almost constant isotopic composition between 400 and 600 Ma (Fig. 5.11), is in equilibrium with its respective whole rock at about 490 Ma. This relationship suggests that the apparent isochron age which would be interpreted as an

homogenisation of whole-rock isotopic compositions at 449 Ma, is not of geological relevance. A homogenisation of the  $^{87}\text{Sr}/^{86}\text{Sr}$  isotopes of the whole-rock systems without affecting the isotopic signatures of the constituting mineral phases seems inconceivable. This controversy between the different data will, however, remain unresolved for the moment, and will be discussed at the end of this chapter together with the data from the other samples.

## 5.4 ROCK PROFILE KB307

### 5.4.1 Character of sample

#### *Geological situation*

Sample KB307 consists of thin-bedded, regularly alternating pelitic and psammitic layers, partly gradational in character. Each layer is about one centimetre thick. The sample location is only a few hundred metres north of the scapolite schist on the farm Dagbreek 365 (Fig. 2.8). The zone is characterised by an intense  $D_3$  deformation. The sample shows a well-developed slaty  $S_3$  cleavage made up of parallel-oriented biotites. Figure 5.12 is a photograph of the sample material.

#### *Outline of the rock profile*

A profile about 7 cm wide was cut perpendicular to the layering of the sample. The rock profile itself was split into 13 contiguous slabs termed A to M, each representing one lithological layer of the sample. The thickness of slabs ranges between 1 and 10 mm. One of the pelite layers (slab J) is followed on both sides by thin light-coloured, quartz-rich horizons. Slab K was cut from one of these layers (1 mm thick). The outline of the rock profile and the position of slabs is illustrated in Figure 5.12.

Whole-rock Rb-Sr analyses were carried out from the 13 contiguous slabs A - M, one muscovite fraction (125-250  $\mu\text{m}$ )

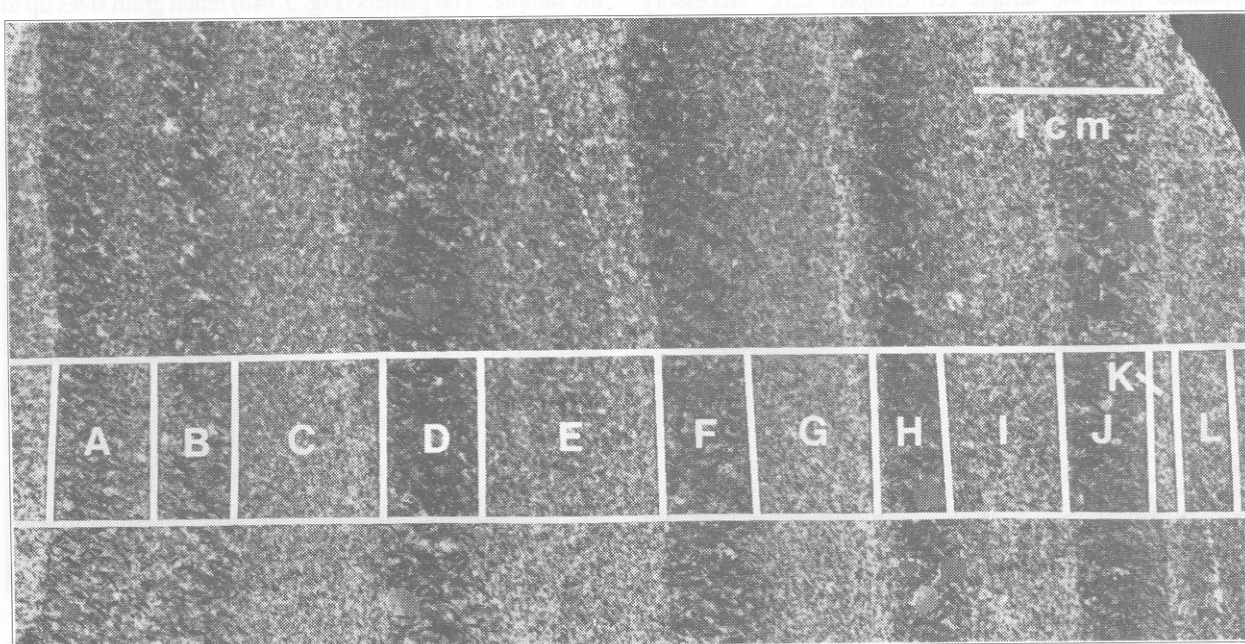


**Figure 5.12:** Sample KB307: Photograph of sample and sketch of the rock profile with the position of individual slabs indicated

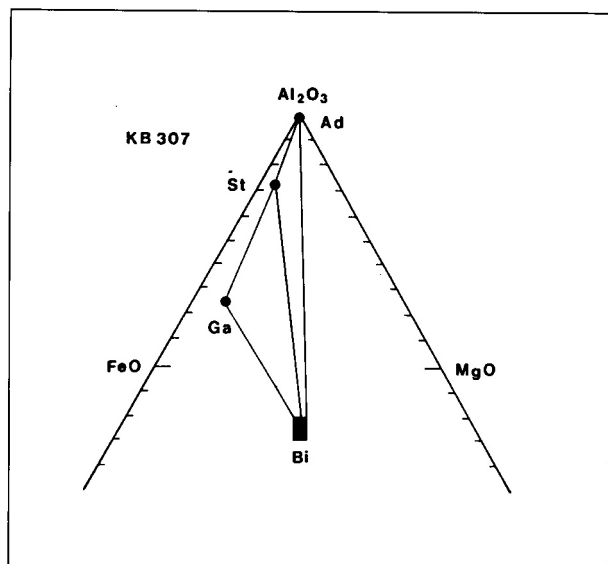


**Figure 5.13:** Sample KB307: AFM projection through the theoretical muscovite showing the assemblage andalusite + staurolite + garnet + biotite

from slab F and one biotite fraction (60-180  $\mu\text{m}$ ) from slab D were also analysed.

#### Petrography

The metamorphic mineral assemblages staurolite + garnet + biotite + muscovite + plagioclase + quartz and andalusite + garnet + biotite + muscovite + plagioclase + quartz occur in the pelitic layers of the rock profile (Fig. 5.13). The same paragenesis occurs in the pelite sample CO418 which is located about a hundred metres to the north. The samples delineate the northern boundary of the andalusite zone within the study traverse (Fig. 2.4). From the presence of andalusite, P-T conditions of metamorphism were inferred to have reached a maximum of 610°C and 3 kb which is well in agreement with garnet-biotite thermometric data obtained from the sample (cf. Chapter 2.5). Accessory phases are opaque minerals, apatite, tourmaline, and zircon as a detrital component.

Quartz and plagioclase occur as xenomorphic grains in the fine-grained matrix of the rock. They are major constituents of psammitic layers, but are subordinate in pelites. Grain sizes are heterogeneous, reaching a maximum of about 100  $\mu\text{m}$ . Both minerals are well recrystallised and share mostly polygonal grain boundaries. Plagioclase is generally untwinned. The chemical composition of the plagioclases ranges between about 7 and 20% An component

Biotite constitutes up to about 40% of the pelitic layers. Three different generations can be distinguished on the basis of their orientation (Fig. 5.14a):  $S_2$  biotites,  $S_3$  biotites which form the most prominent biotite generation, and a late generation which grew post-kinematically and crosscuts older generations.  $S_3$  biotites may reach a grain size of 1 mm, but most biotites are < 500  $\mu\text{m}$ . Post-kinematic biotites are mostly about 1 mm in size. Microprobe analyses revealed no significant or systematic differences in composition for early and late biotites (Table A.2).

Muscovite occurs in two distinctly different generations in the sample. Fine-grained muscovites (mostly < 100  $\mu\text{m}$ ) with a network-like orientation are a major constituent in the matrix of the pelitic layers. A second generation, here termed "late" muscovites, occurs as product of andalusite and staurolite decomposition, forming large (up to 1 mm), platy crystals which are partly intergrown with quartz. Microprobe analyses discerned differences in the composition of matrix and late muscovites. The latter (analysed from slab A) are characterised by a lower celadonite component (average 0.6%) and Si values of about 6.1 compared to matrix muscovites (6.2-6.3 Si; Table A.3). The late muscovites were inferred to have crystallised during a high-temperature retrogressive hydration event (cf. Chapter 2.5). The muscovite fraction used for isotope analyses was 125-250  $\mu\text{m}$  in grain size and thus may be assumed to represent a pure fraction of this late generation of muscovites.

Garnets are developed as euhedral to subhedral grains which are concentrated mainly in the pelitic lithologies of the sample. The garnets (Fig. 5.14b) reach grain sizes up to 5 mm and belong to the late garnet generation III. The crystals show a weak zonation with a slight increase in almand-

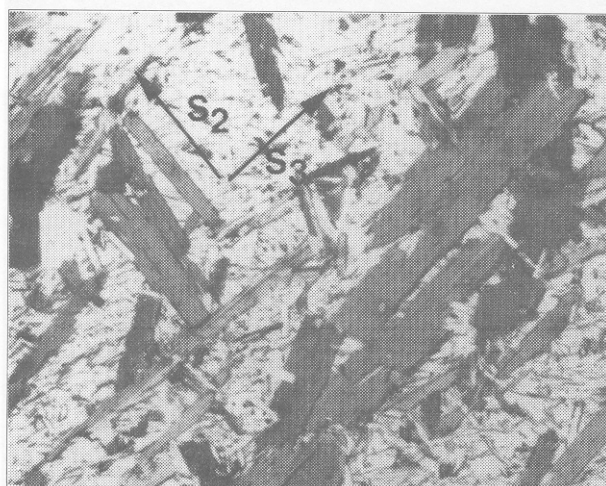


**Figure 5.14a:** Sample KB307: Thin section photomicrograph showing biotite generations aligned within the  $S_2$  and  $S_3$  cleavages (length of photograph is 1.4 mm)

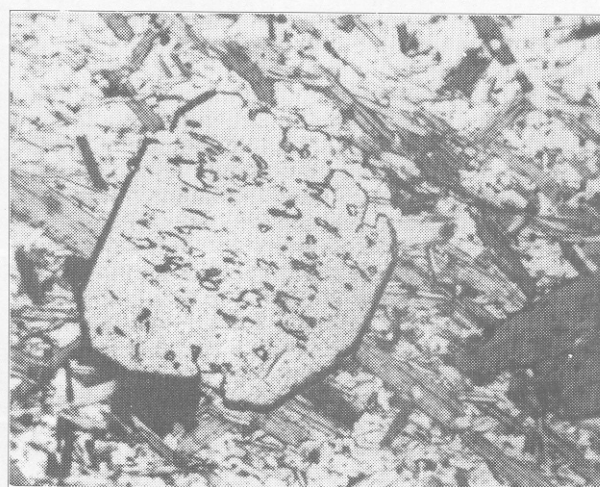


**Figure 5.14b:** Typical garnet of generation III (length of photograph is 2.0 mm)

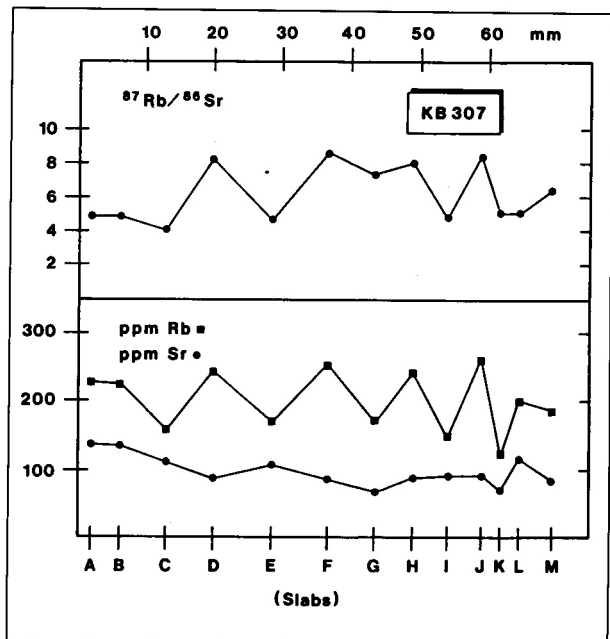


Figure 5.15: Sample KB307: Rb and Sr concentrations and the  $^{87}\text{Rb}/^{86}\text{Sr}$  ratios of the individual slabs of the rock profile

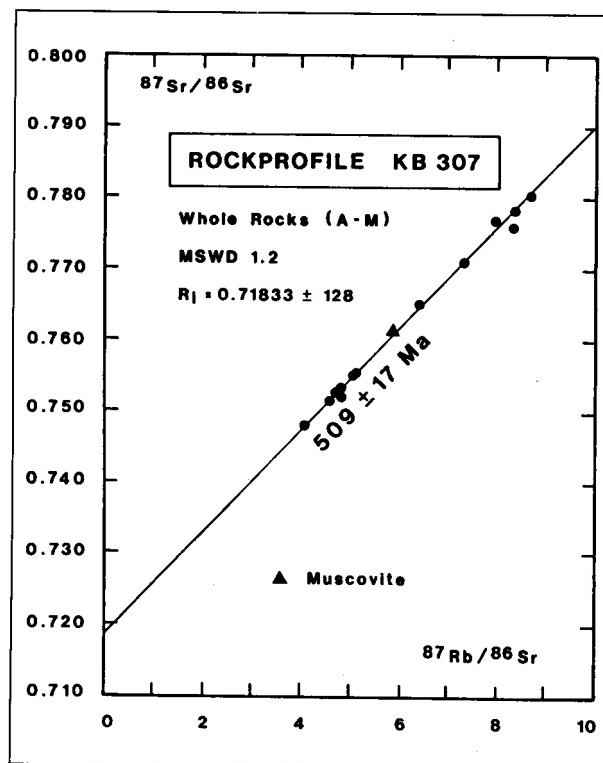


Figure 5.16: Sample KB307: Isochron diagram

ine and pyrope and a decrease in spessartine and grossular end-member components from the core to the rim (Fig. 2.8, Table A.6).

Staurolite occurs rarely as small grains in the pelitic layers. Grain sizes reach only a few millimetres. The crystals show a poikiloblastic texture and are partly sericitised or completely replaced by platy muscovites.

Andalusite occurs as isolated, largely muscovitised relics in the pelitic layers of the sample.

#### 5.4.2 Analytical results

Analytical results are presented in Figures 5.15 and 5.16. Whole-rock element concentrations of the individual slabs vary between 120 ppm Rb/67 ppm Sr for psammitic layers and 263 ppm Rb/137 ppm Sr for pelitic layers. The Rb-Sr ratios range from 4.1 (slab C) to 8.7 (slab F). The Rb and Sr concentrations apparently are not correlated which is due to the variable proportions of micas and plagioclase. The muscovite fraction from the biotite-rich slab F shows comparatively high Sr concentrations (73 ppm) and a relatively low Rb-Sr ratio of only 5.9 in contrast to the Rb-Sr ratio of 8.7 for the respective whole rock.

Put into an isochron diagram (Fig. 5.16), the whole-rock isotope data scatter around a regression line, the slope of which corresponds to an age of  $509 \pm 17$  Ma with an initial  $^{87}\text{Sr}/^{86}\text{Sr}$  ratio of  $0.71833 \pm 0.00128$ . An MSWD of 1.2 indicates that almost all data points fall, within limits of error, onto the regression line. The biotite fraction from slab D yields a biotite-whole-rock age of  $488 \pm 11$  Ma. Age calculations from the muscovite and whole-rock data from slab F do not give relevant age data due to the low  $^{87}\text{Rb}/^{86}\text{Sr}$  ratio of the muscovite; the regression of the data gives only a poorly defined value.

The profile diagram in Figure 5.17 illustrates the spatial

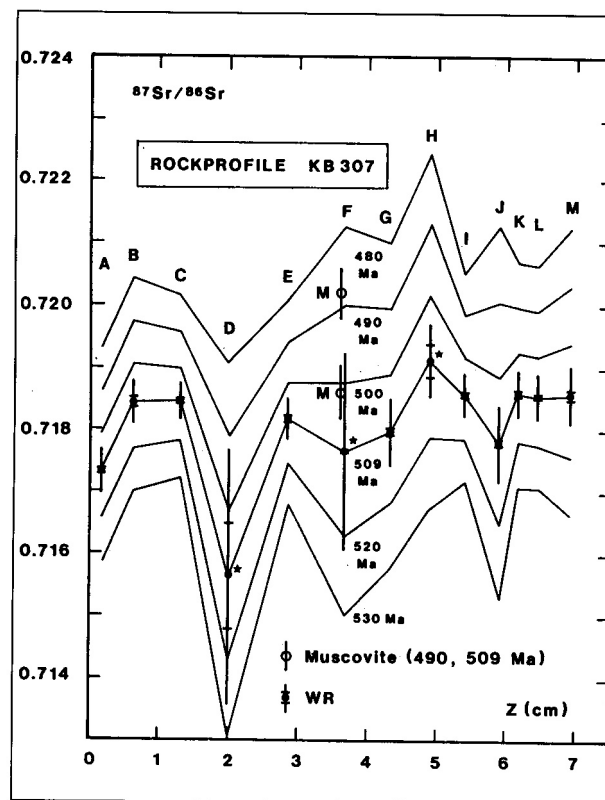


Figure 5.17: Sample KB307: Profile diagram showing computed internal distribution of  $^{87}\text{Sr}/^{86}\text{Sr}$  ratios, calculated for  $t = 480, 490, 500, 509, 520$  and  $530$  Ma. Errors are shown exemplarily for  $t = 509$  Ma. Vertical lines represent an uncertainty of  $\pm 1\%$  assigned to the  $^{87}\text{Rb}/^{86}\text{Sr}$  ratios; limits of error for the  $^{87}\text{Sr}/^{86}\text{Sr}$  ratios are indicated by horizontal bars. Repeated analyses are marked by asterisks

distribution and the computed temporal development of the  $^{87}\text{Sr}/^{86}\text{Sr}$  isotope ratios within the rock profile. Whole-rock  $^{87}\text{Sr}/^{86}\text{Sr}$  ratios were calculated for  $t = 480, 490, 500, 509, 520$  and  $530$  Ma. Errors are shown exemplarily for the whole-rock isotope ratios at 509 Ma. The muscovite fraction from slab F is marked as point M in the profile diagram;  $^{87}\text{Sr}/^{86}\text{Sr}$  ratios were calculated for  $t = 490$  and  $509$  Ma (shown in open circles with a vertical  $^{87}\text{Rb}/^{86}\text{Sr}$  error bar).

The isotope distribution curves clearly show that for no time considered, can a homogeneous distribution of  $^{87}\text{Sr}/^{86}\text{Sr}$  isotope ratios be calculated. The most prominent heterogeneity within the profile's isotope pattern occurs in slab D which has a lower  $^{87}\text{Sr}/^{86}\text{Sr}$  isotope ratio compared to the neighbouring slabs despite its high  $^{87}\text{Rb}/^{86}\text{Sr}$  ratio. Due to the large analytical error (based on the deviation of repeated analyses), however, the data point is neither critical for the regression calculation nor when considering the isotope distribution patterns in the profile diagram. But even neglecting the slab for further considerations of the rock profile's internal isotope distribution, no homogeneous isotope distribution pattern is obtained. Partial equilibria can be calculated for parts of the rock profile (slabs Band C, E to G and K to M) for  $t = 509$  Ma, and for the slabs J-M at 490 Ma. The whole-rock isotope distribution curves show the least variation at about 500 Ma which might be interpreted as the time of a partial equilibration of the whole-rock Rb-Sr system. The isotopic composition of the muscovite fraction from slab F is concordant, within limits of error, with the respective whole-rock isotope ratios between 520 and 480 Ma. The timing of muscovite-whole-rock equilibration thus cannot be deduced precisely.

## 5.5 ROCK PROFILE KB421

### 5.5.1 Character of sample

#### *Geological situation*

Sample KB421 was collected from the northern carbonate- and scapolite-rich sequence which also represents one of the most prominent marker horizons within the Khomas Trough. The sample locality lies on the southern border of the farm Keises 312. The structural situation is characterised by an intense  $D_3$  deformation which is concentrated in a rather narrow zone some hundreds of metres thick. The zone can be traced on the Landsat image for more than a hundred kilometres and is interpreted as one of the major  $D_3$  overthrust zones in the Khomas Trough. Large-scale post-kinematic scapolitisation of the sequence indicates that fluid movement occurred along the thrust zones (P. Kukla, 1990). In contrast to the southern scapolite schists, the formation of scapolite in this sequence was not pervasive; only individual crystals occur, mostly associated with small fractures in the rock. The sequence is carbonate-rich and most of the subordinate psammites contain large quantities of calc-silicates. The psammitic horizons show a strong anastomosing metamorphic banding cleavage (Fig. 5.18) which is correlated with the regional  $S_2$  fabric. The rocks are interspersed with small fractures filled with calcite.

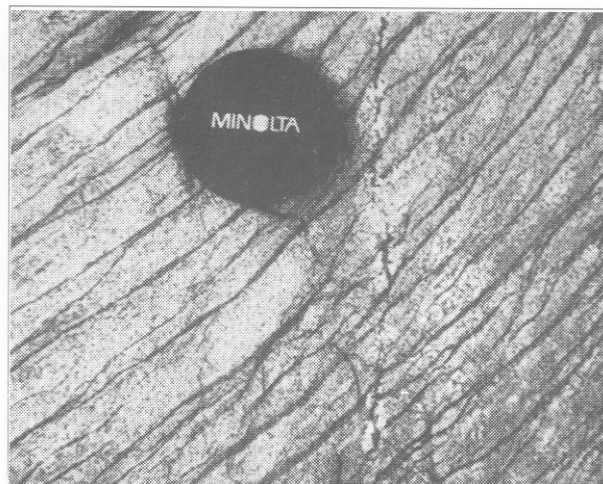


**Figure 5.18:** Sample KB421: Spaced  $S_2$  metamorphic banding in calc-silicate-rich sequence (diameter of lens cap is 4.9 cm); farm Keises 312

#### *Outline of the rock profile*

For Rb-Sr small-domain investigations, psammitic material with a distinct metamorphic banding was selected from the sequence. Figure 5.19a is a photograph of the sample material. A rock profile about 16 cm long was cut perpendicular to the layering of the sample. Half of the rock profile (about 8 cm) was sectioned into 22 contiguous slabs of different composition (between 2 and 5 mm thick). Slabs 31 and 33 were cut from the second half of the profile and were used for hornblende and biotite separation. Small, calcite-filled fractures occur in slabs 16 to 22. Individual scapolite crystals have grown along those fractures. The outline of the rock profile and the relative position of the individual slabs are sketched in Figure 5.19b.

Rb-Sr whole-rock analyses were carried out from contiguous slabs I to 21 and slabs 31 and 33. In addition, one biotite fraction (80-180  $\mu\text{m}$ ) and one hornblende fraction (80-180  $\mu\text{m}$ ) from slab 33 were analysed.

#### *Petrography*

The sample material consists of diffusive masses of calc-silicate rock within an otherwise psammitic matrix. The psammitic parts of the sample show a distinct metamorphic layering made up of biotite-rich P-domains and biotite-poor Q-domains. In the Q-domains, both biotite and hornblende are present. In the calc-silicate-rich parts of the material, the banding is either totally absent or appears only vaguely. The sample in general is rich in calcite, which occurs in fractures as well as in discrete grains in the matrix of the rock. A number of authors have described the paragenesis Ca-amphibole + chlorite + zoisite/epidote + plagioclase + calcite + quartz as being typical for the calc-silicate rocks of the Kuiseb Formation (e.g. Puhon and Hoffer, 1973; Puhon, 1976, 1983; Storre and Nitsch, 1983). In the sample investigated in this study, the predominant mineral assemblages are Ca-amphibole + biotite + clinozoisite + plagioclase + calcite + quartz and biotite + calcite + titanite (Fig. 5.20). Chlorite, however, occurs only as a retrograde phase after biotite.

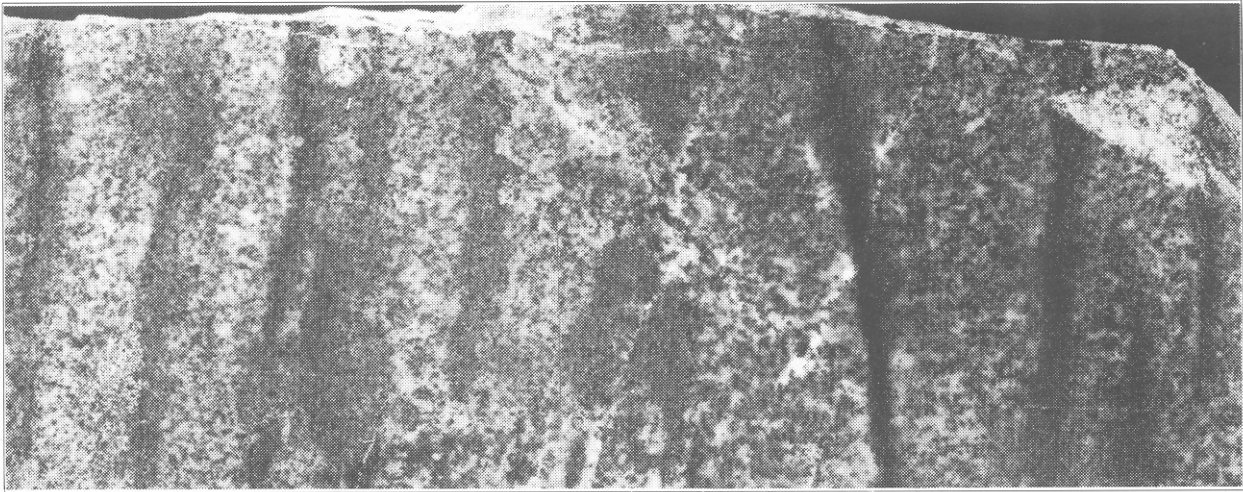


Figure 5.19a

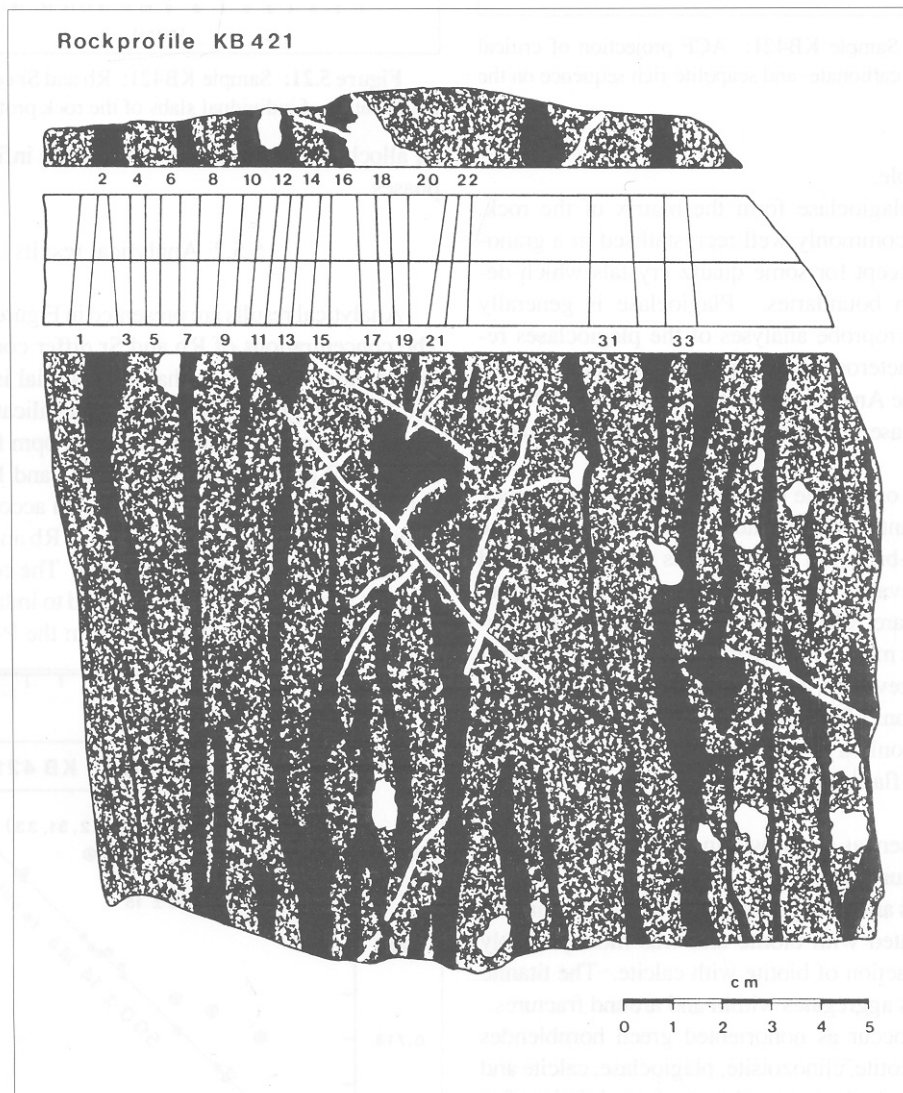


Figure 5.19b

**Figure 5.19:** Sample KB421:

- a) Photograph of the sample material ( length of photograph is 16.7 cm)  
 b) Sketch of the sample; the position of the individual slabs is outlined. Fractures and scapolite crystals occurring in the rock are marked by white lines and small white fields

The paragenesis zoisite/epidote + plagioclase + calcite has been used for a quantitative evaluation of temperature and fluid composition by Storre and Nitsch (1983). The authors obtained metamorphic temperatures of 580-600°C at 4 kb

for the northern Khomas Trough which is well in agreement with P-T estimates derived from the stability fields of mineral assemblages in pelitic rocks from assemblage zone 3 of the study traverse (cf. Chapter 2.5). No quantitative P-T

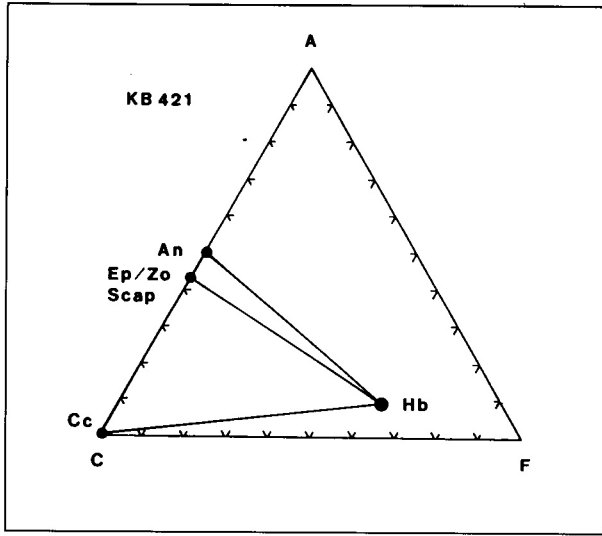


**Figure 5.20:** Sample KB421: ACF projection of critical assemblages in the carbonate- and scapolite-rich sequence on the farm Keises 312

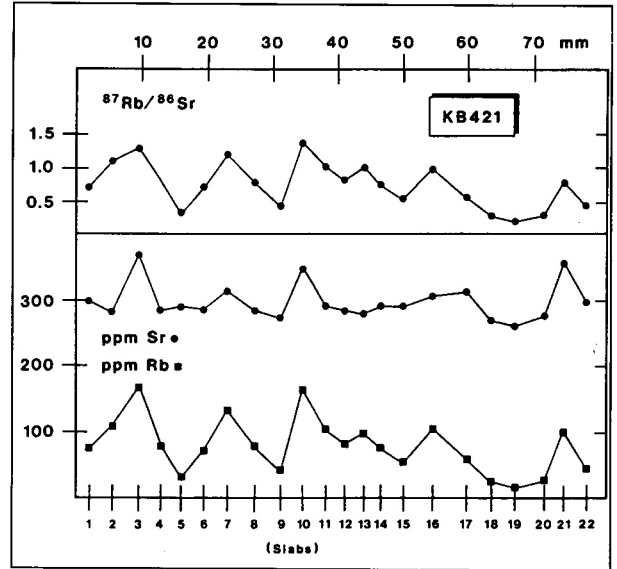


**Figure 5.21:** Sample KB421: Rb and Sr concentrations and Rb-Sr ratios of individual slabs of the rock profile

estimates are available for this sample.

Quartz and plagioclase form the matrix of the rock. Both phases are commonly well recrystallised in a granoblastic texture except for some quartz crystals which developed subgrain boundaries. Plagioclase is generally untwinned. Microprobe analyses of the plagioclases revealed a certain heterogeneity in plagioclase compositions with a range in the An component between 40 and 59% for different plagioclase grains which apparently are unzoned (Table A.1).

Biotite forms one of the major constituents of the rock and is predominantly concentrated in the P-domains. The biotite is reddish-brown in colour and is mostly elongated within the  $S_2$  cleavage. Grain sizes may reach about 1 mm, but most crystals are 500  $\mu\text{m}$  or less. Retrograde chloritisation occurs, but is mostly limited to small fractures. Microprobe analyses revealed no systematic variation in the biotite compositions (Table A.2).

Muscovite is only a subordinate phase in this rock and occurs as isolated flakes up to several hundreds of micrometers in size.

Calcite is present as grains within the matrix of the rock as well as in fracture systems.

Titanite forms anhedral grains in this rock. The mineral is mostly associated with biotite and was most probably formed by the reaction of biotite with calcite. The titanite is concentrated as aggregates within and around fractures.

Amphiboles occur as non-oriented green hornblendes co-existing with biotite, clinzoisite, plagioclase, calcite and quartz. According to the nomenclature of amphiboles after Leake (1978), the investigated amphiboles belong to the group of calcic amphiboles and are more specifically termed "magnesian-hornblendes" with an average hornblende composition of  $(\text{Ca} + \text{Na})_{\text{B}} = 1.98$ ,  $\text{Na}_{\text{B}} = 0.04$ ,  $\text{Si} = 7.06$ ,  $\text{Mg}/(\text{Mg} + \text{Fe}) = 0.59$  (Table A.5).

Scapolite crystals reach cm dimensions and enclose all other mineral phases. Plagioclase has quantitatively been replaced within the limits of the scapolite porphyroblasts. Scapolites are mainly associated with fractures indicating

an allochemical formation through the infiltration of fluid phases.

### 5.5.2 Analytical results

Analytical results are presented in Figures 5.21 and 5.22. The concentrations of Rb and Sr differ considerably from the previous samples in that the material is enriched in Sr due to the high proportions of calc-silicates in the rock. Concentrations range from 17 to 164 ppm for Rb and from 261 to 369 ppm for Sr, respectively, and Rb/Sr ratios are between 0.27 and 1.36 (Fig. 5.21). In accordance with the sample KB117, the concentrations of Rb and Sr are positively correlated, although less distinct. The correlation of the element concentrations is considered to indicate the mobilisation of predominantly quartz from the P-domains of the rock during

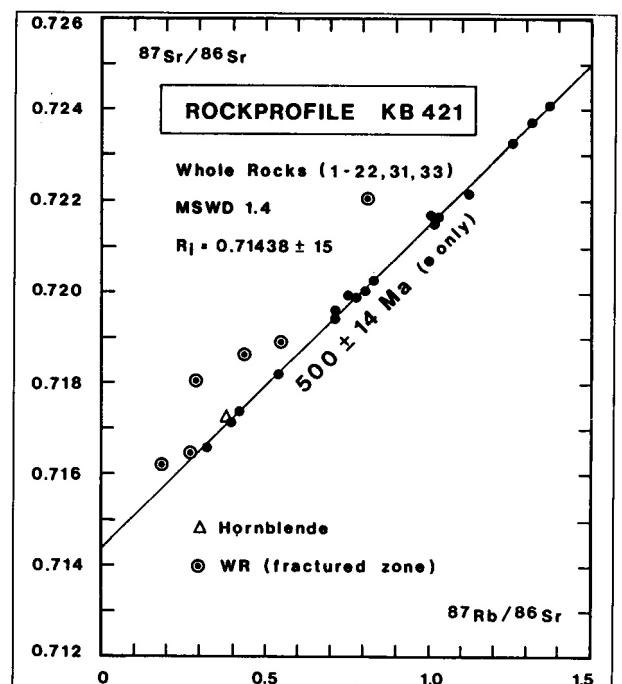


**Figure 5.22:** Sample KB421: Isochron diagram

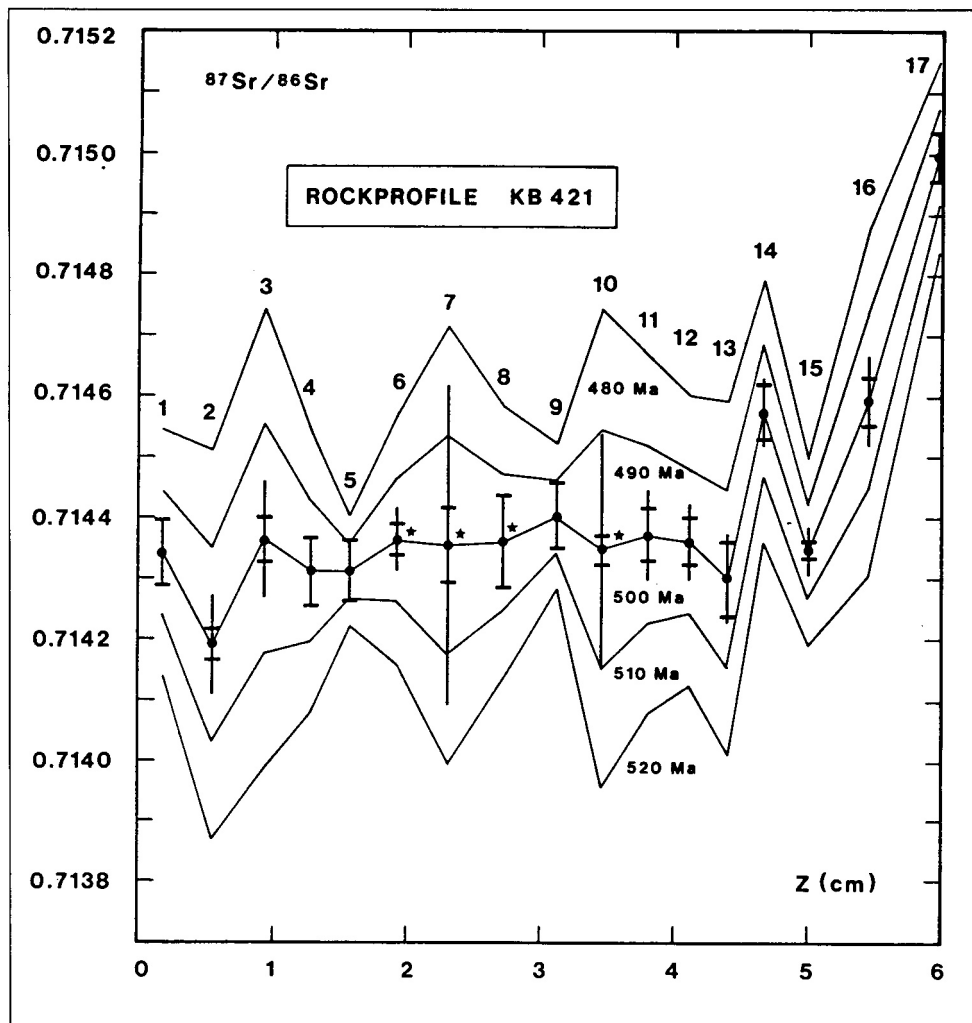


**Figure 5.23:** Sample KB421: Profile diagram showing the internal distribution of  $^{87}\text{Sr}/^{86}\text{Sr}$  ratios, calculated for  $t = 480, 490, 500, 510$  and  $520$  Ma. Errors are shown exemplarily for  $t = 500$  Ma. Vertical lines represent an uncertainty of  $\pm 1\%$  assigned to the  $^{87}\text{Rb}/^{86}\text{Sr}$  ratios. Limits of error for the  $^{87}\text{Sr}/^{86}\text{Sr}$  ratios are indicated by horizontal bars. Repeated analyses are marked by asterisks

prograde metamorphism.

Put into an isochron diagram (Fig. 5.22), most of the analytical data align along a straight line. Six data points, from slabs 17 to 22, are located considerably above the regression line. The slabs were from that portion of the rock profile transected by small fractures where scapolite formation occurred. The data from those slabs were therefore omitted for age calculations. The regression calculation for the first 16 slabs of the rock profile yields an age value of  $500 \pm 14$  Ma and an initial  $^{87}\text{Sr}/^{86}\text{Sr}$  ratio of  $0.71438 \pm 0.00015$ . The slight scatter of data is indicated by an MSWD of 1.4 (for slabs 1-16). The biotite and hornblende analyses from slab 33 revealed a biotite-whole-rock age of  $489 \pm 10$  Ma and a poorly defined hornblende-whole-rock age of  $506 \pm 57$  Ma. The disturbance of the isotopic systems within slabs 17 to 22 is apparently connected to the fracture systems along which scapolite formation occurred. The isotopic signatures of the slabs show a relative enrichment in radiogenic strontium or depletion in rubidium, respectively, compared to the other slabs.

The profile diagram in Figure 5.23 illustrates the spatial distribution and the computed temporal development of the  $^{87}\text{Sr}/^{86}\text{Sr}$  isotope ratios of the first 17 slabs of the rock profile

(the  $^{87}\text{Sr}/^{86}\text{Sr}$  isotopic composition of slabs 18-22 would exceed the range of isotope ratios in the diagram). The whole-rock isotope ratios were calculated for times  $t = 480, 490, 500, 510$  and  $520$  Ma. Errors are shown exemplarily for whole-rock isotope ratios at 500 Ma.

The distribution curves of the calculated whole-rock isotope ratios show the least variation at 500 Ma and become progressively heterogeneous towards higher and lower ages. A homogeneous isotope distribution, however, cannot be calculated for slabs 1-16. According to the diagram, a partial equilibrium of  $^{87}\text{Sr}/^{86}\text{Sr}$  ratios seemed to have been reached between slabs 3 to 13 at 500 Ma.

The generally equilibrated isotope distribution pattern observed for these slabs could mark an event leading to a largely homogenised distribution of isotopes. The elevated  $^{87}\text{Sr}/^{86}\text{Sr}$  ratios of slabs 17-22 are most likely caused by an infiltration of fluids (enriched in radiogenic Sr) along the fracture systems running through the sequence. An allochemical reaction is indicated by the post-kinematic growth of scapolite crystals. The distance over which the reaction occurred, however, seems to be restricted to narrow zones along the fractures. The alteration of the whole-rock isotope compositions apparently is confined to the immediate sur-

roundings of the fractures; the isotopic composition of the other slabs seems not to have been affected. The isotope distribution pattern of the whole-rock isotope ratios at 500 Ma thus most likely reflects a pre-scapolite event of isotopic equilibration between slabs 3 to 13.

## 5.6 ROCK PROFILE KB115

### 5.6.1 Character of sample

#### *Geological situation*

Sample KB115 was collected in the northern Khomas Trough, in the northern part of the farm Keises 312 about 5 km south of the Donkerhuk Granite (Fig. 2.8). The area belongs to the structural domain D which is marked by the appearance of an  $S_4$  crenulation cleavage which was not observed in the adjacent domain C. The metamorphic overprint is characterised by the development of sillimanite-biotite assemblages. Some authors have attributed the growth of sillimanite to thermal metamorphism associated with the intrusion of the Donkerhuk Granite (e.g. Hoffer, 1977; Sawyer, 1983). The sillimanite which was observed up to 15 km south of the granite is, however, interpreted by this author to be of regional metamorphic origin (cf. Chapters 2.5 and 3; P. Kukla *et al.*, 1990). The sample material consists of alternating thin pelitic, semi pelitic and psammitic layers, some of which are gradational in character. The lithological layering is therefore considered to represent original bedding.

#### *Outline of the rock profile*

For Rb-Sr small-domain investigations a rock profile about 4.5 cm long was cut perpendicular to the lithological layering of the sample. Eleven contiguous slabs A-K were cut according to lithological contrasts. The sample weights of the individual slabs are in the order of 2-6 g. The slabs Band C were analysed together, since a 2- to 3-mm-thick, slightly dis-

cordant quartz veinlet cuts across both units. Figure 5.24 is photograph of the specimen and an outline of the rock profile including the position of the slabs.

Rb-Sr whole-rock analyses were carried out from contiguous slabs A-K of the rock profile. In addition, the isotopic composition of biotite and muscovite fractions as well as plagioclase-quartz concentrates was determined for four slabs. The following mineral fractions were analysed:

slab D: one plagioclase-quartz concentrate ( $< 60 \mu\text{m}$ ),

slab E: one plagioclase-quartz concentrate ( $< 40 \mu\text{m}$ ),

one muscovite fraction (60-180  $\mu\text{m}$ ) and two biotite fractions (80-160  $\mu\text{m}$  and 160-250  $\mu\text{m}$ ),

slab F: one plagioclase-quartz concentrate ( $< 60 \mu\text{m}$ ),

slab J: two plagioclase-quartz concentrates ( $< 40 \mu\text{m}$  and  $< 60 \mu\text{m}$ ), one muscovite fraction (60-180  $\mu\text{m}$ ) and one biotite fraction (60-180  $\mu\text{m}$ ).

#### *Petrography*

The pelitic layers of the sample material are characterised by the paragenesis sillimanite + biotite + muscovite + plagioclase + quartz corresponding to assemblage (i) within assemblage zone 3 in Figure 2.5. Sillimanite is rarely present in the psammitic layers. The rock displays a strong  $S_2$  foliation which is defined by the orientation of micas and the elongation of fibrolite nodules.

The P-T conditions of metamorphism in assemblage zone 3 can be roughly estimated from the stability fields of mineral assemblages. The sample locality is close to the last occurrence of staurolite corresponding to assemblage (h) of assemblage zone 3 and thus P-T conditions may be inferred to be close to the equilibrium curve (6) marking staurolite-decomposition after Hoschek (1969) in Figure 2.7. An upper thermal limit is provided through the absence of migmatic structures. Thus P-T conditions may be estimated to range between 600°C/2.5 kb and a maximum of 700°C/7.5 kb.

Quartz is a major constituent in the matrix of the rock and is

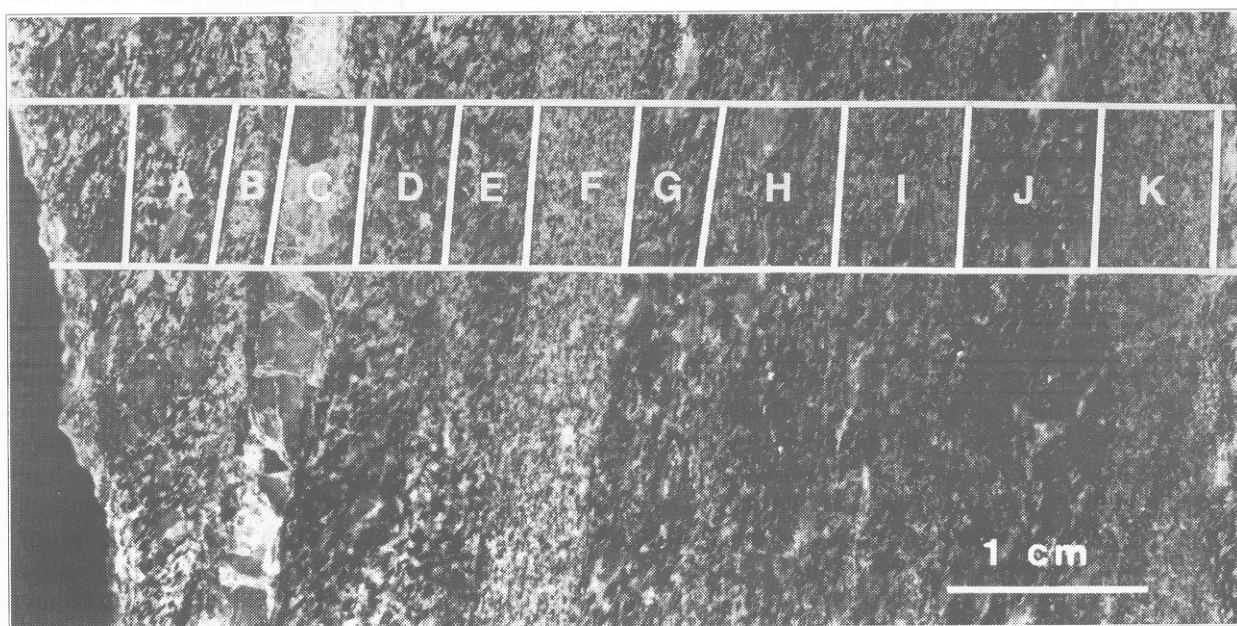
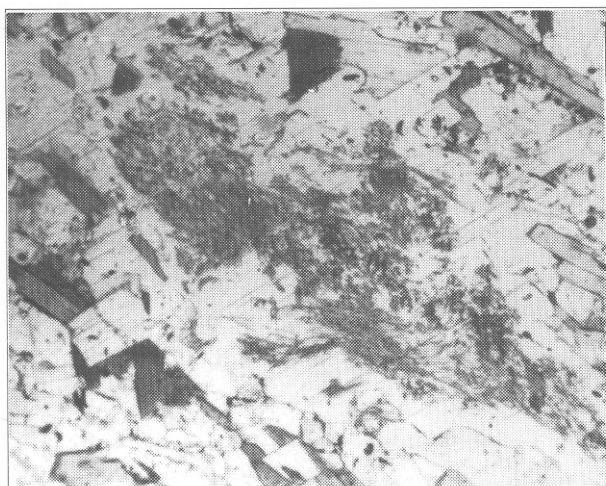
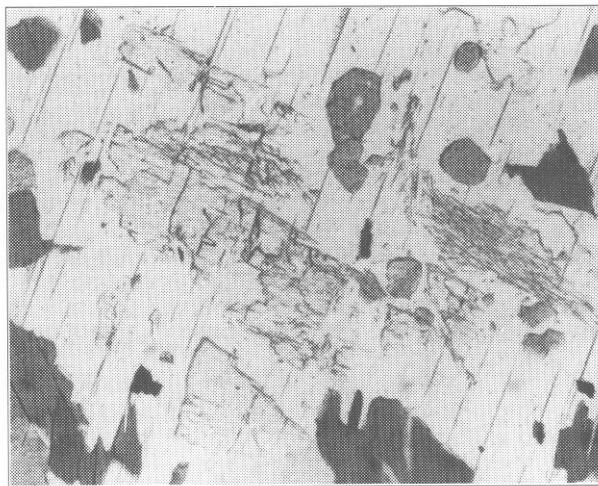


Figure 5.24: Sample KB115: Photograph of the sample and outline of the rock profile; the position of the individual slabs is indicated.



**Figure 5.25a:** Late muscovite porphyroblast with fibrolitic sillimanite in sample KB115 (length of photograph is 1.4 mm)



**Figure 5.25b:** Late muscovite porphyroblast with relictive sillimanite and fibrolite (length of photograph is 1.4 mm)

concentrated in psammitic layers. The grains are generally well recrystallised with polygonal grain boundaries and reach about 200  $\mu\text{m}$  in size, but most are below 100  $\mu\text{m}$ .

Plagioclase is also a major constituent in the matrix of the rock, forming mostly high-angle grain boundaries. Grain sizes are mostly below 100  $\mu\text{m}$ . The plagioclases are generally untwinned and sericitisation is weak. The plagioclase compositions were found to be slightly heterogeneous throughout the sample with An contents ranging between 8.5 and 14.0% (Table A.1).

Biotites are generally oriented within the structural fabric of the rock which is correlated with the regional  $S_2$  cleavage. A subordinate group of biotites grew non-oriented and is mainly associated with the late muscovite porphyroblasts. The biotites reach grain sizes of about 1 mm, but most of the crystals are in the range of 200-500  $\mu\text{m}$ . The biotite content in psammitic layers is about 20% and may reach 40-50% in pelitic layers. Microprobe analyses revealed that there are no significant differences in biotite composition for individual slabs of the rock profile (Table A.2).

Muscovite occurs in two generations. One generation is oriented within the structural fabric of the rock and is mostly interspersed with biotite. A second generation developed as late, crosscutting porphyroblasts frequently intergrown with quartz and fibrolitic sillimanite. The muscovites are inferred to have largely replaced sillimanite in a high-temperature retrogressive event as discussed in Chapter 2.5. Figure 5.25 shows an example of a late muscovite which encloses relictive sillimanite together with fibrolite. The muscovites are characterised by Si values between 6.0 and 6.2. Within this interval, the late muscovites (e.g. slab J) tend towards lower Si values than the first generation (e.g. slab A) which tend towards higher Si values (Table A.3). In other slabs, however, the difference in chemical composition of muscovite generations is less distinct.

Sillimanite occurs in nodular aggregates of fibrolite mainly concentrated in the pelitic layers of the sample. Most of the nodules are largely replaced by late muscovite porphyroblasts.

### Geochemistry

Detailed geochemical analyses of the major and trace element concentrations were carried out for the individual slabs of the rock profile to constrain possible small-scale element mobilities. The intention was to compare element mobilities with the degree of isotope homogeneity between the slabs of the rock profile. The element concentrations are compared with representative bulk rock analyses from pelites and psammites of the Kuiseb Formation from the study area (P. Kukla, 1990). For analytical conditions the reader is referred to Appendix II; analytical results are listed in Table A.7a.

Figures 5.26a and b show the major and minor element distribution along the profile based on XRF, AAS and photometric analyses. The major element concentrations are characterised by a positive correlation of Al with Fe, K, Mg and Ti and a negative correlation of these elements with the Si content. The elements Al, Fe, K, Mg and Ti typically are incorporated in biotites and muscovites, whereas the Si content reflects the amount of quartz. The elements Na and Ca are not correlated with the other elements indicating that the percentage of plagioclase within the individual slabs is variable. Minor element distribution shows a positive correlation of the elements Zr, V, Cr, Rb, Y and Nb which also typically occur in micas and thus are enriched in the pelitic layers of the sample. The latter

elements are also correlated with the elements Al, Fe, K, Mg and Ti (correlation indices are listed in Table A.7b). The data thus essentially reflect the psammitic and pelitic character of the slabs.

Compared to the geochemical data for the Kuiseb Formation given by P. Kukla (1990), most measured element concentrations fall well within the range of the author's data. Only the concentrations of  $\text{P}_2\text{O}_5$  and rubidium (in psammitic layers) exceed maximum values for other Kuiseb Formation samples by more than 10 percent, whereas the whole sample is low in calcium. The element concentrations of slab B/C of the rock profile are slightly lower compared to the rest of the rock profile due to a dilution effect of the quartz veinlet.

Compared to the mean psammite and pelite compositions

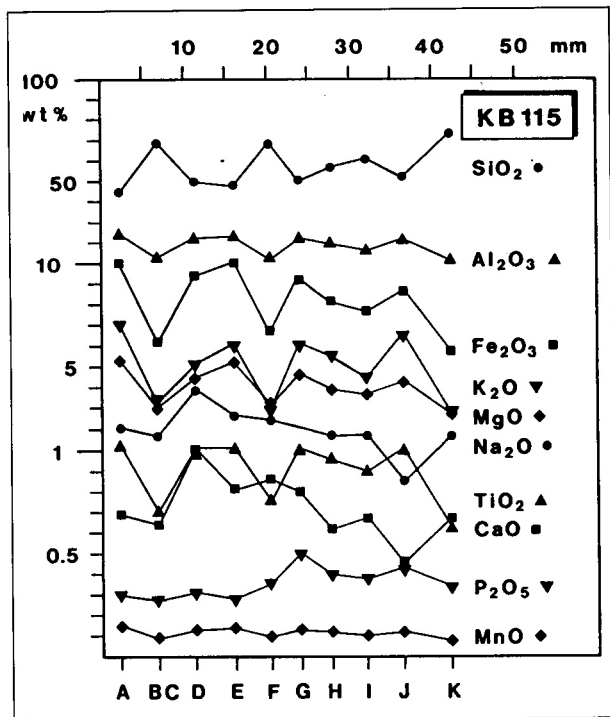


Figure 5.26a (above): Sample KB115: Distribution pattern of major element concentrations within the rock profile

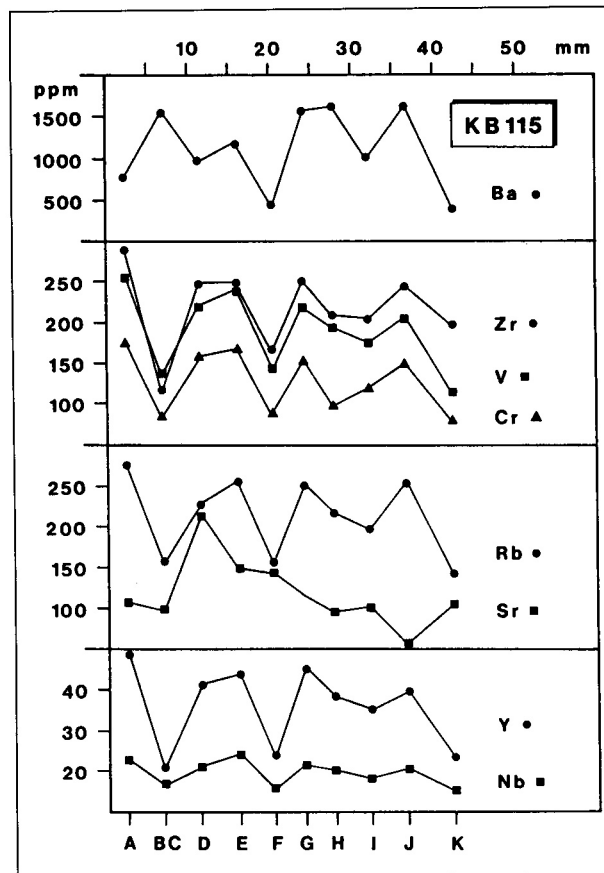


Figure 5.26b(right): Distribution pattern of minor elements within the rock profile

of P. Kukla (1990), individual slabs of the rock profile show an average element distribution. Thus no differentiated statements can be made on the mobility of elements during metamorphic history for the investigated volumes of rock. The concentration gradients between the slabs of the profile have not been equilibrated, but the range of the geochemical concentrations within the Kuseb Schists allows for some percentage of element exchange which cannot be detected by these whole-rock analyses.

### 5.6.2 Analytical results

The results of the isotope analyses are presented in Figures 5.27 and 5.28. The whole-rock compositions of the individual slabs show Rb and Sr concentrations ranging from 134 to 286 ppm and from 56 to 211 ppm, respectively. The measured  $^{87}\text{Rb}/^{86}\text{Sr}$  ratios are between about 3 and 13 for whole rocks and about 12 for analysed muscovite fractions. The Rb and Sr concentrations within the whole rocks apparently are not correlated. The plagioclase concentrates vary in their Rb and Sr concentrations between 1.2 and 9.5 ppm and 144 and 507 ppm which indicates that the different mineral separates comprise different proportions of quartz and plagioclase. It is assumed that the quartz contained in the plagioclase-quartz fractions does not carry any Sr, and therefore the isotopic composition measured for the plagioclase-quartz mixtures is considered to represent that of the plagioclase.

Put into an isochron diagram (Fig. 5.28), the whole-rock data points show a good alignment along a regression line, the

gradient of which corresponds to an age of  $479 \pm 11$  Ma. An initial ratio of  $0.71963 \pm 0.00066$  was calculated. All of the data points fall, within limits of error, onto the regression line as is indicated by an MSWD value of 0.8. Age calculations from muscovite-whole-rock pairs do not yield meaningful data due to similar isotopic compositions of white micas and their respective whole rocks. The data points for the plagioclase-quartz concentrates from slabs D, E, F and J fall onto or slightly below the whole-rock regression line in Figure 5.28a. Ages calculated from plagioclase-whole-rock pairs are  $486 \pm 13$  Ma for slab D,  $492 \pm 16$  Ma for slab E,  $497 \pm 14$  Ma for slab F and  $476 \pm 15$  Ma for slab I. Whole-rock-biotite ages were calculated from the biotite fractions from slabs E and J at  $491 \pm 7$  Ma and  $496 \pm 10$  Ma. The calculated whole-rock and biotite-whole-rock age data still overlap within limits of error. Taking the analytical uncertainties into account, the biotites from the two slabs show a homogeneous  $^{87}\text{Sr}/^{86}\text{Sr}$  ratio with respect to their host rock between 484 and 506 Ma.

The spatial distribution and the computed temporal development of the  $^{87}\text{Sr}/^{86}\text{Sr}$  ratios of the individual slabs are illustrated in the profile diagram in Figure 5.29.  $^{87}\text{Sr}/^{86}\text{Sr}$  ratios were calculated corresponding to 460, 470, 479, 491, 500 and 510 Ma before present. Errors are shown exemplarily for the whole-rock isotope ratios at 479 and 491 Ma.  $^{87}\text{Sr}/^{86}\text{Sr}$  ratios were calculated for the analysed plagioclase-quartz concentrates for an interval between 300 and 600 Ma before present. These isotope ratios are illustrated with rectangular symbols (P) covering the whole range of the ratios as well as analytical uncertainties. For the muscovite fractions,  $^{87}\text{Sr}/^{86}\text{Sr}$  ratios were

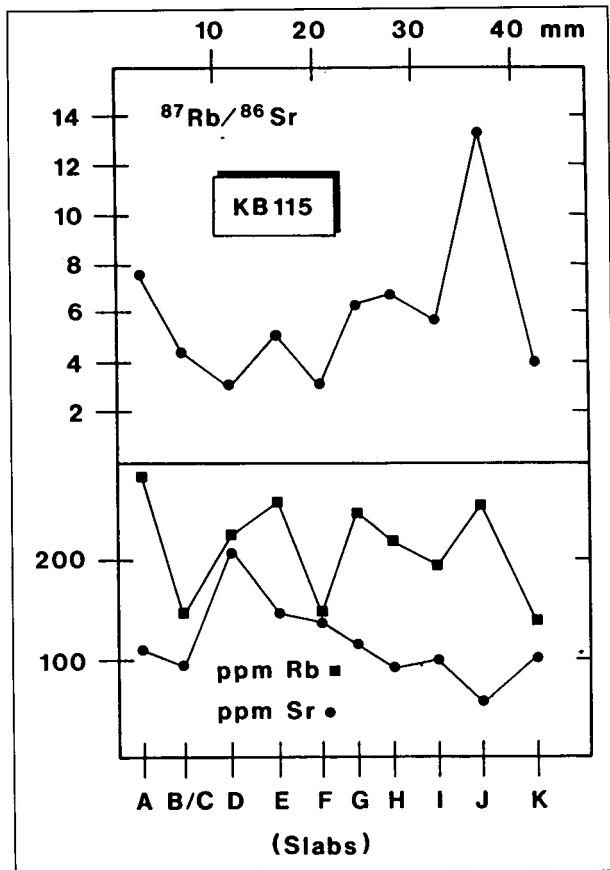


Figure 5.27: Sample KB115: Rb and Sr concentrations for the individual slabs of the rock profile as determined by isotope dilution techniques

calculated at 479 and 491 Ma before present, corresponding to the whole-rock age of the rock profile and the whole-rock-biotite age from slab E. The data points are marked by open circles (M). The analytical error corresponding to an uncertainty of 1% of the  $^{87}\text{Rb}/^{86}\text{Sr}$  ratio is shown as a vertical error bar.

The calculated  $^{87}\text{Sr}/^{86}\text{Sr}$  whole-rock isotope ratios show the least variation at 479 Ma, but become increasingly heterogeneous towards higher and lower ages. The distribution curves below the one corresponding to 479 Ma represent unlikely patterns, since slabs A, E and M have lower  $^{87}\text{Sr}/^{86}\text{Sr}$  ratios despite relatively higher  $^{87}\text{Rb}/^{86}\text{Sr}$  ratios with regard to their neighbouring slabs. The curves of 479 Ma and younger may therefore be regarded as possible distribution patterns.

Taking the assigned analytical uncertainties into account, partial equilibria can be calculated for the whole-rock isotope ratios of slabs E-J or G-K at 479 Ma. A partial isotopic equilibrium persists for slabs E-J until 470 Ma. According to Bachmann *et al.* (1986), the partial equilibria of isotope ratios would represent a geological event leading to the partial homogenisation of isotopic ratios between 479 and 470 Ma. At 491 Ma, a partial equilibrium can be calculated for slabs G-I. At this age, however, the isotope ratio of slab J is, despite its large analytical error and high  $^{87}\text{Rb}/^{86}\text{Sr}$  ratio, distinctly lower than that of adjacent slabs. The same situation is given for other slabs within this distribution curve, which therefore has to be regarded as an unlikely distribution as already men-

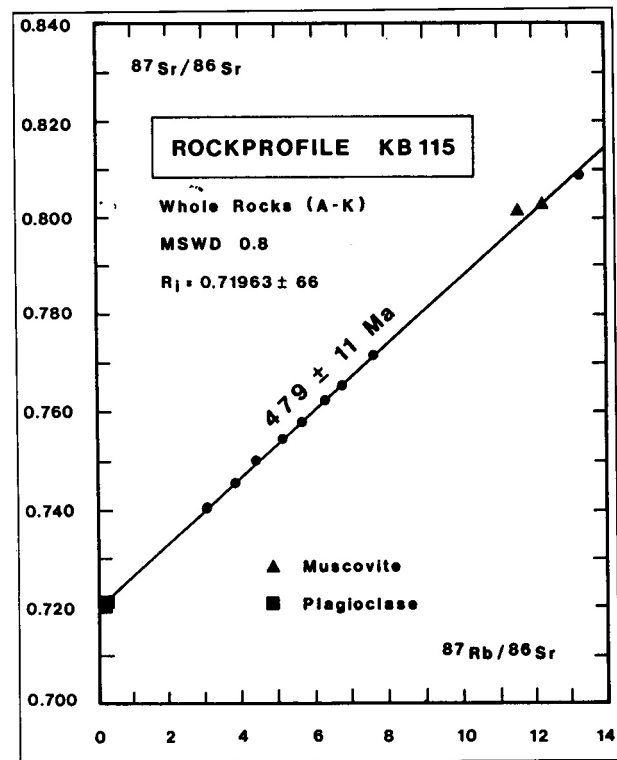


Figure 5.28: Sample KB115: Isochron diagram

tioned above.

Isotope ratios of the plagioclase-quartz fractions from slabs D, E, F and J were calculated for the time between 300 and 600 Ma. Due to the low concentration of Rb within the mineral fractions, the range of the calculated isotope ratios is very narrow and is covered by the extent of the rectangular symbols, including the analytical uncertainties of the isotope ratios. The relative position of the whole-rock isotope ratios with regard to that of the respective plagioclase fraction provides a good control on the timing of plagioclase-whole-rock isotope homogenisation. A relative equilibrium of plagioclase and whole-rock isotopic compositions in slabs D, E and F is reached at about 490 Ma. In contrast, the plagioclase fraction from slab J shows a homogeneous isotopic composition with its whole rock between 479 and about 470 Ma.

The muscovite fraction from slab E is characterised by a distinctly higher  $^{87}\text{Sr}/^{86}\text{Sr}$  ratio than the whole rock despite a lower  $^{87}\text{Rb}/^{86}\text{Sr}$  ratio. The muscovite fraction from slab J, in contrast, shows a homogeneous isotope ratio at 479 Ma with its respective whole rock and with the plagioclase fraction from this slab.

In conclusion, the distribution of the whole-rock and mineral isotope ratios implies a) that only partial equilibria of whole-rock isotope ratios and no complete homogenisation across the width of the rock profile was reached; b) that homogeneity of the plagioclase fractions with the respective whole rocks of slabs D, E and F is observed prior to the whole-rock isotope equilibration; c) that the homogenisation of the plagioclases with their whole rocks occurred non contemporaneously over the profile and d) that the mineral fractions and the whole rock of slab J reached isotopic equilibrium at 479 Ma.

The fact that isotopic equilibrium between the plagioclase

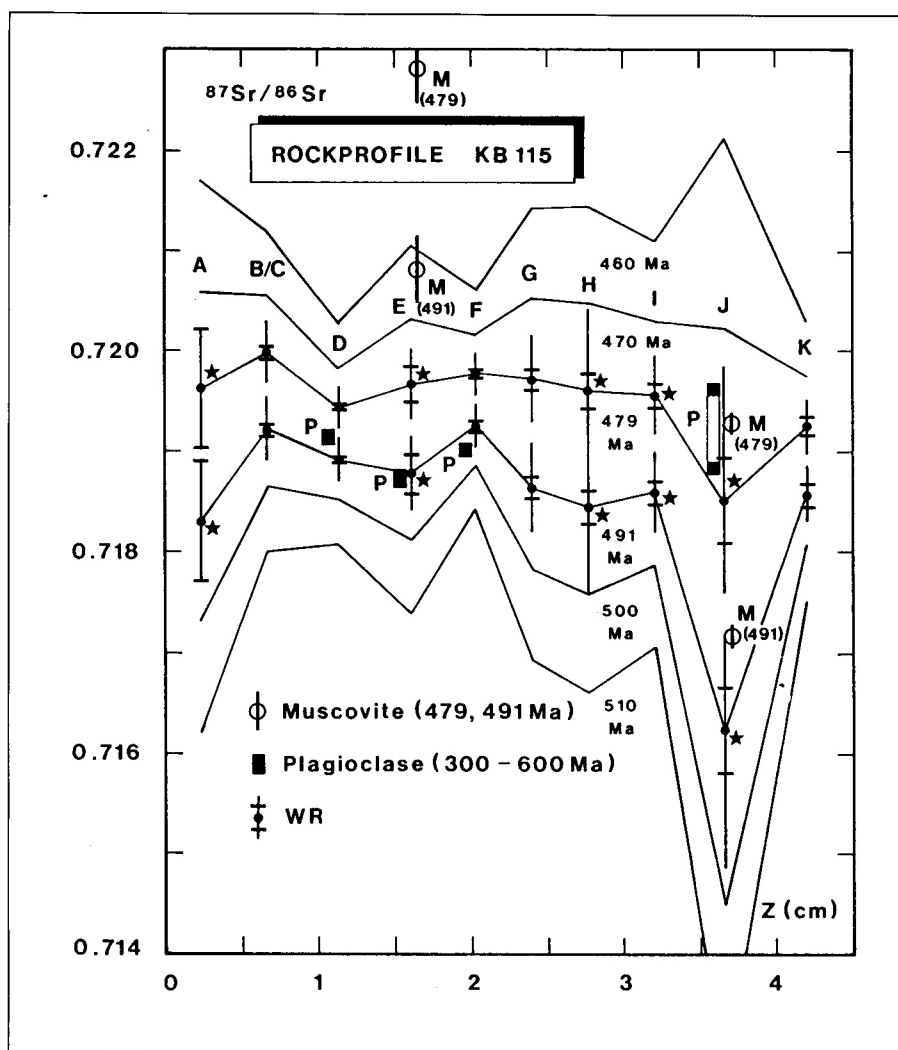


**Figure 5.29:** Sample KB115: Profile diagram showing the internal distribution of  $^{87}\text{Sr}/^{86}\text{Sr}$  ratios of the rock profile, calculated for  $t = 460, 470, 479, 491, 500$  and  $510$  Ma. Errors are shown exemplarily for  $t = 479, 491$  Ma. Vertical lines represent an uncertainty of  $\pm 1\%$  assigned to the  $^{87}\text{Rb}/^{86}\text{Sr}$  ratios. Limits of the error for the  $^{87}\text{Sr}/^{86}\text{Sr}$  ratios are indicated by horizontal bars. Repeated analyses are marked by asterisks.  $^{87}\text{Sr}/^{86}\text{Sr}$  ratios of plagioclase-quartz fractions, calculated between 300 and 600 Ma, are shown as rectangular symbols (P),  $^{87}\text{Sr}/^{86}\text{Sr}$  ratios of muscovite fractions, calculated at 479 and 491 Ma, are shown as open circles (M) with vertical error bars corresponding to the analytical uncertainty in the  $^{87}\text{Rb}/^{86}\text{Sr}$  measured ratio

fractions and the whole rocks of the slabs D-F was reached prior to the whole-rock homogeneity at 479-470 Ma suggests that the latter whole-rock isotope distribution cannot be of geological significance. This is because it is not imaginable that an isotope exchange between the whole-rock isotopic systems of the individual slabs occurred without affecting the isotopic system of the plagioclases which are the major Sr-bearing constituents of the rock.

#### Mass balance of analytical data

Apart from the considerations regarding the isotopic homogeneity of the whole rocks and the mineral fractions, an attempt was made to balance the analytical data for the slabs E and J, i.e. the Rb and Sr concentrations as well as the  $^{87}\text{Sr}/^{86}\text{Sr}$  isotope ratios of the different mineral fractions with regard to the whole-rock composition. Assuming that plagioclase, muscovite and biotite are the main Sr- and Rb-bearing mineral phases, the percentage proportions of the minerals within

the sample were calculated a) from their measured  $^{87}\text{Sr}/^{86}\text{Sr}$  ratios and b) from their Rb and Sr concentrations. Vice versa, a whole-rock  $^{87}\text{Sr}/^{86}\text{Sr}$  ratio calculated from the measured isotopic compositions of the individual minerals and an estimated modal composition should be equivalent to the measured whole-rock composition.

a) Balancing of the measured  $^{87}\text{Sr}/^{86}\text{Sr}$  ratios revealed the following proportions of the different minerals within the whole-rocks of the slabs E and J:

	plagioclase (+ quartz)	muscovite	biotite	rest quartz
KB115E	5.1 %	27.0 %	58.0 %	9.9 %
KB115J	17.6 %	30.0 %	50.0 %	2.4 %

b) Balancing of the Rb and Sr concentrations revealed the following proportions of the different minerals within the whole-rocks of the slabs E and J:

	plagioclase (+ quartz)	muscovite	biotite	rest quartz
KB115E	26.4 %	26.4 %	47.0 %	0.2 %
KB115J	28.1 %	27.0 %	44.8 %	0.1 %

As is evident from the above calculations, different mineral proportions are needed to balance the  $^{87}\text{Sr}/^{86}\text{Sr}$  isotopic ratios (a) and the Rb and Sr element concentrations (b) of the mineral fractions with regard to the respective whole rocks. The plagioclase content calculated on the basis of the Sr concentrations by far exceeds the amount of plagioclase that is needed to balance the  $^{87}\text{Sr}/^{86}\text{Sr}$  ratios. This may be explained either by an additional Sr-bearing mineral phase or that Sr was subsequently added to the whole rock. Although apatite is present within the sample (estimated at about 1%), it is not likely that it compensates either the amount or the isotopic composition of the required Sr. On the other hand, the allochemical introduction of Sr should be evident from the whole-rock isotope systematics of the individual slabs. The good alignment of data points in the isochron diagram is not indicative for a disturbance of whole-rock isotopic signatures, as could be shown for sample KB421. Therefore the existence of an additional Sr-bearing phase (apatite, calcite) has to be considered.

## 5.7 ROCK PROFILE KB103

### 5.7.1 Character of sample

#### *Geological situation*

The migmatites occurring in the northern Khomas Trough play an important part, in delineating the relative timing of metamorphism and granite intrusion in that area. In Chapter 3, anatexis leading to the *in situ* generation of partial melts, was classified as regional metamorphism by means of structural relationships. The migmatites therefore are considered to represent the temperature peak of metamorphism in the Khomas Trough.

On account of the well-developed banding, the migmatites are particularly suited for the application of the Rb-Sr small-domain method. For the isotope analyses one sample was collected from the "Davetsaub type" migmatites in the Davetsaub river near the northern border of the farm Davetsaub 29 (Fig. 2.8). The migmatite sample is characterised by thin leucosome bands which apparently have developed *in situ* (Fig. 5.30a). The leucosomes parallel the main regional fabric of the rocks which is still preserved in the palaeosomes of the rock. This structural fabric is correlated with the regional  $S_2$  cleavage in the non-migmatic metasediments. Within the sample, the composition of the leucosomes is trondhjemitic in character.

#### *Outline of rock profile*

For Rb-Sr investigations, a rock profile was cut perpendicular to the direction of the leucosomes and the metamorphic banding. The profile is about 15 cm long and was cut parallel to the direction of banding into 34 contiguous slabs of contrasting composition. The individual slabs of the profile are between 2 and 10 mm thick and range between 1 and 5 g in weight. Figure 5.30b is a photograph of the sectioned migma-

tite specimen and a sketch of the rock profile with the position of the individual slabs outlined.

The rock profile extends over a sequence of 3 palaeosome and 4 neosome (leucosome + melanosome) domains. Slabs cut from palaeosomes are numbered 5 to 8, 17 to 19 and 28 to 32. The following slabs were cut from the leucosomes of the sample: 1,2,4, 10 to 16,20,22,24,26, 33; melanosomes are represented by slabs 3, 9, 17,21,23, 25, 27 and 34. However, leucosomes and melanosomes could not be successfully separated in all cases.

Rb-Sr analyses were carried out on 31 contiguous slabs of the rock profile (slabs 4 - 34). The following mineral fractions from neosomes as well as palaeosomes were also analysed for their Rb-Sr systematics:

- slab 9: two biotite fractions (125-250 and 250-500  $\mu\text{m}$ );
- slab 13: two biotite fractions (125-250 and 250-500  $\mu\text{m}$ ) and two garnet fractions (125-250 and 250-500  $\mu\text{m}$ );
- slab 23: two biotite fractions (125-250 and 250-500  $\mu\text{m}$ );
- slab 28: two biotite fractions (125-250 and 250-500  $\mu\text{m}$ ).

#### *Petrography*

The palaeosomes of the rock are medium-grained (0.5-1 mm) and are characterised by a distinct metamorphic banding as is common within the non-migmatic metasediments in the northern Khomas Trough. The palaeosomes are well recrystallised, but otherwise resemble the fine-grained, non-migmatic quartz-plagioclase-biotite- or biotite-quartz-plagioclase-schists of the Kuiseb Formation.

The light-coloured leucosomes are fairly coarse-grained (0.5-5 mm) and mainly composed of quartz and plagioclase and clusters of biotite flakes. Garnets occur subordinately and no K-feldspar has been observed. The leucosomes are accompanied by thin melanosomes which are very rich in biotite but depleted in quartz and plagioclase. They do not otherwise significantly differ in composition from the palaeosomes of the rock. Leucosomes and melanosomes together are referred to as neosomes.

The P-T conditions of migmatization were estimated from solidus relations of K-feldspar-free assemblages and from melting experiments of Hofmann (1976; cf. Chapters 2.5 and 3). From various melting reactions (Fig. 2.7) which are considered to approximate true phase relations, temperatures between 650 and 700°C at pressures ( $P_{\text{tot}} = P_{\text{H}_2\text{O}}$ ) of 3.5-5.5 kb were inferred for the onset of partial melting in the metasediments. Solidus temperatures derived from melting experiments on samples of the Kuiseb Formation are in the range of 660 to 700°C at 4 kb (Fig. 2.7). The application of garnet-biotite thermometry yielded temperatures significantly below the above estimations which is most likely due to a retrograde equilibration of the garnet rims.

Quartz forms a major constituent of the rock. In the palaeosomes, quartz is mostly medium-grained (< 500  $\mu\text{m}$ ) and well recrystallised forming polygonal grain boundaries. Undulose extinction of the grains rarely occurs. In the melanosomes, quartz is only subordinate, with more irregular grains of variable grain size (< 1 mm). In the leucosomes, quartz reaches grain sizes of up to several millimetres. The grains are characterised by frequent undulous extinction and subgrain development.

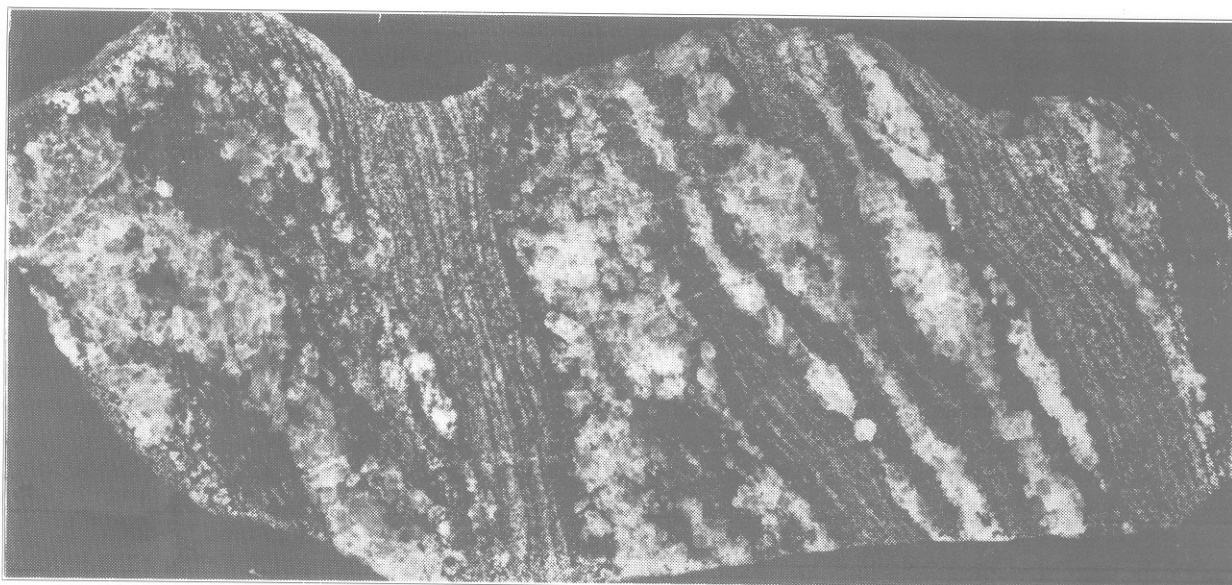


Figure 5.30a: Sample KB103: Photograph of the sample (length of photograph is 17.5 cm)

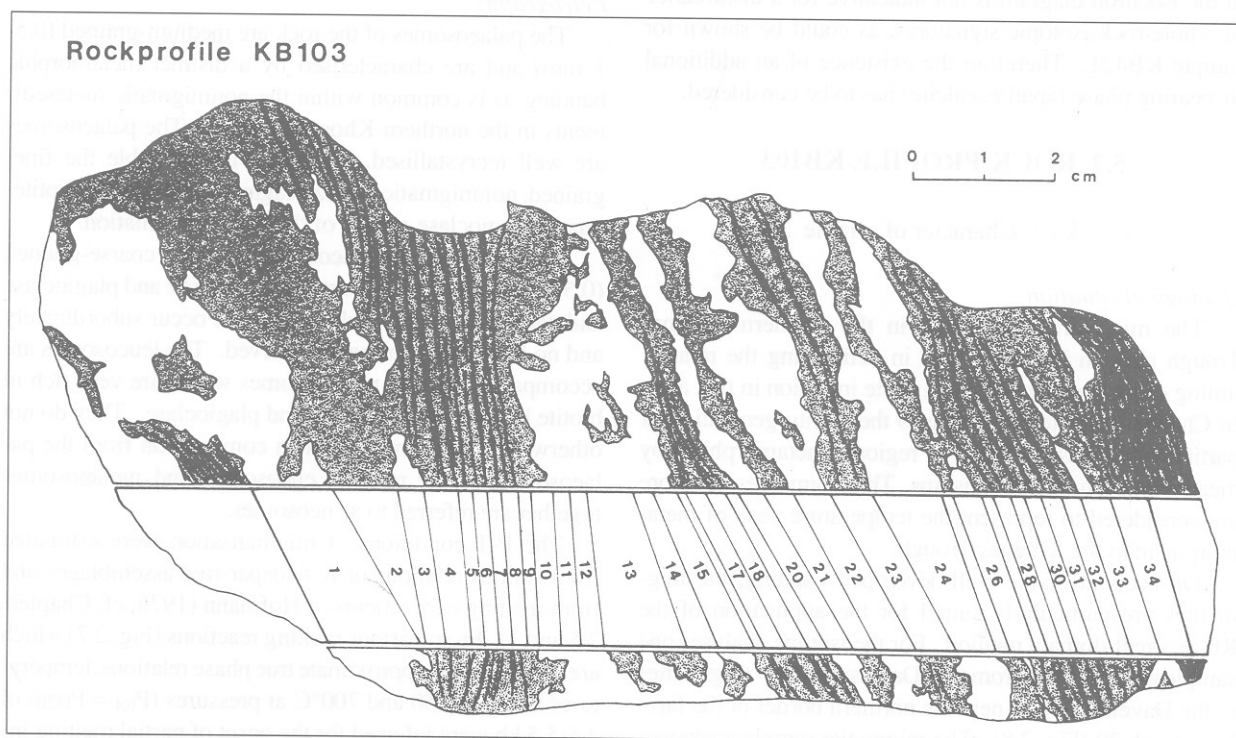


Figure 5.30b: Sketch of the sample with the position of the rock profile and the individual slabs outlined

Plagioclase is one of the major constituents within the palaeosomes and the leucosomes of the sample. In the palaeosomes, plagioclase is fine- to medium-grained ( $< 500 \mu\text{m}$ ) and forms mostly polygonal grain boundaries. Plagioclases in the palaeosomes are generally untwinned. In the leucosomes, the plagioclases in general show lamellar twinning and reach grain sizes of up to several millimetres. Sericitisation of the plagioclases occurs throughout the rock profile. Microprobe analyses revealed no systematic variation in the composition of the plagioclases for the palaeosomes and neosomes. The An contents range between 27 and 31 % (Table A.1).

Biotite is brown and occurs as a major constituent throughout the rock. In palaeosomes, biotites are mostly aligned par-

allel within the  $S_2$  metamorphic banding cleavage. Grain sizes are mostly medium-grained ( $< 1 \text{ mm}$ ). In the melanosomes, the biotites are also oriented parallel to the main structural fabric of the rock. Biotites in the melanosomes associated with the leucosomes (e.g. slab 13) are randomly oriented, forming coarse-grained books. These biotites apparently crystallised during the anatexis of the rocks. Grain sizes are in the order of several millimetres within the neosomes. Microprobe analyses revealed no significant differences for the biotite compositions in palaeosomes and neosomes (Table A.2).

Muscovite occurs only as subordinate component both in palaeosomes and neosomes. In the palaeosomes, muscovite occurs as fine- to medium-grained ( $< 500 \mu\text{m}$ ), isolated flakes

which are intergrown with biotite. In melanosomes and restates, muscovite was found as small isolated flakes, but also as medium-grained (< 1 mm) platy crystals which include fibrolitic sillimanite similar to the late muscovite described in sample KB115.

Fibrolitic sillimanite occurs in the restates of slabs 1 and 34 and in melanosomes in the central portion of the rock profile. The fibrolite is associated with biotite in deformed, elongate aggregates and is partly overgrown by muscovite. Sillimanite was not found in the leucosomes of the rock.

Garnets occur in the neosomes of the rock, with most garnets being concentrated within a thin layer in the central portion of slab 13. The crystals are anhedral and partly fragmented. A crystallisation of the garnets prior to the anatectic event may be assumed. The garnets possibly formed through the decomposition of staurolite and remained stable during partial melting. The rather limited occurrence of the garnets may be a matter of bulk rock composition. The chemical composition is almandine-rich (70% Al) with 13-15% spessartine and 11-14% pyrope component; grossular is only subordinate (2-3%). Unlike the garnets in the previously described samples, the crystals are not zoned with respect to the almandine component (Fig. 2.9e and f; Table A.6). The rims of the crystals show an increase in spessartine component at the expense of pyrope, indicating retrograde cation exchange processes. The lack of any prograde zonation may be due to a re-equilibration of the garnets during the temperature peak of metamorphism which overstepped the critical temperature of about 640°C. Above this temperature, the homogenisation of the compositional variation within gar-

nets is assumed to start (Yardley, 1977).

Accessory phases within the migmatite are tourmaline, monazite, zircon and opaque phases. In contrast to the sillimanite-grade metasediments, the investigated migmatites are very rich in monazite and zircon.

### 5.7.2 Analytical results

Analytical results are presented in Figures 5.31 and 5.32. The whole-rock compositions of slabs 4 to 33 display a wide range in Rb and Sr concentrations between 24 and 335 ppm and 7 and 274 ppm, respectively. Accordingly, Rb-Sr ratios vary between 0.6 and a rather extreme value of 163 for the slab 34 (restite). The Rb and Sr element concentrations are negatively correlated for all parts of the sample, i.e. for palaeosomes as well as for neosomes.

The differentiation of the elements is presumably the result of two superposed processes: a) a metamorphic differentiation which is still preserved as a metamorphic banding cleavage in the palaeosomes of the sample, and b) the anatectic event leading to a differentiation of feldspars and micas. It may be expected, however, that the processes generating a metamorphic banding rather produce a positive correlation of Rb and Sr through the process of quartz pressure solution and possibly precipitation. This is contrary to the partial melting of the metasediments which leads to a fractionation of quartz + feldspar and refractory phases, mainly biotite. The partial melting possibly also affected the palaeosomes and overprinted the older metamorphic banding.

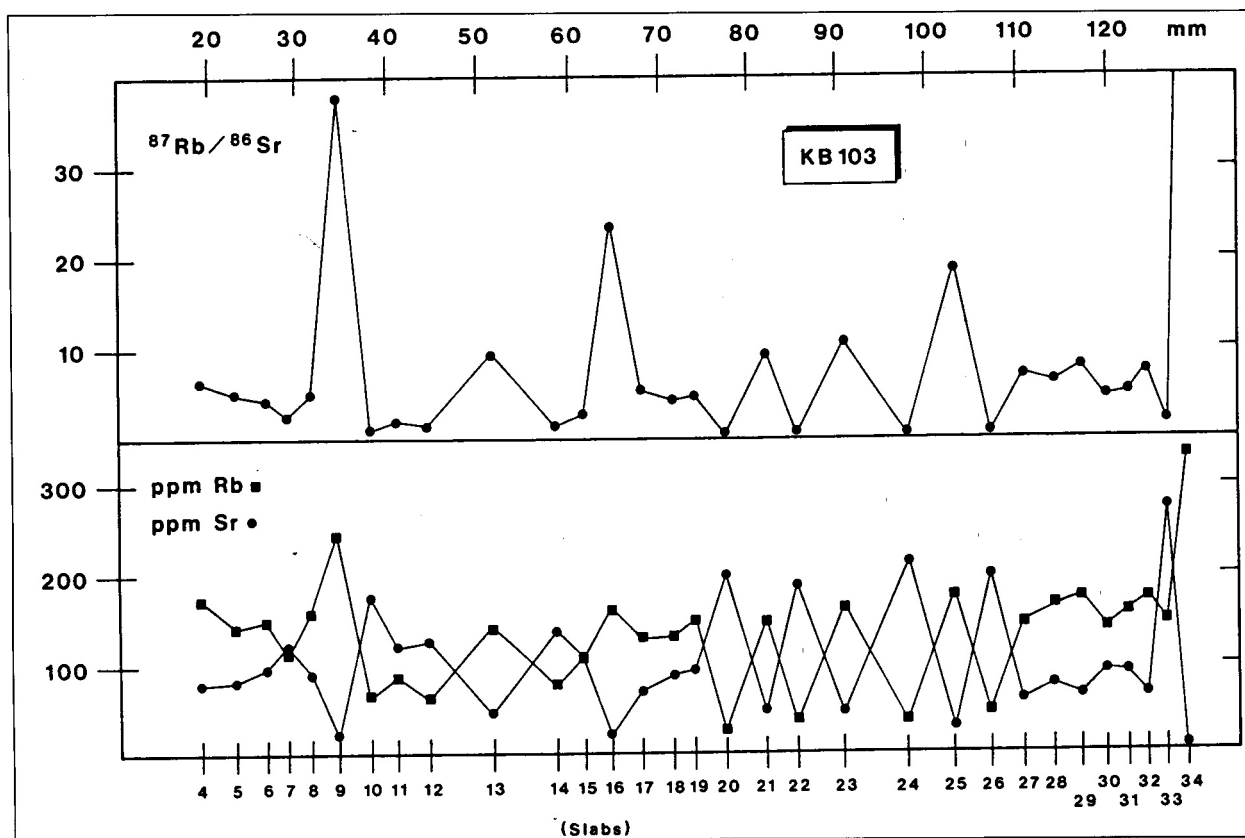


Figure 5.31: Sample KB103: Rb-Sr concentrations and Rb-Sr ratios as determined for the individual slabs of the rock profile

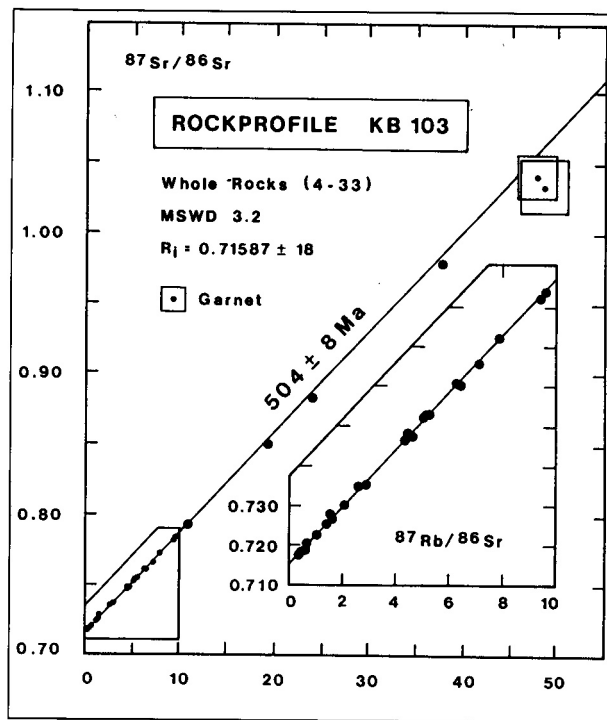


Figure 5.32a (above): Sample KB103: Isochron diagram for the whole-rock analyses of the sample; see inset for detailed position of data points with  $^{87}\text{Rb}/^{86}\text{Sr}$  ratios  $< 10$

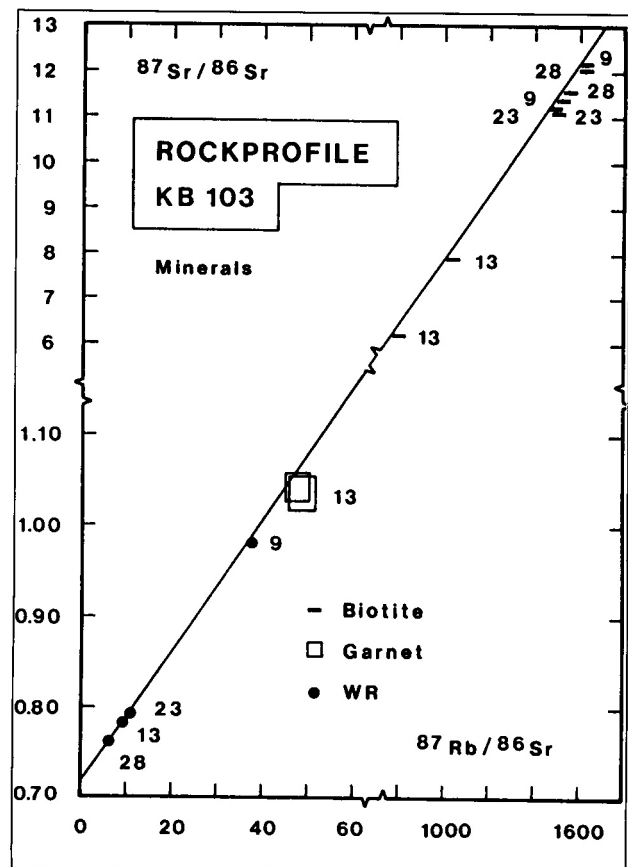


Figure 5.32b (right): Isochron diagram for the analysed mineral fractions of the sample. The whole-rock regression line and the whole-rock compositions of the 4 slabs are given for reference

Put into an isochron diagram (Fig. 5.32a), most data align along a straight line, the slope of which corresponds to an age of  $504 \pm 8$  Ma. An initial ratio of  $0.71587 \pm 0.00018$  was calculated. The slope of the line is largely determined by the greater number of data points having  $^{87}\text{Rb}/^{86}\text{Sr}$  ratios below 10. Due to the large analytical uncertainty in the  $^{87}\text{Rb}/^{86}\text{Sr}$  ratio, the data points in the upper part of the isochron diagram do not play an important part in the age calculation. Besides, not all of the data points fall onto the regression line within limits of error; the scatter of data is represented by an MSWD of 3.2. By calculating ages from different segments of the rock profile, i.e. for palaeosomes and neosomes, regression lines are obtained showing only minor scatter of data with corresponding MSWD values of 0.5. The regression over slabs 5-8 from a palaeosome reveals a whole-rock age of  $501 \pm 17$  Ma; slabs 25-29 (also palaeosome) gave  $498 \pm 20$  Ma; slabs 20-24, all belonging to a neosome, yielded  $499 \pm 7$  Ma and slabs 11-14 gave  $498 \pm 11$  Ma. The large errors obtained from the palaeosomes are based on the low spread of the data.

The calculated data from the different segments all point towards an age of about 500 Ma. The limits of error, however, qualify the apparently well-defined, above-quoted age.

Analytical results for the biotite and garnet fractions are presented in Figure 5.32b. The analyses of the eight biotite fractions revealed differences in the Rb and Sr concentrations for different slabs. Biotites within the same slab were found to show some dependence of the Rb-Sr systematics upon the

grain size. Rb concentrations seem to be higher in the coarse-grained fraction, but Rb-Sr ratios do not vary systematically. This is due to slight differences in the Sr concentrations which easily can be influenced by inclusions (e.g. apatite). However, the biotite fractions are aligned along the biotite-whole-rock regression lines calculated for each of the four slabs indicating a relation between element concentrations and grain size of the minerals. Ages were calculated from both biotite fractions and the whole-rock data of the respective slab, except for slab 23 where independent biotite-whole-rock ages were calculated for both biotite fractions. The following ages were obtained from the analysed biotites:  $496 \pm 7$  Ma for slab 9,  $485 \pm 7$  Ma for slab 13,  $498 \pm 10$  Ma for the 125-250  $\mu\text{m}$  biotite fraction of slab 23,  $486 \pm 10$  Ma for the 250-500  $\mu\text{m}$  biotite fraction of slab 23 and  $493 \pm 7$  Ma for slab 28. The age values obtained from the biotite fractions of all slabs vary by more than 10 Ma, but still overlap within limits of error. The two biotite fractions from slab 23 show a considerable difference, which is attributed to analytical uncertainties.

The two garnet fractions of slab 13 yielded Rb and Sr concentrations in the order of 1 and 0.1 ppm, respectively, giving rise to a high level of uncertainty for the isotopic ratios making the garnet data unsuitable for age calculations. Within the isochron diagram, however, the garnets fall within their limits of error onto the whole-rock regression line (Fig. 5.32a, b) which is shown as reference line in the mineral isochron diagram.

The spatial distribution and the computed temporal devel-

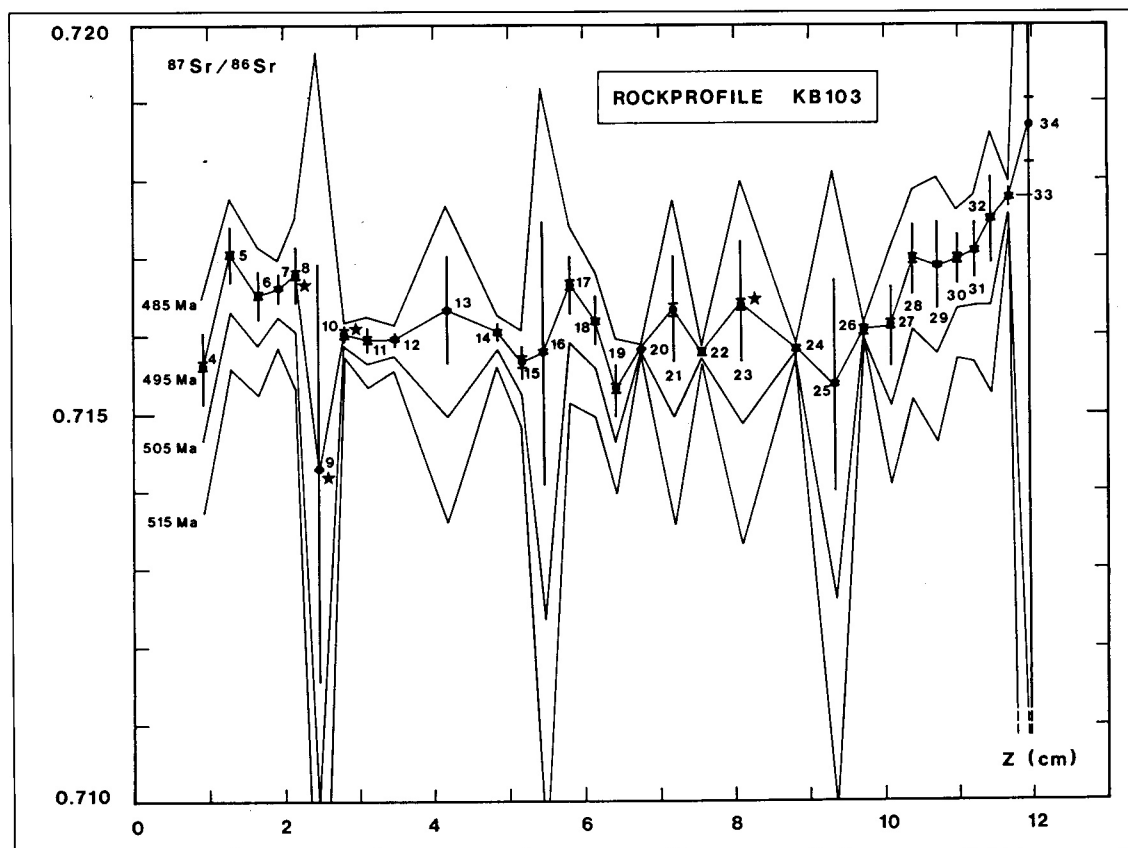


**Figure 5.33:** Sample KB103: Profile diagram showing the internal distribution and the computed temporal development of  $^{87}\text{Sr}/^{86}\text{Sr}$  ratios, calculated for  $t = 485, 495, 505$  and  $515$  Ma. Errors are shown exemplarily for  $t = 495$  Ma. Vertical lines represent an uncertainty of  $\pm 1\%$  assigned to the  $^{87}\text{Rb}/^{86}\text{Sr}$  ratios. Limits of error for the  $^{87}\text{Sr}/^{86}\text{Sr}$  ratios are indicated by horizontal bars. Repeated analyses are marked by asterisks

opment of the  $^{87}\text{Sr}/^{86}\text{Sr}$  ratios of the individual slabs is illustrated in the profile diagram in Figure 5.33. Whole-rock  $^{87}\text{Sr}/^{86}\text{Sr}$  ratios were calculated corresponding to  $t = 485, 495, 505$  and  $515$  Ma before present. Errors are shown exemplarily for the whole-rock isotope ratios at  $495$  Ma.

At first glance, the distribution of the  $^{87}\text{Sr}/^{86}\text{Sr}$  isotope ratios seems to be very irregular. For no time can an equilibrated distribution of isotopes be calculated. The  $^{87}\text{Sr}/^{86}\text{Sr}$  ratios of the biotite-rich melanosomes and restates in slabs 9, 16, 25 and particularly 34 increase rapidly within the given time interval. The isotope ratios of these slabs thus are not relevant when considering the degree of isotope homogeneity within the rock profile. The best degree of homogeneity or the least variation in the isotope ratios, however, is reached between  $495$  and  $505$  Ma, giving some domains of the rock profile a uniform isotope signature. By splitting the rock profile into several units, areas of isotopic equilibrium may be defined which show, within limits of error, a homogeneous distribution of isotope ratios. Partial isotopic equilibrium is reached in slabs 5-8, 10-14, 20-25 and 28-32. These domains coincide largely with the macroscopically and genetically defined entities, i.e. palaeosomes and neosomes. The absolute values of the initial  $^{87}\text{Sr}/^{86}\text{Sr}$  ratios differ significantly between the considered units, but are similar for the palaeosomes (slabs 5-8 and 28-32) and the neosomes in the central part of the profile.

As the isotopic equilibrium is only partially developed, the above calculated Rb-Sr whole-rock regression line may not

be interpreted in terms of an isochron age. Ages are more appropriately to be calculated from the individual, isotopically homogeneous domains within the rock profile. It can be concluded that apparently either no equilibrium distribution of Sr isotopes was reached during anatexis over the length of the profile or it has subsequently been disturbed. However, partial isotope equilibria exist within the palaeosomes and neosomes of the profile.

## 5.8 INTERPRETATION OF RB-SR SMALL-DOMAIN DATA

The previous sections of this chapter were concerned with the character of the investigated rock profiles and the analytical results from the Rb-Sr small-domain analyses. In this section the isotopic data from the various whole-rock and mineral analyses will be summarised and discussed. The analytical results will be discussed with regard to a) the element distribution patterns of Rb and Sr in the whole rocks of the individual slabs of the rock profiles, b) the homogeneity of the  $^{87}\text{Sr}/^{86}\text{Sr}$  isotope ratios within the rock profiles, and c) the geological relevance of the calculated whole-rock and mineral age data. An evaluation of the regional significance of the Rb-Sr isotope data for the timing of metamorphic events in the Khomas Trough, however, is largely based on the complementary U-Pb and K-Ar isotope data (cf. Chapter 6). Re-

gional geochronological aspects will therefore be discussed in Chapter 7.

All calculated age data from the investigated mineral fractions and their respective whole-rock ages from the rock profiles are compiled in Figure 5.34 and Table A.15.

### 5.8.1 Interpretation of mineral data

The Rb-Sr small-domain whole-rock analyses were accompanied by Rb-Sr analyses of mineral fractions separated from some individual slabs of the six rock profiles and from the sample CO117. Analyses were carried out on 17 biotite fractions, 4 muscovite fractions, 6 plagioclase-quartz fractions, 2 garnet fractions and one fraction each of hornblende and apatite. Not all of the mineral fractions, however, are equally suited for the calculation of ages based on mineral-whole-rock pairs. The minerals either have very low Rb and/or Sr concentrations so that the analytical uncertainty of the isotope data increases drastically, or there is too little spread in the analytical data from the minerals and their respective whole rocks. This applies to most of the minerals investigated in this study except the biotites.

Biotites were analysed from all six rock profiles. The analysed fractions in most cases represent a mixture of more than one biotite generation, comprising synkinematic ( $D_2$  and  $D_3$ ) as well as post-kinematic (post- $D_4$ ) biotites. The biotite-whole-rock ages from most of the biotite fractions range between  $485 \pm 10$  and  $498 \pm 10$  Ma, while only two fractions yielded younger ages.

The muscovite fractions analysed from the metasediments in general are characterised by high concentrations of Sr (41-73 ppm) and comparatively low concentrations of Rb (147 - 234 ppm) compared to magmatic muscovites. The  $^{87}\text{Rb}/^{86}\text{Sr}$  ratios and the isotope signatures of the muscovites in most cases are not much different from those of the respective whole rocks. The calculation of ages from whole-rock-muscovite pairs therefore results mostly in a high degree of uncertainty for the age data, but they mostly tend towards higher ages than the biotites.

Plagioclases were analysed in form of plagioclase-quartz concentrates from the two samples KB117 and KB115. Although no Rb and Sr concentrations could be determined for the plagioclases, their isotopic composition is regarded to be equivalent to the  $^{87}\text{Sr}/^{86}\text{Sr}$  ratios of the plagioclase-quartz mixtures. The quartz present within the analysed fractions is considered to be devoid of Sr and thus not to influence the  $^{87}\text{Sr}/^{86}\text{Sr}$  ratios. Ages calculated from 4 of 5 whole-rock-plagioclase pairs range between  $486 \pm 13$  Ma and  $497 \pm 14$  Ma; one plagioclase fraction yielded an age of  $476 \pm 15$  Ma. It is remarkable that the largest spread in data occurs within one sample (KB115).

Apatites were analysed from the sample CO117. The apatites contain only about 2 ppm Rb. The calculated apatite-whole-rock age, however, is not well constrained and thus it is not critical to geochronological constraints. This applies also to the analysed garnets which have extremely low concentrations of both Rb and Sr. Accordingly, the  $^{87}\text{Rb}/^{86}\text{Sr}$  and  $^{87}\text{Sr}/^{86}\text{Sr}$  ratios are only poorly defined.

The overall distribution of the calculated mineral-whole-rock and whole-rock ages as illustrated in Figure 5.34 is

characterised by a rather low variation in the biotite, and plagioclase age data. This implies that the resetting of the isotope systems within the investigated minerals (i.e. most of the biotites and plagioclases) occurred within, limited period. In contrast, the whole-rock ages from the individual slabs of the rock profiles show a greater variability. The relationship between of the mineral ages and their respective whole-rock ages was found to be quite heterogeneous for the different rock profiles. In four of the samples, the mineral data are either younger than or equal within limits of error to the whole-rock data, but the reverse order does also occur (samples KB117 and KB115).

In general, the calculated mineral-whole-rock ages are regarded to denote the isotope exchange between the respective mineral and its surrounding whole rock. This is valid particularly for minerals forming major constituents of the rock. In the case of minor constituents and accessory phases, an isotopic homogenisation of the mineral and the bulk rock may not always be expected. In samples KB167, KB307, KB421 and KB103, isotope exchange between the analysed biotites and the whole rocks occurred either contemporaneously or after the equilibration of the whole rocks within the rock profiles. This confirms that the resetting of the isotope system within single grains outlasted the isotopic homogenisation of the whole-rocks. From the uniformity of the mineral data it may be inferred that this resetting of the isotope systems within the minerals was governed by similar or the same processes.

The isotopic re-equilibration of minerals is most commonly attributed to the self diffusion of Sr which is effective during regional cooling of the rocks down to a certain blocking temperature (cf. Chapter 4), below which the radiogenic daughter isotope is quasi-quantitatively retained. The assumed blocking temperature for radiogenic Sr in biotites ranges between 300 and 400°C (Purdy and Jäger, 1976; Verschure *et al.*, 1980; Del Moro *et al.*, 1982). The metasediments investigated in this study have all been subjected to metamorphic temperatures significantly above the estimated blocking temperatures. The same applies to muscovites, for which blocking temperatures for radiogenic Sr were estimated at about  $500 \pm 50^\circ\text{C}$  (Purdy and Jäger, 1976). Taking into account that there is a difference of about 100°C in peak metamorphic temperatures within the Khomas Trough, the cooling below a certain isotherm would last longer in the northern Khomas Trough than in the southern part, provided that the uplift rate was the same throughout the area. The apparent uniformity of the biotite data, however, does not meet the model of a uniform degree of cooling for the Khomas Trough. The data rather suggest either that cooling proceeded at different geothermal gradients within the area or the resetting of the minerals was influenced by other factors.

In accordance with a number of investigations on the closure behaviour of minerals (e.g. Chopin and Maluski, 1980), other factors than a temperature-induced diffusion of Sr during cooling of the rock have to be taken into account. These factors include pervasive structural overprints and the interaction of the rock with fluid phases. These processes commonly induce the recrystallisation of the minerals and/or retrograde mineral reactions. The investigated meta-sediments of the Kuiseb Formation were shown largely to have

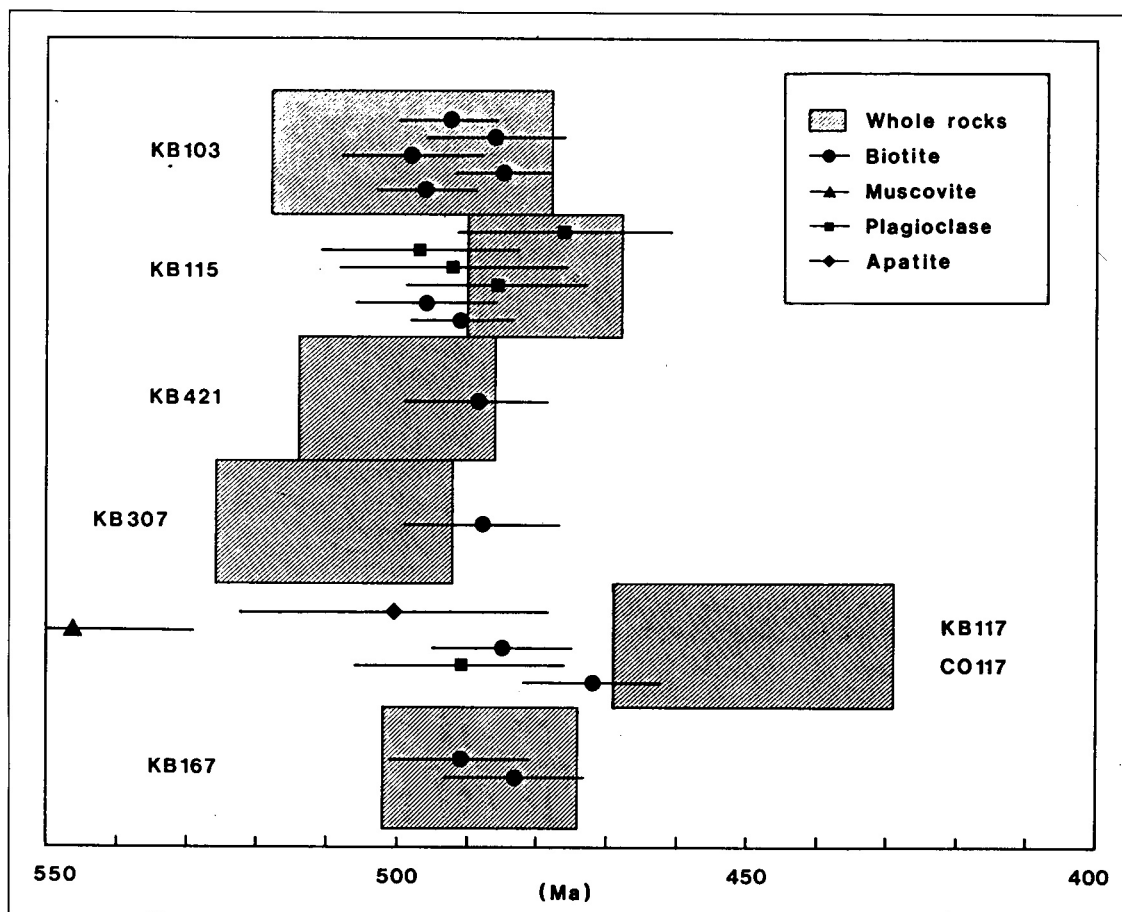


**Figure 5.34:** Diagram showing the distribution of the apparent age data calculated from whole rocks and minerals of the investigated rock profiles. The extent of the hatched areas corresponds to the  $2\delta$  errors of the whole-rock age data; the horizontal bars represent the errors obtained for the mineral whole-rock data

undergone post-kinematic recrystallisation (cf. Chapter 2.5). A post-kinematically crystallised generation of coarse muscovites and chlorites and/or biotites frequently occurs in pelitic rocks. This indicates that the thermal peak of metamorphism outlasted the (main) structural evolution in the area. The latest structural overprint is a locally developed crenulation which is about the same age as the intrusion of the Donkerhuk Granite (cf. Chapter 3) and is probably also associated with the late crystallisation of muscovites.

Microprobe analyses carried out to investigate the variation in the chemical composition of the different mineral generations, revealed no significant or systematic differences for the biotites. In contrast, the analysed synkinematic and post-kinematic muscovites may be differentiated by their Si cation positions. The microprobe data suggest that the investigated biotites were petrographically (re-)equilibrated, although some of them show no apparent recrystallisation. The application of the muscovite-biotite thermometer after Hoisch (1989) also revealed that the minerals had equilibrated at temperatures significantly below the peak metamorphic temperatures, i.e. at some retrograde stages of the metamorphic P-T path.

Taking into account this retrograde, petrographic equilibration of the micas within the investigated samples, it might be expected that the isotope signatures of these mineral phases also reflect the closure of the minerals at a retrograde stage of

the P-T-path. Comparing a petrographic and an isotopic equilibration of minerals, it has to be emphasised, however, that there is a difference in the closure behaviour of the minerals with regard to a) the element exchange (petrographic equilibration) and b) the isotope exchange between mineral phases. In the case of a) a net transport of ions due to a chemical potential gradient takes place, whereas b) is commonly ascribed to self diffusion.

### 5.8.2 Interpretation of whole-rock data

#### *Aspects of the Rb and Sr element distribution*

The element distribution patterns of Rb and Sr within the investigated rock profiles show characteristic features which most likely are related to the mechanisms of metamorphic banding formation. The element distribution patterns were found to be distinctly different in the sedimentary layered samples and the metamorphically banded samples.

The Rb and Sr concentrations could be expected to be negatively correlated in the case of sedimentary interlayered pelitic and psammitic horizons. This negative correlation is due to the predominance of either plagioclase and quartz or phyllosilicates in the respective layers. This distribution pattern originates from the composition of the sedimentary precursor and the sedimentary processes during deposition. A distinct

negative correlation of the elements Sr and Rb was, however, only found in the migmatite sample KB103 although the layering of the sample originates from metamorphic differentiation: The sedimentary layered samples KB167, KB307 and KB115, however, do not show a significant positive or negative correlation of Rb and Sr. In contrast, the metamorphically banded samples KB117 and KB421 both show a positive correlation of the elements. The element distribution pattern indicates that both plagioclase and micas are enriched in the P-domains whereas quartz apparently has been removed. The passive enrichment in plagioclase and mica gives rise to high concentrations of both Rb and Sr. With regard to the current hypotheses of metamorphic banding formation which have been outlined in Chapter 2.5, the depletion in quartz in the P-domains could most likely be explained by pressure solution mechanisms. Pressure solution is favoured as the main process governing the development of P-Q-fabrics by most authors (e.g. Beach 1977, 1979, 1982; Wright and Platt, 1982). The geochemical distribution pattern of Rb and Sr in this study indicates that pressure solution predominantly affecting quartz has played a major part in the formation of the metamorphic banding cleavage within the investigated rocks of the Kuiseb Formation. This is consistent with the structural situation, since the  $S_2$  metamorphic banding is axial planar to  $F_2$  folds and shows a distinct fanning of the cleavage in most cases. This is difficult to explain by the dewatering hypothesis as favoured by Behr *et al.* (1983). One of the problems of the former theory, however, is the question of transport distance of the dissolved quartz and the site of precipitation.

#### *Rb-Sr isotope characteristics*

Each of the investigated rock profiles is characterised by its own isotope systematics; only few features in the isotope distributions were found to be common to all the investigated samples.

Put onto isochron diagrams, the isotope data of all six rock profiles align along straight lines. In most cases there is only minor scatter of data except for rock profile KB421. It could be shown, however, that the isotope systems within some of the slabs of the profile were disturbed by processes leading to the late, post-kinematic formation of scapolite associated with a set of small joints. The other slabs show a good alignment of data points. The only minor scatter of data points is represented by MSWD values between 0.5 and 1.7 for five of the rock profiles, and a maximum of 3.2 for the migmatite sample KB103. In samples KB117 and KB115, the MSWD values are 0.5 and 0.8, respectively. The calculated regression lines for these samples thus formally meet the requirements for interpretation as isochrons.

The interpretation of the isotope data and the calculated whole-rock ages, however, is based on the internal distribution of the isotope signatures of the individual slabs of the rock profiles. The spatial distribution and temporal development of the  $^{87}\text{Sr}/^{86}\text{Sr}$  isotope ratios of the individual slabs were illustrated in the profile diagrams and discussed for each rock profile in the previous sections of this chapter. The most striking feature of the profile diagrams is that for most samples no homogeneous distribution of isotope ratios could

be calculated. However, partial isotope equilibria apparently exist within the rock profiles as is evident for example in the rock profile KB103, but the time of partial equilibrium is not necessarily equal to the age calculated from all slabs of the respective rock profile. In accordance with the work of Bachmann and Grauert (1986), the isotope distribution patterns which show the least variation of isotope ratios, may be interpreted as representing a metamorphic event leading to a partial equilibration of the isotope ratios, although the regression lines do not represent true isochrons. This dating by means of disequilibrium distributions may be applied to samples KB167, KB307, KB421 and KB103. The ages calculated from these rock profiles are in the range of  $488 \pm 13$  to  $509 \pm 17$  Ma. For rock profiles KB117 and KB115, within limits of error, homogeneous whole-rock isotope distributions may be calculated. The two rock profiles revealed comparatively low whole-rock ages of  $449 \pm 20$  and  $479 \pm 11$  Ma.

With regard to the relation between the mineral and whole-rock isotope data, the latter rock profiles appear to be most important for an evaluation of the significance of the apparent whole-rock ages. In samples KB117 and KB115, the relationship of the mineral-whole-rock and whole-rock data is more complex than in the other rock profiles. The regression of the whole-rock data from the individual slabs of these rock profiles revealed younger ages than the mineral-whole-rock pairs from single slabs from the rock profiles. The data would imply that the whole rocks of the rock profiles had equilibrated after the major mineral constituents of the rocks had been closed to radiogenic Sr. An opening of the whole-rock Rb-Sr system, however, without affecting the isotope systems of the constituting minerals seems unlikely. This apparent discrepancy most likely originates from the whole-rock isotope systematics of the two rock profiles.

Within the profile diagrams, both rock profiles show homogeneous distributions of their  $^{87}\text{Sr}/^{86}\text{Sr}$  ratios for the time of the calculated whole-rock ages. In both samples, plagioclase-quartz concentrates were analysed which clearly showed that there is no homogeneity of isotopes between the plagioclases and the respective whole rocks at the time of the apparent whole-rock equilibrium. In three slabs of the rock profile, the analysed plagioclase-quartz fractions rather show a homogeneous isotope distribution with the respective whole rock at the calculated biotite-whole-rock ages (above 490 Ma). Furthermore, it could be shown for rock profile KB115 that the homogenisation of the plagioclases with their respective whole rocks occurred discontinuously within different slabs. The difference in the  $^{87}\text{Sr}/^{86}\text{Sr}$  ratios of the plagioclase-quartz fractions, calculated for the time between 600 and 300 Ma before present, indicates that there was apparently no isotope exchange between the plagioclases of these slabs. These apparent isotope heterogeneities strongly suggest that the "isochrons" obtained from the two samples do not denote the timing of whole-rock isotope homogenisation, since the major constituents of the rocks do not show isotope equilibrium with their respective whole rocks at that time. The good alignment of whole-rock isotope ratios within the isochron diagrams in these cases should rather be regarded as spurious isochrons.

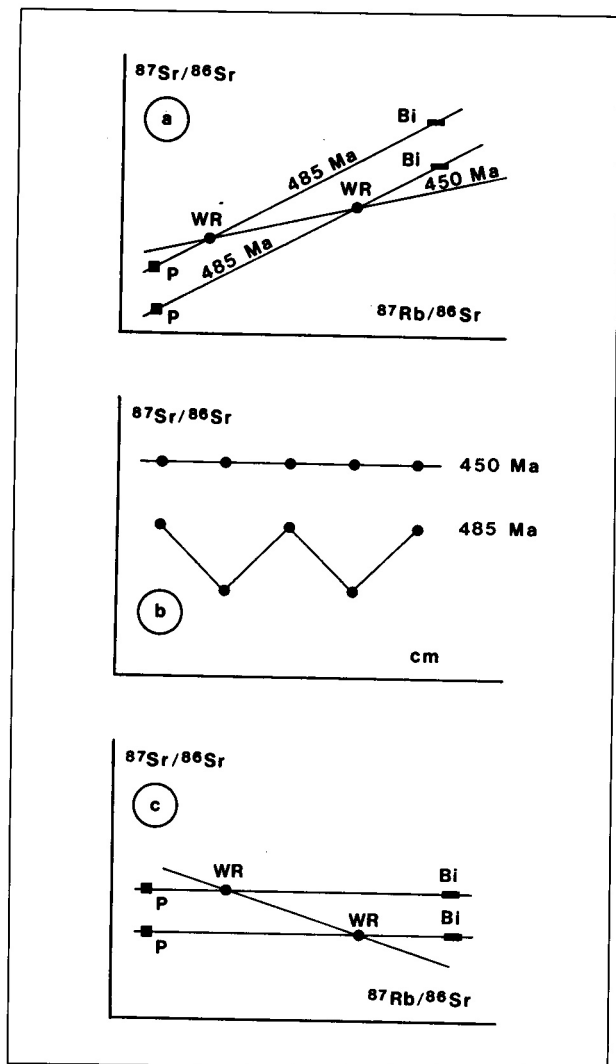


**Figure 5.35:** a) Isochron diagram showing the measured ratios of plagioclase (P), whole rock (WR) and biotite (Bi) from two slabs of a fictitious rock profile. The minerals and the whole-rock data for each slab reveal an isochron age of 485 Ma; the whole rocks of the different slabs of the rock profile are aligned along a spurious isochron corresponding to 450 Ma. b) Profile diagram showing the spatial distribution of whole-rock data from contiguous slabs of the rock profile. At 485 Ma no isotopic equilibrium exists. c) Isochron diagram at 485 Ma showing a homogeneous distribution of isotopes between the minerals and the whole rock of each slab and a negative slope for the whole rocks of the different slabs

Two theories may be discussed to explain the quite uncommon relationship between the mineral and whole-rock ages within the two rock profiles. These models are illustrated in the Figures 5.35 and 5.36, which are based on the calculated age data of the rock profile KB117.

The first model is based on the assumptions that no isotope exchange occurred between the whole rocks of the individual slabs, but between the minerals within the individual slabs. In the isochron diagram (Fig. 5.35a) each slab forms a mineral isochron between plagioclase, whole rock and biotite, the slope of which corresponds to an age of 485 Ma. The whole-rock data from the different slabs align along a straight line corresponding to an age of 450 Ma. In the profile diagram (Fig. 5.35b) the isotope distribution pattern of the whole rocks

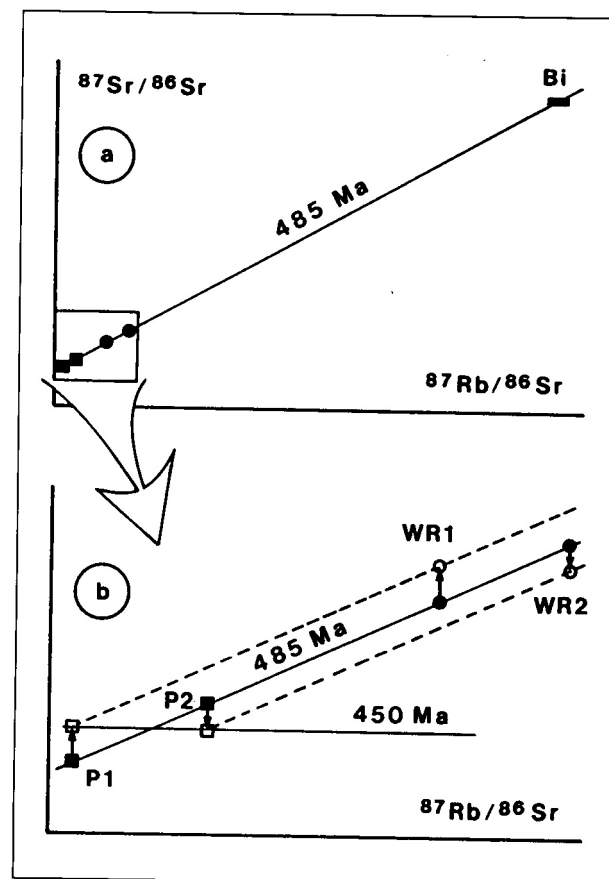


**Figure 5.36:** a) Isochron diagram. b) Isochron diagram at 450 Ma showing a homogenisation of the plagioclases from the contiguous slabs

at 485 Ma shows isotopic heterogeneities which develop into an equilibrated isotope distribution at 450 Ma. The latter distribution, however, does not reflect a homogenisation event. In the isochron diagram at 485 Ma (Fig. 5.35c), the minerals and their respective whole rock show a homogeneous distribution of isotopes, whereas the whole rocks of the different slabs start off with a negative slope. It seems unlikely, however, that no isotope exchange at all occurred between the mm- to em-thick slabs of the investigated amphibolite facies metasediments.

The second model (Fig. 5.36) is based on the assumptions that the equilibration of plagioclases only continued until 450 Ma, whereas the homogenisation of the plagioclases with the respective biotites and whole rocks within and between the contiguous slabs ceased at 485 Ma. The isochron diagram (Fig. 5.36a) shows an alignment of the mineral and whole-rock data from contiguous slabs of a rock profile with a corresponding age of 485 Ma. The isotope exchange between the whole rocks and between the whole rocks and minerals of contiguous slabs ceased at 485 Ma. The isochron diagram at 450 Ma shows the equilibration of the plagioclases of contiguous slabs which align along an isochron. The whole rocks as well as the other minerals do not homogenise at this stage. This model would imply that plagioclase closes at a later stage than biotite which, however, has not yet been observed in other investigations on the Rb-Sr system in minerals.

Neither of the above models is compelling for the inter-

pretation of the isotope systematics of the two rock profiles. A third possible mode of explanation would encounter an open system behaviour of the whole rocks. It might be assumed that the interaction of the rock with fluid phases, for example by an addition of Sr in an interstitial phase, can alter either the whole-rock isotopic composition or the concentrations of the elements. The minerals would remain closed systems. In practice, there are arguments for and against an open system behaviour of the rocks.

The occurrence of retrograde mineral phases as the late muscovites and also the local sericitisation of plagioclases and the chloritisation of biotite confirms the presence of a fluid phase in the late stages of metamorphism. Retrograde muscovites occur particularly in the rock profiles KB307 and KB115. The retrograde formation of muscovite after staurolite and  $Al_2SiO_5$  as described by Eugster (1970) and Carmichael (1969) involves a hydration of the minerals as well as an exchange of potassium. Since rubidium usually substitutes for potassium within the minerals, it may be expected that rubidium is also involved in these retrograde reactions.

The balancing of the isotope ratios and concentrations undertaken for two slabs of the rock profile KB115 (cf. Chapter 5,6) constitute a further argument for open system behaviour. It was shown that the measured isotope ratios of plagioclase, muscovite and biotite do not account for both the whole-rock element

concentrations and the isotopic composition of the respective slab, however, it is an oversimplification to take into account only these latter minerals.

On the other hand, an open system behaviour associated with the alteration of the whole-rock isotope compositions and concentrations of Rb and/or Sr should disturb the good alignment of the whole-rock data points within the isochron diagram. For sample KB421, it was shown that the late scapolite-forming reactions affected only limited portions of the rock. This example indicates a largely closed system behaviour of the whole-rock systems since the time of their last isotopic equilibration. The geochemical data from the rock profile KB115 would allow for small changes in the whole-rock compositions and thus cannot contribute significantly to the discussion on a closed or open system behaviour of the whole rocks.

None of the above theories satisfactorily accounts for the observed isotope systematics of the investigated rock profiles. The presence of isotope heterogeneities at mm and cm scale, however, is regarded to be essential to the interpretation of any Rb-Sr whole-rock analyses. For the two rock profiles KB115 and KB117, it is suggested that the calculated whole-rock ages are not geologically significant. The geological significance of the other rock profiles will be discussed within the framework of the complementary isotope data from this study and other available geochronological data from the Damara Orogen.

## 6. COMPLEMENTARY ISOTOPE ANALYSES

### 6.1 INTRODUCTION

Although the main interest of the study focused on Rb-Sr small-domain investigations, complementary isotope analyses were carried out in order to provide independent geochronological constraints on the sediment sources of the Kuiseb Formation and the metamorphic and post-metamorphic evolution of the metasediments and migmatites in the Khomas Trough. In particular, the following investigations were undertaken:

- U-Pb analyses of detrital zircons from the Kuiseb Formation (Chapter 6.2);
- U-Pb analyses of magmatic and metamorphic monazites from the Donkerhuk Granite and associated rocks as well as from the Kuiseb Formation metasediments (Chapter 6.3);
- Rb-Sr analyses of mineral fractions separated from the Donkerhuk Granite (Chapter 6.4);
- K-Ar and  $^{40}\text{Ar}$ - $^{39}\text{Ar}$  analyses of selected mica fractions from the investigated rock profiles of the Kuiseb Formation metasediments (Chapter 6.5).

### 6.2 U-PB ANALYSES OF DETRITAL ZIRCONS FROM THE KUISEB FORMATION

#### 6.2.1 Character of sample

For the extraction of detrital zircons, a several-metres-thick meta-greywacke layer from the central Khomas Trough (farm Kaan 309) was sampled. The psammitic material exhibits a strong  $S_2$  metamorphic banding cleavage. Apart from U-Pb investigations of the main zircon fractions, Rb-Sr analyses were carried out on apatite and mica fractions from a representative split of the sample. A small specimen was used for Rb-Sr small-domain investigations utilising the metamorphic layering of the sample material (rock profile KB117). A detailed petrographic description of sample CO117 has therefore been presented in Chapter 5.3.

The heavy mineral fraction of the sample is dominated by apatite. Subordinate are tourmaline, opaque phases and zircons. Apatite and tourmaline are developed as clear and, in the case of tourmaline, euhedral crystals. This indicates a metamorphic origin of the minerals or recrystallisation during the metamorphic overprint of the sediments.

#### 6.2.2 Zircon fractions

The zircons can be grouped into different fractions on the basis of their colour and habit. Most zircon crystals are turbid or metamict. Transparent and translucent grains are in most cases pale pink, with some nearly colourless, clear crystals. Turbid and metamict zircons are a more intensive orange colour. Crystal forms and habits vary considerably. The majority of the grains are partially to well-rounded, but euhedral

crystals are also present. Euhedral crystals are mostly elongate, with length-width ratios of 3: 1 and dominating prism faces. Pyramids occur both as (110) and (211) faces. Only a small fraction shows a predominant development of pyramidal faces. The most common zircon morphologies occurring in the sample are shown in Figure 6.1. All zircons of the sample show a more-or-less pitted and corroded surface which strongly suggests a detrital origin of the grains.

The internal structures of the zircons were investigated by means of cathodoluminescence of polished crystals. The intensity of cathodoluminescence depends on the concentration of foreign atoms trapped in the crystal structure, causing defects in the crystal lattice. The concentration of foreign atoms may vary for subsequent stages of growth leading to a growth zonation, and may also vary for individual crystal forms resulting in sector zoning (Vavra, 1990). The internal structuring of zircon crystals is illustrated in Figure 6.2. The investigated zircons in most cases exhibit a distinct growth zonation (Fig. 6.2a-d), in some cases also involving sector zoning (Fig 6.2e). Some of the crystals are polyphase, showing older cores which have been overgrown (Fig. 6.2a, f). The zircon crystals shown in Figure 6.2g and Figure 6.2h exhibit complex internal structures, the origin of which is not yet known.

For conventional U-Pb analyses, the zircons were sorted according to morphological criteria and colour. Only transparent crystals were used. The following fractions were analysed:

- euhedral, prismatic crystals, pale pink coloured, sieve fractions 40-60  $\mu\text{m}$ , 60-80  $\mu\text{m}$  and 80-100  $\mu\text{m}$ ;
- subhedral crystals, colourless to pale pink coloured, sieve fraction 60-80  $\mu\text{m}$ ;
- well-rounded grains, sieve fractions 40-60  $\mu\text{m}$  and 80-100  $\mu\text{m}$ .

#### 6.2.3 Analytical results

Analytical results for the zircon fractions are presented in the concordia diagram in Figure 6.3 and Table A.16. The data for the zircon fractions are highly discordant with data points showing only a poorly defined trend in the concordia diagram. The scatter of data, however, is not surprising, bearing in mind the complex internal structures even of morphologically similar crystals. For the euhedral zircons, the concentrations of V and total Pb range from 582 to 801 ppm and 61 to 67 ppm, respectively, and are negatively correlated with grain size. For the rounded zircons V concentrations of 413 and 661 ppm and a total Pb content of 51 and 76 ppm were obtained. Concentrations of V and Pb decrease from euhedral through subhedral to rounded zircons of comparable grain size. A correlation of zircon morphology, grain size and isotope characteristics is indicated by the above results. The fractions of rounded zircons show the highest degree of discordance. The euhedral zircons show the lowest apparent ages, but a correlation of degree of discordance and grain

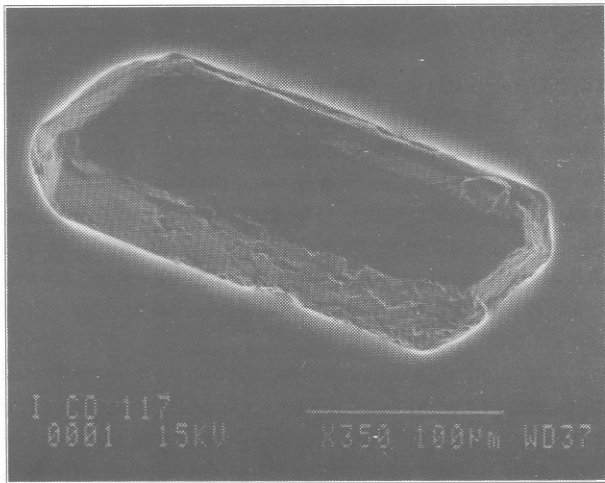


Figure 6.1a

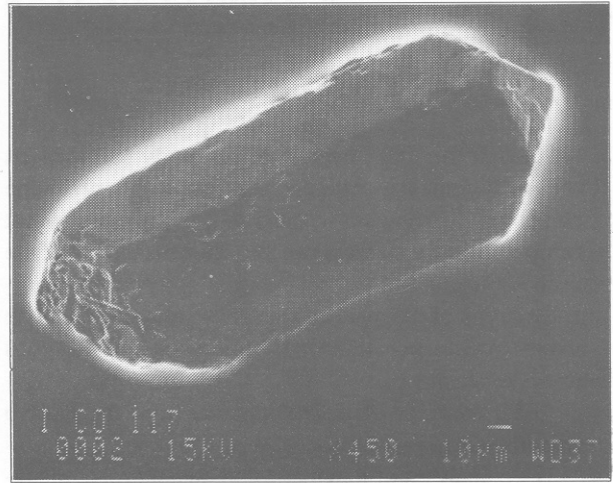


Figure 6.1b

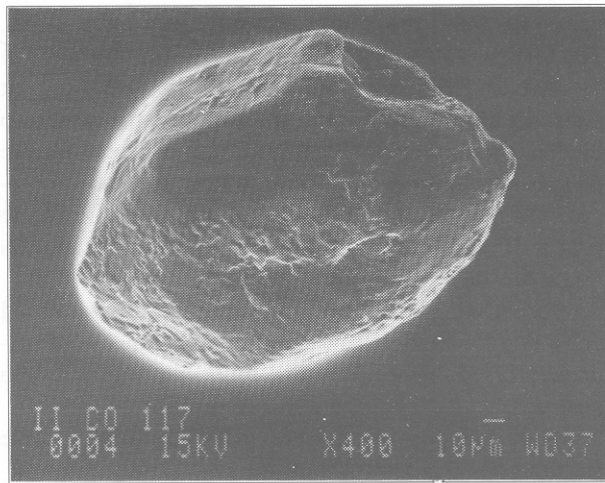


Figure 6.1c

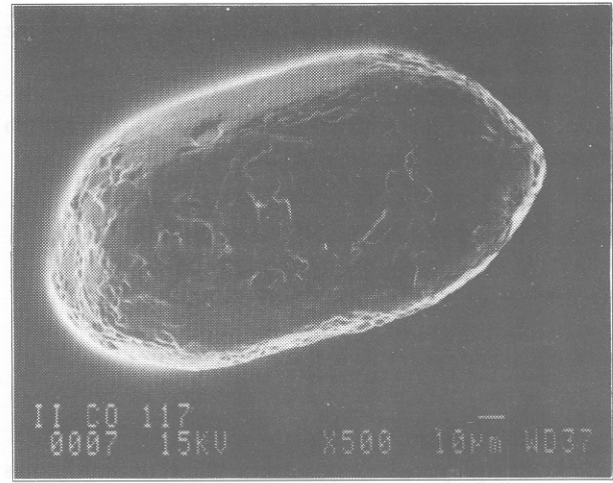


Figure 6.1d

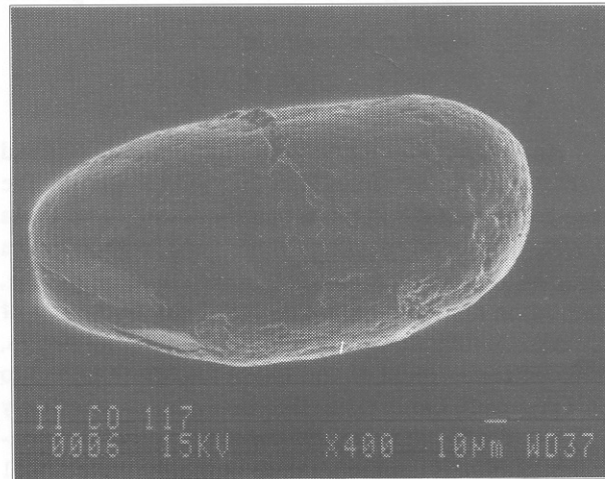


Figure 6.1e

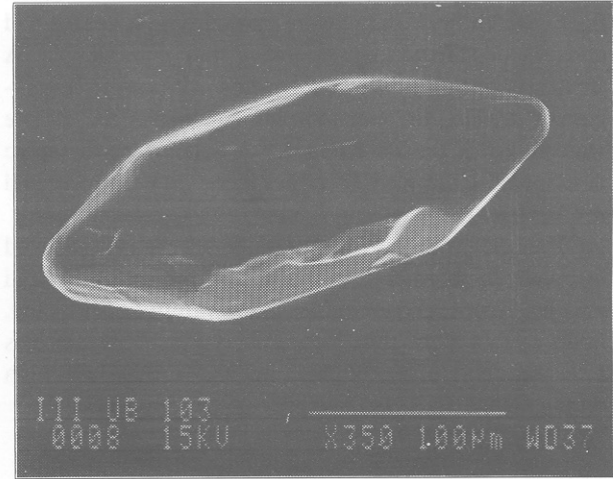
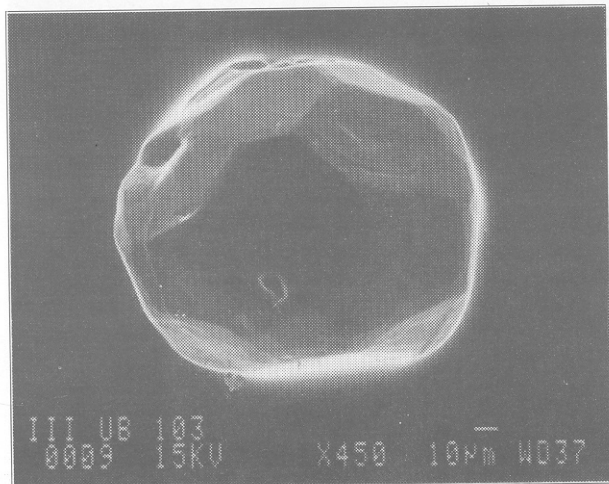


Figure 6.1f



**Figure 6.1 (opposite page and left):** SEM images of selected zircons:

a) - e) zircons from sample CO117 showing typically pitted surfaces.

Zircon fractions: a) and b) euhedral, prismatic;

c) and d) subhedral to partially rounded;

e) well rounded;

f) and g) euhedral zircons from migmatite sample KB103

**Figure 6.1g (left)**

size cannot be observed.

The position of the data points for the euhedral zircons in the concordia diagram below the approximate peak of Pan-African regional metamorphism (>500 Ma) indicates lead loss thereafter (recent lead loss, continuous lead loss).

#### 6.2.4 Interpretation

The various morphological zircon types present in the investigated meta-greywacke point towards either an involvement of more than one sediment source or to a sediment source containing a variety of zircon fractions. The U-Pb zircon data do not allow conclusions on the absolute age of the sediment sources to be drawn, but the  $^{207}\text{Pb}/^{206}\text{Pb}$  apparent ages may be interpreted in terms of minimum ages. The cathodoluminescence images clearly depict the heterogeneity of the analysed zircon fractions. The internal structures of the zircons reveal a complex history of zircon genesis which involves in a number of cases at least two phases of repeated corrosion and overgrowth. The obtained data might thus represent a complex mixing of U-Pb characteristics from the different phases depicted from the cathodoluminescence images (Fig. 6.2). A successful provenance study in the Kuseb Formation by means of radiometric dating of detrital minerals could be achieved by systematic analyses of single zircons in order to avoid mixing of genetically inconsistent components.

### 6.3 U-PB ANALYSES OF MAGMATIC AND METAMORPHIC MONAZITES

In the course of this study some emphasis was put on the contact relationships between the Kuseb Formation metasediments, the Donkerhuk Granite and the migmatites occurring locally along the northern margin of the Khomas Trough. In Chapter 3 some ideas on the migmatite generation in the Davetsaub area in the northernmost Khomas Trough have been raised. U-Pb analyses of monazites from the different units were carried out to put constraints on the timing of deformation, metamorphism - with special regard to the anatectic event - and granite intrusion in the Khomas Trough during the final stages of the Pan-African orogeny. Dating of monazites has so far only been applied to the alaskitic intrusions in the Central Zone (Briqueu *et al.*, 1980). As has been discussed in Chapter 4, monazite analyses are expected to give the most

reliable approximation of the emplacement or crystallisation of the granites and the temperature peak of metamorphism in medium- to high-grade metamorphic rocks.

#### 6.3.1 Monazites from granitic rocks

Monazites from the following granitic rocks were analysed:

- one sample from the Donkerhuk Granite (CO343) close to its southern border on the farm Nomatsaus 29;
- a xenolith of foliated granodiorite (CO453) incorporated into the Donkerhuk Granite;
- a foliated vein about 5 cm thick which intruded into the migmatites (CO444). The rock is free of K-feldspar, but contains a high portion of muscovite. The foliation can be correlated with the  $S_4$  crenulation developed in the pelitic rocks in the area.

Sample localities are shown in Figure 6.4. For a description of the sampled rock types see Chapter 3.

Monazites recovered from the granitic samples are dark-yellow, partly greenish colour. Most crystals are turbid or metamict, but for analytical purposes only transparent grains were used. In contrast to the commonly round grain shape, the monazites from sample CO444 are characterised by a euhedral, platy crystal form.

#### 6.3.2 Monazites from the Kuseb Formation metasediments and migmatites

According to the work of Smith and Barreiro (1990), monazites form at or near the P-T conditions of the "staurolite-in" isograd in pelitic schists. Pelite samples from the Kuseb Formation were taken from different parts of the study traverse, corresponding to different metamorphic grades. However, monazites of considerable size and number could only be recovered from the high-grade (sillimanite-biotite-grade) part of the metasedimentary series. The formation of monazite might depend on the whole-rock composition and/or the metamorphic grade of the sample as has been discussed, but in any case the monazite occurring in the investigated Kuseb metasediments is regarded to be of metamorphic origin. Monazites are by far best developed in the migmatised metasediments of the Kuseb Formation in the vicinity of the

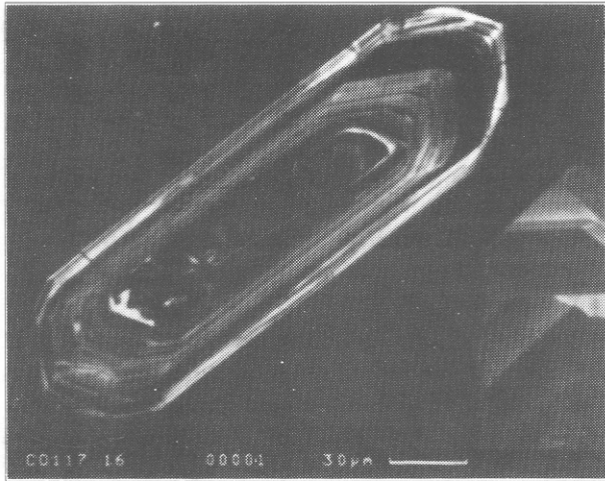


Figure 6.2a

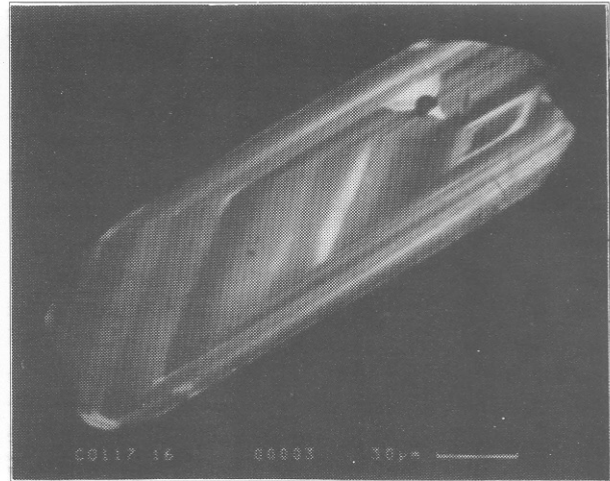


Figure 6.2b

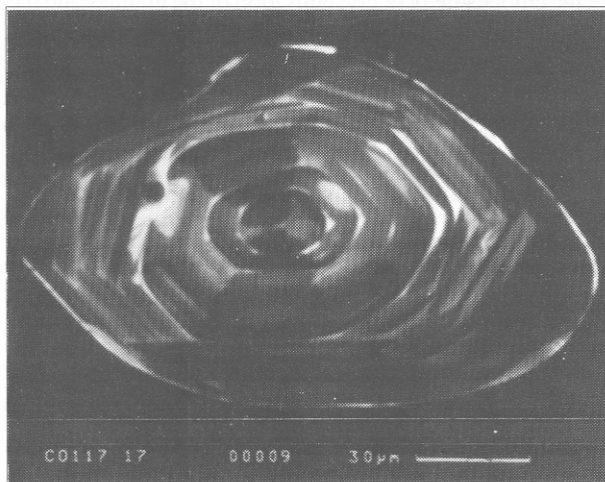


Figure 6.2c

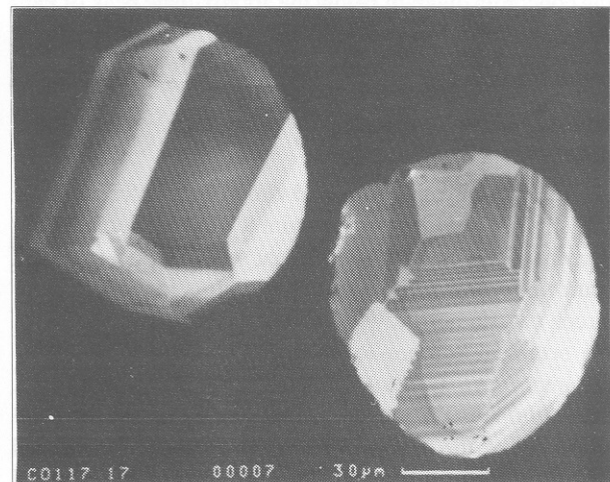


Figure 6.2d

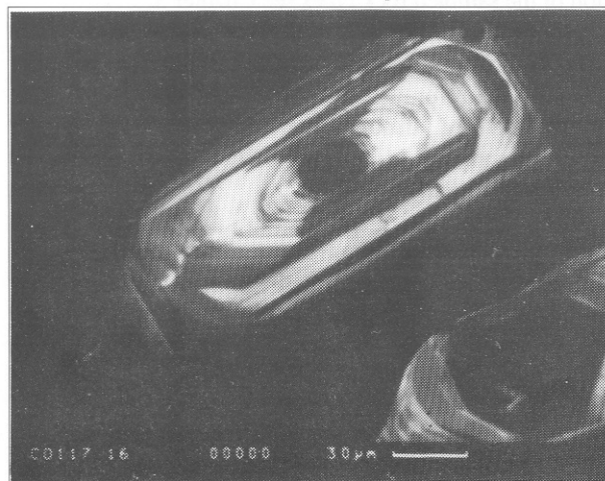


Figure 6.2e

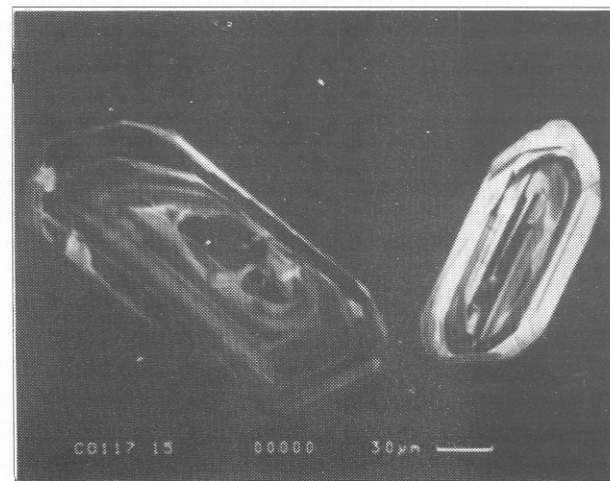


Figure 6.2f

**Figure 6.2 (above and opposite page):** Cathodoluminescence images of polished zircons from sample CO117 showing the internal structures of the grains.

a) - d) polyphase crystal with older corroded core; d) well-rounded relics of large zoned crystals; e) crystal showing sector zoning with younger overgrowths; f) polyphase crystal with corroded older cores and younger overgrowths; g) and h) crystals showing complex internal structures with thin overgrowths

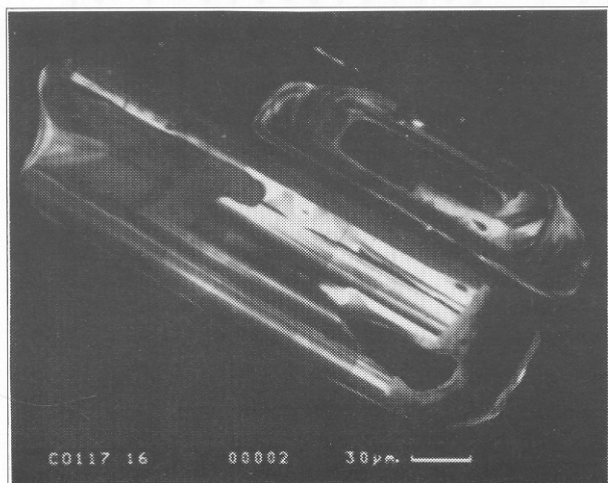


Figure 6.2g

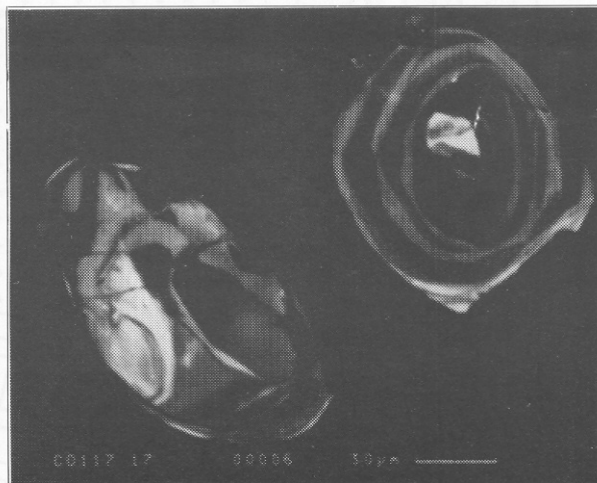


Figure 6.2h

Donkerhuk Granite. For sample KB103 an *in situ* anatexis is indicated by thin leucosome bands paralleling the main fabric of the rock. Since monazites are almost exclusively concentrated in the anatectic domains of the migmatite, the formation of the monazites is attributed to the anatectic event. The monazite-bearing sample CO437 represents a more discordant, massive type of leucosome. In general, monazite crystals from migmatitic rocks are typically clear and bright yellow in colour, partly euhedral and reach grain sizes of 200  $\mu\text{m}$ , in contrast to the much smaller monazite crystals of the sillimanite-grade metasediments. In Figure 6.5, SEM images of

selected monazites from the migmatite sample KB103 and the granitic veinlet CO444 are shown.

### 6.3.3 Analytical results

Analytical results are presented in Figure 6.6 and Table A.17. The U-Pb data for magmatic and metamorphic monazites essentially form two clusters in the concordia diagram.

Metamorphic monazites from migmatite samples KB103 and CO437 scatter in their  $^{207}\text{Pb}/^{235}\text{U}$  apparent ages between 521 and 525 Ma. However, the data points apparently plot slightly above the concordia curve. The monazites from the

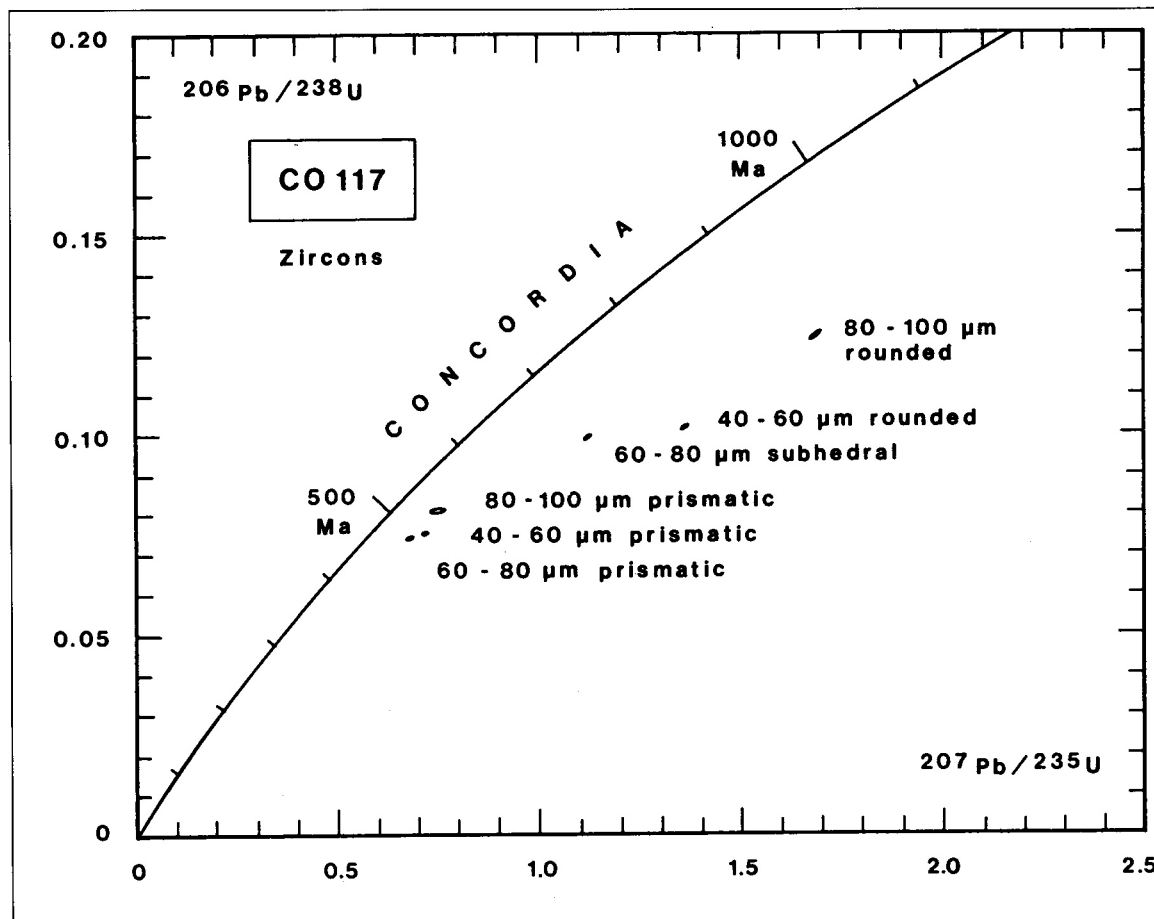


Figure 6.3: Concordia diagram for U-Pb data of various zircon fractions from sample CO117

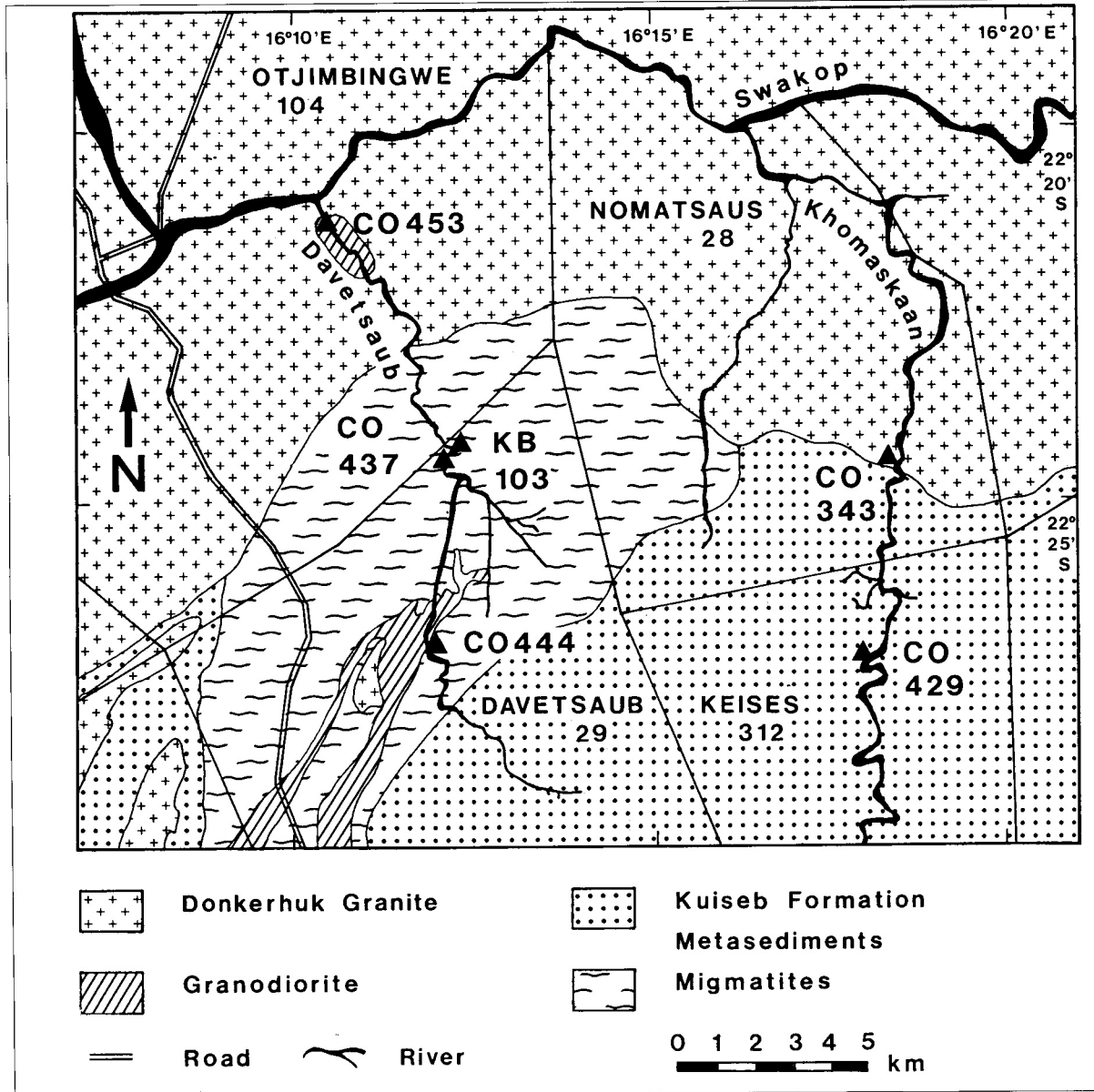


Figure 6.4: Localities of samples used for U-Pb monazite analysis

Kuseb Formation pelite CO429 show slightly discordant data points with apparent ages, between 513 to 518 Ma. Monazites from the suite of granitic rocks CO343, CO444 and CO453 seem to be more concordant, showing relatively younger apparent ages between 500 and 510 Ma. The monazite fraction from the Donkerhuk Granite CO343 yields, within limits of error ( $2\delta$ ), a concordant age of  $505 \pm 4$  Ma.

#### 6.3.4 Interpretation of data

As shown above, monazites from migmatites and granites form two clusters in the concordia diagram. A geologically relevant age difference is, however, not directly evident from these data because some of the monazite fractions appear to plot slightly above the concordia curve. If systematic errors affecting all analyses (e.g. the uncertainty of the U-Pb ratio in the spike solution) are neglected, it becomes even more evident that monazites from the migmatite samples plot systematically above the concordia curve. The other monazites

apparently yield more concordant data. There are two ways to explain the different behaviour of data points in the concordia diagram: a) predominant incorporation of  $^{230}\text{Th}$  of the U decay series might have caused excess  $^{206}\text{Pb}$  (Schärer, 1984). In this case the geological ages would be approximated by the  $^{207}\text{Pb}/^{235}\text{U}$  apparent ages; b) although the initial lead incorporated during crystallisation is a subordinate component of monazites (d. Table 6.1), the isotopic composition of this initial lead has some influence on the position of the data points. Calculation of the initial lead composition using a higher model age shifts the overconcordant data points towards the concordia curve, but is of minor importance in the case of high  $^{206}\text{Pb}/^{204}\text{Pb}$  ratios, as it cannot account for a high degree of discordance. In this case the geological ages would tend towards the  $^{206}\text{Pb}/^{238}\text{U}$  apparent ages.

Depending on the cause of the slight discordance of the monazite data, the time interval between the anatexis of the metasediments and the subsequent intrusion of granitic melts may vary by some million years, but a discontinuity of events

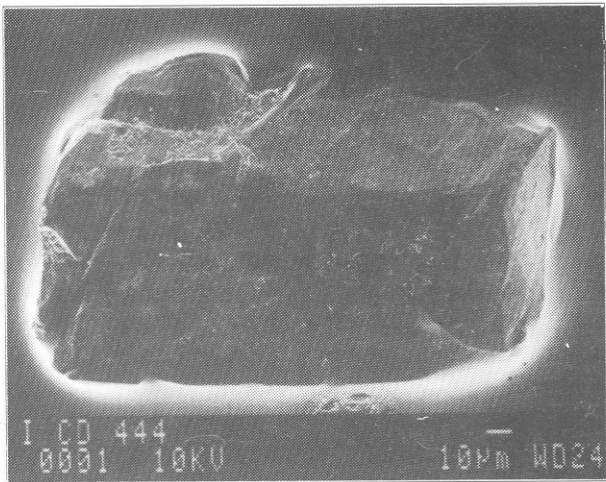


Figure 6.5a

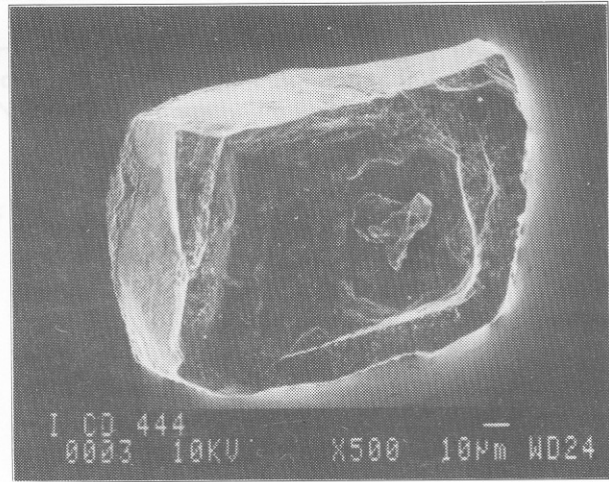


Figure 6.5b

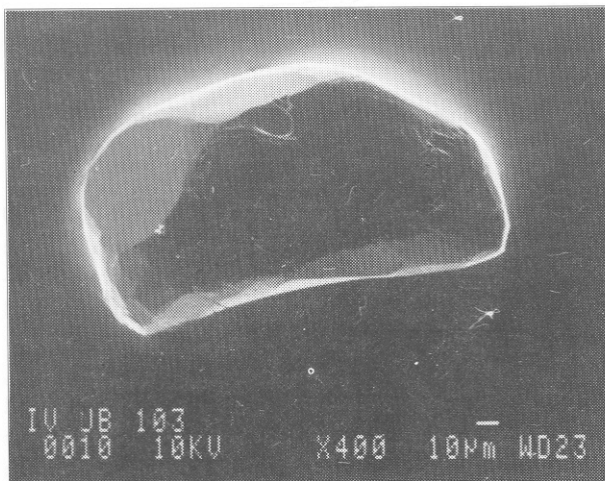


Figure 6.5c

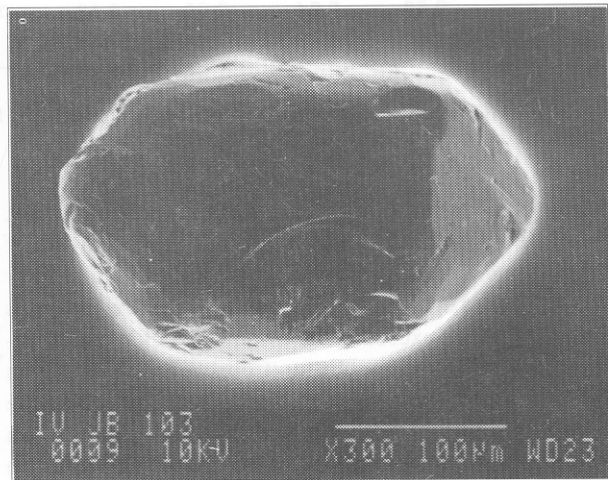


Figure 6.5d

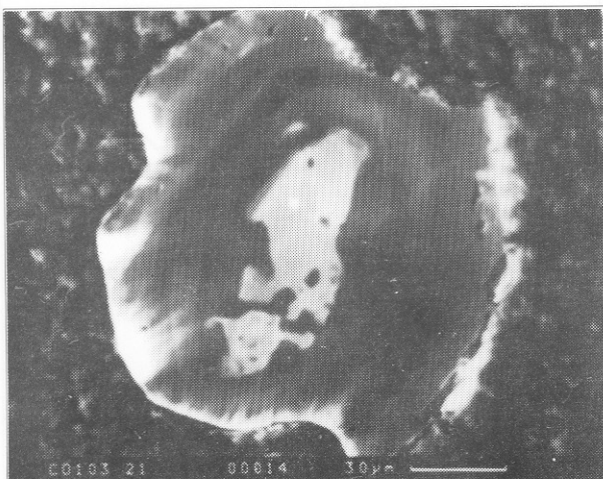


Figure 6.5e

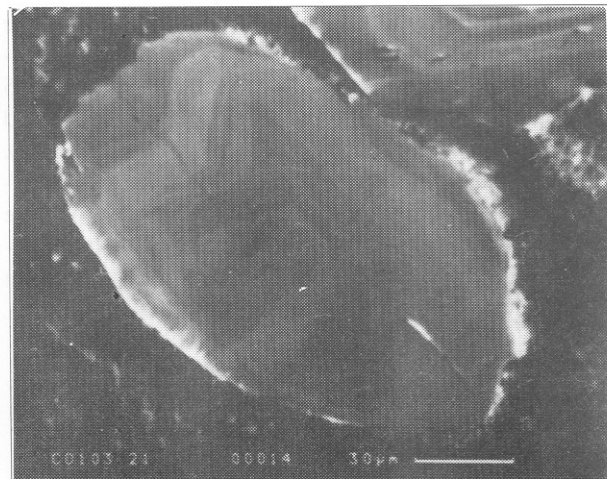


Figure 6.5f

**Figure 6.5:**

- a) - d) SEM images of selected monazite grains.
- a) and b) euhedral tabular monazite crystals, sample CO444;
- c) and d) euhedral monazite crystals, sample KB103;
- e) and f) cathodoluminescence images of polished monazite grains showing an internal zonation of the crystals, sample KB103

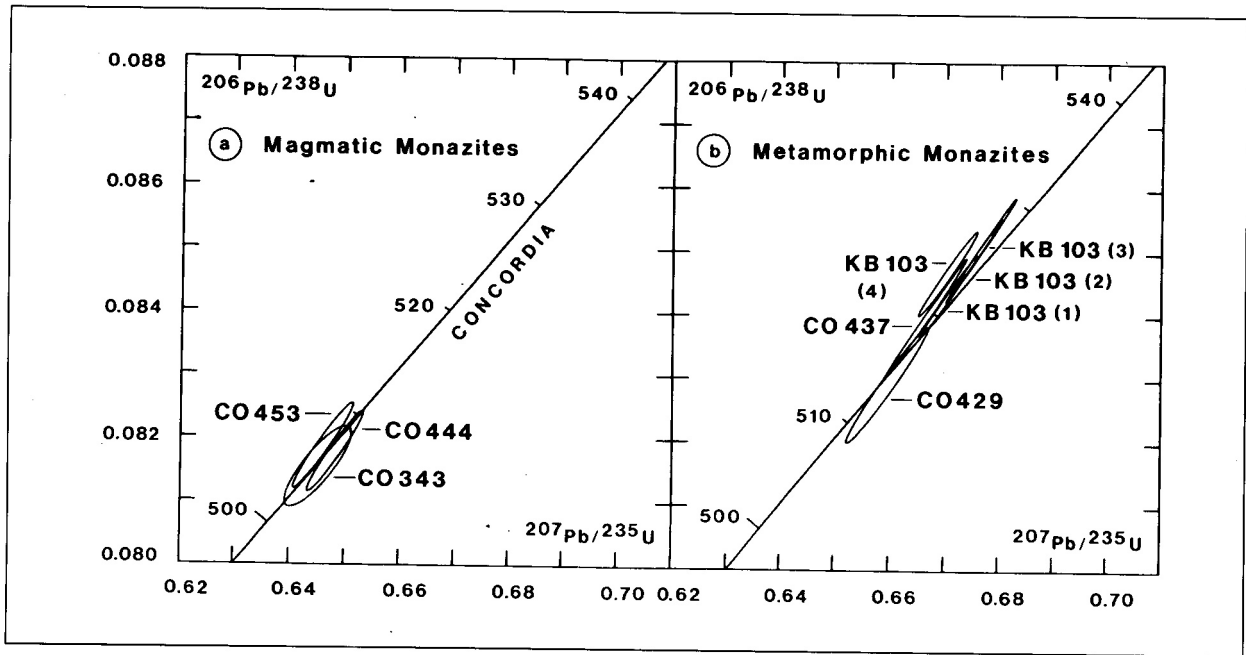


Figure 6.6: Concordia diagram for the U-Pb monazite data for a) magmatic monazites, and b) metamorphic monazites

is constrained. In the case of the granitic samples, it is believed that the U-Pb monazite ages reflect the time of crystallisation subsequent to the intrusion into the country rocks. This is because the temperature of the intruding melts should not have exceeded the assumed blocking temperature for lead in monazites by far (Copeland *et al.*, 1988). In contrast, the anatectic event providing an upper limit for the regional metamorphic peak is less well constrained, but its age must fall within the range of the apparent ages for the migmatite monazites. The temperature peak of metamorphism may further be approximated by the monazite data for the Kuiseb Formation metapelite sample.

In conclusion, the sequence of events reflected by the U-Pb monazite data is in accordance with the field relationships. These confirm the anatectic event in the range of 515 to 525 Ma, postdated by the granitic intrusions around 505 Ma and a contemporaneous weak deformation ( $S_4$ ). These results differ slightly from published data (e.g. Blaxland *et al.*, 1979). In the case of the Otjimbingwe syenite one could speculate upon a reinterpretation of the hornblende-whole-rock age of Haack *et al.* (1988) as a resetting of the Rb-Sr system during the regional metamorphic overprint.

#### 6.4 RB-SR ANALYSES OF MINERAL FRACTIONS FROM THE DONKERHUK GRANITE

Rb-Sr isotope analyses were carried out of selected mineral fractions from sample CO343 of the Donkerhuk Granite. The sample site is located at the southern margin of a massive granite body on the farm Nomatsaus 29. The white granite comprises porphyric K-feldspars and primary muscovite. Blaxland *et al.* (1979) investigated samples of the Donkerhuk Granite from the same area; their analytical data have already been discussed above.

In this study, two sieve fractions of muscovite (125-250 and 250-500  $\mu\text{m}$ ), one biotite fraction (160-250  $\mu\text{m}$ ) and one apatite fraction (250  $\mu\text{m}$ ) as well as the whole-rock composition of the granite were analysed. Results are presented in Figure 6.7 and Table A. 14.

Ages were calculated from mica-whole-rock pairs, yielding an age of  $492 \pm 10$  Ma for the biotite fraction and  $506 \pm 7$  Ma for the muscovites. Within limits of error, the Rb-Sr muscovite-whole-rock age is concordant with the U-Pb monazite age of  $505 \pm 4$  Ma obtained from the same sample. The analysed

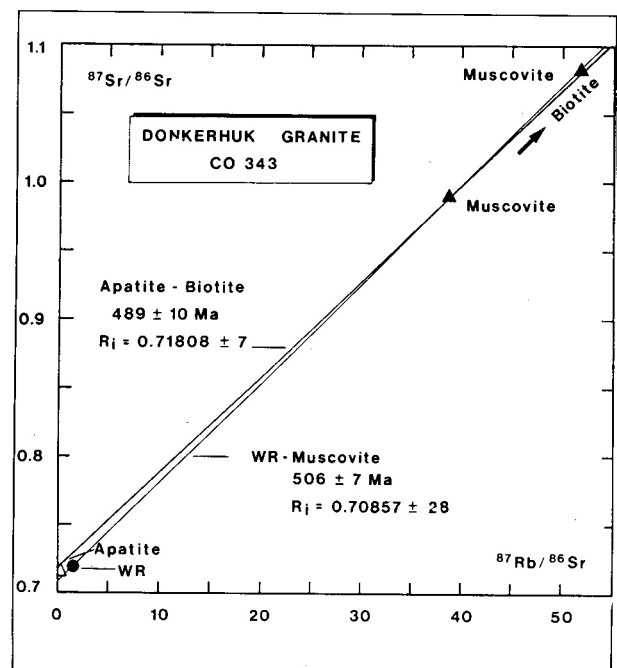
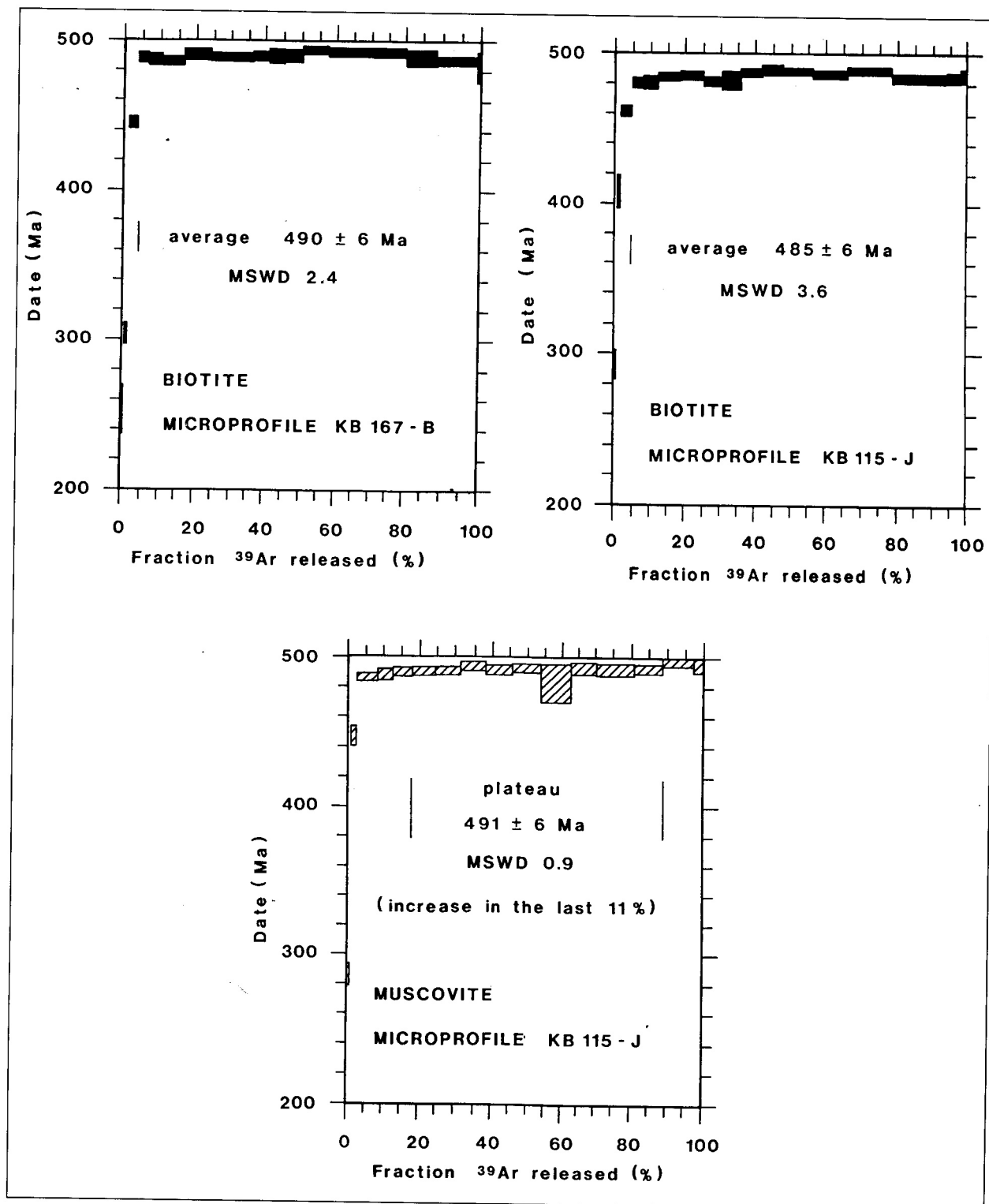


Figure 6.7: Isochron diagram showing whole-rock and mineral data of sample CO343 from the Donkerhuk Granite



**Figure 6.8:** Spectra of  $^{39}\text{Ar}/^{40}\text{Ar}$  dates from a) biotite of rock profile KB167, slab B;  
 b) biotite of rock profile KB115, slab J;  
 c) muscovite of rock profile KB115, slab J

apatite fraction shows an isotopic composition of  $0.718111 \pm 0.000035$  which is slightly lower in radiogenic Sr than the respective bulk rock composition ( $0.718775 \pm 0.000056$ ). A regression over apatite and biotite yields an age of  $489 \pm 10$  Ma, which might reflect a prolonged isotope exchange between biotite and apatite during cooling of the pluton.

The biotite and muscovite ages of the present study agree, within limits of error, with the data of Blaxland *et al.* (1979).

The calculated initial ratios fall well into the range of initial ratios given by these authors for different parts of the Donkerhuk pluton. Since there is no evidence for a metamorphic event postdating the intrusion of the Donkerhuk Granite, the obtained Rb-Sr mineral data might be interpreted to reflect stages of cooling. For the muscovite fractions it is not possible to differentiate between crystallisation and cooling age within limits of error.

### 6.5 K-AR AND AR-AR ANALYSES OF MICAS FROM THE INVESTIGATED ROCK PROFILES

K-Ar and  $^{40}\text{Ar}$ - $^{39}\text{Ar}$  analyses were carried out on 6 selected mica fractions from samples which had already been analysed for their Rb-Sr systematics. The intention was to compare the response of the different isotopic systems in the micas to metamorphic processes connected with the late stages of metamorphism. K-Ar and  $^{40}\text{Ar}$ - $^{39}\text{Ar}$  determinations on mineral fractions have previously been reported from a variety of Damaran rocks, including the Kuiseb Formation and the Donkerhuk Granite (Clifford, 1967; Haack and Hoffer, 1976; Clauer and Kröner, 1979; Ahrendt *et al.*, 1983; Hawkesworth *et al.*, 1983). Summarised, the data range between 520 and 420 Ma, and generally have been interpreted by the authors as reflecting cooling below a 300°C isotherm.

Both K-Ar and  $^{40}\text{Ar}$ - $^{39}\text{Ar}$  determinations were carried out in the cases of an adequate sample size. The following mineral separates were analysed:

- KB167, slab B: one biotite fraction (60-180  $\mu\text{m}$ ), K-Ar and  $^{40}\text{Ar}$ - $^{39}\text{Ar}$  determinations,
- CO117: one biotite fraction (80-160  $\mu\text{m}$ ), K-Ar determination,
- KB307, slab F: one muscovite fraction (125-250  $\mu\text{m}$ ), K-Ar determination.
- KB115, slab J: one biotite fraction (60-180  $\mu\text{m}$ ), K-Ar and  $^{40}\text{Ar}$ - $^{39}\text{Ar}$  determination and one muscovite fraction (60-180  $\mu\text{m}$ ),  $^{39}\text{Ar}$ - $^{40}\text{Ar}$  determination.

Analytical data from  $^{40}\text{Ar}$ - $^{39}\text{Ar}$  analyses are shown in Figure 6.8 and Tables A.18-A.20. The following K-Ar age data were obtained from the mica fractions: KB167-B biotites  $483 \pm 5$  Ma. CO117 biotites  $490 \pm 5$  Ma, KB307-F muscovites  $491 \pm 5$  Ma and KB115-J biotites  $491 \pm 5$  Ma.  $^{39}\text{Ar}$ - $^{40}\text{Ar}$  determinations yielded  $490 \pm 6$  Ma for the KB167-B biotites,  $485 \pm 6$  Ma for the KB115-J biotites and  $491 \pm 6$  Ma for the KB115-J

muscovites. The term "average" used for the biotites of samples KB167-B and KB115-J applies to the fact that no plateau was reached as in the case of the muscovite fraction from sample KB115-1. Nevertheless, the data obtained from  $^{40}\text{Ar}$ - $^{39}\text{Ar}$  and conventional K-Ar determinations are concordant, within limits of error, with the Rb-Sr data calculated from whole-rock-mineral pairs of the same samples. For the biotite fraction from rock profile KB167, K-Ar and  $^{40}\text{Ar}$ - $^{39}\text{Ar}$  data of  $483 \pm 5$  Ma and  $490 \pm 6$  Ma were determined which overlap within limits of error. Rb-Sr analyses from the same sample yielded whole-rock-biotite ages of  $491 \pm 10$  Ma (slab B) and  $483 \pm 10$  Ma (slab C). Since it is unlikely that the micas in adjacent slabs of the rock profile either closed or rejuvenated at different times, the difference in the data is assigned to analytical rather than geological uncertainties.

The range in K-Ar data from 483 to 491 Ma might be explained solely by analytical uncertainties and there is apparently no regional variation in K-Ar ages along the study traverse. Moreover, the narrow range of the K-Ar data compares well with the quite uniform Rb-Sr ages as determined from whole-rock-mineral pairs (cf. Chapter 5). Regarding individual samples, K-Ar data and Rb-Sr mineral ages for all analysed biotite fractions overlap within limits of error. For the muscovites no comparison can be made for Rb-Sr and K-Ar data, but muscovite and biotite fractions yielded very similar K-Ar ages. According to the theory of cooling ages, muscovite will close at higher temperatures with respect to radiogenic Sr, but at about the same temperature as biotite with regard to the K-Ar system (e.g. Jäger, 1979). The K-Ar data which fit into the regional distribution of previously determined K-Ar data (Haack, 1983), would also be in accordance with the theory of blocking temperatures. Compared to the U-Pb monazite data which were interpreted to bracket the peak of regional metamorphism between 505 and 520 Ma in the area under consideration, the K-Ar as well as the Rb-Sr mineral results date a retrograde stage on the metamorphic P-T path.

## 7. EFFECTS OF PAN-AFRICAN METAMORPHISM ON THE ISOTOPE SYSTEMATICS OF THE KUISEB-FORMATION - DISCUSSION AND CONCLUSIONS

A final discussion of the isotope characteristics of the Kuiseb Formation metasediments has to consider the two principle aspects emphasised in the objectives of the isotope analyses (cf. Chapter 4). One problem is regional in character and concerns with the timing of metamorphic and magmatic processes in the northwestern Khomas Trough during the Damara orogeny. The other problem is the principle behaviour of the Rb-Sr isotope system during the metamorphic evolution of the Kuiseb Formation and the applicability of the Rb-Sr small-domain method to the dating of metamorphic events. This chapter will present a synopsis of the data obtained from the different isotope systems and a comparison with previous investigations.

### 7.1 TIMING OF METAMORPHISM AND GRANITE INTRUSION AS DEDUCED FROM THIS STUDY

The thermal evolution of the Damara Orogen has been discussed by a number of authors. The problem of polymetamorphic development is still a matter of debate, although no conclusive evidence has yet been found to prove a multi-stage development. Models concerning particularly the thermal evolution and the cooling history of the Khomas Trough were proposed by Haack (1983), Behr *et al.* (1983) and Kasch (1983c). The models of Haack (1983) and Behr *et al.* (1983) assume a single-phase metamorphic development. In contrast, Kasch (1983c) proposed a two-stage metamor-

phic development of the Khomas Trough. Based on micro-textural features, he proposed one syn- and one post-tectonic metamorphic peak of comparable P-T conditions, related both metamorphic phases to the continental collision of the Congo and Kalahari Cratons. Haack (1983) published a cooling model for the rocks exposed in the Southern Zone of the Damara Orogen. Figure 7.1 a (from Haack, 1983) shows the presently exposed erosion level in relation to isotherms at the time of metamorphism; in Figure 7.1 b shows the proposed

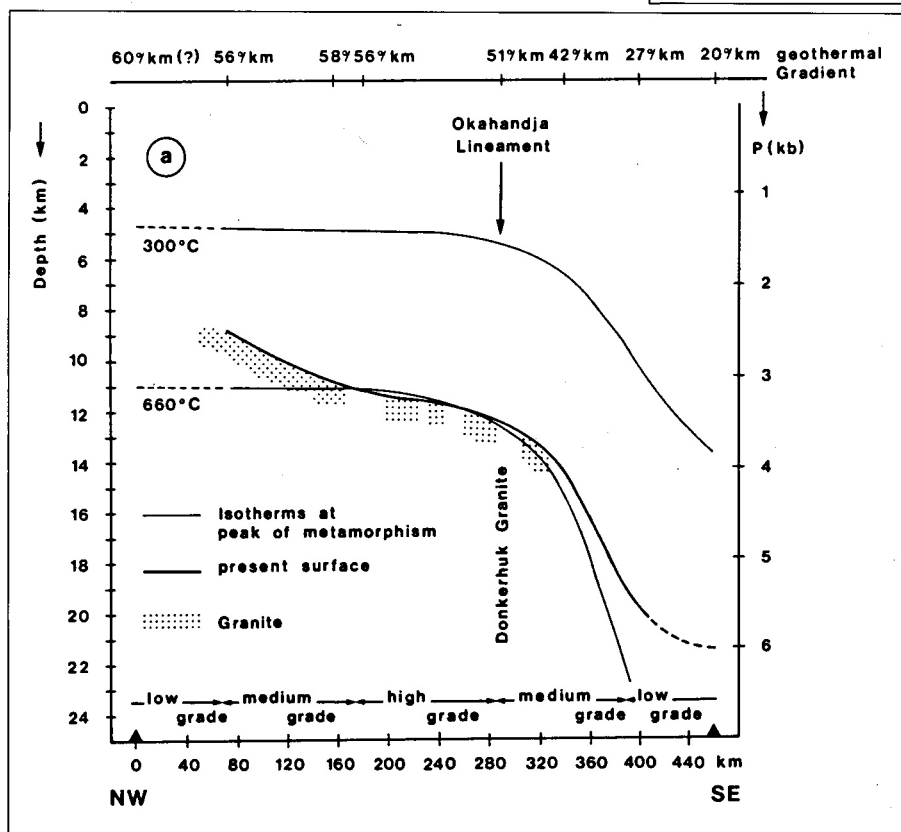
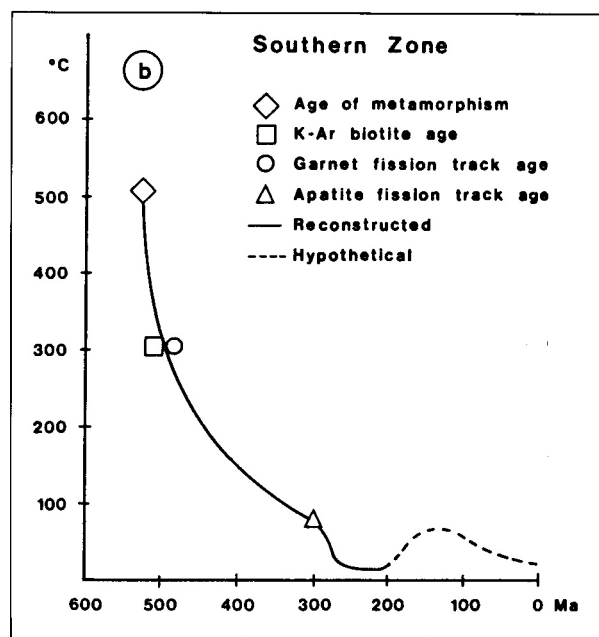


**Figure 7.1:** a) (left): Currently exposed erosion level of the Damara Orogen in relation to isotherms at the peak of metamorphism on a profile perpendicular to the Okahandja Lineament (from Haack, 1983). b) (above): Cooling curve of the present surface for the Southern Zone (from Haack, 1983); the dashed line corresponds to the Karoo-age burial of the Khomas Trough

cooling curve for the Southern Zone of the Damara Orogen. According to Haack, cooling proceeded rapidly within the Southern Zone.

Behr *et al.* (1983) proposed P-T-t paths for the Khomas Trough (Fig. 7.2) based on fluid inclusion data and incorporated data from Hoffer (1977), and various radiometric data (cf. Chapter I). They suggested that different P-T regimes had governed the metamorphic development of the northern and southern Khomas Trough (Fig. 7.2), and assumed that the pressure peak of metamorphism had been reached prior to 550 Ma, while the temperature peak occurred throughout the Khomas Trough at about 530 Ma.

During this study, the conditions of metamorphism as well as its relative and absolute timing have been discussed in detail. The following structural and textural evidence was put forward to constrain the relative timing and the nature of metamorphism:

- Micro-textural features confirm that the temperature peak of metamorphism outlasted the main regional deformation which includes the D<sub>1</sub> to D<sub>3</sub> phases of deformation and the pressure peak of metamorphism. The timing of metamorphic banding formation was inferred as syn-F<sub>2</sub>. The element distribution patterns of Rb and Sr within the investigated rock profiles suggest that quartz pressure solution was the dominant mechanism during metamorphic banding formation within the metasediments. In contrast, Behr *et al.*

(1983) favoured a dewatering hypothesis for the genesis of the P-Q-fabrics.

- The conditions of metamorphism were inferred at a minimum of 550°C/5-8 kb for the southern Khomas Trough and reached between 650 and 700°C at a minimum pressure of 3.5 kb in the northern part. The rocks of the Khomas Trough do not, however, reflect a continuous series of rising isotherms as proposed by Hoffer (1977). Through the presence of andalusite, a low-pressure zone might be mapped in the centre of the Khomas Trough which is due to differential uplift after the peak of metamorphism.

- The formation of trondhjemitic partial melts within the metasediments in the northernmost Khomas Trough was classified by means of structural relationships as a regional metamorphic event which is postdated by the intrusion of granitic melts in the area of the Okahandja Lineament.

- So far no relics of an earlier high-pressure metamorphism have been recorded nor is there any conclusive evidence favouring a polymetamorphic development of the investigated metasediments as suggested by Kasch (1983c).

With regard to the overall tectonic setting of the Khomas Trough and the apparent absence of a high-pressure metamorphism, the metamorphism of the Kuiseb Formation within the Khomas Trough is related to crustal thickening and subsequent thermal relaxation caused by the collision of the Congo and the Kalahari Cratons during late Pan-African

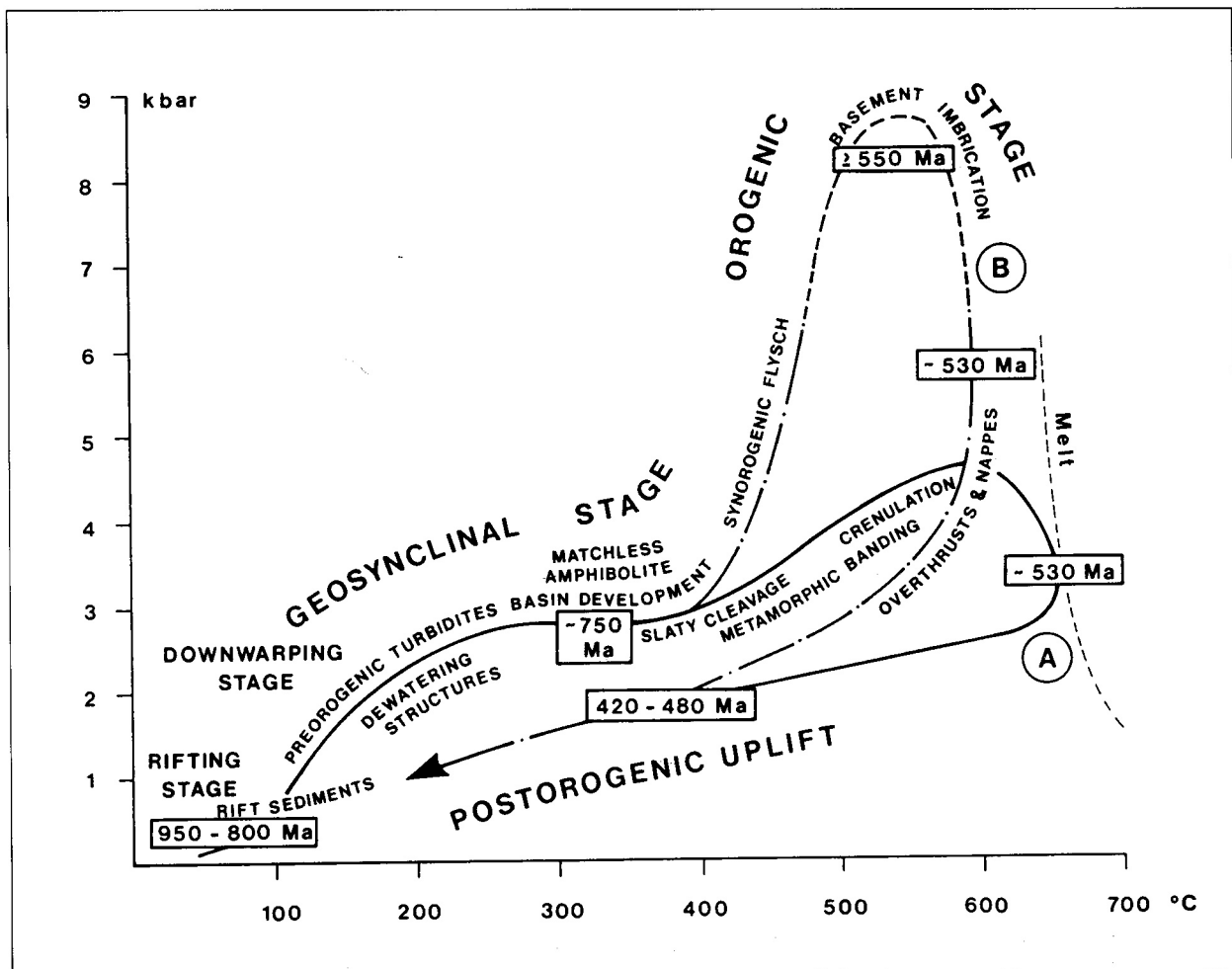


Figure 7.2: P-T-t paths for the southern (A) and the northern (B) Khomas Trough (from Behr *et al.*, 1983)

times.

To constrain the absolute timing of metamorphism, U-Pb monazite analyses were carried out on migmatite samples, a pelite sample from the Kuiseb Formation, as well on samples of Donkerhuk Granite and associated rocks. The data imply that the intrusion of the Donkerhuk Granite and other investigated granitic rocks occurred after 510 Ma. A concordant age of  $505 \pm 4$  Ma was obtained from the Donkerhuk Granite. The emplacement of the granitic rocks terminates the T peak of metamorphism and the main deformation in the Khomas Trough. In accordance with the structural relationships, the U-Pb data from the migmatites and the pelite sample form one cluster in the concordia diagram with  $^{207}\text{Pb}/^{235}\text{U}$  apparent ages ranging between 515 and 525 Ma. The distribution of the data suggest that the anatectic event belongs to the regional metamorphism. These U-Pb monazite data are interpreted to mark the temperature peak of regional metamorphism in the investigated area.

Compared to the U-Pb monazite age of the Donkerhuk Granite, the Rb-Sr muscovite-whole-rock age of  $506 \pm 7$  Ma obtained from the same sample is concordant within limits of error. The biotite-whole-rock age of  $492 \pm 10$  Ma from the Donkerhuk Granite is compatible with the Rb-Sr and K-Ar biotite ages from the metasediments as well as with previously published data of Blaxland *et al.* (1979). In this study, however, the emplacement and crystallisation of the granite is inferred at about 505 Ma.

Figure 7.3 shows a compilation of most geochronological data obtained from this study. The diagram includes Rb-Sr small-domain whole-rock data, biotite-whole-rock data, plagioclase-whole-rock data and K-Ar/Ar-Ar biotite and muscovite data from the investigated rock profiles as well as U-Pb monazite data. Uncertainties are shown as 2 b errors for the Rb-Sr and K-Ar/Ar-Ar data. The spread of the apparent ages for the monazite data is indicated.

Compared to the U-Pb monazite ages, all of the Rb-Sr and the K-Ar/Ar-Ar biotite, muscovite and plagioclase data clearly fall below the supposed peak of metamorphism. Taking the assigned uncertainties into account, the data mostly range between 475 and 505 Ma. The calculated Rb-Sr biotite-whole-rock ages and K-Ar biotite ages from the metasediments as well as those from the Donkerhuk Granite are characterised by a pronounced uniformity despite the differences in the structural and metamorphic overprint of the samples. This points towards a regional event or regionally significant processes responsible for the isotopic equilibration of the minerals after the peak of regional metamorphism. As discussed in Chapter 5.8, the data may either reflect the regional cooling of the rocks (conventionally below a blocking temperature of 300-400°C) or mark the time of a late deformation which led to a partial recrystallization of the minerals and the resetting of the isotopic systems. It is not possible, however, to prove either interpretation. Nevertheless, the Rb-Sr and K-Ar biotite data are consistent with the previously published biotite age data of metamorphic as well as magmatic rocks from the southern Damara Orogen (Blaxland *et al.*, 1979; Haack, 1983; Hawkesworth *et al.*, 1983).

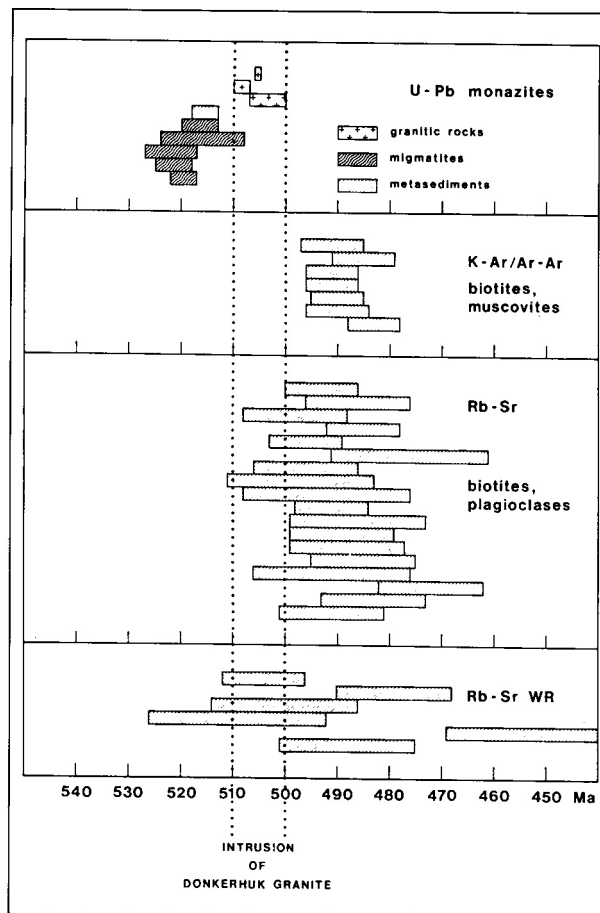


**Figure 7.3:** Compilation of age data obtained in this study. Length of bars represents the uncertainty obtained for the Rb-Sr and K-Ar/Ar-Ar data; length of bars for the U-Pb data corresponds to the spread of the apparent ages

In contrast to the mineral data, the Rb-Sr isotope systems within contiguous slabs of the six rock profiles apparently do not follow a common principle of isotopic re-equilibration. The apparent ages calculated by isochron modelling of whole-rock data from contiguous slabs of the rock profiles vary considerably between the inferred temperature peak of regional metamorphism and the Rb-Sr and K-Ar biotite ages. The data clearly show that it was not possible to date the formation of prograde features like the metamorphic banding cleavage using this method. From the relation of whole-rock and mineral isotopic compositions within the samples KB117 and KB115, it could further be shown that the apparent whole-rock isochrons of the two samples are not geologically relevant, since the analysed biotite and plagioclase fractions do not reflect the resetting of the whole-rock systems. The good alignment of the whole-rock data is interpreted as reflecting spurious isochrons. In accordance with the method of dating through isotope disequilibrium distributions (Bachmann and Grauert, 1986), the whole-rock data of the other four rock profiles might be interpreted as representing the time of partial isotope homogenisation during the late stages of Pan-African metamorphism. The results from samples KB117 and KB115, however, cast doubt on the geological relevance of the other whole-rock data as well.

## 7.2 ASPECTS OF STRONTIUM ISOTOPE HOMOGENISATION IN THE METASEDIMENTS OF THE KUISEB FORMATION IN THE WESTERN KHOMAS TROUGH

The Rb-Sr small-domain analyses of the Kuiseb Formation metasediments have revealed that no complete isotopic homogeneity exists between the contiguous slabs of the investigated rock profiles. The  $^{87}\text{Sr}/^{86}\text{Sr}$  distribution patterns instead show heterogeneities which are not attributed to a later alteration of the isotope ratios. It may be concluded that no complete isotopic homogenisation had been reached on a cm scale during the final stages of metamorphic evolution. The exact mechanisms and processes which led to the partial homogenisation of strontium isotopes and/or the preservation of isotope heterogeneities, however, can only be speculated about.

Generally, the mass transfer during metamorphic reactions as well as the resetting of isotope systems is controlled by diffusional processes. Diffusion is defined as a process in inhomogeneous, multicomponent one-phase systems finally leading to an equilibration of concentration by non-convective fluxes of the components under the action of a chemical potential gradient (Schmalzried, 1981). Diffusion in a crystalline solid occurs by volume diffusion, grain boundary diffusion and/or surface diffusion (Freer, 1981). Volume diffusion is based on lattice defects. Grain boundary and surface diffusion involve line or surface defects. According to Freer (1981), volume diffusion will, in most cases, be the dominant mechanism at high temperatures, whereas grain boundary diffusion will be dominant in fine-grained polycrystalline rocks at low temperatures. If a fluid phase is present, fluid transport rather than true grain boundary diffusion will be the dominant mechanism of transport between the reactant and the product of a metamorphic reaction (Walther and Wood, 1984).

In contrast to the above definitions, the term "self diffusion" describes the mobility of particles without the driving force of a concentration gradient. Self diffusion is therefore particularly dependent on temperature which is applied within the concept of closure temperatures (Dodson, 1976; Purdy and Jäger, 1976).

Diffusional processes may, however, be enhanced by factors other than temperature increase, for instance deformation, metamorphic reactions, the presence of fluids and the recrystallisation of minerals. According to Yund and Tullis (1991), the rate of compositional and isotopic exchange between minerals is significantly enhanced through the contemporaneous deformation of the rock. The authors attribute the enhanced exchange rate to a reduction in grain size (shorter distance for volume diffusion), dissolution and mineral growth through pressure solution, and the migration of grain boundaries during recrystallisation.

A number of experimental studies have investigated the diffusion coefficients of elements or isotopic tracers within synthetic and natural minerals and glasses (compiled by Freer, 1981). Experimentally determined diffusion coefficients for strontium in feldspars (for temperatures above 800°C, Misra and Venkatasubramanian, 1977) would indicate a

cm-scale Sr diffusion in one million years. Empirical studies on the extent of strontium diffusion under metamorphic conditions through isotope analyses of natural samples were undertaken by a number of authors (e.g. Pidgeon and Compston, 1965; Aftalion and Van Breemen, 1980; Springer *et al.*, 1983; Tembusch and Grauert, 1983; Van Breemen and Dallmeyer, 1984; Bachmann, 1985; Bachmann and Grauert, 1986; Buhl, 1987). These studies resulted in various estimates of the extent of Sr diffusion, but in general limited distances of Sr isotope equilibration (cm scale) were reported. Tembusch and Grauert (1983) and Bachmann (1985) estimated time-integrated Sr diffusion coefficients in amphibolite facies gneisses of 0.1-0.3 and 0.2-0.5 cm<sup>2</sup> per million years; Buhl's (1987) analyses yielded up to 3 cm<sup>2</sup> per million years for granulite facies rocks. In contrast to this study, however, most of the previous investigations used polymetamorphic rocks. It has been suggested that self diffusion would be the dominant process during isotope homogenisation in polymetamorphic rocks (Tembusch and Grauert, 1983) which results in mostly small volumes of isotope homogenisation. Isotope equilibration up to several metres based on fluid-rock interaction was reported by Bickle and Chapman (1990). In conclusion, a homogenisation of strontium isotopes at least at cm scale may be expected for the amphibolite facies metasediments of the Kuiseb Formation.

This study, however, showed a) that cm-scale isotope heterogeneities exist within the amphibolite facies metasediments, and b) that apparent "isochron" ages derived from Rb-Sr whole-rock small-domain analyses of metasedimentary rocks can lead to geologically meaningless ages. This casts doubt on the use of the Rb-Sr small-domain method as a tool in dating metamorphic events and on the significance of previous Rb-Sr whole-rock data from metamorphic rocks. The existence of  $^{87}\text{Sr}/^{86}\text{Sr}$  heterogeneities between the plagioclase and the respective whole-rock at the time of the apparent whole-rock equilibration strongly suggests that the computed whole-rock ages obtained from different slabs of a rock profile, cannot denote the timing of an isotope homogenisation event, since the main constituents of the rock are not in isotopic equilibrium with their respective whole-rock at that time. However, the formation of the apparently equilibrated whole-rock isotope distribution patterns is not yet resolved.

In Chapter 5.8 three different models were proposed to explain the phenomenon that in rock profiles KB117 and KB115 no isotopic homogeneity existed between the investigated plagioclases and their respective whole rocks at the time of the apparent resetting of the whole-rock systems. The first model is based on the assumption that no isotope exchange had occurred between the whole-rocks of the individual slabs. In accordance with the previous work on the extent of strontium isotope exchange and experimentally determined diffusion coefficients as discussed above, this hypothesis is unlikely. The second model is based on the assumption that an equilibration between the plagioclases continued, whereas the homogenisation of the plagioclases with their surrounding whole-rocks, i.e. the sum of the other mineral phases, within and between contiguous slabs, had ceased at an earlier time. This model would imply that plagioclase closed at a later stage than biotite, which, however, has

not been observed in previous studies. A third possible explanation is the open system behaviour of the rock. It may be assumed that the interaction of a rock with a fluid phase will lead to an alteration of the  $^{87}\text{Sr}/^{86}\text{Sr}$  ratios or the Rb and Sr element concentrations, e.g. through the addition of Sr in an interstitial phase. The minerals would remain closed systems.

The evolution of the investigated amphibolite facies metamorphic rocks will now be discussed with regard to processes potentially leading to isotopic homogenisation.

Considering the metamorphic overprint of the investigated pelites and greywackes, a different potential for isotope exchange within the whole-rock isotope systems may be assigned to the different stages of diagenesis and metamorphism. The most profound and effective exchange of Rb and Sr isotopes, in accordance with changes in mineralogy, may be expected for reactions involving the decomposition and/or formation of Rb- and Sr-bearing rock-forming mineral phases, as well as reactions releasing significant amounts of water. Many such reactions occur during low-grade metamorphism, e.g. the transformation from clay minerals to muscovite and chlorite and the subsequent reaction from muscovite and chlorite to biotite. An example of the importance of these reactions for isotope exchange was reported by Graham and Korsch (1989) who obtained Rb-Sr resetting ages from a turbidite sequence in the accretionary wedge of the Torlesse Complex, New Zealand. The Rb-Sr and K-Ar systems of the sediments there had been reset some 15-20 Ma after deposition in the course of prograde mineral transformations (the conversion of clay minerals to white mica and chlorite and the albitisation of feldspars) as well as a high fluid flux within the accretionary wedge. The Sr isotopic homogenisation is reported to extend over several cubic metres. In general, high fluid fluxes occur within accretionary

wedges, which provide an excellent medium through which Sr isotope homogenisation may be accomplished. Mineral reactions which were inferred to have taken place at elevated P-T conditions mostly involve the exchange of Fe and Mg and the formation of isolated porphyroblasts within the rock. These reactions may be assumed to have less bearing on the Rb-Sr isotope system of the total rock.

It may be inferred that strontium isotope homogenisation during prograde metamorphism results from a combination of a continuous, temperature induced self diffusion and, more episodically, increases in the rate and extent of isotope exchange due to deformational processes associated with fluid circulation, metamorphic reactions and dynamic recrystallisation of minerals. The change in the physical conditions of metamorphism along with the change in the mineralogy of the rocks might result in a change in the mechanisms (grain boundary diffusion, fluid transport, self-diffusion), rate and extent of isotope homogenisation. It might be inferred that self diffusion would become the most important mechanism of isotope homogenisation when the main deformation and also most mineral reactions would have ceased. The differences in the  $^{87}\text{Rb}/^{86}\text{Sr}$  ratios within compositionally different layers of the samples would, however, permanently enforce the development of gradients in the  $^{87}\text{Sr}/^{86}\text{Sr}$  between these layers. This process operates against the diffusional processes which are responsible for a homogenisation of the isotopes. The existence of strontium isotope heterogeneities within the isotope distribution patterns of the investigated rock profiles for the time of the apparent whole-rock ages, suggests that the extent of strontium self diffusion during the final stages of the Pan-African metamorphism did not exceed a few centimetres.



## 8. REFERENCES

- Aftalion, M. and Van Breemen, O. 1980. U-Pb zircon, monazite and Rb-Sr whole rock systematics of granitic gneiss and psammitic to semi-pelitic host gneiss from Glenfinnan, Northwestern Scotland. *Contr. Miner. Petrol.*, **72**, 87-98.
- Ahrendt, H., Behr, H.J., Clauer, N., Porada, H. and Weber, K. 1983. K-Ar age determinations from the northern Damara branch and their implications for the structural and metamorphic evolution of the Damara Orogen, South West Africa/Namibia. *Spec. Publ. geol. Soc. S. Afr.*, **11**, 299-306.
- Allègre, C.J., Albarede, F., Grünenfelder, M. and Köppel, V. 1974.  $^{238}\text{U}/^{206}\text{Pb}$ - $^{235}\text{Pb}/^{207}\text{Pb}$ - $^{232}\text{Th}/^{208}\text{Pb}$  zircon geochronology in alpine and non-alpine environment. *Contr. Miner. Petrol.*, **43**, 163-194.
- Ashworth, J.R. 1985. *Migmatites*. Blackie, Glasgow, 302 pp.
- Bachmann, G. 1985. *Untersuchungen zum Strontium-Isotopenaustausch in polymetamorphen Bändergneisen Nordwest-Argentiniens*. Diss. (unpubl.), Universität Münster, 162 p.
- Bachmann, G. and Grauert, B. 1986. Altersbestimmungen mit  $^{87}\text{Sr}/^{86}\text{Sr}$ -Ungleichgewichten. *Fortschr. Min.*, **64**, Bh. 1, 12.
- Barnes, S.-J. and Sawyer, E.W. 1980. An alternative model for the Damara Mobile Belt. Ocean crust subduction and continental convergence. *Precamb. Res.*, **13**, 297-336.
- Bates, R.L. and Jackson, J.A. 1987. *Glossary of geology*. American Geological Institute, Alexandria, 788 pp.
- Bayly, B. 1968. *Introduction to petrology*. Prentice Hall, Englewood Cliffs, N.J., 371 pp.
- Beach, A. 1977. Vein arrays, hydraulic fractures and pressure-solution structures in a deformed flysch sequence, S.W. England. *Tectonophysics*, **40**, 201-225.
- Beach, A. 1979. Pressure solution as a metamorphic process in deformed terrigenous sedimentary rocks. *Lithos*, **12**, 51-58.
- Beach, A. 1982. Chemical processes in deformation at low metamorphic grades. Pressure solution and hydraulic fracturing. *Episodes*, **4**, 22-25.
- Behr, H.-J., Horn, E.E. and Porada, H. 1983. Fluid inclusions and genetic aspects of the Damara Orogen, 611-654. In: Martin, H. and Eder, E.W., Eds, *Intra-continental Fold Belts - Case studies in the Variscan Belt of Europe and the Damara Belt in Namibia*. Springer, Berlin, 945 pp.
- Berman, R.G. 1988. Internally consistent thermodynamic data for minerals in the system  $\text{Na}_2\text{O}$ - $\text{K}_2\text{O}$ - $\text{CaO}$ - $\text{MgO}$ - $\text{FeO}$ - $\text{Fe}_2\text{O}_3$ - $\text{Al}_2\text{O}_3$ - $\text{SiO}_2$ - $\text{TiO}_2$ - $\text{H}_2\text{O}$ - $\text{CO}_2$ . *J. Petrol.*, **29**, 445-522.
- Berman, R.G., Brown, T.H. and Greenwood, H.J. (1985). An internally consistent thermodynamic data base for minerals in the system  $\text{K}_2\text{O}$ - $\text{Na}_2\text{O}$ - $\text{CaO}$ - $\text{MgO}$ - $\text{FeO}$ - $\text{Fe}_2\text{O}_3$ - $\text{Al}_2\text{O}_3$ - $\text{SiO}_2$ - $\text{TiO}_2$ - $\text{H}_2\text{O}$ - $\text{CO}_2$ . *At. Energy Can. Techn. Rep.*, **377**, 1-62.
- Bickle, M.J. and Chapman, H.J. 1990. Strontium and oxygen isotope decoupling in the Hercynian Trois Seigneurs Massif, Pyrenees: evidence for fluid circulation in a brittle regime. *Contr. Miner. Petrol.*, **104**, 332-347.
- Black, L.P. 1987. Recent Pb loss in zircon: a natural or laboratory-induced phenomenon? *Chem. Geol. (Isotope Geoscience Section)*, **65**, 25-33.
- Black, L.P., Fitzgerald, J.D. and Harley, S.L. 1984. Pb isotopic composition, colour, and microstructure of monazites from a polymetamorphic rock in Antarctica. *Contr. Miner. Petrol.*, **85**, 141-148.
- Blaine, J.L. 1977. Tectonic evolution of the Waldau Ridge structure and the Okahandja Lineament in part of the Central Damara Orogen, west of Okahandja, South West Africa. *Bull. Precamb. Res. Unit, Univ. Cape Town*, **21**, 99 pp.
- Blaxland, A., Gohn, E., Haack, U. and Hoffer, E. (1979). Rb/Sr ages of late-tectonic granites in the Damara Orogen, Southwest Africa/Namibia. *Neues Jb. Miner. Mh.*, **11**, 498-508.
- Bouma, A.H. 1962. *Sedimentology of some flysch deposits: a graphic approach to facies interpretation*. Elsevier, Amsterdam, 168 pp.
- Breitkopf, J.H. and Maiden, K.J. 1988. Tectonic setting of the Matchless pyritic copper deposits, Namibia. *Econ. Geol.*, **83**, 710-723.
- Brereton, N.R. 1970. Corrections for interfering isotopes in the  $^{40}\text{Ar}/^{39}\text{Ar}$  dating method. *Earth Planet. Sci. Lett.*, **8**, 427-433.
- Briqueu, L., Lancelot, J.P., Valois, J.P. and Walgenwitz, F. 1980. Géochronologie U-Pb et genèse d'un type de minéralisation uranifère: les alaskites de Goanikontes (Namibie) et leur encaissant. *Bull. Cent. Réch. Explor. - Prod., Elf-Aquitaine*, **4**, 759-811.
- Bröcker, M., Kreuzer, H., Matthews, A. and Okrusch, M. (in press).  $^{40}\text{Ar}/^{39}\text{Ar}$  and oxygen isotope studies of polymetamorphism from Tinos Island, Cycladic blue-shist belt, Greece. *J. met. Geol.*
- Buhl, D. 1987. *U-Pb- und Rb-Sr-Altersbestimmungen und Untersuchungen zum Strontiumisotopenaustausch an Granuliten Südiindiens*. Dissertation (unpubl.), Universität Münster.
- Burger, A.J., Clifford, T.N. and Miller, R.McG. 1976. Zircon U-Pb ages of the Franzfontein Granitic Suite, northern South West Africa. *Precamb. Res.*, **3**, 415-431.
- Carmichael, D.M. 1969. On the mechanism of prograde metamorphic reactions in quartz-bearing pelitic rocks. *Contr. Miner. Petrol.*, **20**, 244-267.
- Carmichael, D.M. 1970. Intersecting isograds in the Whetstone Lake Area, Ontario. *J. Petrol.*, **11**, 147-181.
- Chatterjee, N.D. and Johannes, W. 1974. Thermal stability and standard thermodynamic properties of synthetic 2M<sub>1</sub>-muscovite,  $\text{KAl}_2[\text{AlSi}_3\text{O}_{10}(\text{OH})_2]$ . *Contr. Miner. Petrol.*, **48**, 89-114.

- Chopin, C. and Maluski, H. 1980.  $^{40}\text{Ar}$ - $^{39}\text{Ar}$  dating of high pressure metamorphic micas from the Gran Paradiso Area (Western Alps): Evidence against the blocking temperature concept. *Contr. Miner. Petrol.*, **74**, 109-122.
- Clauer, N. and Kröner, A. 1979. Strontium and argon isotopic homogenization of pelitic sediments during low-grade regional metamorphism: the Pan-African Upper Damara Sequence of northern Namibia (SWA). *Earth. Planet. Sci. Lett.*, **43**, 117-131.
- Clifford, T.N. 1967. The Damaran episode in the Upper Proterozoic - Lower Palaeozoic structural history of southern Africa. *Spec. Pap. geol. Soc. Amer.*, **92**, 100 pp.
- Copeland, P., Parrish, R.R. and Harrison, T.M. 1988. Identification of inherited radiogenic Pb in monazite and its implications for U-Pb systematics and the age of Himalayan leucogranites. *Abstr. Trans. Am. geophys. Un. (EOS)*, **69**, 520.
- Corfu, E. 1987. Inverse age stratification in the Archean crust of the Superior Province; evidence for infra- and sub-crustal accretion from high resolution U-Pb zircon and monazite ages. *Precamb. Res.*, **36**, 259-275.
- Dallmeyer, R.D. 1979.  $^{40}\text{Ar}$ / $^{39}\text{Ar}$  dating: principles, techniques, and applications in orogenic terranes, 77-104. In: Jäger, E. and Hunziker, J.C., Eds, *Lectures in Isotope Geology*. Springer, Berlin, Heidelberg, New York, 329 pp.
- Dalrymple, G.B. and Lanphere, M.A. 1971.  $^{40}\text{Ar}$ - $^{39}\text{Ar}$  technique of K/Ar dating: A comparison with conventional technique. *Earth Planet. Sci. Lett.*, **12**, 300-308.
- Dalrymple, G.B. and Lanphere, M.A. 1974.  $^{40}\text{Ar}$ - $^{39}\text{Ar}$  age spectra of some undisturbed terrestrial samples. *Geochim. cosmochim. Acta*, **38**, 715-738.
- Del Moro, A., Puxeddu, M., Radicati di Brozolo, E and Villa, L.M. 1982. Rb-Sr and K-Ar ages on minerals at temperatures of 300-400°C from deep wells in the Lardello geothermal field (Italy). *Contr. Miner. Petrol.*, **81**, 340-349.
- Dempster, T.J. 1985. Garnet zoning and metamorphism of the Barrovian Type Area, Scotland. *Contr. Miner. Petrol.*, **89**, 30-38.
- Deutsch, A. and Steiger, R.H. 1985. Hornblende K-Ar ages and the climax of Tertiary metamorphism in the Lepontine Alps (south-central Switzerland): an old problem reassessed. *Earth Planet. Sci. Lett.*, **72**, 175-189.
- Dodson, M.H. 1973. Closure temperatures in cooling geochronological and petrological systems. *Contr. Miner. Petrol.*, **40**, 259-274.
- Dodson, M.H. 1976. Kinetic processes and thermal history of slowly cooling solids. *Nature*, **259**, 551-553.
- Dodson, M.H. 1979. Theory of cooling ages, 194-202. In: Jäger, E. and Hunziker, J.C., Eds, *Lectures in isotope geology*. Springer, Berlin, Heidelberg, New York, 329 pp.
- Downing, K.N. 1983. The stratigraphy and palaeoenvironment of the Damara Sequence in the Okavango Lineament area. *Spec. Publ. geol. Soc. S.Afr.*, **11**, 37-41.
- Downing, K.N. and Coward, M.P. 1981. The Okavango Lineament and its significance for Damaran tectonics in Namibia. *Geol. Rdsch.*, **70**, 972-1000.
- Engelder, T. and Marshak, S. 1985. Disjunctive cleavage formed at shallow depth in sedimentary rocks. *Jour. struct. Geol.*, **7**, 327-343.
- Etheridge, M.A., Wall, V.J. and Vernon, R.H. 1983. The role of the fluid phase during regional metamorphism and deformation. *J. metam. Geol.*, **1**, 205-226.
- Etheridge, M.A., Wall, V.J., Cox, S.E. and Vernon, R.H. 1984. High fluid pressures during regional metamorphism and deformation: implications for mass transport and deformation mechanisms. *J. Geophys. Res.*, **89**, 4344-4358.
- Eugster, H.P. 1970. Thermal and ionic equilibria among muscovite, K-feldspar and aluminosilicate assemblages. *Fortschr. Miner.*, **47**, 106-123.
- Faupel, J. 1974. Geologisch-mineralogische Untersuchungen am Donkerhoek Granit (Karibib District, Südwestafrika). *Göttinger Arb. Geol. Paläont.*, **Nr. 15**, 95 S.
- Faure, G. 1986. *Principles of isotope geology*. John Wiley & Sons, New York, 589 pp.
- Ferry, J.M. 1982. A comparative geochemical study of pelitic schists and metamorphosed carbonate rocks from south-central Maine, USA. *Contr. Miner. Petrol.*, **80**, 59-72.
- Faure, G. and Powell, J.L. 1972. *Strontium isotope geology*. Springer, New York, 188 pp.
- Ferry, J.M. and Spear, E.S. 1978. Experimental calibration of the partitioning of Fe and Mg between biotite and garnet. *Contr. Miner. Petrol.*, **66**, 113-117.
- Finnemore, S.H. 1978. The geochemistry and origin of the Matchless amphibolite belt, Windhoek District, South West Africa. *Spec. Publ. geol. Soc. S.Afr.*, **4**, 433-477.
- Franz, L. and Häussinger, H. 1990. Die Anwendung interaktiver Programme in der Mineralogie am Beispiel des Programms "Amphibol". *Europ. J. Mineral., Beih.*, **1**, 68.
- Freer, R. 1981. Diffusion in silicate minerals and glasses: a data digest and guide to literature. *Contr. Miner. Petrol.*, **76**, 440-454.
- Gebauer, D. and Grünenfelder, M. 1979. U-Th-Pb dating of minerals 105-131. In: Jäger, E. and Hunziker, J.C., Eds, *Lectures in Isotope Geology*. Springer, Berlin, Heidelberg, New York, 329 pp.
- Gevers, T.W. 1963. Geology along the northwestern margin of the Khomas Highlands between Otjimbingwe-Karibib and Okavango, South West Africa. *Trans. and Proceed. geol. Soc. S. Afr.*, **66**, 199-258.
- Graham, I.J. and Korsch, R.J. 1989. Rb-Sr resening ages and chemical characterization of turbidites in an accretionary wedge: Torlesse Complex, Otaki Gorge, New Zealand. *Geol. Soc. Am. Bull.*, **101**, 355-363.
- Grauert, B. 1974. Rb-Sr isotopic study on whole rocks and minerals from the Baltimore Gneiss of the Phoenix Dome, Baltimore County, Maryland. *Carnegie Inst. Wash. Yearb.*, **73**, 1003-1007.
- Grauert, B. and Hall, L.M. 1974. Rb-Sr isotopic study on small whole-rock slabs and their minerals from the Manhattan Schist, Manhattan Prong, New York. *Carnegie Inst. Wash. Yearb.*, **73**, 1007-1010.

- Grauert, B., Hännly, R. and Soptrajanova, G. 1974. Geochronology of a polymetamorphic and anatectic gneiss region: The Moldanubicum of the area Lam-Deggen-dorf, eastern Bavaria, Germany. *Contr. Miner. Petrol.*, **45**, 37-63.
- Grauert, B., Grosse-Westermann, U. and Albat, F. 1990. Interpretation konkordanter D-Th-Pb-Monozitalter moldanubischer Gneise - Schlußfolgerungen aufgrund vergleichen der D-Th-Pb, Sm-Nd und Rb-Sr Isotopen analysen. *Europ. J. Miner.*, **2**, Beih. 1, 81.
- Gray, D.R. 1979a. Cleavages in deformed psammitic rocks from southeastern Australia: Their nature and origin. *Geol. Soc. Am. Bull.*, **89**, 577-590.
- Gray, D.R. 1979b. Microstructure of crenulation cleavage: an indicator of cleavage origin. *Am. J. Sci.*, **279**, 97-128.
- Guidotti, C.V. 1970. The mineralogy and petrology of the transition from the lower to upper sillimanite zone in the Oquossoc Area, Maine. *J. Petrol.*, **11**, 277-336.
- Haack, U. 1983. Reconstruction of the cooling history of the Damara Orogen by correlation of radiometric ages with geography and altitude, 873-884. In: Martin, H. and Eder, E.W., Eds, *Intracontinental Fold Belts - Case studies in the Variscan Belt of Europe and the Damara Belt in Namibia*. Springer, Berlin, 945 pp.
- Haack, D. and Hoffer, E. 1976. K/ Ar age of biotites from the Damara Orogen, South West Africa. *Trans. geol. Soc. S. Afr.*, **79**, 213-216.
- Haack, D., Gohn, E. and Klein, J.A. 1980. Rb/Sr ages of granitic rocks along the middle reaches of the Omaruru River and the timing of orogenetic events in the Damara Belt (Namibia). *Contr. Miner. Petrol.*, **74**, 349-360.
- Haack, U. and Martin, H. 1983. Geochronology of the Damara Orogen - a review, 839-846. In: Martin, H. and Eder, E.W., Eds, *Intracontinental Fold Belts - Case studies in the Variscan Belt of Europe and Damara Belt in Namibia*. Springer, Berlin, 945 pp.
- Haack, D., Gohn, E., Brandt, R. and Feldmann, H. 1988. Rb-Sr data on the Otjimbingwe Alkali Complex in the Damara Orogen, South West Africa, Namibia. *Chem. Erde*, **48**, 131-140.
- Hälbich, I.W. 1977. Structure and tectonics along the southern margin of the Damara mobile belt, South West Africa. *Annale Univ. Stellenbosch, Ser. A1 (Geol)*, **2**, 149-247.
- Hansen, B.T. and Friderichsen, J.D. 1989. The influence of lead loss on the interpretation of disturbed D-Pb systems in zircons from igneous rocks in East Greenland. *Lithos*, **23**, 209-223.
- Hartmann, O., Hoffer, E. and Haack, D. 1983. Regional metamorphism in the Damara Orogen: Interaction of crustal motion and heat transfer. *Spec. Publ. geol. Soc. S. Afr.*, **11**, 233-241.
- Hartnady, C. 1978. The stratigraphy and structure of the Naukluft nappe complex. *14th and 15th an. Rep. Pre-camb. Res. Unit, Univ. Cape Town*, 163-170.
- Hartnady, C., Joubert, P. and Stowe, C. 1985. Proterozoic crustal evolution in southwestern Africa. *Episodes*, **8**, 236-244.
- Häußinger, H. 1990. *Geochemische und petrologische Untersuchungen an metasedimentären Nebengesteinen und assoziierten Metabasiten der Sulfidervorkommen von Gorob, Damara Orogen, Namibia*. Dissertation (unpubl.), Dniversitat Würzburg.
- Hawkesworth, C.J., Kramers, J.D. and Miller, R.McG. 1981. Old model Nd ages in Namibian Pan-African rocks. *Nature*, **289**, 278-282.
- Hawkesworth, C.J., Gledhill, A.R., Roddick, J.C., Miller, R.McG. and Kröner, A. 1983. Rb-Sr and <sup>40</sup>Ar/<sup>39</sup>Ar studies bearing on models of the thermal evolution of the Damara belt, Namibia. *Spec. Publ. geol. Soc. S. Afr.*, **11**, 323-338.
- Hoernes, S. and Hoffer, E. 1979. Equilibrium relations of prograde metamorphic mineral assemblages. A stable isotope study of the Damara Orogen, from Namibia. *Contr. Miner. Petrol.*, **68**, 377-389.
- Hoffer, E. 1977. *Petrologische Untersuchungen zur Regional metamorphose Al-reicher Metapelite im südlichen Damara Orogen (SüdwestAfrika)*. Habilitationsschrift (unpubl.), Dniv. Göttingen, 150 S.
- Hoffer, E. 1978a. Melting experiments in aluminous metapelites: Stability limits of biotite + sillimanite + quartz in the presence of albite. *N. Jb. Miner., Mh.*, 396-407.
- Hoffer, E. 1978b. On the "late" formation of paragonite and its breakdown in pelitic rocks of the southern Damara Orogen (Namibia). *Contr. Miner. Petrol.*, **67**, 209-219.
- Hoffer, E. 1983. Compositional variation of minerals in metapelites involved in low- to medium grade isograd reactions in the southern Damara Orogen, Namibia, South West Africa 745-765. In: Martin, H. and Eder, E.W., Eds, *Intracontinental Fold Belts - Case studies in the Variscan Belt of Europe and Damara Belt in Namibia*. Springer, Berlin, 945 pp.
- Hoffmann, C. 1976. Granites and migmatites of the Damara Belt, South West Africa. Petrography and melting experiments. *Geol. Rdsch.*, **65**, 939-966.
- Hoffmann, C. and Winkler, H.G.E 1973. *Petrographische und experimentelle Untersuchungen an granitischen Gesteinen und Migmatiten des Damara Orogens, SW-Afrika*. DFG Report (unpubl.), Univ. Göttingen.
- Hoffmann, K.H. 1983. Lithostratigraphy and facies of the Swakop Group of the Southern Damara Belt, SWA/Namibia. *Spec. Publ. geol. Soc. S. Afr.*, **11**, 43-63.
- Hofmann, A.W. 1972. Effect of regional metamorphism on the behavior of Rb and Sr in micas and whole-rock systems of the Belt Series, northern Idaho. *Carnegie Inst. Wash. Yearb.*, **71**, 559-563.
- Hofmann, A.W. 1979. Rb-Sr dating of thin slabs: an Imperfect method to determine the age of metamorphism, 27-29. In: Jäger, E. and Hunziker, J.C., Eds, *Lectures in isotope geology*. Springer, Berlin, Heidelberg, New York, 329 pp.
- Hofmann, A.W. and Grauert, B. 1973. Effect of regional metamorphism on whole-rock Rb-Sr systems in sediments. *Carnegie Inst. Wash. Yearb.*, **72**, 299-302.
- Hoinkes, G. 1986. Effect of grossular content in garnet on the partitioning of Fe and Mg between garnet and biotite. *Contr. Miner. Petrol.*, **92**, 393-399.

- Hoisch, T.D. 1989. A muscovite-biotite geothermometer. *Am. Miner.*, **74**, 565-572.
- Holdaway, M.J. 1971. Stability of andalusite and the aluminium silicate phase diagram. *Am. J. Sci.*, **271**, 97-131.
- Holdaway, M.J., Dutrow, B.L. and Hinton, R.W. 1988. Devonian and Carboniferous metamorphism in west-central Maine: The muscovite-almandine geobarometer and the staurolite problem revisited. *Am. Miner.*, **73**, 20-47.
- Horstmann, U.E. 1987. Die metamorphe Entwicklung im Damara Orogen, Südwest Afrika/Namibia, abgeleitet aus K/Ar-Datierungen an detritischen Hellglimmem aus Molassesedimenten der Nama Group. *Göttingen Arb. Geol. Paläont.*, **32**, 95 pp.
- Hoschek, G. 1969. The stability of staurolite and chloritoid and their significance in metamorphism of pelitic rocks. *Contr. Miner. Petrol.*, **22**, 208-232.
- Indares, A. and Martignole, J. 1985. Biotite-garnet geothermometry in the granulite facies: the influence of Ti and Al in biotite. *Am. Miner.*, **70**, 272-278.
- Jacob, R.E. 1974. Geology and metamorphic petrology of part of the Damara Orogen along the lower Swakop river, South West Africa. *Bull. Precamb. Res. Unit., Univ. Cape Town*, **17**, 185 pp.
- Jacob, R.E., Kröner, A. and Burger, A.J. 1978. A real extent and first U/Pb age of the pre-Damara Abbabis Complex in the central Damara belt of South West Africa (Namibia). *Geol. Rdsch.*, **67**, 706-718.
- Jaffey, A.H., Flynn, K.F., Glendenin, L.F., Bentley, W.C. and Essling, A.M. 1971. Precision measurements of half-lives and specific activities of  $^{235}\text{U}$  and  $^{238}\text{U}$ . *Phys. Rev. C.*, **4**, 1889-1906.
- Jäger, E. 1979. Introduction to Geochronology, 1-12. In: Jäger, E. and Hunziker, J.C., Eds, *Structures in Isotope Geology*. Springer, Berlin, Heidelberg, New York, 329 pp.
- Johannes, W. 1978. Melting of plagioclase in the system Ab-An-H<sub>2</sub>O and Qz-Ab-An-H<sub>2</sub>O at  $P_{\text{H}_2\text{O}} = 5$  kbars, an equilibrium problem. *Contr. Miner. Petrol.*, **66**, 295-303.
- Johannes, W. 1984. Beginning of melting in the granite system Qz-Or-Ab-An-H<sub>2</sub>O. *Contr. Miner. Petrol.*, **86**, 264-273.
- Johannes, W. 1985. The significance of experimental studies for the formation of migmatites, 36-85. In: Ashworth, J.R. Ed., *Migmatites*. Blackie, Glasgow, 302 pp.
- Kasch, K.W. 1983a. Continental collision, suture progradation and thermal relaxation: a plate tectonic model for the Damara Orogen in central Namibia. *Spec. Publ. geol. Soc. S. Afr.*, **11**, 423-429.
- Kasch, K.W. 1983b. Folding and thrust tectonics in the southeastern portion of the Damara Orogen around Omitara, Namibia. *Spec. Publ. geol. Soc. S. Afr.*, **11**, 175-184.
- Kasch, K.W. 1983c. Regional P-T variations in the Damara Orogen with particular reference to early high-pressure metamorphism along the Southern Margin. *Spec. Publ. geol. Soc. S. Afr.*, **11**, 243-254.
- Kasch, K.W. 1987. Metamorphism of pelites in the Upper Black Nossob River area of the Damara Orogen. *Com-muns geol. Surv. S. W Afr./Namibia*, **3**, 63-81.
- Kerrick, D.M. 1972. Experimental determination of muscovite + quartz stability with  $P_{\text{H}_2\text{O}}$ . *Am. J. Sci.*, **272**, 946-958.
- Kerrick, D.M. 1988. Al<sub>2</sub>SiO<sub>5</sub>-bearing segregations in the Lepontine Alps, Switzerland: Aluminium mobility in metapelites. *Geology*, **16**, 636-640.
- Killick, A.M. 1983. Sulphide mineralization at Gorob and its genetic relationships to the Matchless Member, Damara Sequence, SWA/Namibia. *Spec. Publ. geol. Soc. S. Afr.*, **11**, 381-384.
- Kingsbury, J.A., Miller, C.F., Wooden, J.L. and Harrison, T.M. 1990. Utility of monazite in geochronology: Examples from the Old Woman-Piute mountains, southeastern California. *Abstr. Trans. Am. Geophys. Union, (EOS)*, **71**, 654.
- Klemd, R., Maiden, K.J. and Okrusch, M. 1987. The Matchless copper deposit SWA/Namibia: A deformed and metamorphosed massive sulfide deposit. *Econ. Geol.*, **82**, 163-171.
- Klemd, R., Maiden, K.J., Okrusch, M. and Richter, P. 1989. Geochemistry of the metamorphosed massive sulfide deposit Matchless, South West Africa/Namibia: wall-rock alteration during submarine ore-forming processes. *Econ. Geol.*, **84**, 603-617.
- Klemd, R. and Okrusch, M. 1990. Phase relationships and fluid-inclusion characteristics of the metamorphosed massive sulfide deposit Matchless, Namibia. *Geol. Rdsch.*, **79**, 433-449.
- Köppel, V. and Grünenfelder, M. 1975. Concordant U-Pb ages of monazites from the Central Alps and timing of the high temperature Alpine metamorphism, a preliminary report. *Schweiz. miner. petrograph. Mitt.*, **55**, 129-132.
- Köppel, V., Günthert, A. and Grünenfelder, M. 1980. Patterns of U-Pb zircon and monazite ages in polymetamorphic units of the Swiss Central Alps. *Schweiz. miner. petrograph. Mitt.*, **61**, 97-119.
- Krogh, T.E. 1973. A low-contamination method for hydrothermal decomposition of zircon and extraction of U and Pb for isotopic age determinations. *Geochim. cosmochim. Acta*, **37**, 485-494.
- Krogh, T.E., Davis, G.L., Aldrich, L.T., Hart, S.R. and Stueber, A. 1968. Geological history of the Grenville Province. *Carnegie Inst. Wash. Yearb.*, **66**, 528-536.
- Krogh, T.E. and Davis, G.L. 1969. Geochronology of the Grenville Province. *Carnegie Inst. Wash. Yearb.*, **67**, 224-233.
- Krogh, T.E. and Davis, G.L. 1971. Paragneiss studies in the Georgian Bay area 90 km southeast of the Grenville Front. *Carnegie Inst. Wash. Yearb.*, **69**, 339-341.
- Krogh, T.E. and Davis, G.L. 1973. The effect of regional metamorphism on U-Pb systems in zircons and a comparison with Rb-Sr systems in the same whole rock and its constituent minerals. *Carnegie Inst. Wash. Yearb.*, **72**, 601-610.

- Kröner, A. 1982. Rb/Sr geochronology and tectonic evolution of the Pan-African Damara Belt of Namibia, South West Africa. *Am. J. Sci.*, **282**, 1471-1507.
- Kröner, A. and Hawkesworth, C. 1977. Late Pan-African emplacement ages for Rössing alaskitic granite (Damara belt) and Rooi Lepel bostonite (Gariiep belt) in Namibia and their significance for the timing of metamorphic events. *20th a. Rep. Res. inst. afr. Geol., Univ. Leeds*, 14-17.
- Kröner, A., Halpern, M. and Jacob, R.E. 1978. Rb/Sr geochronology in favour of polymetamorphism in the Pan-African Damara Belt of Namibia (South West Africa). *Geol. Rdsch.*, **67**, 688-706.
- Kukla, C., Kramm, U., Okrusch, M. and Grauert, R. 1990a. Isotope studies and their implication for metamorphic processes in the Kuiseb Formation of the southern Damara Orogen, Namibia. *Ext. Abst. 23rd Earth Sci. Congr., Geol. Soc. S. Afr., Cape Town*, 305-308.
- Kukla, C., Kramm, U., Okrusch, M. and Grauert, R. 1990b. Sr-Isotopen homogenisierung in Metasedimenten am Beispiel von Kleinbereichsprofilen aus der Kuiseb Formation, Damara Orogen, Zentral Namibia. *Europ. J. Mineral.*, **2**, Beih., 1, 144.
- Kukla, C., Kramm, U., Kukla, P.A. and Okrusch M. 1991. U-Pb monazite data relating to metamorphism and granite intrusion in the northwestern Khomas Trough, Damara Orogen, central Namibia. *Communs geol. Surv. Namibia*, **7**, 49-54.
- Kukla, P.A. 1990. *Tectonics and sedimentation of a Late Proterozoic Damaran convergent continental margin, Khomas Hochland, Central Namibia*. PhD thesis (unpubl.), University of the Witwatersrand, Johannesburg, 287 pp.
- Kukla, P.A., Opitz, C., Stanistreet, I.G. and Charlesworth, E.G. 1988. New aspects of the sedimentology and structure of the Kuiseb Formation in the western Khomas Trough, Damara Orogen, SWA/Namibia. *Communs geol. Surv. S.W.Afr./Namibia*, **4**, 33-42.
- Kukla, P.A., Charlesworth, E.G., Stanistreet, I.G. and Kukla, C. 1989. Downward-facing structures in the Khomas Trough of the Damara Orogen, Namibia. *Communs geol. Surv. S.W.Afr./Namibia*, **5**, 53-57.
- Kukla, P.A., Kukla, C., Stanistreet, I.G. and Okrusch, M. 1990. Unusual preservation of sedimentary structures in sillimanite-bearing metaturbidites of the Damara Orogen, Namibia. *J. Geol.*, **98**, 91-99.
- Kukla, P.A. and Stanistreet, I.G. 1991. Record of the Damaran Khomas Hochland accretionary prism in central Namibia: Refutation of an "ensialic" origin of a Late Proterozoic orogenic belt. *Geology*, **19**, 473-476.
- Lanphere, M.A. and Dalrymple, G.B. 1971. A test of  $^{40}\text{Ar}/^{39}\text{Ar}$  age spectrum technique on some terrestrial materials. *Earth Planet. Sci. Lett.*, **12**, 359-372.
- Leake, R.E. 1978. Nomenclature of amphiboles. *Am. Miner.*, **63**, 1023-1052.
- Ludwig, K.R. 1980. Calculation of uncertainties for U-Pb isotope data. *Earth Planet. Sci. Lett.*, **46**, 212-220.
- Malling, S. 1978. Some aspects of the lithostratigraphy and tectonometamorphic evolution in the Nauchas-Rehoboth area, S.W.A. *Ann. Rep. Precamb. Res. Unit, Univ. Cape Town*, **14/15**, 183-193.
- Martin, H. 1965. The Precambrian geology of South West Africa and Namaqualand. *Precamb. Res. Unit, Univ. Cape Town*, 159 pp.
- Martin, H. 1983. Overview of the geosynclinal, structural and metamorphic development of the intracratonic branch of the Damara Orogen, 473-502. In: Martin, H. and Eder, E.W., Eds, *Intracontinental Fold Belts - Case studies in the Variscan Belt of Europe and Damara Belt in Namibia*. Springer, Berlin, 945 pp.
- Martin, H. and Porada, H. 1977. The intracratonic branch of the Damara Orogen in South West Africa. I. Discussion of the geodynamic models. II. Discussion of relationships with the Pan-African Mobile Belt system. *Precamb. Res.*, **5**, 311-357.
- Martin, H. and Eder, E.W. 1983. *Intracontinental Fold Belts - Case studies in the Variscan Belt of Europe and the Damara Belt in Namibia*. Springer, Berlin, 945 pp.
- Masonne, H.-J. and Schreyer, W. 1987. Phengite barometry based on the limiting assemblage with K-feldspar, phlogopite, and quartz. *Contr. Miner. Petrol.*, **96**, 212-224
- Mattinson, J.M. 1971. Preparation of ultrapure HF, HCl and  $\text{HNO}_3$ . *Carnegie Inst. Wash. Yearb.*, **70**, 266-268.
- McDougall, I. 1974. The  $^{40}\text{Ar}$ - $^{39}\text{Ar}$  method of K-Ar determination of rocks using HIFAR reactor. *Atom. Energy Australia, Aust. Atom. Energy Comm.*, **17**, 3, 3-12.
- Mehnert, K.R. 1968. *Migmatites and the origin of granitic rocks*. Elsevier, Amsterdam, 393 pp.
- Merrill, C.M. and Turner, G. 1966. Potassium-argon dating by activation with fast neutrons. *J. geophys. Res.*, **71**, 2852-2857.
- Miller, R.McG. 1979. The Okahandja Lineament, a fundamental tectonic boundary in the Damara Orogen of South West Africa/Namibia. *Trans. geol. Soc. S. Afr.*, **82**, 349-361.
- Miller, R.McG. 1983a. The Pan-African Damara Orogen of South West Africa/Namibia. *Spec. Publ. geol. Soc. S. Afr.*, **11**, 431-515.
- Miller, R.McG. 1983b. Evolution of the Damara Orogen of South West Africa/Namibia. *Spec. Publ. geol. Soc. S. Afr.*, **11**, 515 pp.
- Miller, R.McG., Barnes, S.-J. and Balkwill, G. 1983. Possible active margin deposits within the southern Damara Orogen: The Kuiseb Formation between Okahandja and Windhoek. *Spec. Publ. geol. Soc. S. Afr.*, **11**, 73-88.
- Miller, R.McG. and Burger, A.J. 1983a. U-Pb zircon age of the Early Damaran Naauwpoort Formation. *Spec. Publ. geol. Soc. S. Afr.*, **11**, 267-272.
- Miller, R.McG. and Burger, A.J. 1983b. U-Pb zircon ages of members of the Salem Granitic Suite along the northern edge of the central Damara granite belt. *Spec. Publ. geol. Soc. S. Afr.*, **11**, 273-280.

- Misra, N.K. and Venkatasubramanian, V.S. 1977. Strontium diffusion in feldspars - a laboratory study. *Geochim. cosmochim. Acta*, **41**, 837-838.
- Montel, J.-M. 1986. Experimental determination of the solubility of Ce-monazite in  $\text{SiO}_2$ - $\text{Al}_2\text{O}_3$ - $\text{K}_2\text{O}$ - $\text{Na}_2\text{O}$  melts at 800°C, 2 kbar, under  $\text{H}_2\text{O}$ -saturated conditions. *Geology*, **14**, 659-662.
- Montgomery, C.W. and Hurley, P.M. 1978. Total-rock U-Pb and Rb-Sr systematics in the Imataca Series, Guayana Shield, Venezuela. *Earth Planet. Sci. Lett.*, **39**, 281-290.
- Mutti, E. and Ricci Lucchi, E. 1975. Turbidite facies and facies associations, 21-36. In: Mutti, E. et al., Eds., Examples of turbidite facies and associations from selected formations of the Northern Apennines. *Field Trip Guidebook A-II. 9th IAS Congress. Nice*.
- Nash, W.P. 1984. Phosphate minerals in terrestrial igneous and, metamorphic rocks, 215-241. In: Nriagu, J.O. and Moore, P.B. Eds, *Phosphate minerals*. Springer, Berlin, Heidelberg, New York, Tokyo, 442 pp.
- Nelson, C.H. and Nilsen, T. 1984. Modern and ancient deep-sea fan sedimentation. *Soc. Econ. Paleont. Miner. Short course*, **14**, 404 pp.
- Neumann, W. and Huster, E. 1974. The half-life of  $^{87}\text{Rb}$  measured as difference between the isotopes  $^{87}\text{Rb}$  and  $^{85}\text{Rb}$ . *Z. Physik.*, **270**, 121-127.
- Nicolaysen, L.O. 1957. Solid diffusion in radioactive minerals and the measurement of the absolute age. *Geochim. cosmochim. Acta*, **11**, 41-59.
- Nieberding, E. 1976. Die Grenze der zentralen Granitzone Südwestlich Otjimbingwe (Karibib District, Südwestafrika): Intrusions verband, Tektonik, Petrographie. *Göttingen Arb. Geol. Paläont.*, **19**, 78 S.
- Overstreet, W.C. 1967. The geologic occurrence of monazite. *U.S. Geol. Surv. prof. pap.*, **530**.
- Papike, J.J., Cameron, K.L. and Baldwin, K. 1974. Amphiboles and pyroxenes: characterization of other than quadrilateral components and estimates of ferric iron from microprobe data. *Geol. Soc. Am. Abstr. with Progr.*, **6**.
- Parrish, R.R. 1988. U-Pb systematics of monazite and its closure temperature based on natural examples. *Geol. Assoc. Can. Progr. Abstr.*, **13**, A94.
- Perchuk, L.L. and Lavrent'eva, I.V. 1983. Experimental investigation of exchange equilibria in the system cordierite-garnet-biotite, 199-239. In: Saxena, S.K., Ed., *Kinetics and equilibrium in mineral reactions*. Springer, New York, 273 pp.
- Peucat, J.J. and Martin, H. 1985. Are Rb-Sr thin slabs migmatite ages always meaningful? *N. Jb. Miner. Abh.*, **152**, 1-21.
- Phillips, G.N., Groves, D.L. and Reed, K. 1989. Geochemical evolution of the Kuiseb schists, Windhoek, Namibia. *Communs geol. Surv. Namibia*, **5**, 19-30.
- Pickering, K.T., Stow, D.A.V., Watson, M.P. and Hiscott, R.N. 1986. Deep-water facies, processes and models: a review and classification scheme for modern and ancient sediments. *Earth Sci. Rev.*, **23**, 75-174.
- Pidgeon, R.T. and Compston, W. 1965. The age and origin of the Cooma Granite and its associated metamorphic zones, New South Wales. *J. Petrol.*, **6**, 193-222.
- Poldervaart, A. 1950. Statistical studies of zircon as a criterion in granitisation. *Nature*, **165**, 574-575.
- Porada, H. 1979. The Damara-Ribeira Orogen of the Pan-African Brasiliano cycle in Namibia (South West Africa) and Brazil as interpreted in terms of continental collision. *Tectonophysics*, **57**, 237-265.
- Porada, H. 1983. Geodynamic model for the geosynclinal development of the Damara Orogen, Namibia/South West Africa, 503-541. In: Martin, H. and Eder, E.W., Eds, *Intra-continental Fold Belts - Case studies in the Variscan Belt of Europe and Damara Belt in Namibia*. Springer, Berlin, 945 pp.
- Porada, H. and Wittig, R. 1983. Turbidites and their significance for the geosynclinal evolution of the Damara Orogen, South West Africa/Namibia. *Spec. Publ. geol. Soc. S. Afr.*, **11**, 21-36.
- Preussinger, H. 1987. *Die geologische Situation der Erzlinsie Vendome, Gorob Bezirk, SWA/Namibia*. Diplomarbeit (unpubl.), Universität Würzburg.
- Preussinger, H. 1990. Host rock geology of the metamorphosed massive sulfide deposits at Gorob in the Pan-African Damara Orogen, Namibia. *J. Afr. Earth Sci.*, **10**, 717-732.
- Preussinger, H., Maiden, K. and Okrusch, M. 1987. Contrasting styles of sedimentation in metasediments of the Kuiseb Formation near Gorob, SWA/Namibia. *Communs geol. Surv. S.W.Afr./Namibia*, **3**, 105-109.
- Puhan, D. 1976. Metamorphic temperature determined by means of the dolomite-calcite solvus geothermometer - examples from the central Damara Orogen (South West Africa). *Contr. Miner. Petrol.*, **58**, 23-28.
- Puhan, D. 1983. Temperature and pressure of metamorphism in the central Damara Orogen. *Spec. Publ. geol. Soc. S. Afr.*, **11**, 219-223.
- Puhan, D. and Hoffer, E. 1973. Phase relations of talc and tremolite in metamorphic calcite - dolomite sediments in the southern portion of the Damara Belt (SW Africa). *Contr. Miner. Petrol.*, **40**, 207-214.
- Pupin, J.P. 1980. Zircon and granite petrology. *Contr. Miner. Petrol.*, **73**, 207-220.
- Purdy, J.W. and Jäger, E. 1976. K-Ar ages on rock-forming minerals from the Central Alps. *Mem. Inst. Geol. e Min., Univ. Padova*, **30**, 31 S.
- Rapp R.P. and Watson, E.B. 1986. Monazite solubility and dissolution kinetics: implications for the thorium and light rare earth chemistry of felsic magmas. *Contr. Miner. Petrol.*, **94**, 304-316.
- Reid, D.L., Malling, S. and Allsopp, H.L. 1988. Rb-Sr ages of granitoids in the Rehoboth-Nauchas area, South West Africa/Namibia. *Communs geol. Surv. S.W.Afr./Namibia*, **4**, 19-28.
- Rittmann, K.L. 1984. *Argon in Hornblende, Biotite und Muscovit beider geologischen Abkühlung -  $^{40}\text{Ar}$ - $^{39}\text{Ar}$  - Untersuchungen*. Diss. Thesis (unpubl.), Universität Heidelberg.

- Roddick, J.C. and Compston, W. 1977. Strontium isotopic equilibration: a solution to a paradox. *Earth Planet. Sci. Lett.*, **34**, 238-246.
- Sawyer, E.W. 1981. Damaran structural and metamorphic geology of an area southeast of Walvis Bay, SWA/Namibia. *Mem. geol. Surv. S.W. Afr./Namibia*, **7**, 94 pp.
- Sawyer, E.W. 1983. Structures in the contact strain aureole of the Donkerhuk Granite, Gross Barmen area, South West Africa/Namibia. *Spec. Publ. geol. Soc. S. Afr.*, **11**, 209-217.
- Schärer, U. 1984. The effect of initial  $^{230}\text{Th}$  disequilibrium on young U-Pb ages: the Makalu case, Himalaya. *Earth Planet. Sci. Lett.*, **67**, 191-204.
- Schärer, U. and Allégre, C.J. 1983. The Palung granite (Himalaya); high-resolution U-Pb systematics in zircon and monazite. *Earth Planet. Sci. Lett.*, **63**, 423-432.
- Schmalzried, H. 1981. *Solid state reactions*. Verlag Chemie, Weinheim, Deerfield Beach, Basel, 254 pp.
- Schmidt, A. and Wedepohl, K.H. 1983. Chemical composition and genetic relations of the Matchless Amphibolite (Damara Orogenic Belt). *Spec. Publ. geol. Soc. S. Afr.*, **11**, 139-145.
- Schneider, A. 1983. The chemical composition of the common metamorphic sediments of the Damara Orogen, 655-677. In: Martin, H. and Eder, E.W., Eds, *Intracontinental Fold Belts - case studies in the Variscan Belt of Europe and the Damara Belt in Namibia*. Springer, Berlin 945 pp.
- Seidel, E., Kreuzer, H. and Harre, W. 1982. A late Oligocene/early Miocene high pressure belt in the External Hellenides. *Geol. Jb.*, **23**, 165-206.
- Seifert, N. 1986. Geochronologie am Südrand des Damara Orogens, S.W.A./Namibia: Hydrothermale Beeinflussungen von Isotopensystemen und Abkühlalter in präkambrischen Basementgesteinen. *Schweiz. miner. petrograph. Mitt.*, **66**, 413-451.
- Silver, L.T. and Deutsch, S. 1963. Uranium lead variations in zircon: a case study. *J. Geol.*, **71**, 747-758.
- Smith, D.A.M. 1965. The geology of the area around the Khan and Swakop rivers in South West Africa. *Mem. geol. Surv. S. Afr., S.W. Afr. Ser.*, **3**, 113 pp.
- Smith, H.A. and Barreiro, B. 1990. Monazite U-Pb dating of staurolite grade metamorphism in pelitic schists. *Contr. Miner. Petrol.*, **105**, 602-615.
- South African Committee for Stratigraphy (SACS) 1980. Stratigraphy of South Africa. Part 1 (Comp. Kent, L.E.) Lithostratigraphy of the Republic of South Africa, South West Africa/Namibia and the Republics of Bophuthatswana, Transkei and Venda. *Handb. geol. Surv. S. Afr.*, **8**, 690 pp.
- Spear, E.S. and Cheney, J.T. 1989. A petrogenetic grid for pelitic schists in the system  $\text{SiO}_2\text{-Al}_2\text{O}_3\text{-FeO-MgO-K}_2\text{O-H}_2\text{O}$ . *Contr. Miner. Petrol.*, **101**, 149-164.
- Springer, N., Pedersen, S., Bridgwater, D. and Glassley W.E. 1983. One dimensional diffusion of radiogenic  $^{87}\text{Sr}$  and fluid transport of volatile elements across the margin of a metamorphosed Archean basic dyke from Saglek, Labrador. *Contr. Miner. Petrol.*, **82**, 26-33.
- Stacey, J.S. and Kramers, J.D. 1975. Approximation of terrestrial lead isotope evolution by a two-stage model. *Earth Planet. Sci. Lett.*, **26**, 207-221.
- Steiger, R.H. and Jäger, E. 1977. Subcommission on Geochronology: Convention on the use of decay constants in geo- and cosmochronology. *Earth Planet. Sci. Lett.*, **36**, 359-362.
- Stephens, M.B., Glasson, M.G. and Keays, R.R. 1979. Structural and chemical aspects of metamorphic layering development in metasediments from Clunes, Australia. *Am. J. Sci.*, **279**, 129-160.
- Storre 1973. *Experimentelle Untersuchungen zur Stabilität von Glimmern, insbesondere von Margarit und von Muskovit*. Habilitationsschrift (unpubl.), Univ. Göttingen.
- Storre, B. and Nitsch, K.-H. 1983. Experimental investigation of the stability conditions of a petrologically significant calc-silicate assemblage observed in originally marly rocks in the Kuiseb Formation of the Damara Orogen, 795-801. In: Martin, H. and Eder, E.W., Eds, *Intracontinental Fold Belts - case studies in the Variscan Belt of Europe and the Damara Belt in Namibia*. Springer, Berlin, 945 pp.
- Tegtmeyer, A. and Kröner, A. 1985. U-Pb zircon ages for granitoid gneisses in northern Namibia and their significance for Proterozoic crustal evolution of southwestern Africa. *Precamb. Res.*, **28**, 311-326.
- Tembusch, H. und Grauert, B. 1983. Zur Diffusion von Strontium in heterogenen Metasedimenten. *Fortschr. Miner.*, **61**, Beih. 1, 255-256.
- Teufel, S. 1988. Vergleichende U-Pb- und Rb-Sr-Altersbestimmungen an Gesteinen des Übergangsbereiches Saxothuringikum/Moldanubikum, NE-Bayern. *Göttinger Arb. Geol. Paläont.*, **35**, 87 pp.
- Thompson, A.B. 1976. Mineral reactions in pelitic rocks: II. Calculation of some P-T-X(Fe-Mg) phase relations. *Am. J. Sci.*, **276**, 425-454.
- Thompson, A.B. and Algor, J.R. 1977. Model systems for anatexis in pelitic rocks. *Contr. Miner. Petrol.*, **63**, 247-269.
- Thompson, A.B. and Tracy, R.J. 1979. Model systems for anatexis of pelitic rocks. *Contr. Miner. Petrol.*, **70**, 429-438.
- Tilton, G.R. 1960. Volume diffusion as a mechanism for discordant lead ages. *J. Geophys. Res.*, **65**, 2933-2945.
- Van Breemen, O., Aftalion, M., Bowes, D.R., Dudek, A., Misar, Z., Povondra, P. and Vrana, S. 1982. Geochronological studies of the Bohemian Massif, Czechoslovakia, and their significance in the evolution of central Europe. *Trans. Roy. Soc. Edinburgh: Earth Sciences*, **73**, 89-108.
- Van Breemen, O. and Dallmeyer, R.D. 1984. The scale of Sr isotopic diffusion during post-metamorphic cooling of gneisses in the Inner Piedmont of Georgia, southern Appalachians. *Earth Planet. Sci. Lett.*, **68**, 141-150.
- Vavra, G. 1990. On the kinematics of zircon growth and its petrogenetic significance: a cathodoluminescence study. *Contr. Miner. Petrol.*, **106**, 90-99.
- Verschure, R.H., Andriessen, P.A.M., Boelrijk, N.A.I.M., Hebeda, E.H., Maijer, C., Priem, H.N.A. and Verdurmen, E.A.Th. 1980. On the thermal stability of Rb-Sr and K-Ar biotite systems: evidence from coexisting Sveconorwe-

- gian (ca. 870 Ma) and Caledonian (ca. 400 Ma) biotites in SW Norway. *Contr. Miner. Petrol.*, **74**, 245-252.
- Von Blanckenburg, E, Villa, I.M., Baur, H., Morteani, G. and Steiger, R.H. 1989. Time calibration of a PT-path from the Western Tauern Window, Eastern Alps: the problem of closure temperatures. *Contr. Miner. Petrol.*, **101**, 1-11.
- Wagner, G.A., Reimer, G.M. and Jäger, E. 1977. Cooling ages derived by apatite fission track, mica Rb-Sr and K-Ar dating: the uplift and cooling history of the central Alps. *Mem. Inst. Geol. Univ. Padova*, **30**, 27 pp.
- Waldron, H.M. and Sandiford, M. 1988. Deformation volume and cleavage development in metasedimentary rocks from the Ballarat slate belt. *J. Struct. Geol.*, **10**, 1, 53-62.
- Walther, J.V. and Wood. B.J. 1984. Rate and mechanism in prograde metamorphism. *Contr. Miner. Petrol.*, **88**, 246-259.
- Wasserburg, G.J. 1963. Diffusion processes in lead-uranium systems. *J. Geophys. Res.*, **68**, 4823-40846.
- Watters, B.R. 1976. Possible late Precambrian subduction Zone in South West Africa. *Nature*, **259**, 471-472.
- Wetherill, G.S. 1976. Discordant uranium-lead ages I. *Trans. Am. Geophys. Un.*, **37**, 320-326.
- Wetherill, G.S. 1963. Discordant uranium-lead ages II. Discordant ages resulting from diffusion of lead and uranium. *J. Geophys. Res.*, **68**, 2957-2965.
- Wickham, S.M. 1987. Crustal anatexis and granite petrogenesis during low-pressure regional metamorphism: the Trois Seigneurs Massif, Pyrenees, France. *J. Petrol.*, **28**, 127-169.
- Williams, P.E. 1972. Development of metamorphic layering and cleavage in low grade metamorphic rocks at Bermagui, Australia. *Am. J. Sci.*, **272**, 1-47.
- Winkler, H.G.E. 1983. A survey of granitic rocks of the Damara Orogen and considerations on their origin, 817-837. In: Martin, H. and Eder, E.W., Eds, *Intra-continental Fold Belts - Case studies in the Variscan Belt of Europe and the Damara Belt in Namibia*. Springer, Berlin, 945 pp.
- Wright, T.O. and Platt, L.B. 1982. Pressure Dissolution and Cleavage in the Martinsburg Shale. *Am. J. Sci.*, **282**, 122-135.
- Yardley, B.W.D. 1977. An empirical study of diffusion in garnet. *Am. Miner.*, **62**, 793-800.
- York, D. 1969. Least squares fitting of a straight line with correlated errors. *Earth Planet. Sci. Lett.*, **5**, 320-324.
- Yund, R.A. and Tullis, J. 1991. Compositional changes of minerals associated with dynamic recrystallization. *Contr. Miner. Petrol.*, **108**, 346-355.
- Zeitler, P.K. 1989. The geochronology of metamorphic processes, 131-147. In: Daly, J.S., Cliff, R.A. and Yardley, B.W.D., Eds, *Evolution of metamorphic belts*. Geol. Soc. Spec. Publ., **43**, 131-147.

## APPENDIX I: MICROPROBE ANALYSES

### ANALYTICAL CONDITIONS AND CALCULATION OF MINERAL FORMULAE

Analyses were carried out on a CAMECA SX 50 electron microprobe with standard operating conditions of 15 kV accelerating potential and 10 nA sample current. Matrix corrections were made with PAP program of CAMECA.

Analytical data are presented for plagioclases, biotites, muscovites, chlorites, amphibolites and garnets from the investigated rock profiles KB167, KB117, KB307, KB421, KB115 and KB103 and sample CO137 from the southern border of the Khomas Trough. The calculation of cations per formula unit was carried out with the help of interactive computer programmes on the basis of the Framework III<sup>c</sup> software (by ASHTON TATE GmbH) compiled by Franz and Häussinger (1990) as follows:

- Plagioclases were calculated on the basis of 8 oxygens. End members are based on Na, Ca and K concentrations.

- Biotites were calculated on an anhydrous basis of 22 oxygens. End member calculations followed Holdaway *et al.* (1988). The solid solution series phlogopite-annite and eastonite-siderophyllite corresponds to a coupled substitution of  $\text{Al}^{3+}$  (oct.) +  $\text{Al}^{3+}$  (tetr.) through  $(\text{Fe}, \text{Mg}, \text{Mn})^{2+} + \text{Si}^{4+}$ . Abbreviations: Ba-Bt = Ba-biotite, Ti-Bt = Ti-biotite, Tlc-Min = talc-minnesotaite, Ms = muscovite, Eas-Sid = eastonite-siderophyllite, Won = wonesite, Phl-Ann = phlogopite-annite.

- White micas were calculated correspondingly on an anhydrous basis of 22 oxygens and end-member concentrations following Holdaway *et al.* (1988). Abbreviations: Ba-Ms = Ba-muscovite, Ti-Ms = Ti-muscovite, Phl-Ann = phlogopite-annite. Ce = celadonite, Prl = pyrophyllite, Pg = paragonite.

- The cation distribution of chlorites was calculated on an anhydrous basis of 28 oxygens. Total Fe is given as  $\text{Fe}^{2+}$ .

- Amphibolites were calculated on an anhydrous basis of 23 oxygens.  $\text{Fe}^{3+}$  was estimated according to the method of Papike *et al.* (1974) employing a value intermediate between the maximum and the minimum values for which a balance of charges is achieved. The distribution of cations was calculated following Leake (1978) according to the general formula  $\text{A}_{0-1} \text{B}_2 \text{C}_5^{\text{VI}} \text{T}_8^{\text{IV}} \text{O}_{22}(\text{OH}, \text{F}, \text{Cl})_2$ .

- Garnets were calculated on the basis of 24 oxygens. Deficiencies in cations in the octahedral site were filled with  $\text{Fe}^{3+}$  to an ideal value of 6.00. Abbreviations: Uv = uvarovite, Ad = andradite, Gr = grossular, Al = almandine, Sp = spessartine. Py = pyrope.

## ANALYTICAL DATA

Table A.1: Plagioclase microprobe analyses

Rock profile KB167 (data averaged for individual slabs of the profile)

	Pl slab A	Pl slab C	Pl slab D	Pl slab K	Pl slab L
SiO <sub>2</sub>	62.61	60.99	60.99	63.40	62.33
Al <sub>2</sub> O <sub>3</sub>	23.76	24.62	25.03	23.27	24.27
MgO	0	0	0	0	0
CaO	5.21	5.96	6.46	4.55	5.54
MnO	0	0.05	0.03	0.02	0.02
FeO	0.10	0.07	0.08	0.11	0.25
BaO	0	0.01	0.03	0.02	0.03
Na <sub>2</sub> O	8.67	8.11	7.91	8.91	8.50
K <sub>2</sub> O	0.10	0.06	0.07	0.06	0.04
total	100.45	99.88	100.59	100.35	101.00
cations based on 8 <O>					
Si	2.762	2.712	2.696	2.793	2.740
Al	1.235	1.290	1.304	1.208	1.257
Mg	0	0	0	0	0
Ca	0.246	0.284	0.306	0.215	0.261
Mn	0	0.002	0.001	0.001	0.001
Fe	0.004	0.003	0.003	0.004	0.009
Ba	0	0	0	0	0.001
Na	0.741	0.700	0.677	0.761	0.724
K	0.006	0.004	0.004	0.003	0.002
total	4.994	4.994	4.992	4.986	4.995
Si+Al	3.997	4.002	4.000	4.001	3.997
Na+Ca+K	0.993	0.988	0.988	0.980	0.988
AN	24.83	28.82	31.03	21.92	26.40
AB	74.60	70.80	68.55	77.70	73.30
OR	0.57	0.36	0.37	0.35	0.24
CE	0	0.02	0.05	0.03	0.06
(grains/ points)	(1/2)	(1/3)	(3/6)	(2/4)	(1/2)

Table A.1 continued: Plagioclase microprobe analyses

## Sample CO117

	PL 112	PL 113	PL 114	PL 115	PL 116	PL 132	PL 133
SiO <sub>2</sub>	67.33	65.45	65.80	66.32	64.85	64.21	66.18
Al <sub>2</sub> O <sub>3</sub>	20.52	21.64	21.70	21.59	21.66	22.95	22.02
MgO	0.01	0	0	0	0	0	0
CaO	1.45	2.73	2.82	2.55	2.78	4.21	2.82
MnO	0.01	0	0.02	0	0.01	0.01	0.05
FeO	0.08	0.08	0.12	0.15	0.05	0.16	0.05
BaO	0.02	0.01	0.04	0	0	0.02	0.03
Na <sub>2</sub> O	10.55	10.16	9.80	10.10	10.04	9.19	10.24
K <sub>2</sub> O	0.04	0.09	0.05	0.08	0.11	0.08	0.04
total	100.01	100.17	100.36	100.78	99.49	100.84	101.44
cations based on 8 <O>							
Si	2.946	2.876	2.882	2.892	2.869	2.813	2.872
Al	1.059	1.121	1.120	1.109	1.129	1.185	1.126
Mg	0.001	0	0	0	0	0	0
Ca	0.068	0.129	0.133	0.119	0.132	0.198	0.131
Mn	0	0	0.001	0	0	0	0.002
Fe	0.003	0.003	0.005	0.005	0.002	0.006	0.002
Ba	0	0	0.001	0	0	0	0.001
Na	0.895	0.866	0.832	0.853	0.861	0.780	0.862
K	0.002	0.005	0.003	0.004	0.006	0.004	0.002
total	4.974	4.999	4.976	4.983	4.999	4.987	4.997
Si+Al	4.004	3.996	4.002	4.001	3.999	3.998	3.998
Na+Ca+K	0.966	0.999	0.968	0.977	0.999	0.983	0.995
AN	7.08	12.88	13.68	12.19	13.17	20.11	13.18
AB	92.64	86.62	85.94	87.38	86.22	79.41	86.56
OR	0.26	0.48	0.31	0.43	0.61	0.45	0.20
CE	0.03	0.02	0.07	0	0	0.03	0.05
(points/ grain)	5	2	3	2	3	3	1

Table A.1 continued: Plagioclase microprobe analyses

## Sample CO117 continued

	PL 72	PL 101	PL 102	PL 103	PL 104	PL 105	PL 111
SiO <sub>2</sub>	66.41	64.45	64.40	65.31	66.08	63.99	65.62
Al <sub>2</sub> O <sub>3</sub>	22.07	22.50	22.25	22.03	21.86	22.34	21.74
MgO	0	0	0	0	0	0	0
CaO	2.76	3.78	3.53	3.02	2.80	3.91	2.75
MnO	0	0.01	0	0.03	0.01	0.01	0.03
FeO	0.10	0.02	0.11	0.12	0.10	0.14	0.14
BaO	0.04	0	0.03	0	0.06	0.04	0.03
Na <sub>2</sub> O	9.89	9.36	9.61	9.80	10.04	9.30	9.77
K <sub>2</sub> O	0.09	0.13	0.09	0.09	0.10	0.09	0.09
total	101.36	100.26	100.03	100.41	101.05	99.82	100.16
cations based on 8 <O>							
Si	2.879	2.834	2.840	2.863	2.877	2.830	2.880
Al	1.128	1.166	1.157	1.138	1.122	1.165	1.124
Mg	0	0	0	0	0	0	0
Ca	0.128	0.178	0.167	0.142	0.130	0.185	0.129
Mn	0	0	0	0.001	0	0.001	0.001
Fe	0.004	0.001	0.004	0.004	0.004	0.005	0.005
Ba	0.001	0	0	0	0.001	0.001	0
Na	0.832	0.798	0.822	0.833	0.848	0.798	0.831
K	0.005	0.008	0.005	0.005	0.005	0.005	0.005
total	4.976	4.986	4.995	4.987	4.988	4.989	4.976
Si+Al	4.007	4.000	3.996	4.001	3.999	3.995	4.004
Na+Ca+K	0.965	0.984	0.995	0.980	0.985	0.988	0.965
AN	13.26	18.10	16.79	14.46	13.24	18.76	13.37
AB	86.14	81.13	82.65	85.04	86.10	80.68	86.08
OR	0.52	0.77	0.51	0.50	0.55	0.50	0.50
CE	0.07	0.00	0.05	0	0.11	0.07	0.05
(points/ grain)	1	3	3	3	5	3	2

**Table A.1 continued: Plagioclase microprobe analyses**  
**Rock profile KB307 (data averaged for individual slabs of the profile)**

	Pl slab A	Pl slab B	Pl slab F	Pl slab J	Pl slab L
SiO <sub>2</sub>	64.46	63.28	63.92	64.89	62.99
Al <sub>2</sub> O <sub>3</sub>	22.72	23.25	23.25	22.79	23.97
MgO	0	0.01	0	0.01	0
CaO	3.66	4.29	3.98	3.63	5.00
MnO	0	0.03	0.01	0.01	0.02
FeO	0.14	0.21	0.12	0.21	0.13
BaO	0.04	0.03	0	0.04	0.03
Na <sub>2</sub> O	9.27	8.95	9.30	9.70	8.82
K <sub>2</sub> O	0.08	0.08	0.07	0.08	0.06
total	100.38	100.14	100.65	101.34	101.01
cations based on 8 <O>					
Si	2.831	2.793	2.804	2.827	2.762
Al	1.176	1.210	1.202	1.170	1.239
Mg	0	0.001	0	0	0
Ca	0.172	0.203	0.187	0.169	0.235
Mn	0	0.001	0	0	0.001
Fe	0.005	0.008	0.005	0.008	0.005
Ba	0.001	0.001	0	0.001	0
Na	0.789	0.766	0.791	0.819	0.750
K	0.005	0.005	0.004	0.004	0.003
total	4.978	4.987	4.992	5.000	4.995
Si+Al	4.006	4.003	4.006	3.997	4.001
Na+Ca+K	0.967	0.974	0.982	0.994	0.988
AN	17.81	20.86	19.06	17.05	23.76
AB	81.62	78.61	80.54	82.44	75.85
OR	0.49	0.47	0.40	0.44	0.34
CE	0.07	0.06	0	0.07	0.05
(grains/ points)	(4/8)	(4/7)	(4/5)	(1/2)	(1/1)

Table A.1 continued: Plagioclase microprobe analyses

## Rock profile KB421

	Pl 321	Pl 351	Pl 361	Pl 101	Pl 102
SiO <sub>2</sub>	56.58	54.95	57.05	57.44	52.77
Al <sub>2</sub> O <sub>3</sub>	27.02	28.63	27.26	26.35	29.30
MgO	0	0	0	0	0
CaO	9.45	11.17	9.60	8.37	12.16
MnO	0.08	0.03	0	0.02	0.02
FeO	0	0.11	0.10	0	0.08
BaO	0.02	0.03	0	0.05	0.01
Na <sub>2</sub> O	6.17	5.30	6.15	6.78	4.53
K <sub>2</sub> O	0.10	0.11	0.15	0.10	0.09
total	99.41	100.33	100.30	99.10	98.95
cations based on 8 <O>					
Si	2.555	2.472	2.554	2.595	2.413
Al	1.438	1.518	1.438	1.403	1.580
Mg	0	0	0	0	0
Ca	0.457	0.539	0.461	0.405	0.596
Mn	0.003	0.001	0	0.001	0.001
Fe	0	0.004	0.004	0	0.003
Ba	0	0.001	0	0.001	0
Na	0.541	0.462	0.534	0.594	0.402
K	0.006	0.006	0.008	0.006	0.005
total	4.999	5.003	4.998	5.004	5.000
Si+Al	3.993	3.990	3.992	3.997	3.993
Na+Ca+K	1.004	1.008	1.003	1.006	1.003
AN	45.54	53.44	45.92	40.30	59.41
AB	53.86	45.86	53.25	59.03	40.07
OR	0.57	0.64	0.84	0.58	0.50
CE	0.04	0.06	0	0.09	0.01
(points/ grain)	(1)	(7)	(1)	(2)	(5)

Table A.1 continued: Plagioclase microprobe analyses

## Rock profile KB115, slab F

	Pl F1	Pl F2	Pl F3	Pl F4	Pl F5	avg slab F
SiO <sub>2</sub>	65.22	65.38	64.98	65.73	64.93	65.19
Al <sub>2</sub> O <sub>3</sub>	22.07	21.76	22.13	21.91	22.03	22.02
MgO	0	0	0	0	0	0
CaO	2.97	2.65	-2.87	2.76	2.73	2.83
MnO	0.01	0	0.01	0.01	0.03	0.01
FeO	0.11	0.01	0.16	0.09	0.10	0.11
BaO	0.04	0.07	0.05	0.01	0.04	0.04
Na <sub>2</sub> O	9.63	9.96	10.07	10.08	10.25	10.00
K <sub>2</sub> O	0.08	0.07	0.12	0.09	0.10	0.10
total	100.13	99.90	100.40	100.69	100.21	100.29
cations based on 8 <O>						
Si	2.864	2.877	2.854	2.872	2.856	2.862
Al	1.143	1.129	1.146	1.128	1.142	1.140
Mg	0	0	0	0	0	0
Ca	0.140	0.125	0.135	0.129	0.129	0.133
Mn	0	0	0	0	0.001	0
Fe	0.004	0	0.006	0.003	0.004	0.004
Ba	0.001	0.001	0.001	0	0.001	0.001
Na	0.820	0.850	0.857	0.854	0.874	0.851
K	0.004	0.004	0.007	0.005	0.005	0.005
total	4.977	4.986	5.006	4.993	5.012	4.996
Si+Al	4.007	4.005	3.999	4.001	3.999	4.002
Na+Ca+K	0.965	0.980	1.000	0.989	1.009	0.990
AN	14.47	12.77	13.52	13.08	12.76	13.43
AB	85.00	86.73	85.71	86.37	86.64	85.96
OR	0.46	.37	0.68	0.53	0.53	0.54
CE	0.07	.13	0.08	0.02	0.07	0.07
(points/ grains)	(3/1)	(1/1)	(3/1)	(2/1)	(3/1)	(12/5)

Table A.1 continued: Plagioclase microprobe analyses

## Rock profile KB115, Slab J

	Pl J1	Pl J3	Pl J4	Pl J5	Pl J23	Pl J25	Pl J31	avg slab J
SiO <sub>2</sub>	65.88	66.22	65.78	64.72	65.03	63.98	64.21	65.34
Al <sub>2</sub> O <sub>3</sub>	21.75	21.26	22.21	21.82	21.87	21.54	21.96	21.73
MgO	0	0	0	0	0	0	0	0
CaO	2.33	1.77	2.77	2.78	2.80	2.84	2.94	2.49
MnO	0.03	0.01	0.01	0.02	0	0.02	0	0.02
FeO	0.05	0.19	0.09	0.08	0.12	0	0.09	0.10
BaO	0.09	0.01	0.01	0.02	0.03	0	0	0.03
Na <sub>2</sub> O	10.37	10.50	10.13	10.27	9.88	10.19	9.89	10.25
K <sub>2</sub> O	0.06	0.06	0.08	0.07	0.12	0.08	0.09	0.07
total	100.57	100.01	101.08	99.80	99.85	98.66	99.20	100.03
cations based on 8 <O>								
Si	2.881	2.906	2.864	2.859	2.867	2.859	2.852	2.874
Al	1.121	1.099	1.140	1.136	1.136	1.134	1.149	1.127
Mg	0	0	0	0	0	0	0.001	0
Ca	0.109	0.083	0.129	0.132	0.132	0.136	0.140	0.118
Mn	0.001	0	0	0.001	0	0.001	0	0.001
Fe	0.002	0.007	0.003	0.003	0.005	0	0.003	0.004
Ba	0.002	0	0	0	0	0	0	0
Na	0.879	0.893	0.855	0.880	0.844	0.883	0.852	0.874
K	0.003	0.003	0.004	0.004	0.007	0.005	0.005	0.004
total	4.999	4.993	4.996	5.015	4.991	5.018	5.002	5.002
Si+Al	4.003	4.005	4.004	3.995	4.003	3.993	4.001	4.001
Na+Ca+K	0.994	0.980	0.989	1.015	0.984	1.023	0.997	0.997
AN	11.01	8.50	13.05	12.95	13.44	13.27	14.03	11.79
AB	88.49	91.15	86.48	86.61	85.82	86.26	85.44	87.75
OR	0.34	0.33	0.45	0.39	0.70	0.47	0.53	0.42
CE	0.16	0.01	0.03	0.04	0.04	0	0	0.04
(points/ grains)	(2/1)	(3/1)	(2/1)	(3/1)	(1/1)	(1/1)	(1/1)	(13/7)

Table A.1 continued: Plagioclase microprobe analyses

## Rock profile KB115, slab K

	Pl K1	Pl K2	Pl K3	Pl K4	Pl K5	avg slab K
SiO <sub>2</sub>	64.80	64.85	64.68	64.89	64.88	64.83
Al <sub>2</sub> O <sub>3</sub>	21.98	21.86	22.16	21.85	21.89	21.93
MgO	0.01	0.02	0	0.02	0	0.01
CaO	2.80	2.65	2.81	2.74	2.73	2.75
MnO	0.04	0.04	0	0	0	0.02
FeO	0.11	0.08	0.24	0	0.13	0.09
BaO	0.03	0.04	0.07	0.01	0.02	0.03
Na <sub>2</sub> O	9.96	9.97	10.00	9.97	10.10	9.98
K <sub>2</sub> O	0.08	0.07	0.08	0.11	0.07	0.08
total	99.79	99.58	100.04	99.60	99.81	99.73
cations based on 8 <O>						
Si	2.859	2.866	2.851	2.866	2.862	2.862
Al	1.143	1.138	1.151	1.138	1.138	1.141
Mg	0	0.002	0	0.001	0	0.001
Ca	0.132	0.125	0.133	0.130	0.129	0.130
Mn	0.001	0.001	0	0	0	0.001
Fe	0.004	0.003	0.009	0	0.005	0.003
Ba	0	0.001	0.001	0	0	0.001
Na	0.852	0.854	0.855	0.854	0.864	0.855
K	0.004	0.004	0.005	0.006	0.004	0.005
total	4.998	4.994	5.003	4.995	5.002	4.997
Si+Al	4.002	4.004	4.002	4.004	4.000	4.003
Na+Ca+K	0.989	0.984	0.993	0.990	0.997	0.990
AN	13.36	12.75	13.36	13.10	12.96	13.12
AB	86.16	86.77	86.05	86.22	86.61	86.35
OR	0.43	0.41	0.46	0.65	0.40	0.47
CE	0.05	0.07	0.12	0.03	0.03	0.05
(points/ grains)	(3/1)	(2/1)	(1/1)	(2/1)	(1/1)	(9/5)

**Table A.1 continued: Plagioclase microprobe analyses**  
**Rock profile KB103 (data averaged for individual slabs of the profile)**

	Pl slab 1	Pl slab 2	Pl slab 5	Pl slab 11	Pl slab 12	Pl slab 13	Pl slab 19	Pl slab 20
SiO <sub>2</sub>	60.59	62.13	61.79	61.65	61.49	61.87	61.51	62.01
Al <sub>2</sub> O <sub>3</sub>	25.11	24.18	24.54	24.48	24.66	24.23	24.22	24.22
MgO	0	0	0	0	0	0	0	0
CaO	6.47	5.58	5.67	5.80	5.96	5.58	5.73	5.69
MnO	0.06	0.03	0.02	0	0.01	0	0.01	0.04
FeO	0.26	0.01	0.05	0.05	0.10	0.03	0.06	0.05
BaO	0	0.03	0.04	0.03	0.08	0.01	0.04	0.02
Na <sub>2</sub> O	7.81	8.33	8.27	8.11	8.07	8.20	8.36	8.18
K <sub>2</sub> O	0.09	0.24	0.19	0.18	0.12	0.21	0.16	0.29
total	100.40	100.53	100.56	100.30	100.48	100.12	100.09	100.50
cations based on 8 <O>								
Si	2.687	2.742	2.727	2.727	2.718	2.740	2.730	2.739
Al	1.312	1.258	1.276	1.277	1.285	1.264	1.267	1.261
Mg	0	0	0	0	0	0	0	0
Ca	0.307	0.264	0.268	0.275	0.282	0.265	0.273	0.269
Mn	0.002	0.001	0.001	0	0	0	0	0.001
Fe	0.010	0	0.002	0.002	0.004	0.001	0.002	0.002
Ba	0	0	0.001	0.001	0.001	0	0.001	0
Na	0.672	0.713	0.708	0.696	0.692	0.704	0.720	0.700
K	0.005	0.014	0.010	0.010	0.007	0.012	0.009	0.016
total	4.996	4.992	4.994	4.987	4.989	4.986	5.001	4.989
Si+Al	3.999	4.000	4.004	4.004	4.003	4.004	3.997	4.000
Na+Ca+K	0.985	0.991	0.987	0.982	0.982	0.981	1.002	0.986
AN	31.22	26.66	27.16	28.03	28.71	26.98	27.19	27.28
AB	68.24	71.93	71.70	70.91	70.44	71.79	71.81	71.02
OR	0.54	1.37	1.06	1.01	0.71	1.22	0.93	1.66
CE	0	0.05	0.07	0.05	0.14	0.01	0.07	0.04
	(2/4)	(2/4)	(2/5)	(1/2)	(1/3)	(1/3)	(5/13)	(3/6)

Table A.2: Biotite microprobe analyses

Sample CO138

Rock profile KB167 (data averaged for individual slabs of the profile)

Avg Bi 138		Bi slab A	Bi slab B	Bi slab D	Bi slab E	Bi slab K	Bi slab L	
SiO <sub>2</sub>	36.70	SiO <sub>2</sub>	36.54	37.18	37.05	36.50	36.52	36.59
TiO <sub>2</sub>	1.59	TiO <sub>2</sub>	1.41	1.32	1.87	1.85	1.64	1.50
Al <sub>2</sub> O <sub>3</sub>	18.78	Al <sub>2</sub> O <sub>3</sub>	18.40	17.99	17.69	18.04	18.22	18.24
Cr <sub>2</sub> O <sub>3</sub>	0.06	Cr <sub>2</sub> O <sub>3</sub>	0.03	0.11	0.08	0.04	0.07	0.03
MgO	10.70	MgO	11.53	11.67	11.50	11.30	11.33	11.31
CaO	0.01	CaO	0.02	0.00	0.01	0.01	0.01	0.00
MnO	0.10	MnO	0.09	0.11	0.07	0.11	0.11	0.04
FeO	17.93	FeO	17.28	17.15	17.82	17.84	17.99	17.71
CuO	0	CuO	0	0	0	0	0	0
ZnO	0	ZnO	0	0	0	0	0	0
BaO	0.11	BaO	0.04	0.05	0.03	0.10	0.06	0.07
Na <sub>2</sub> O	0.14	Na <sub>2</sub> O	0.19	0.15	0.18	0.17	0.18	0.17
K <sub>2</sub> O	9.23	K <sub>2</sub> O	9.18	9.30	9.15	9.10	9.06	9.18
total	95.36	total	94.69	95.05	95.45	95.06	95.22	94.85
cations based on 22<0>								
Si	5.524	Si	5.523	5.594	5.567	5.516	5.509	5.534
Al <sup>IV</sup>	2.476	Al <sup>IV</sup>	2.477	2.406	2.433	2.484	2.491	2.466
tetr.	8.000	tetr.	8.000	8.000	8.000	8.000	8.000	8.000
Al <sup>VI</sup>	0.855	Al <sup>VI</sup>	0.801	0.784	0.699	0.728	0.749	0.785
Cr	0.007	Cr	0.004	0.013	0.009	0.005	0.009	0.003
Ti	0.180	Ti	0.160	0.150	0.212	0.210	0.186	0.171
Fe <sup>2+</sup> tot	2.257	Fe <sup>2+</sup> tot	2.185	2.158	2.239	2.254	2.270	2.240
Mn	0.012	Mn	0.011	0.014	0.008	0.014	0.015	0.006
Mg	2.401	Mg	2.599	2.618	2.575	2.544	2.548	2.549
Cu	0	Cu	0	0	0	0	0	0
Zn	0	Zn	0	0	0	0	0	0
octa.	5.712	octa.	5.759	5.736	5.743	5.755	5.776	5.753
Ba	0.006	Ba	0.002	0.003	0.002	0.006	0.004	0.004
Ca	0.002	Ca	0.002	0.000	0.002	0.002	0.002	0.000
Na	0.040	Na	0.055	0.045	0.054	0.050	0.054	0.050
K	1.773	K	1.770	1.785	1.754	1.754	1.743	1.771
interl.	1.821	interl.	1.836	1.833	1.812	1.812	1.803	1.825
total	15.533	total	15.581	15.570	15.554	15.567	15.579	15.578
end members (after Holdaway et al. 1988)								
Ba-Bi	0.32	Ba-Bt	0.12	0.16	0.09	0.29	0.19	0.22
Ti-Bi	9.00	Ti-Bt	7.99	7.49	10.60	10.52	9.30	8.56
Tlc-Min	8.64	Tlc-Min	8.40	8.17	9.32	9.13	9.66	8.51
Ms	5.18	Ms	3.95	5.48	2.11	1.54	1.71	3.70
Eas-Sid	32.38	Eas-Sid	32.13	28.23	30.73	33.31	34.03	31.85
Won	1.98	Won	2.75	2.23	2.68	2.50	2.68	2.49
Phl-Ann	42.50	Phl-Ann	44.66	48.23	44.47	42.71	42.43	44.68
(grains/ points)	(22/38)	(grains/ points)	(2/4)	(1/1)	(5/9)	(2/3)	(2/4)	(2/3)

Table A.2 continued: Biotite microprobe analyses

Sample CO117 (data averaged for individual slabs, for S<sub>2</sub> biotites and for the total sample)

	Bi slab 3	Bi slab 5	Bi slab 7	Bi slab 8	Avg Bi S <sub>2</sub>	Avg Bi 117
SiO <sub>2</sub>	35.89	36.17	35.97	36.27	35.87	36.14
TiO <sub>2</sub>	2.48	2.32	2.37	2.28	2.42	2.33
Al <sub>2</sub> O <sub>3</sub>	17.74	18.15	17.97	17.45	17.84	17.78
Cr <sub>2</sub> O <sub>3</sub>	0.04	0.04	0.03	0.04	0.05	0.04
MgO	9.43	9.36	9.57	9.47	9.47	9.44
CaO	0.02	0.01	0.01	0.02	0.01	0.02
MnO	0.27	0.23	0.23	0.26	0.27	0.25
FeO	19.90	19.81	20.00	19.98	19.99	19.92
CuO	0	0	0	0	0	0
ZnO	0	0	0	0	0	0
BaO	0.06	0.12	0.06	0.06	0.06	0.08
Na <sub>2</sub> O	0.12	0.13	0.13	0.12	0.12	0.13
K <sub>2</sub> O	9.29	9.11	9.23	9.22	9.20	9.20
total	95.24	95.46	95.58	95.16	95.28	95.33
cations based on 22 <O>						
Si	5.486	5.500	5.475	5.543	5.479	5.512
Al <sup>IV</sup>	2.514	2.500	2.525	2.457	2.521	2.488
tetr.	8.000	8.000	8.000	8.000	8.000	8.000
Al <sup>VI</sup>	0.682	0.752	0.698	0.686	0.689	0.708
Cr	0.005	0.005	0.004	0.004	0.006	0.005
Ti	0.285	0.265	0.271	0.262	0.277	0.268
Fe <sup>2+</sup> tot	2.543	2.519	2.546	2.554	2.554	2.541
Mn	0.035	0.030	0.030	0.033	0.035	0.032
Mg	2.149	2.122	2.170	2.157	2.155	2.147
octa.	5.699	5.694	5.719	5.697	5.716	5.701
Ba	0.004	0.007	0.004	0.004	0.003	0.005
Ca	0.003	0.002	0.002	0.003	0.002	0.003
Na	0.035	0.039	0.038	0.036	0.035	0.037
K	1.811	1.768	1.793	1.797	1.792	1.789
interl.	1.852	1.816	1.837	1.840	1.833	1.829
total	15.551	15.510	15.556	15.538	15.549	15.533
end members (after Holdaway et al. 1988)						
Ba-Bt	0.18	0.35	0.18	0.19	0.17	0.24
Ti-Bt	14.27	13.26	13.54	13.11	13.87	13.38
Tlc-Min	7.21	8.87	7.99	7.78	8.17	8.07
Ms	0.67	1.87	0.80	1.90	0.48	1.57
Eas-Sid	32.75	33.89	33.32	30.51	33.52	32.25
Won	1.75	1.94	1.92	1.82	1.76	1.86
Phl-Ann	43.17	39.83	42.25	44.68	42.03	42.63
(grains/ points)	(3/4)	(5/9)	(2/4)	(7/12)	(3/6)	(15/27)

Table A.2 continued: Biotite microprobe analyses

Rock profile KB307 (data averaged for individual slabs of the profile)

	Bi slab A	Bi slab B	Bi slab F	Bi slab H	Bi slab L
SiO <sub>2</sub>	35.98	35.74	35.65	36.03	35.58
TiO <sub>2</sub>	1.87	1.89	1.92	2.03	1.78
Al <sub>2</sub> O <sub>3</sub>	18.97	18.87	18.94	18.99	19.11
Cr <sub>2</sub> O <sub>3</sub>	0.06	0.04	0.05	0.01	0.03
MgO	10.69	10.65	10.75	10.65	10.86
CaO	0	0.01	0.01	0	0
MnO	0.15	0.18	0.16	0.17	0.21
FeO	18.29	18.37	18.32	18.25	18.20
CuO	0.06	0.05	0.05	0	0
ZnO	0.09	0.08	0.09	0	0
BaO	0.03	0.04	0.02	0.05	0.04
Na <sub>2</sub> O	0.14	0.13	0.14	0.13	0.18
K <sub>2</sub> O	9.08	9.16	9.05	9.14	9.05
total	95.42	95.20	95.14	95.46	95.05
cations based on 22<O>					
Si	5.429	5.415	5.400	5.430	5.390
Al <sup>IV</sup>	2.571	2.585	2.600	2.570	2.610
tetr.	8.000	8.000	8.000	8.000	8.000
Al <sup>VI</sup>	0.804	0.785	0.782	0.804	0.803
Cr	0.007	0.005	0.006	0.001	0.003
Ti	0.212	0.215	0.218	0.230	0.202
Fe <sup>2+</sup> tot	2.308	2.328	2.320	2.301	2.306
Mn	0.020	0.023	0.021	0.022	0.027
Mg	2.405	2.405	2.427	2.393	2.453
Cu	0.007	0.006	0.006	0	0
Zn	0.010	0.009	0.010	0	0
octa.	5.771	5.775	5.790	5.751	5.794
Ba	0.002	0.002	0.001	0.003	0.003
Ca	0.001	0.001	0.002	0.000	0.001
Na	0.041	0.039	0.040	0.038	0.054
K	1.747	1.770	1.749	1.757	1.749
interl.	1.791	1.812	1.793	1.798	1.807
total	15.562	15.587	15.583	15.549	15.601
end members (after Holdaway et al. 1988)					
Ba-Bt	0.10	0.11	0.07	0.16	0.13
Ti-Bt	10.62	10.74	10.91	11.52	10.11
Tlc-Min	10.36	9.29	10.29	9.93	9.54
Ms	1.14	0.66	0.36	1.05	0.98
Eas-Sid	37.90	37.92	38.35	38.12	38.21
Won	2.05	1.94	2.02	1.92	2.69
Phl-Ann	37.83	39.33	37.99	37.31	38.35
(grains/ points)	(9/16)	(5/7)	(5/10)	(1/2)	(2/4)

**Table A.2 continued: Biotite microprobe analyses**  
**Rock profile KB421 (data averaged for individual slabs of the profile)**

	Bi slab 12	Bi slab 14	Bi slab 16
SiO <sub>2</sub>	37.49	37.48	37.04
TiO <sub>2</sub>	1.56	1.84	1.61
Al <sub>2</sub> O <sub>3</sub>	16.86	16.55	16.63
Cr <sub>2</sub> O <sub>3</sub>	0.04	0.06	0.08
MgO	12.17	11.99	11.59
CaO	0.08	0.04	0.01
MnO	0.43	0.42	0.32
FeO	17.07	17.24	17.75
CuO	0	0	0
ZnO	0	0	0
BaO	0.13	0.05	0.10
Na <sub>2</sub> O	0.11	0.10	0.06
K <sub>2</sub> O	9.27	9.27	9.57
total	95.21	95.04	94.76
cations based on 22 <O>			
Si	5.645	5.657	5.636
Al <sup>IV</sup>	2.355	2.343	2.364
tetr.	8.000	8.000	8.000
Al <sup>VI</sup>	0.637	0.600	0.618
Cr	0.005	0.007	0.009
Ti	0.176	0.209	0.185
Fe <sup>2+</sup> tot	2.150	2.176	2.258
Mn	0.055	0.054	0.041
Mg	2.731	2.696	2.628
Cu	0	0	0
Zn	0	0	0
octa.	5.754	5.742	5.739
Ba	0.008	0.003	0.006
Ca	0.013	0.006	0.001
Na	0.032	0.030	0.018
K	1.780	1.784	1.858
interl.	1.832	1.824	1.883
total	15.586	15.566	15.622
end members (after Holdaway et al. 1988)			
Ba-Bt	0.38	0.15	0.28
Ti-Bt	8.81	10.46	9.24
Tlc-Min	8.01	8.66	5.59
Ms	3.17	2.22	3.61
Eas-Sid	25.52	25.55	23.66
Won	1.60	1.51	0.88
Phl-Ann	52.51	51.45	56.74
(grains/ points)	(2/4)	(2/3)	(1/2)

Table A.2 continued: Biotite microprobe analyses

Rock profile KB115 (data averaged for individual slabs of the profile)

	Bi slab B/C	Bi slab D	Bi slab E	Bi slab I	Bi slab J
SiO <sub>2</sub>	36.04	35.50	35.59	35.63	36.08
TiO <sub>2</sub>	2.37	2.41	2.38	2.35	2.26
Al <sub>2</sub> O <sub>3</sub>	18.66	18.31	18.46	18.56	18.40
Cr <sub>2</sub> O <sub>3</sub>	0.03	0.01	0.03	0.03	0.04
MgO	9.85	9.87	9.89	10.02	9.87
CaO	0	0	0.01	0.01	0
MnO	0.36	0.32	0.27	0.30	0.38
FeO	18.81	19.45	19.17	19.09	19.76
CuO	0	0	0	0.03	0.03
ZnO	0	0	0	0.11	0.05
BaO	0.05	0.04	0.02	0.03	0.09
Na <sub>2</sub> O	0.21	0.20	0.20	0.21	0.15
K <sub>2</sub> O	9.11	9.05	9.06	8.85	8.93
total	95.51	95.15	95.07	95.22	96.04
cations based on 22 <O>					
Si	5.452	5.415	5.422	5.415	5.450
Al <sup>IV</sup>	2.548	2.585	2.578	2.585	2.550
tetr.	8.000	8.000	8.000	8.000	8.000
Al <sup>VI</sup>	0.779	0.707	0.736	0.738	0.727
Cr	0.003	0.001	0.004	0.004	0.005
Ti	0.270	0.276	0.273	0.268	0.256
Fe <sup>2+</sup> tot	2.380	2.482	2.442	2.427	2.497
Mn	0.046	0.041	0.035	0.039	0.048
Mg	2.221	2.243	2.245	2.270	2.223
Cu	0	0	0	0.003	0.003
Zn	0	0	0	0.012	0.005
octa.	5.700	5.749	5.735	5.761	5.764
Ba	0.003	0.002	0.001	0.002	0.005
Ca	0	0.001	0.001	0.002	0
Na	0.063	0.060	0.059	0.063	0.045
K	1.757	1.760	1.760	1.715	1.722
interl.	1.823	1.823	1.821	1.781	1.772
total	15.523	15.573	15.556	15.542	15.536
end members (after Holdaway et al. 1988)					
Ba-Bi	0.15	0.12	0.06	0.08	0.26
Ti-Bi	13.50	13.82	13.64	13.41	12.82
Tlc-Min	8.70	8.72	8.89	10.87	11.13
Ms	1.43	0.32	0.34	0.40	0.29
Eas-Sid	36.09	34.69	36.11	36.10	35.76
Won	3.13	3.00	2.93	3.15	2.26
Phl-Ann	36.99	39.34	38.03	35.99	37.48
(grains/ points)	(2/3)	(2/4)	(2/3)	(3/4)	(2/2)

Table A.2 continued: Biotite microprobe analyses  
 Rock profile KB103 (data averaged for individual slabs of the profile)

	Bi slab 1	Bi slab 2	Bi slab 5	Bi slab 11	Bi slab 12	Bi slab 24
SiO <sub>2</sub>	35.12	35.25	35.24	35.49	35.57	35.23
TiO <sub>2</sub>	2.83	3.23	3.55	3.51	1.95	2.66
Al <sub>2</sub> O <sub>3</sub>	19.13	18.90	18.94	19.03	19.65	19.38
Cr <sub>2</sub> O <sub>3</sub>	0.07	0.02	0.04	0.02	0.05	0.01
MgO	8.97	8.85	8.72	8.46	8.87	8.68
CaO	0.02	0	0	0.01	0.02	0
MnO	0.19	0.23	0.16	0.19	0.27	0.21
FeO	19.41	19.06	19.17	19.20	19.47	10.23
CuO	0	0	0	0	0	0
ZnO	0	0	0	0	0	0
BaO	0.02	0.02	0.03	0.04	0.02	0.03
Na <sub>2</sub> O	0.10	0.10	0.18	0.15	0.11	0.16
K <sub>2</sub> O	9.34	9.41	9.24	9.24	9.33	9.37
total	95.18	95.07	95.27	95.34	95.32	94.96
cations based on 22 <O>						
Si	5.357	5.377	5.362	5.391	5.409	5.380
Al <sup>IV</sup>	2.643	2.623	2.638	2.609	2.591	2.620
tetr.	8.000	8.000	8.000	8.000	8.000	8.000
Al <sup>VI</sup>	0.796	0.774	0.758	0.798	0.929	0.868
Cr	0.008	0.003	0.004	0.002	0.006	0.001
Ti	0.324	0.370	0.406	0.401	0.223	0.305
Fe <sup>2+</sup> tot	2.476	2.432	2.439	2.440	2.476	2.456
Mn	0.024	0.029	0.021	0.025	0.034	0.027
Mg	2.040	2.012	1.978	1.917	2.010	1.975
Cu	0	0	0	0	0	0
Zn	0	0	0	0	0	0
octa.	5.668	5.620	5.606	5.583	5.678	5.633
Ba	0.001	0.001	0.002	0.002	0.001	0.002
Ca	0.003	0.001	0.001	0.001	0.004	0
Na	0.029	0.029	0.054	0.043	0.033	0.047
K	1.817	1.831	1.794	1.790	1.810	1.825
interl.	1.849	1.862	1.850	1.837	1.848	1.874
total	15.518	15.483	15.456	15.419	15.526	15.506
end members (after Holdaway et al. 1988)						
Ba-Bi	0.05	0.05	0.08	0.11	0.06	0.09
Ti-Bi	16.21	18.52	20.29	20.07	11.17	15.27
Tlc-Min	7.49	6.83	7.43	8.06	7.54	6.22
Ms	1.01	0.54	0.35	1.21	4.79	3.07
Eas-Sid	37.79	37.63	37.18	37.48	36.90	37.25
Won	1.44	1.47	2.69	2.16	1.65	2.36
Phl-Ann	36.01	34.95	31.98	30.90	37.91	35.73
(grains/ points)	(2/3)	(4/5)	(2/6)	(1/3)	(2/4)	(3/6)

Table A.3: Muscovite microprobe analyses

Sample CO138

Sample CO117

(average muscovite analyses)

	Avg Ms 138		Ms slab 8	Ms slab 4 7
SiO <sub>2</sub>	47.30	SiO <sub>2</sub>	47.19	47.51
TiO <sub>2</sub>	0.84	TiO <sub>2</sub>	0.81	0.59
Al <sub>2</sub> O <sub>3</sub>	34.63	Al <sub>2</sub> O <sub>3</sub>	34.41	34.44
Cr <sub>2</sub> O <sub>3</sub>	0.10	Cr <sub>2</sub> O <sub>3</sub>	0.04	0.05
MgO	0.88	MgO	1.02	1.12
CaO	0.01	CaO	0	0
MnO	0.01	MnO	0	0.07
FeO	1.69	FeO	1.51	1.45
CuO	0	CuO	0	0
ZnO	0	ZnO	0	0
BaO	0.50	BaO	0.40	0.49
Na <sub>2</sub> O	0.71	Na <sub>2</sub> O	0.41	0.42
K <sub>2</sub> O	9.80	K <sub>2</sub> O	10.31	10.11
total	96.47	total	96.11	96.25
cations based on 22<O>				
Si	6.227	Si	6.239	6.264
Al <sup>IV</sup>	1.773	Al <sup>IV</sup>	1.761	1.736
tetr.	8.000	tetr.	8.000	8.000
Al <sup>VI</sup>	3.602	Al <sup>VI</sup>	3.600	3.618
Cr	0.010	Cr	0.005	0.005
Ti	0.084	Ti	0.080	0.059
Fe <sup>2+</sup> tot	0.187	Fe <sup>2+</sup> tot	0.167	0.160
Mn	0.001	Mn	0.001	0.008
Mg	0.172	Mg	0.201	0.219
Cu	0	Cu	0	0
Zn	0	Zn	0	0
octa.	4.056	octa.	4.054	4.068
Ba	0.026	Ba	0.021	0.026
Ca	0.002	Ca	0	0
Na	0.182	Na	0.106	0.107
K	1.646	K	1.739	1.701
interl.	1.855	interl.	1.865	1.833
total	13.911	total	13.920	13.902
end members (after Holdaway et al. 1988)				
Ba-Ms	1.28	Ba-Ms	1.03	1.28
Ti-Ms	4.18	Ti-Ms	4.02	2.95
Phl-Ann	2.78	Phl-Ann	2.72	3.42
Ce	5.45	Ce	6.24	5.75
Prl	7.22	Prl	6.74	8.53
Pg	9.09	Pg	5.30	5.35
Ms	70.01	Ms	73.94	72.72
(grains/ points)	(3/5 ) points)	(grains/ points)	(1/2)	(2/3)

Table A.3 continued: Muscovite microprobe analyses

Rock profile KB307 (data averaged for individual slabs of the profile)

	Ms slab A	Ms slab B	Ms slab F
SiO <sub>2</sub>	46.07	47.34	46.69
TiO <sub>2</sub>	0.45	0.39	0.51
Al <sub>2</sub> O <sub>3</sub>	36.54	34.82	35.53
Cr <sub>2</sub> O <sub>3</sub>	0.05	0.03	0.07
MgO	0.46	0.87	0.73
CaO	0.01	0.03	0.01
MnO	0.03	0	0.04
FeO	0.81	1.07	1.03
CuO	0.12	0	0.03
ZnO	0.12	0.01	0.11
BaO	0.30	0.36	0.29
Na <sub>2</sub> O	1.37	1.20	1.11
K <sub>2</sub> O	8.94	9.17	9.33
total	95.28	95.30	95.46
cations based on 22 <O>			
Si	6.098	6.265	6.178
Al <sup>IV</sup>	1.902	1.735	1.822
tetr.	8.000	8.000	8.000
Al <sup>VI</sup>	3.798	3.695	3.719
Cr	0.005	0.003	0.007
Ti	0.045	0.039	0.050
Fe <sup>2+</sup> tot	0.090	0.119	0.114
Mn	0.003	0	0.004
Mg	0.091	0.172	0.144
Cu	0.012	0	0.003
Zn	0.011	0.001	0.011
octa.	4.056	4.028	4.052
Ba	0.016	0.019	0.015
Ca	0.002	0.004	0.001
Na	0.351	0.307	0.285
K	1.510	1.549	1.575
interl.	1.879	1.879	1.876
total	13.935	13.908	13.927
end members (after Holdaway et al. 1988)			
Ba-Ms	0.79	0.94	0.74
Ti-Ms	2.26	1.95	2.52
Phl-Ann	2.81	1.42	2.58
Ce	0.63	8.29	2.66
Prl	6.67	5.97	6.63
Pg	17.54	15.37	14.25
Ms	69.29	66.05	70.63
(grains/ points)	(2/5)	(1/2)	(5/7)

Rock profile KB115 (data averaged for individual slabs of the profile)

	Ms slab A	Ms slab D	Ms slab E	Ms slab I	Ms slab J
SiO <sub>2</sub>	46.24	46.09	46.61	46.40	45.15
TiO <sub>2</sub>	0.48	0.58	0.67	0.66	0.61
Al <sub>2</sub> O <sub>3</sub>	35.92	36.05	35.39	35.72	36.27
Cr <sub>2</sub> O <sub>3</sub>	0.04	0.05	0.03	0.05	0
MgO	0.70	0.56	0.64	0.65	0.61
CaO	0	0	0.01	0.01	0
MnO	0.04	0.01	0.05	0.01	0.02
FeO	0.96	0.82	0.97	0.99	1.08
CuO	0	0	0	0.02	0.04
ZnO	0	0	0	0	0.09
BaO	0.82	0.19	0.32	0.61	0.24
Na <sub>2</sub> O	1.04	1.10	1.07	1.12	1.18
K <sub>2</sub> O	9.52	9.53	9.50	9.30	9.56
total	94.75	94.97	95.27	95.54	94.86
cations based on 22<O>					
Si	6.194	6.123	6.182	6.145	6.035
Al <sup>IV</sup>	1.806	1.877	1.818	1.855	1.965
tetr.	8.000	8.000	8.000	8.000	8.000
Al <sup>VI</sup>	3.705	3.769	3.714	3.722	3.748
Cr	0.004	0.005	0.003	0.006	0
Ti	0.048	0.058	0.067	0.066	0.061
Fe <sup>2+</sup> tot	0.108	0.091	0.108	0.110	0.121
Mn	0.005	0.001	0.005	0.001	0.002
Mg	0.140	0.111	0.127	0.128	0.122
Cu	0	0	0	0.002	0.004
Zn	0	0	0	0	0.009
octa.	4.010	4.035	4.024	4.035	4.067
Ba	0.043	0.010	0.017	0.032	0.013
Ca	0	0	0.001	0.001	0
Na	0.269	0.283	0.275	0.288	0.305
K	1.626	1.615	1.608	1.571	1.631
interl.	1.938	1.908	1.901	1.892	1.948
total	13.948	13.942	13.925	13.927	14.015
end members (after Holdaway et al. 1988)					
Ba-Ms	2.16	0.49	0.84	1.59	0.64
Ti-Ms	2.40	2.90	3.34	3.30	3.05
Phl-Ann	0.60	1.73	1.21	1.75	3.34
Ce	8.53	1.99	4.77	3.34	0.60
Prl	3.20	4.65	5.06	5.46	2.95
Pg	13.46	14.15	13.74	14.42	15.23
Ms	69.64	74.09	71.04	70.14	74.21
(grains/ points)	(2/3)	(1/3)	(5/10)	(2/4)	(1/2)

Table A.4: Chlorite microprobe analyses

Sample CO138

Rock profile KB167 (data  
averaged for individual slabs of the  
profile)

	Avg Ch 138 (prograde)	Avg Ch 138 (retrograde)		Ch slab C	Ch slab D	Ch slab E
SiO <sub>2</sub>	25.66	23.57	SiO <sub>2</sub>	25.32	25.01	25.01
TiO <sub>2</sub>	0.13	0.08	TiO <sub>2</sub>	0.03	0.08	0.08
Al <sub>2</sub> O <sub>3</sub>	22.80	21.57	Al <sub>2</sub> O <sub>3</sub>	22.91	22.90	22.87
MgO	16.89	10.42	MgO	17.20	17.67	17.33
CaO	0.02	0.01	CaO	0.02	0.03	0.03
MnO	0.16	0.20	MnO	0.19	0.19	0.15
FeO	22.00	31.53	FeO	21.60	21.63	21.84
Na <sub>2</sub> O	0.02	0.04	Na <sub>2</sub> O	0.02	0.01	0.01
K <sub>2</sub> O	0.03	0.21	K <sub>2</sub> O	0.06	0.02	0.03
total	87.70	87.63	total	87.35	87.55	87.38
cations based on 28 <O>						
Si	5.299	5.169	Si	5.246	5.177	5.192
Ti	0.021	0.014	Ti	0.005	0.013	0.013
Al	5.550	5.577	Al	5.596	5.587	5.596
Mg	5.199	3.407	Mg	5.311	5.452	5.363
Ca	0.004	0.004	Ca	0.003	0.006	0.008
Mn	0.027	0.037	Mn	0.033	0.033	0.027
Fe	3.799	5.784	Fe	3.744	3.745	3.792
Na	0.008	0.016	Na	0.009	0.005	0.005
K	0.007	0.059	K	0.015	0.005	0.008
total	19.913	20.066	total	19.962	20.022	20.003
Al <sup>IV</sup>	2.701	2.831	Al <sup>IV</sup>	2.754	2.823	2.808
Si+Al	8.000	8.000	Si+Al	8.000	8.000	8.000
Al <sup>VI</sup>	2.849	2.746	Al <sup>VI</sup>	2.842	2.764	2.788
Ti,Mg,Fe, Mn,Na,Ca,	11.913	12.066	Ti,Mg,Fe, Mn,Na,Ca,	11.962	12.022	12.003
(grains/ points)	(4/2)	(1/2)	(grains/ points)	(1/1)	(1/2)	(4/6)

Table A.5: Hornblende microprobe analyses

Rock profile KB421 (data averaged for individual slabs of the profile)

	Hb slab 10	Hb slab 14	Hb slab 15	Hb slab 20	Hb slab 22
SiO <sub>2</sub>	47.75	47.30	48.93	48.48	46.61
TiO <sub>2</sub>	0.46	0.52	0.44	0.48	0.58
Al <sub>2</sub> O <sub>3</sub>	7.96	8.44	7.28	7.52	9.15
Fe <sub>2</sub> O <sub>3</sub>	0.81	0.98	0.96	0.59	0.49
Cr <sub>2</sub> O <sub>3</sub>	0.03	0.03	0.04	0.02	0.05
MgO	11.54	11.61	12.05	11.97	11.20
CaO	12.27	12.07	12.17	12.19	12.20
MnO	0.65	0.59	0.58	0.59	0.60
FeO	14.54	14.11	14.21	14.00	14.40
Na <sub>2</sub> O	0.66	0.71	0.63	0.63	0.79
K <sub>2</sub> O	0.83	0.85	0.62	0.70	0.94
total	97.50	97.22	97.92	97.17	97.00
cations based on 23 <O>					
T					
Si	7.066	7.008	7.172	7.155	6.936
Al	0.934	0.992	0.828	0.845	1.064
Cr	0	0	0	0	0
Fe <sup>3+</sup>	0	0	0	0	0
total	8.000	8.000	8.000	8.000	8.000
C					
Al	0.454	0.483	0.430	0.463	0.540
Cr	0.004	0.004	0.005	0.003	0.006
Fe <sup>3+</sup>	0.090	0.109	0.106	0.066	0.055
Ti	0.052	0.058	0.049	0.053	0.065
Mg	2.544	2.564	2.632	2.634	2.485
Fe <sup>2+</sup>	1.799	1.748	1.742	1.728	1.792
Mn	0.058	0.033	0.036	0.053	0.057
total	5.000	5.000	5.000	5.000	5.000
B					
Mg	0	0	0	0	0
Fe <sup>2+</sup>	0	0	0	0	0
Mn	0.023	0.041	0.035	0.021	0.019
Ca	1.945	1.916	1.912	1.927	1.945
Na	0.031	0.043	0.053	0.052	0.036
total	2.000	2.000	2.000	2.000	2.000
A					
Na	0.158	0.161	0.127	0.127	0.191
K	0.157	0.161	0.115	0.132	0.178
total	0.315	0.322	0.243	0.259	0.369
(grains/ points)	(1/2)	(2/4)	(1/2)	(1/3)	(1/2)

Table A.6: Garnet microprobe analyses

## Sample CO138 (garnet III)

	138/2	138/3	138/4	138/6	138/7	138/9	138/11	138/12	138/13	138/14
SiO <sub>2</sub>	37.09	37.21	36.78	37.65	37.28	37.30	37.55	37.54	36.92	36.69
TiO <sub>2</sub>	0	0.04	0.03	0.01	0.01	0.03	0.04	0.10	0.02	0.14
Al <sub>2</sub> O <sub>3</sub>	21.35	21.31	21.25	21.26	21.55	21.37	21.03	20.93	21.16	21.09
Cr <sub>2</sub> O <sub>3</sub>	0.02	0.03	0.03	0.09	0.05	0.06	0	0	0.03	0.06
Fe <sub>2</sub> O <sub>3</sub>	0.87	0.63	0.91	0.30	0.53	0.74	0.44	0.39	1.04	0.37
MgO	3.57	3.37	3.43	3.76	3.54	2.89	2.25	2.16	2.08	1.96
CaO	2.16	2.07	1.90	2.36	2.41	2.80	3.22	3.20	3.35	3.43
MnO	2.32	2.63	2.99	1.88	2.18	3.43	6.57	7.13	7.80	7.37
FeO	33.49	33.62	33.11	33.37	33.48	32.86	30.19	29.74	28.90	28.93
total	100.87	100.91	100.44	100.68	101.03	101.47	101.29	101.19	101.29	100.04
cations based on 24 <O>										
Si	5.913	5.934	5.900	5.985	5.924	5.928	5.990	5.997	5.909	5.934
Al <sup>IV</sup>	0.012	0.006	0.018	0	0.036	0.003	0	0	0	0.020
Fe <sup>3+</sup>	0.075	0.059	0.082	0.015	0.039	0.070	0.010	0.003	0.091	0.045
Z	6.000	6.000	6.000	6.000	6.000	6.000	6.000	6.000	6.000	6.000
Al <sup>VI</sup>	4.000	4.000	4.000	3.983	4.000	4.000	3.953	3.941	3.992	3.999
Ti	0	0.005	0.004	0.001	0.001	0.004	0.005	0.012	0.003	0.017
Cr	0.002	0.003	0.004	0.012	0.006	0.007	0	0	0.003	0.007
Fe <sup>3+</sup>	0.029	0.016	0.028	0.021	0.024	0.019	0.043	0.045	0.035	0
Y	4.031	4.024	4.036	4.006	4.026	4.027	4.007	4.009	4.032	4.033
Fe <sup>2+</sup>	4.465	4.485	4.441	4.437	4.449	4.367	4.028	3.973	3.869	3.913
Mn	0.312	0.355	0.407	0.253	0.294	0.462	0.887	0.965	1.057	1.009
Mg	0.849	0.801	0.821	0.890	0.837	0.684	0.535	0.515	0.495	0.473
Ca	0.369	0.354	0.326	0.402	0.410	0.477	0.550	0.547	0.574	0.594
X	5.997	5.995	5.994	5.983	5.990	5.989	6.000	6.000	5.995	5.989
total	16.028	16.019	16.030	15.999	16.022	16.019	16.002	15.997	16.028	16.012
UV	0.05	0.08	0.10	0.29	0.16	0.18	0	0	0.08	0.18
AD	0.73	0.51	0.80	0.54	0.62	0.57	1.21	1.41	0.93	0.43
GR	5.43	5.39	4.63	6.15	6.21	7.38	7.96	7.71	8.63	9.47
AL	74.41	74.75	74.02	73.95	74.15	72.79	67.13	66.22	64.48	65.22
SP	5.23	5.92	6.78	4.22	4.90	7.70	14.79	16.08	17.62	16.82
PY	14.15	13.36	13.68	14.84	13.96	11.39	8.92	8.58	8.25	7.88

Table A.6 continued: Garnet microprobe analyses

## Sample CO138 continued

	138/15	138/16	138/17	138/18	138/19	138/20	138/21	138/22	138/23	138/24
SiO <sub>2</sub>	36.90	37.02	36.84	36.40	37.19	36.86	37.19	37.08	37.29	37.30
TiO <sub>2</sub>	0.11	0.06	0.07	0.09	0.06	0.05	0.08	0.02	0.03	0.01
Al <sub>2</sub> O <sub>3</sub>	21.12	21.29	21.10	20.83	21.18	21.15	21.21	21.12	21.24	21.28
Cr <sub>2</sub> O <sub>3</sub>	0.00	0.02	0	0	0.04	0	0.11	0	0.02	0
Fe <sub>2</sub> O <sub>3</sub>	0.47	0.50	0.70	1.20	0.68	1.42	0.95	0.74	0.57	0.35
MgO	2.03	1.96	2.03	2.11	2.46	2.60	2.72	3.70	3.73	3.31
CaO	3.53	3.53	3.36	3.56	3.21	3.26	3.09	2.21	2.16	1.91
MnO	8.11	8.27	8.14	7.04	5.25	5.01	4.50	1.85	1.77	2.70
FeO	28.23	28.35	28.43	28.83	31.04	31.07	31.54	33.49	33.74	33.80
total	100.49	101.02	100.67	100.07	101.11	101.43	101.39	100.21	100.53	100.66
cations based on 24<0>										
Si	5.939	5.932	5.927	5.897	5.941	5.882	5.921	5.940	5.950	5.962
Al <sup>IV</sup>	0.006	0.021	0.001	0	0	0	0	0	0	0.008
Fe <sup>3+</sup>	0.055	0.047	0.072	0.103	0.059	0.118	0.079	0.060	0.050	0.031
Z	6.000	6.000	6.000	6.000	6.000	6.000	6.000	6.000	6.000	6.000
Al <sup>VI</sup>	4.000	4.000	4.000	3.977	3.989	3.978	3.979	3.987	3.994	4.000
Ti	0.013	0.008	0.009	0.011	0.007	0.006	0.010	0.003	0.003	0.001
Cr	0	0.003	0	0	0.005	0	0.014	0	0.002	0
Fe <sup>3+</sup>	0.002	0.012	0.013	0.043	0.022	0.053	0.035	0.029	0.018	0.012
Y	4.029	4.028	4.021	4.031	4.023	4.037	4.037	4.019	4.018	4.012
Fe <sup>2+</sup>	3.800	3.799	3.825	3.905	4.148	4.147	4.199	4.486	4.503	4.518
Mn	1.106	1.122	1.109	0.967	0.710	0.677	0.607	0.251	0.239	0.366
Mg	0.486	0.469	0.487	0.510	0.585	0.619	0.645	0.883	0.886	0.789
Ca	0.608	0.606	0.579	0.618	0.549	0.558	0.527	0.379	0.369	0.327
X	6.000	5.996	6.000	6.000	5.992	6.000	5.978	6.000	5.997	6.000
total	16.016	16.019	16.021	16.031	16.015	16.037	16.016	16.019	16.015	16.012
UV	0.01	0.07	0	0	0.13	0	0.36	0	0.05	0.00
AD	0.39	0.51	0.54	1.35	0.72	1.49	1.11	0.79	0.54	0.31
GR	9.74	9.60	9.11	8.96	8.43	7.81	7.67	5.53	5.61	5.13
AL	63.33	63.32	63.75	65.09	69.13	69.11	69.98	74.77	75.04	75.30
SP	18.43	18.70	18.49	16.11	11.83	11.28	10.12	4.19	3.98	6.10
PY	8.10	7.82	8.11	8.50	9.75	10.31	10.76	14.72	14.77	13.16

Table A.6 continued: Garnet microprobe analyses - Rock profile KB167, slab K (garnet I)

	K 1/3	K 1/4	K 1/5	K 1/6	K 1/8	K 1/9	K 1/10	K 1/11	K 1/12	K 1/13	K 1/14	K 1/15	K 1/16	K 1/17	K 1/18	K 1/19	K 1/20
SiO <sub>2</sub>	37.20	36.62	36.56	36.97	36.80	36.65	36.04	36.24	36.32	36.37	36.84	36.35	36.70	36.76	36.82	36.96	36.70
TiO <sub>2</sub>	0.03	0.03	0.06	0.06	0.17	0.17	0.06	0.09	0.17	0.13	0.16	0.09	0.12	0.03	0.07	0	0
Al <sub>2</sub> O <sub>3</sub>	21.14	21.30	20.93	21.09	20.71	20.56	21.11	20.70	20.92	20.98	20.98	20.62	20.92	21.12	21.30	21.03	21.37
Cr <sub>2</sub> O <sub>3</sub>	0.02	0	0.01	0.01	0.11	0.04	0	0	0.01	0.01	0	0.08	0.08	0	0	0.08	0
Fe <sub>2</sub> O <sub>3</sub>	0.73	0.90	1.16	0.72	0.77	1.29	1.13	1.35	1.24	0.46	0.38	1.61	1.04	1.21	0.56	0.68	0.65
MgO	2.97	2.91	2.59	2.31	2.11	2.16	2.07	2.09	2.13	2.14	2.46	2.31	2.64	2.85	2.96	2.82	2.75
CaO	3.07	3.16	3.51	4.02	3.88	4.18	4.22	4.59	4.02	3.88	3.75	3.84	3.53	3.22	3.00	2.80	2.39
MnO	4.24	5.30	6.88	7.62	8.99	9.61	9.29	9.43	9.89	9.42	8.06	8.02	5.71	5.08	4.83	4.19	4.17
FeO	31.34	30.02	28.37	27.71	26.37	25.40	25.64	24.97	25.37	25.73	27.08	27.02	29.42	30.39	30.64	31.62	32.42
total	100.73	100.26	100.08	100.50	99.91	100.05	99.55	99.46	100.08	99.12	99.70	99.94	100.15	100.67	100.20	100.18	100.44
cations based on 24 <O>																	
Si	5.945	5.887	5.901	5.935	5.950	5.924	5.856	5.891	5.875	5.922	5.950	5.889	5.912	5.893	5.915	5.947	5.903
Al <sup>IV</sup>	0	0.036	0	0	0	0	0.044	0	0	0.027	0.004	0	0	0	0.033	0	0.051
Fe <sup>3+</sup>	0.055	0.077	0.099	0.065	0.050	0.076	0.100	0.109	0.125	0.052	0.046	0.111	0.088	0.107	0.051	0.053	0.047
Z	6.000	6.000	6.000	6.000	6.000	6.000	6.000	6.000	6.000	6.000	6.000	6.000	6.000	6.000	6.000	6.000	6.000
Al <sup>VI</sup>	3.982	4.000	3.981	3.990	3.946	3.917	4.000	3.965	3.988	4.000	3.990	3.937	3.972	3.991	4.000	3.989	4.000
Ti	0.003	0.004	0.008	0.008	0.020	0.020	0.007	0.011	0.020	0.016	0.020	0.011	0.015	0.004	0.008	0	0
Cr	0.002	0	0.001	0.001	0.014	0.005	0	0	0.001	0.001	0	0.011	0.010	0	0	0.010	0
Fe <sup>3+</sup>	0.032	0.032	0.042	0.022	0.043	0.081	0.038	0.057	0.027	0.005	0	0.085	0.038	0.040	0.017	0.029	0.032
Y	4.019	4.036	4.031	4.020	4.024	4.023	4.045	4.033	4.036	4.022	4.010	4.044	4.034	4.034	4.025	4.028	4.032
Fe <sup>2+</sup>	4.189	4.036	3.829	3.719	3.566	3.433	3.484	3.395	3.431	3.503	3.657	3.660	3.963	4.075	4.117	4.255	4.361
Mn	0.574	0.722	0.940	1.036	1.231	1.316	1.278	1.299	1.355	1.299	1.103	1.100	0.779	0.690	0.658	0.571	0.569
Mg	0.709	0.697	0.622	0.553	0.509	0.521	0.502	0.506	0.514	0.518	0.592	0.558	0.634	0.682	0.710	0.676	0.658
Ca	0.525	0.545	0.607	0.691	0.673	0.723	0.735	0.800	0.697	0.678	0.648	0.666	0.609	0.553	0.516	0.483	0.412
X	5.997	6.000	5.999	5.999	5.979	5.993	6.000	6.000	5.998	5.998	6.000	5.984	5.985	6.000	6.000	5.985	6.000
total	16.016	16.036	16.030	16.019	16.003	16.016	16.045	16.033	16.034	16.020	16.010	16.028	16.019	16.034	16.025	16.013	16.032
UV	0.05	0	0.02	0.02	0.35	0.12	0	0	0.03	0.03	0	0.27	0.25	0	0	0.25	0
AD	0.89	0.91	1.25	0.74	1.59	2.53	1.14	1.68	1.18	0.52	0.50	2.40	1.32	1.09	0.64	0.75	0.81
GR	7.86	8.18	8.88	10.77	9.62	9.52	11.11	11.65	10.44	10.78	10.31	8.71	8.83	8.13	7.96	7.32	6.06
AL	69.82	67.27	63.82	61.99	59.43	57.22	58.07	56.58	57.19	58.39	60.96	61.00	66.06	67.92	68.61	70.92	72.68
SP	9.56	12.04	15.66	17.26	20.52	21.93	21.31	21.65	22.59	21.64	18.38	18.33	12.98	11.50	10.96	9.52	9.48
PY	11.81	11.61	10.37	9.22	8.48	8.68	8.37	8.44	8.57	8.64	9.86	9.29	10.57	11.37	11.83	11.26	10.97

Table A.6 continued: Garnet microprobe analyses

Rock profile KB307, slab F (garnet III)

	F 1/1	F 1/2	F 1/3	F 1/4	F 1/5	F 1/6	F 1/7	F 1/8	F 1/9	F 1/10	F 1/11
SiO <sub>2</sub>	36.25	36.36	35.97	36.70	36.36	36.63	36.11	36.34	36.62	36.77	36.03
TiO <sub>2</sub>	0.09	0	0.04	0.02	0.10	0.01	0.04	0.10	0.04	0.03	0.06
Al <sub>2</sub> O <sub>3</sub>	21.51	21.23	21.28	21.36	21.61	21.50	21.54	21.14	21.22	21.16	21.45
Cr <sub>2</sub> O <sub>3</sub>	0.02	0.03	0	0.06	0.01	0.05	0.14	0.06	0.08	0.05	0
Fe <sub>2</sub> O <sub>3</sub>	0.68	1.16	1.09	0.50	0.53	0.07	0.98	0.56	0.73	0.33	1.15
MgO	2.81	3.30	3.07	3.06	3.05	2.90	3.01	3.04	3.14	3.13	3.27
CaO	0.80	0.67	0.79	0.94	1.02	1.06	1.01	1.03	0.81	0.98	0.71
MnO	8.13	7.79	8.34	8.41	8.95	9.01	9.25	8.98	8.89	8.33	7.67
FeO	30.12	29.79	29.25	29.29	28.69	28.67	28.20	28.26	28.74	29.05	29.88
total	100.41	100.34	99.84	100.34	100.32	99.90	100.29	99.51	100.27	99.83	100.23
cations based on 24 <O>											
Si	5.856	5.866	5.841	5.911	5.861	5.921	5.831	5.902	5.905	5.943	5.823
Al <sup>IV</sup>	0.095	0.037	0.072	0.055	0.105	0.079	0.099	0.046	0.032	0.031	0.086
Fe <sup>3+</sup>	0.049	0.096	0.087	0.035	0.034	0	0.070	0.052	0.063	0.027	0.091
Z	6.000	6.000	6.000	6.000	6.000	6.000	6.000	6.000	6.000	6.000	6.000
Al <sup>VI</sup>	4.000	4.000	4.000	4.000	4.000	4.016	4.000	4.000	4.000	4.000	4.000
Ti	0.011	0	0.005	0.002	0.012	0.001	0.005	0.012	0.005	0.004	0.007
Cr	0.003	0.004	0	0.008	0.001	0.006	0.018	0.008	0.010	0.006	0
Fe <sup>3+</sup>	0.034	0.045	0.047	0.027	0.030	0.009	0.050	0.016	0.025	0.014	0.049
Y	4.047	4.048	4.052	4.037	4.044	4.032	4.073	4.036	4.040	4.024	4.056
Fe <sup>2+</sup>	4.069	4.020	3.973	3.945	3.867	3.875	3.809	3.838	3.876	3.926	4.039
Mn	1.112	1.065	1.147	1.147	1.222	1.233	1.265	1.235	1.214	1.140	1.050
Mg	0.677	0.794	0.743	0.735	0.733	0.699	0.724	0.736	0.755	0.754	0.788
Ca	0.138	0.116	0.137	0.162	0.176	0.184	0.175	0.179	0.140	0.170	0.123
X	5.996	5.994	6.000	5.989	5.998	5.990	5.973	5.988	5.985	5.990	6.000
total	16.043	16.043	16.052	16.025	16.042	16.023	16.046	16.025	16.025	16.015	16.056
UV	0.06	0.10	0	0.19	0.03	0.16	0.45	0.19	0.25	0.16	0
AD	1.11	1.11	1.29	0.72	1.06	0.25	1.37	0.72	0.76	0.45	1.41
GR	1.20	0.82	1.00	1.98	1.87	2.81	1.54	2.27	1.58	2.38	0.64
AL	67.81	67.00	66.21	65.74	64.46	64.58	63.48	63.97	64.60	65.44	67.32
SP	18.54	17.74	19.12	19.12	20.36	20.56	21.09	20.59	20.24	19.01	17.50
PY	11.28	13.23	12.38	12.24	12.21	11.64	12.07	12.26	12.58	12.57	13.13

Table A.6 continued: Garnet microprobe analyses

## Rock profile KB103, slab 1

	1 1/1	1 1/2	1 1/4	1 1/5	1 1/6	1 1/8	1 1/9	1 1/10	1 1/11	1 1/12	1 1/13	1 1/14	1 1/15
SiO <sub>2</sub>	36.61	36.71	36.89	36.55	36.80	36.74	36.64	36.30	36.44	36.90	36.61	36.78	37.00
TiO <sub>2</sub>	0	0	0.02	0.01	0.02	0.03	0	0	0.04	0.02	0	0.04	0.03
Al <sub>2</sub> O <sub>3</sub>	21.14	21.41	21.39	21.36	21.15	20.89	21.28	21.30	21.11	21.16	21.05	21.25	20.86
Cr <sub>2</sub> O <sub>3</sub>	0	0	0.01	0.03	0.03	0.02	0	0	0	0	0	0.03	0
Fe <sub>2</sub> O <sub>3</sub>	0.25	0.38	0.57	0.72	0.62	0.93	0.71	0.78	0.74	0.52	0.72	0.55	0.19
MgO	3.14	3.24	3.39	3.36	3.44	3.37	3.21	3.26	3.10	3.13	2.88	2.66	2.61
CaO	1.04	1.05	1.07	1.12	1.05	1.05	1.01	1.00	1.04	0.98	1.06	1.04	1.11
MnO	6.54	6.21	6.18	6.04	5.87	5.80	5.81	5.89	6.28	6.45	6.54	7.26	7.09
FeO	30.65	31.11	31.06	30.92	31.05	31.20	31.62	31.25	31.06	31.21	31.24	31.11	31.04
total	99.36	100.11	100.58	100.11	100.02	100.04	100.29	99.79	99.81	100.35	100.10	100.70	99.94
cations based on 24 <O>													
Si	5.944	5.916	5.914	5.890	5.929	5.931	5.903	5.879	5.904	5.940	5.923	5.922	5.992
Al <sup>IV</sup>	0.045	0.067	0.042	0.058	0.016	0	0.042	0.066	0.032	0.014	0.014	0.032	0
Fe <sup>3+</sup>	0.012	0.018	0.044	0.052	0.054	0.069	0.054	0.055	0.064	0.046	0.063	0.046	0.008
Z	6.000	6.000	6.000	6.000	6.000	6.000	6.000	6.000	6.000	6.000	6.000	6.000	6.000
Al <sup>VI</sup>	4.000	4.000	4.000	4.000	4.000	3.974	4.000	4.000	4.000	4.000	4.000	4.000	3.982
Ti	0	0	0.003	0.001	0.002	0.003	0	0	0.004	0.002	0	0.005	0.004
Cr	0	0	0.001	0.004	0.004	0.002	0	0	0	0	0	0.003	0
Fe <sup>3+</sup>	0.019	0.028	0.025	0.036	0.021	0.044	0.032	0.040	0.026	0.017	0.026	0.020	0.016
Y	4.019	4.028	4.029	4.040	4.027	4.024	4.032	4.040	4.031	4.019	4.026	4.028	4.001
Fe <sup>2+</sup>	4.162	4.193	4.165	4.168	4.184	4.212	4.261	4.233	4.209	4.201	4.226	4.188	4.203
Mn	0.899	0.848	0.839	0.825	0.801	0.793	0.793	0.807	0.862	0.879	0.896	0.989	0.973
Mg	0.759	0.777	0.811	0.807	0.827	0.810	0.771	0.787	0.748	0.751	0.694	0.638	0.630
Ca	0.180	0.181	0.184	0.194	0.182	0.182	0.174	0.173	0.180	0.169	0.183	0.179	0.193
X	6.000	6.000	5.998	5.994	5.994	5.997	6.000	6.000	6.000	6.000	6.000	5.995	6.000
total	16.019	16.028	16.027	16.034	16.021	16.021	16.032	16.040	16.031	16.019	16.026	16.023	16.001
UV	0	0	0.03	0.10	0.10	0.05	0	0	0	0	0	0.08	0
AD	0.47	0.70	0.69	0.91	0.57	1.19	0.80	1.01	0.76	0.48	0.64	0.61	0.49
GR	2.54	2.32	2.38	2.33	2.46	1.85	2.10	1.88	2.24	2.33	2.41	2.37	2.73
AL	69.36	69.88	69.41	69.47	69.74	70.20	71.02	70.54	70.16	70.02	70.44	69.81	70.06
SP	14.98	14.14	13.98	13.74	13.34	13.21	13.22	13.46	14.37	14.65	14.94	16.49	16.22
PY	12.65	12.95	13.51	13.45	13.79	13.51	12.85	13.11	12.47	12.51	11.57	10.64	10.51

Table A.6 continued: Garnet microprobe analyses

## Rock profile KB103, slab 13

	13 1/1	13 1/2	13 1/3	13 1/6	13 1/7	13 1/9	13 1/10	13 1/11	13 1/12	13 1/13	13 1/14	13 1/16	13 1/17
SiO <sub>2</sub>	36.35	36.22	36.14	36.35	36.40	36.74	36.82	36.38	36.54	36.66	36.63	37.11	36.52
TiO <sub>2</sub>	0.01	0	0	0.01	0.02	0	0	0.01	0	0.01	0	0	0
Al <sub>2</sub> O <sub>3</sub>	20.99	21.05	21.32	21.10	21.36	21.18	21.26	20.92	21.06	21.20	21.26	21.04	21.24
Cr <sub>2</sub> O <sub>3</sub>	0.02	0	0	0.03	0	0	0.04	0	0.01	0	0.04	0	0
Fe <sub>2</sub> O <sub>3</sub>	0.46	0.85	0.87	0.69	0.48	0.20	0.04	0.96	0.34	0.81	0.53	0.25	0.07
MgO	2.18	2.95	3.31	3.76	3.71	3.93	3.90	3.73	3.67	3.64	3.63	3.60	3.08
CaO	1.03	1.13	1.06	1.06	1.10	1.03	1.07	1.09	1.08	1.07	1.01	1.10	1.04
MnO	7.79	5.82	5.68	4.66	4.67	4.59	4.61	4.72	4.78	4.95	4.80	4.94	5.92
FeO	30.86	31.48	31.23	31.35	31.55	31.31	31.33	31.36	31.35	31.66	31.74	31.69	31.30
total	99.68	99.49	99.60	99.00	99.28	98.98	99.06	99.17	98.83	100.01	99.64	99.73	99.16
cations based on 24 <O>													
Si	5.929	5.894	5.863	5.905	5.895	5.950	5.956	5.908	5.942	5.906	5.917	5.980	5.940
Al IV	0.036	0.037	0.077	0.041	0.077	0.042	0.044	0.004	0.036	0.026	0.046	0	0.060
Fe <sup>3+</sup>	0.035	0.068	0.060	0.054	0.027	0.008	0	0.088	0.023	0.068	0.037	0.020	0
Z	6.000	6.000	6.000	6.000	6.000	6.000	6.000	6.000	6.000	6.000	6.000	6.000	6.000
Al VI	4.000	4.000	4.000	4.000	4.000	4.000	4.009	4.000	4.000	4.000	4.000	3.996	4.011
Ti	0.001	0	0	0.001	0.003	0	0	0.001	0	0.001	0	0	0
Cr	0.003	0	0	0.003	0	0	0.005	0	0.001	0	0.005	0	0
Fe <sup>3+</sup>	0.022	0.035	0.046	0.030	0.031	0.017	0.005	0.029	0.019	0.030	0.028	0.011	0.009
Y	4.026	4.035	4.046	4.034	4.034	4.017	4.019	4.030	4.020	4.031	4.033	4.007	4.020
Fe <sup>2+</sup>	4.210	4.285	4.237	4.259	4.274	4.241	4.238	4.259	4.263	4.265	4.287	4.270	4.257
Mn	1.076	0.802	0.780	0.641	0.641	0.630	0.631	0.649	0.659	0.676	0.657	0.674	0.815
Mg	0.529	0.715	0.799	0.911	0.895	0.950	0.940	0.903	0.890	0.875	0.873	0.865	0.747
Ca	0.180	0.198	0.184	0.184	0.191	0.179	0.185	0.190	0.187	0.184	0.175	0.190	0.181
X	5.996	6.000	6.000	5.995	6.000	6.000	5.993	6.000	5.999	6.000	5.992	6.000	6.000
total	16.022	16.035	16.046	16.029	16.034	16.017	16.012	16.030	16.019	16.031	16.025	16.007	16.020
UV	0.07	0	0	0.08	0	0	0.12	0	0.02	0	0.13	0	0
AD	0.58	0.88	1.14	0.78	0.85	0.42	0.14	0.76	0.49	0.78	0.69	0.27	0.22
GR	2.42	2.41	1.92	2.29	2.33	2.58	2.94	2.40	2.64	2.30	2.22	2.90	2.79
AL	70.17	71.42	70.61	70.98	71.23	70.68	70.63	70.98	71.05	71.08	71.46	71.17	70.95
SP	17.94	13.37	13.00	10.68	10.68	10.50	10.52	10.81	10.98	11.26	10.95	11.24	13.59
PV	8.82	11.92	13.32	15.18	14.91	15.83	15.66	15.04	14.83	14.58	14.55	14.42	12.45

**APPENDIX II: GEOCHEMICAL DATA FOR ROCK PROFILE KB115**

Ten individual slabs (A - K) of the rock profile KB115 from the Kuiseb Formation were analysed for their whole-rock composition. Analytical data are presented for the major and trace element concentrations in Table A.7 (major element concentrations are given in percent, trace elements in ppm).

All elements except Na, Mg and P were determined by XRF analyses (PHILIPS PW 1540). Na<sub>2</sub>O and MgO were determined by AAS (PERKIN & ELMER PE 300) and P<sub>2</sub>O<sub>5</sub> with a ZEISS PMD 2 spectrophotometer.

**Table A.7: Geochemical data for rock profile KB115**

	<b>KB115A</b>	<b>KB115BC</b>	<b>KB115D</b>	<b>KB115E</b>	<b>KB115F</b>	<b>KB115G</b>	<b>KB115H</b>	<b>KB115I</b>	<b>KB115J</b>	<b>KB115K</b>
SiO <sub>2</sub>	43.92	69.68	49.86	47.84	69.36	50.01	56.94	61.60	51.95	73.08
TiO <sub>2</sub>	1.27	0.70	1.07	1.18	0.75	1.09	0.96	0.90	1.06	0.62
Al <sub>2</sub> O <sub>3</sub>	24.77	12.45	21.90	22.60	12.40	21.92	19.07	15.97	21.69	11.38
Fe <sub>2</sub> O <sub>3</sub>	10.89	6.17	9.35	10.15	6.64	9.26	8.04	7.63	8.73	5.71
MnO	0.15	0.09	0.13	0.14	0.10	0.13	0.12	0.11	0.12	0.08
MgO	5.35	3.00	4.50	5.20	3.15	4.65	3.93	3.68	4.30	2.70
CaO	0.69	0.64	1.16	0.81	0.86	0.80	0.62	0.68	0.45	0.67
Na <sub>2</sub> O	2.05	1.70	3.95	2.70	2.27	2.05	1.65	1.70	0.85	1.75
K <sub>2</sub> O	7.00	3.30	5.14	6.12	2.85	6.13	5.42	4.46	6.57	2.73
P <sub>2</sub> O <sub>5</sub>	0.30	0.27	0.31	0.28	0.35	0.50	0.40	0.38	0.43	0.34
<b>TOTAL</b>	<b>96.39</b>	<b>98.00</b>	<b>97.37</b>	<b>97.02</b>	<b>98.93</b>	<b>96.54</b>	<b>97.15</b>	<b>97.11</b>	<b>96.15</b>	<b>99.06</b>
Rb	277	155	230	257	153	252	219	197	254	140
Sr	109	98	215	148	143	116	96	103	57	108
Y	49	21	41	43	23	45	37	35	39	24
Zr	293	116	249	250	167	251	208	205	245	144
Nb	23	17	21	24	16	22	20	18	21	15
Ba	772	1552	969	1213	434	1556	1611	1010	1649	390
V	259	134	218	242	142	220	193	176	208	112
Cr	176	83	158	164	88	155	98	120	150	77



---

## APPENDIX III: RB-SR AND U-PB ISOTOPE ANALYSES - ANALYTICAL TECHNIQUES

### Sample preparation for Rb-Sr analyses

The preparation of the whole-rock sample CO343 from the Donkerhuk Granite followed standard methods (washing, breaking, splitting and grinding of a 1.5 kg sample). The preparation of rock profiles for Rb-Sr small-domain investigations, however, had to be modified as follows: small slabs were cut perpendicular to the layering of the banded metasedimentary samples to be cut further according to their compositional layering into slabs of mm to cm thickness and some grams in weight. The individual specimens were then washed with H<sub>2</sub>O<sup>\*\*<sup>(1)</sup></sup> (the relative purity of the reagents) and ground to analytical grade in a small swing mill.

Mineral fractions (biotite, muscovite, plagioclase, garnet, hornblende) were separated from slabs adjacent to the corresponding whole-rock slab of the rock profile. Slabs for mineral separation were washed and ground for 2-5 seconds in a swing mill. The material was carefully elutriated to remove the powder fraction. Micas were preconcentrated by means of magnetic separation. To remove inclusions (apatite etc.) the micas were carefully ground under ethanol in an agate mortar. The micas were split into sieve fractions and finally handpicked to 100% purity. Plagioclase (An 15-25) could only be separated as plagioclase-quartz concentrate which was obtained by means of magnetic and heavy liquid (bromoform) separation. Garnet and hornblende could also be enriched by magnetic separation and were handpicked afterwards. Before dissolution, hornblende, plagioclase and mica fractions were washed in ethanol, garnets were treated for 5 minutes with hot 2N HNO<sub>3</sub>.

### Sample preparation for U-Pb analyses

The mechanical preparation for extraction of zircons involved breaking and crushing of the sample. The sample weight was in the order of 50-100 kg. The material was split into sieve fractions < 250 µm, 250-500 µm and > 500 µm. Heavy minerals were enriched in the fraction < 250 µm by means of a WILFLEY Table. The heavy mineral concentrate was then further processed by heavy liquid separation using bromoform and methylene iodide. Finally, zircons were concentrated to nearly 100 % purity by magnetic separation with a FRANTZ Isodynamic Separator. The nonmagnetic fraction was split into sieve fractions in 20 µm intervals. Zircon fractions were handpicked according to their colour and habit. The crystals were not abraded prior to dissolution.

For extraction of monazites, samples of 3-10 kg weight were used. After crushing the material was ground for 2-5 seconds and subsequently elutriated to remove the powder fraction. After sieving a fraction of < 250 µm was used directly for heavy liquid separation with bromoform and methylene iodide. Monazites could be highly enriched in the heavy mineral concentrates by magnetic separation. Depending on the amount and the size of the monazite crystals, some of the final concentrates could be split further into sieve fractions < 60 µm, 60-125 µm, 125-180 µm and 180-250 µm. Monazites were handpicked and, if possible, only clear crystals were used.

---

<sup>(1)</sup> The asterisks mark the relative purity of the reagent; see page 120 for explanation

## Chemical procedure

For Rb-Sr analyses 100 mg of whole-rock powder or 10-65 mg of a mineral fraction were mixed with a  $^{87}\text{Rb}/^{84}\text{Sr}$  spike solution and dissolved with 5-10 ml of a  $\text{HF}^{***}-\text{HNO}_3^{***(1)}$  mixture (5:1) at 100°C in a Teflon beaker. The sample solution was evaporated and transformed into chloride with 6N  $\text{HCl}^{***(1)}$ . Remaining insoluble residue was extracted with a centrifuge. Rb and Sr were chemically isolated in quartz glass columns filled with 5 ml ion exchange resin (AG 50Wx8, 200-400 mesh). Sr was purified in a second run.

The analytical procedure for decomposition of zircon and the separation of U and Pb essentially followed the method of Krogh (1973). The mode of dissolution the chemical treatment of monazites was the same. Before dissolution, handpicked zircon fractions (2.1-3.9 mg) were treated 5 min with 2N  $\text{HCl}^{***(1)}$ , monazites (0.6-4.0 mg) were washed for 5 min in 2N  $\text{HNO}_3^{***(1)}$ . Samples were decomposed for 3-10 days at 180°C in a Teflon capsule enclosed by a stainless steel jacket. For decomposition of zircons 48%  $\text{HF}^{***(1)}$ , for dissolution of monazites 6N  $\text{HCl}^{***(1)}$  was employed. The solution was then evaporated to dryness and, in the case of zircon samples, transferred into chloride by dilution with 6N  $\text{HCl}^{***(1)}$ . For determination of U and Pb concentrations isotope dilution (Faure and Powell, 1972) was employed. The sample solutions were split into aliquots. One third of the solution was mixed with a  $^{235}\text{U}$ - $^{208}\text{Pb}$  spike. The remaining two thirds were used for determination of the Pb isotopic composition. U and Pb were chemically isolated in Teflon columns (500  $\mu\text{l}$  volume) filled with anion exchange resin (DOWNEX, AG 1x8, 100-200 mesh). Pb was purified in a second run (columns with 100  $\mu\text{l}$  volume).

<sup>(1)</sup>Relative purity of the used reagents:

	*	**	***	****
H <sub>2</sub> O	i	1Q	2Q	two-bottle still
HCl	-	pa	1Q	two-bottle still
HF	-	-	sp	two-bottle still
HNO <sub>3</sub>	-	-	sp	two-bottle still

(Abbreviations: i: ion exchange column, 1Q: first constant boiling quartz-glass still, 2Q: second constant boiling quartz-glass still, two-bottle still: two-bottle sub-boiling still described by Mattinson (1971), pa: pro analysi, sp: supra pure).

## Blanks

All reagents used in the laboratory were checked for their blank concentrations. Blank concentrations are below 0.003 ng/g for Rb and Sr, and below 0.020 ng/g for Pb. No blank determinations were made for U. Total blanks (ng) were determined in a procedure identical to that of the sample treatment. The following blank values were measured:

Rb	Sr	U	Pb
0.09	0.66	0.14	0.30
0.05	0.33	0.0	0.55
0.06	0.04		0.14
0.003	0.05		0.20
0.003	0.04		
0.004	0.92		
0.26	0.59		
0.11	0.58		
0.40	0.10		
0.01	0.06		
0.01	0.07		
0.01	0.04		
0.03	0.05		
0.01	0.05		
0.03	0.06		
0.02	0.07		
0.007	0.20		
0.02	0.13		
0.04	0.25		
0.03	0.09		
0.07	0.22		
0.03	0.36		
0.02	0.37		
0.04			
0.14			

### Mass spectrometry

The mass spectrometric measurements at the Zentrallabor für Geochronologie, Münster were carried out on a TELEDYNE NBS-type 12''90° solid source thermal ion mass spectrometer with a single Faraday cup collector and on-line data processing on a HP 9830 computer.

Rubidium was loaded with H<sub>2</sub>O on a tantalum double filament, Sr with H<sub>3</sub>PO<sub>4</sub> on a tantalum single filament. U and Pb were loaded on rhenium single filaments using Ta<sub>2</sub>O<sub>5</sub> + H<sub>2</sub>O and H<sub>3</sub>PO<sub>4</sub> + silica gel, respectively. Temperatures reached during measurements were: 1400°C for Rb (central filament), 1340 - 1380°C for Sr, 1280 - 1350°C for U and 1230 - 1250°C for Pb.

### Decay constants and isotopic ratios

Decay constants and isotopic ratios used are those recommended by the IUGS Subcommittee on Geochronology (Steiger and Jäger 1977):

$$\lambda^{87}\text{Rb} = 1.42 \times 10^{-11} \text{ a}^{-1} \text{ (Neumann and Huster 1974)}$$

$$\lambda^{238}\text{U} = 1.55125 \times 10^{-10} \text{ a}^{-1} \text{ (Jaffey et al. 1971)}$$

$$\lambda^{235}\text{U} = 9.8485 \times 10^{-10} \text{ a}^{-1} \text{ (Jaffey et al. 1971)}$$

$$^{86}\text{Sr}/^{88}\text{Sr} = 0.1194 \text{ (Steiger and Jäger 1977)}$$

$$^{84}\text{Sr}/^{86}\text{Sr} = 0.056584 \text{ (Steiger and Jäger 1977)}$$

$$^{238}\text{U}/^{235}\text{U} = 137.88 \text{ (Steiger and Jäger 1977)}$$

Pb isotope ratios were corrected for mass fractionation with 0.12 ‰/amu as estimated from measurements of the NBS SRM 981 standard. U isotope ratios were not corrected.

For blank corrections the following isotopic ratios were used:

$$^{207}\text{Pb}/^{204}\text{Pb} = 15.52$$

$$^{206}\text{Pb}/^{204}\text{Pb} = 17.72$$

For common lead correction, isotopic compositions according to the model of Stacey and Kramers (1975) were employed. Model ages of 510 and 520 Ma were used for magmatic and metamorphic monazites, respectively. For zircons, model ages between 850 Ma and 1.6 Ga were employed for calculation of the initial lead composition.

### Age calculation and error evaluation

Errors are quoted as follows:

$^{87}\text{Sr}/^{86}\text{Sr}$ : the measured, individual errors are quoted on a 95% confidence level (2 $\sigma$ ) in diagrams and tables.

$^{87}\text{Rb}/^{86}\text{Sr}$ : an uncertainty of 1% is estimated from repeated analyses.

$^{206}\text{Pb}/^{238}\text{U}$  and  $^{207}\text{Pb}/^{235}\text{U}$ : the calculation of errors for the  $^{206}\text{Pb}/^{238}\text{U}$  and  $^{207}\text{Pb}/^{235}\text{U}$  ratios was according to Ludwig (1980). Error ellipses are given on a 95% confidence level. The calculated errors account for measured errors, the uncertainty of the U/Pb ratio of the mixed spike and the uncertainty of the common lead and blank lead corrections.

The reproducibility of data (based on 21 replicate determinations) is generally better than 1% for  $^{87}\text{Rb}/^{86}\text{Sr}$  ratios, but for some samples the reproducibility was only between 1 and 3%. In repeated analyses,  $^{87}\text{Sr}/^{86}\text{Sr}$  ratios could be determined to 0.02% precision, but a maximum deviation of 0.1% was obtained. The high mica content of the pelitic sample material is held responsible for the poor reproducibility. Apparently a homogenisation of the sample powders could not be achieved for all samples. Analytical data of repeated analyses were average for age calculations, but are presented separately in Tables A.8 - A.14.

The calculation of ages and initial ratios followed the regression method of York (1969). Errors used for age calculations are the measured, individual errors for the  $^{87}\text{Sr}/^{86}\text{Sr}$  ratios and a uniform uncertainty of 1% for the  $^{87}\text{Rb}/^{86}\text{Sr}$  ratios. Errors given for age calculations are quoted as

- statistical error which accounts for the scatter of data around a regression line, or
- analytical ("a-priori") error based on the individual errors of the regressed data. It is used for two-point regression calculations and in cases where the analytical error of the data points exceeds the statistical error.

Errors given for the computed  $^{87}\text{Sr}/^{86}\text{Sr}$  ratios in the profile diagrams are

- the statistical errors of the measured  $^{87}\text{Sr}/^{86}\text{Sr}$  ratios (bracketed by horizontal error bars), which are enlarged by a factor resulting from an uncertainty of 1% in the measured  $^{87}\text{Rb}/^{86}\text{Sr}$  ratios (corresponding to the length of the vertical error bars);
- for repeated analyses which are marked by asterisks in the profile diagrams, the error obtained from the deviation of the repeated analyses is added to the statistical error of the measured  $^{87}\text{Sr}/^{86}\text{Sr}$  ratio.

## Measurements of standard reference materials

For correction of measured isotope ratios following standard reference materials were used:

Rb:	NBS SRM 984
Sr:	NBS SRM 987
U:	NBS SRM U-500
Pb:	NBS SRM 981
	NBS SRM 983

**NBS SRM 984: Nominal value  $^{85}\text{Rb}/^{87}\text{Rb} = 2.593 \pm 2$**

Measured  $^{85}\text{Rb}/^{87}\text{Rb}$  ratios and deviation from nominal value (in %):

2.60891 ± 72	0.6	2.61804 ± 140	0.9
2.61205 ± 207	0.7	2.61078 ± 109	0.7
2.60553 ± 201	0.5	2.60278 ± 166	0.4
2.60665 ± 51	0.5	2.59784 ± 382	0.2
2.60782 ± 127	0.6	2.60494 ± 202	0.5
2.60336 ± 196	0.4	2.58712 ± 636	-0.2
2.60592 ± 254	0.5	2.60538 ± 96	0.5
2.60625 ± 145	0.5	2.60996 ± 46	0.7
2.59502 ± 357	0.08	2.60630 ± 296	0.5
2.60285 ± 599	0.4	2.59737 ± 136	0.2
2.60984 ± 100	0.6	2.59475 ± 75	0.07
2.60090 ± 188	0.3	2.59013 ± 170	-0.1
2.60350 ± 45	0.4	2.60268 ± 70	0.4
2.60095 ± 201	0.3	2.59238 ± 78	-0.02
2.59078 ± 271	-0.09	2.60983 ± 216	0.6

In accordance with the measured  $^{85}\text{Rb}/^{87}\text{Rb}$  ratios of NBS SRM 984 a correction factor of 0.99527 was determined.

**NBS SRM 987: Nominal value:  $^{87}\text{Sr}/^{86}\text{Sr} = 0.71014 \pm 20$** Measured  $^{87}\text{Sr}/^{86}\text{Sr}$  ratios and deviation from nominal value (in %):

0.710275 ± 59	0.02	0.710198 ± 44	0.008
0.710155 ± 73	0.002	0.710287 ± 41	0.02
0.710312 ± 93	0.02	0.710229 ± 53	0.01
0.710285 ± 100	0.02	0.710266 ± 22	0.02
0.710261 ± 43	0.02	0.710298 ± 60	0.02
0.710235 ± 52	0.01	0.710293 ± 50	0.02
0.710330 ± 36	0.03	0.710332 ± 55	0.03
0.710299 ± 32	0.02	0.710322 ± 50	0.03
0.710299 ± 58	0.02	0.710246 ± 64	0.01
0.710183 ± 35	0.006	0.710243 ± 86	0.01
0.710221 ± 37	0.01	0.710298 ± 49	0.02
0.710311 ± 115	0.02	0.710311 ± 59	0.02
0.710294 ± 63	0.02	0.710372 ± 61	0.03
0.710262 ± 65	0.02	0.710244 ± 90	0.01
0.710277 ± 27	0.02	0.710300 ± 62	0.02
0.710233 ± 39	0.01		

Measured  $^{87}\text{Sr}/^{86}\text{Sr}$  ratios have been normalised to a natural  $^{87}\text{Sr}/^{86}\text{Sr}$  ratio of 0.1194 (Steiger and Jäger, 1977).

**NBS SRM U-500: Nominal value:  $^{238}\text{U}/^{235}\text{U} = 1.0003 \pm 10$** Measured  $^{238}\text{U}/^{235}\text{U}$  ratio and deviation from nominal value (in %):

0.998476 ± 716	-0.2
0.997162 ± 346	-0.3
0.998274 ± 300	-0.2
0.998941 ± 1221	-0.1

**NBS SRM 981: Nominal values:  $^{208}\text{Pb}/^{206}\text{Pb} = 2.1681 \pm 8$**

$^{207}\text{Pb}/^{206}\text{Pb} = 0.91464 \pm 33$

$^{204}\text{Pb}/^{206}\text{Pb} = 0.059042 \pm 37$

Measured ratios and deviations from nominal values (in %):

$^{208}\text{Pb}/^{206}\text{Pb}$	$^{207}\text{Pb}/^{206}\text{Pb}$	$^{204}\text{Pb}/^{206}\text{Pb}$
2.162128 ± 236 (-0.3)	0.913648 ± 43 (-0.1)	0.059175 ± 24 (0.2)
2.161528 ± 356 (-0.3)	0.913669 ± 93 (-0.1)	0.059186 ± 9 (0.2)
2.161728 ± 348 (-0.3)	0.913689 ± 54 (-0.1)	0.059193 ± 16 (0.3)
2.161816 ± 222 (-0.3)	0.913731 ± 51 (-0.1)	0.059164 ± 14 (0.2)

**NBS SRM 983: Nominal values:  $^{208}\text{Pb}/^{206}\text{Pb} = 0.013619 \pm 24$**

$^{207}\text{Pb}/^{206}\text{Pb} = 0.071201 \pm 40$

$^{204}\text{Pb}/^{206}\text{Pb} = 0.000371 \pm 20$

Measured ratios and deviations from nominal values (in %):

$^{208}\text{Pb}/^{206}\text{Pb}$	$^{207}\text{Pb}/^{206}\text{Pb}$	$^{204}\text{Pb}/^{206}\text{Pb}$
0.013846 ± 4 (1.7)	0.071240 ± 4 (0.05)	0.000382 ± 2 (3.0)
0.013668 ± 7 (0.4)	0.071129 ± 8 (-0.1)	0.000375 ± 3 (1.1)
0.013655 ± 7 (0.3)	0.071097 ± 35 (-0.1)	0.000376 ± 2 (1.3)
0.013695 ± 12 (0.6)	0.071112 ± 58 (-0.1)	0.000375 ± 2 (1.1)
0.013692 ± 2 (0.5)	0.071145 ± 5 (-0.1)	0.000378 ± 3 (1.9)



## APPENDIX IV: Rb-Sr ISOTOPE ANALYSES - ANALYTICAL DATA

## Rb-Sr data

Abbreviations: WR = whole rock, WR rep. = repeated analyses

**Table A.8: Rb-Sr analytical data for rock profile KB167,  
Kuiseb Formation (farm Usambara 304)**

Sample	(mg)	Conc. Rb (ppm)	Conc. Sr (ppm)	$^{87}\text{Rb}/^{86}\text{Sr}$	$^{87}\text{Sr}/^{86}\text{Sr}$
KB167A WR	(103.1)	114.1	90.8	$3.6497 \pm 0.0042$	$0.743644 \pm 0.000017$
KB167B WR	(101.6)	149.7	96.0	$4.5287 \pm 0.0020$	$0.750101 \pm 0.000050$
KB167C WR	(103.9)	156.1	103.6	$4.3746 \pm 0.0051$	$0.748108 \pm 0.000040$
KB167D WR	(100.9)	55.7	105.3	$1.5346 \pm 0.0037$	$0.729155 \pm 0.000068$
KB167E WR	(101.1)	69.8	140.2	$1.4423 \pm 0.0006$	$0.728391 \pm 0.000040$
KB167F WR	(104.0)	98.4	110.3	$2.5874 \pm 0.0020$	$0.735980 \pm 0.000038$
KB167G WR	(101.0)	140.2	121.5	$3.3480 \pm 0.0051$	$0.741772 \pm 0.000266$
KB167G WR rep.	(101.4)	141.4	121.8	$3.3688 \pm 0.0018$	$0.741557 \pm 0.000056$
KB167H WR	(101.2)	90.1	106.1	$2.4639 \pm 0.0082$	$0.735512 \pm 0.000042$
KB167I WR	(105.4)	89.1	100.2	$2.5803 \pm 0.0065$	$0.736885 \pm 0.000072$
KB167J WR	(103.0)	167.8	111.1	$4.3891 \pm 0.0010$	$0.748935 \pm 0.000034$
KB167K WR	(110.1)	168.1	137.5	$3.5490 \pm 0.0043$	$0.743717 \pm 0.000054$
KB167B Bi 80-160 $\mu\text{m}$	(35.7)	479.3	1.7	$1778.2961 \pm 29\ 6202$	$13.149154 \pm 0.001146$
KB167C Bi 80-160 $\mu\text{m}$	(50.0)	482.7	1.7	$1735.6077 \pm 12.5563$	$12.674650 \pm 0.001386$

Table A.9: Rb-Sr analytical data for rock profile KB117 and sample CO117,  
Kuseb Formation (farm Kaan 109)

Sample	(mg)	Conc. Rb (ppm)	Conc. Sr (ppm)	$^{87}\text{Rb}/^{86}\text{Sr}$	$^{87}\text{Sr}/^{86}\text{Sr}$
KB117B WR	(99.1)	89.5	107.7	2.4119 ± 0.0021	0.734355 ± 0.000058
KB117C WR	(100.2)	143.0	132.1	3.1427 ± 0.0036	0.739020 ± 0.000036
KB117D WR	(100.3)	129.2	117.4	3.1931 ± 0.0030	0.739668 ± 0.000079
KB117D WR rep.	(103.2)	130.3	117.1	3.2291 ± 0.0034	0.739681 ± 0.000047
KB117E WR	(100.8)	99.6	109.7	2.6333 ± 0.0014	0.735970 ± 0.000111
KB117F WR	(106.4)	154.2	127.3	3.5144 ± 0.0044	0.741821 ± 0.000081
KB117F WR rep.	(108.3)	157.6	127.2	3.5986 ± 0.0160	0.741610 ± 0.000062
KB117G WR	(99.8)	75.6	90.8	2.4148 ± 0.0009	0.734484 ± 0.000048
KB117H WR	(103.0)	179.0	133.0	3.9092 ± 0.0018	0.744294 ± 0.000096
KB117H WR rep.	(100.7)	179.7	132.9	3.9282 ± 0.0098	0.743820 ± 0.000026
KB117I WR	(104.8)	85.4	92.9	2.6667 ± 0.0016	0.736198 ± 0.000049
KB117J WR	(100.9)	157.0	123.0	3.7061 ± 0.0050	0.742546 ± 0.000047
KB117J WR rep.	(100.8)	156.5	123.1	3.6892 ± 0.0022	0.742330 ± 0.000033
KB117K WR	(103.9)	80.9	86.8	2.7036 ± 0.0038	0.736308 ± 0.000155
KB117L WR	(94.1)	142.7	114.5	3.6179 ± 0.0025	0.742288 ± 0.000189
KB117M WR	(101.3)	116.1	96.7	3.4856 ± 0.0029	0.741363 ± 0.000070
KB117B Plag-Qz <60 μm	(139.5)	1.0	249.9	0.0115 ± 0.0000	0.717569 ± 0.000036
KB117B Bi 60-180 μm	(60.2)	454.6	3.8	445.4359 ± 0.2363	3.710902 ± 0.000017
CO117 WR	(101.5)	100.7	130.3	2.2414 ± 0.0016	0.732984 ± 0.000111
CO117 Ap 60-100 μm	(18.1)	2.4	109.2	0.0628 ± 0.0001	0.717457 ± 0.000060
CO117 Mu 60-100 μm	(7.9)	233.6	41.2	16.6248 ± 0.0157	0.844963 ± 0.000113
CO117 Bi 60-180 μm	(50.4)	446.7	2.8	679.2046 ± 1.5372	5.415362 ± 0.000385

Table A.10: Rb-Sr analytical data for rock profile KB 307

(farm Kaan 309)

Sample	(mg)	Conc. Rb (ppm)	Conc. Sr (ppm)	$^{87}\text{Rb}/^{86}\text{Sr}$	$^{87}\text{Sr}/^{86}\text{Sr}$
KB307A WR	(104.7)	227.9	137.5	4.8170 ± 0.0025	0.752259 ± 0.000040
KB307B WR	(101.9)	225.8	136.3	4.8139 ± 0.0070	0.753357 ± 0.000084
KB307C WR	(111.1)	158.2	112.4	4.0881 ± 0.0072	0.748114 ± 0.000027
KB307D WR	(106.4)	244.7	86.9	8.2039 ± 0.0121	0.776589 ± 0.000089
KB307D WR rep.	(100.0)	255.4	87.7	8.4837 ± 0.0768	0.775743 ± 0.000061
KB307E WR	(102.4)	169.7	107.7	4.5764 ± 0.0037	0.751393 ± 0.000038
KB307F WR	(107.1)	253.8	86.2	8.5846 ± 0.0163	0.780735 ± 0.000048
KB307F WR rep.	(100.5)	260.4	86.2	8.8026 ± 0.0330	0.780724 ± 0.000076
KB307G WR	(104.1)	169.5	67.3	7.3347 ± 0.0063	0.771194 ± 0.000055
KB307H WR	(100.8)	238.9	87.5	7.9549 ± 0.0217	0.776795 ± 0.000040
KB307H WR rep.	(103.6)	237.9	86.9	7.9723 ± 0.0191	0.777061 ± 0.000059
KB307I WR	(106.5)	146.5	90.7	4.6966 ± 0.0053	0.752684 ± 0.000055
KB307J WR	(100.9)	262.7	91.5	8.3667 ± 0.0348	0.778514 ± 0.000043
KB307K WR	(109.1)	120.2	69.1	5.0594 ± 0.0143	0.755346 ± 0.000049
KB307L WR	(102.2)	202.3	116.2	5.0622 ± 0.0036	0.755312 ± 0.000025
KB307M WR	(100.9)	187.2	84.9	6.4192 ± 0.0072	0.765185 ± 0.000087
KB307D Bi 80-160 $\mu\text{m}$	(34.6)	427.4	3.7	435.4693 ± 0.8725	3.761227 ± 0.000038
KB307F Mu 125-250 $\mu\text{m}$	(52.9)	147.0	72.9	5.8664 ± 0.0176	0.761239 ± 0.000063

Table A.11: Rb-Sr analytical data for rock profile KB421,  
Kuseb Formation (farm Keises 312)

Sample	(mg)	Conc. Rb (ppm)	Conc. Sr (ppm)	$^{87}\text{Rb}/^{86}\text{Sr}$	$^{87}\text{Sr}/^{86}\text{Sr}$
KB421.01 WR	(105.1)	73.2	298.0	0.7116 ± 0.0004	0.719411 ± 0.000055
KB421.02 WR	(100.9)	108.6	280.0	1.1233 ± 0.0017	0.722195 ± 0.000026
KB421.03 WR	(101.2)	167.8	368.8	1.3181 ± 0.0012	0.723757 ± 0.000036
KB421.04 WR	(102.0)	79.1	283.9	0.8075 ± 0.0008	0.720066 ± 0.000055
KB421.05 WR	(100.9)	31.8	288.9	0.3184 ± 0.0005	0.716582 ± 0.000051
KB421.06 WR	(101.2)	70.7	286.2	0.7157 ± 0.0013	0.719454 ± 0.000022
KB421.06 WR rep.	(112.8)	70.2	285.5	0.7123 ± 0.0013	0.719454 ± 0.000052
KB421.07 WR	(102.6)	133.8	313.2	1.2381 ± 0.0035	0.723279 ± 0.000033
KB421.07 WR rep.	(101.3)	137.7	313.0	1.2748 ± 0.0038	0.723341 ± 0.000069
KB421.08 WR	(101.6)	76.2	284.4	0.7755 ± 0.0033	0.719885 ± 0.000062
KB421.08 WR rep.	(100.2)	77.3	285.1	0.7853 ± 0.0011	0.719963 ± 0.000035
KB421.09 WR	(101.2)	39.5	272.6	0.4201 ± 0.0003	0.717400 ± 0.000055
KB421.10 WR	(106.2)	163.8	349.2	1.3594 ± 0.0007	0.724145 ± 0.000028
KB421.10 WR rep.	(102.9)	166.7	348.6	1.3859 ± 0.0056	0.724121 ± 0.000063
KB421.11 WR	(118.5)	103.3	291.1	1.0277 ± 0.0018	0.721700 ± 0.000045
KB421.12 WR	(104.6)	81.3	283.1	0.8322 ± 0.0003	0.720297 ± 0.000040
KB421.13 WR	(105.3)	97.5	278.6	1.0144 ± 0.0007	0.721535 ± 0.000061
KB421.14 WR	(105.5)	74.9	288.1	0.7536 ± 0.0015	0.719951 ± 0.000045
KB421.15 WR	(109.0)	53.9	288.1	0.5420 ± 0.0026	0.718214 ± 0.000014
KB421.16 WR	(127.7)	106.2	306.7	1.0031 ± 0.0061	0.721748 ± 0.000039
KB421.17 WR	(100.6)	59.2	312.4	0.5489 ± 0.0048	0.718913 ± 0.000041
KB421.18 WR	(100.1)	25.3	269.8	0.2718 ± 0.0006	0.716467 ± 0.000070
KB421.19 WR	(103.1)	16.8	261.4	0.1865 ± 0.0001	0.716201 ± 0.000040
KB421.20 WR	(103.1)	27.5	275.6	0.2887 ± 0.0008	0.718032 ± 0.000047
KB421.21 WR	(105.1)	100.8	358.9	0.8140 ± 0.0014	0.722082 ± 0.000035
KB421.22 WR	(108.8)	43.9	294.6	0.4319 ± 0.0012	0.718629 ± 0.000040
KB421.31 WR	(105.0)	39.6	292.4	0.3918 ± 0.0011	0.717136 ± 0.000077
KB421.33 WR	(107.1)	72.4	294.0	0.7134 ± 0.0118	0.719653 ± 0.000011
KB421.33 Hb 60-180 μm	(18.0)	6.3	48.0	0.3778 ± 0.0009	0.717228 ± 0.000041
KB421.33 Bi 60-180 μm	(32.1)	637.9	3.6	782.5059 ± 1.2350	6.180050 ± 0.000569

Table A.12: Rb-Sr analytical data for rock profile KB115,  
Kuibeb Formation (farm Keises 312)

Sample	(mg)	Conc. Rb (ppm)	Conc. Sr (ppm)	$^{87}\text{Rb}/^{86}\text{Sr}$	$^{87}\text{Sr}/^{86}\text{Sr}$
KB115A WR	(104.5)	285.9	109.4	7.6049 ± 0.0077	0.771471 ± 0.000055
KB115A WR rep.	(100.9)	286.1	108.5	7.6770 ± 0.0031	0.772058 ± 0.000042
KB115BC WR	(117.1)	143.9	94.2	4.4403 ± 0.0152	0.750296 ± 0.000050
KB115D WR	(100.6)	222.7	210.8	3.0657 ± 0.0035	0.740367 ± 0.000028
KB115E WR	(103.2)	257.1	146.6	5.0954 ± 0.0025	0.754432 ± 0.000062
KB115E WR rep.	(108.0)	257.8	146.4	5.1171 ± 0.0058	0.754625 ± 0.000033
KB115F WR	(101.8)	144.5	137.9	3.0417 ± 0.0062	0.740553 ± 0.000054
KB115G WR	(101.9)	247.8	114.8	6.2814 ± 0.0309	0.762616 ± 0.000100
KB115H WR	(102.0)	217.6	92.9	6.8128 ± 0.0293	0.765812 ± 0.000109
KB115H WR rep.	(101.7)	213.2	92.7	6.6932 ± 0.0056	0.765640 ± 0.000023
KB115I WR	(101.0)	194.1	99.6	5.6676 ± 0.0439	0.758047 ± 0.000092
KB115I WR rep.	(100.9)	192.7	99.7	5.6169 ± 0.0034	0.758163 ± 0.000060
KB115J WR	(101.1)	255.8	55.8	13.3886 ± 0.0428	0.809463 ± 0.000089
KB115J WR rep.	(100.5)	249.7	55.3	13.1925 ± 0.0062	0.809040 ± 0.000040
KB115K WR	(105.1)	135.9	102.3	3.8599 ± 0.0177	0.745630 ± 0.000098
KB115D Pl-Qz <60 μm	(68.4)	1.2	221.7	0.0157 ± 0.0000	0.719242 ± 0.000046
KB115E Pl-Qz <40 μm	(77.2)	3.5	507.1	0.0197 ± 0.0000	0.718868 ± 0.000041
KB115F Pl-Qz <60 μm	(147.2)	1.3	227.2	0.0169 ± 0.0000	0.719135 ± 0.000029
KB115J Pl-Qz <60 μm	(111.3)	9.5	143.9	0.1908 ± 0.0001	0.720489 ± 0.000043
KB115J Pl-Qz <40 μm	(28.7)	8.1	159.9	0.1466 ± 0.0000	0.720168 ± 0.000056
KB115E Mu 60-180 μm	(14.4)	174.9	44.2	11.5558 ± 0.0471	0.801680 ± 0.000046
KB115J Mu 60-180 μm	(61.4)	189.2	45.0	12.2631 ± 0.0142	0.803010 ± 0.000058
KB115E Bi 80-160 μm	(47.5)	450.7	2.5	808.2278 ± 1.3171	6.359609 ± 0.000411
KB115E Bi 160-250 μm	(19.2)	442.2	2.5	808.2365 ± 3.1181	6.389556 ± 0.000528
KB115J Bi 60-180 μm	(41.2)	451.2	2.3	953.0697 ± 2.3188	7.449806 ± 0.000320

Table A.13: Rb-Sr analytical data for rock profile KB103,  
Kuisseb Formation (farm Davetsaub 29)

Sample	(mg)	Conc. Rb (ppm)	Conc. Sr (ppm)	$^{87}\text{Rb}/^{86}\text{Sr}$	$^{87}\text{Sr}/^{86}\text{Sr}$
KB103.04 WR	(101.8)	173.5	78.9	6.3994 ± 0.0354	0.760719 ± 0.000050
KB103.05 WR	(103.0)	143.6	82.1	5.0838 ± 0.0166	0.752900 ± 0.000056
KB103.06 WR	(104.6)	148.1	96.8	4.4459 ± 0.0108	0.747881 ± 0.000059
KB103.07 WR	(107.6)	110.8	122.4	2.6263 ± 0.0053	0.735133 ± 0.000030
KB103.08 WR	(101.6)	159.3	91.0	5.0888 ± 0.0025	0.752665 ± 0.000033
KB103.08 WR rep.	(109.9)	158.9	91.0	5.0731 ± 0.0038	0.752597 ± 0.000042
KB103.09 WR	(105.4)	245.3	19.3	37.8536 ± 0.3553	0.980071 ± 0.000072
KB103.09 WR rep.	(105.6)	242.5	19.2	37.5157 ± 0.0459	0.980055 ± 0.000082
KB103.10 WR	(106.1)	63.4	177.0	1.0382 ± 0.0007	0.723432 ± 0.000051
KB103.10 WR rep.	(103.1)	64.1	176.8	1.0506 ± 0.0010	0.723366 ± 0.000031
KB103.11 WR	(101.7)	87.5	120.5	2.1063 ± 0.0016	0.730812 ± 0.000053
KB103.12 WR	(109.0)	60.9	125.9	1.4028 ± 0.0017	0.725837 ± 0.000037
KB103.13 WR	(105.8)	142.6	44.1	9.4215 ± 0.0047	0.782780 ± 0.000038
KB103.14 WR	(100.4)	74.9	139.4	1.5583 ± 0.0022	0.727037 ± 0.000039
KB104.15 WR	(100.7)	108.2	109.4	2.8707 ± 0.0125	0.735903 ± 0.000083
KB103.16 WR	(100.5)	163.6	20.1	23.9249 ± 0.0064	0.884536 ± 0.000043
KB103.17 WR	(100.5)	127.7	70.6	5.2574 ± 0.0027	0.753733 ± 0.000066
KB103.18 WR	(100.5)	130.4	87.5	4.3295 ± 0.0244	0.746739 ± 0.000047
KB103.19 WR	(103.2)	149.3	93.6	4.6354 ± 0.0094	0.747994 ± 0.000063
KB103.20 WR	(106.5)	24.0	199.7	0.3485 ± 0.0002	0.718303 ± 0.000034
KB103.21 WR	(100.7)	148.6	44.9	9.6547 ± 0.0082	0.784441 ± 0.000077
KB103.22 WR	(101.6)	35.9	186.2	0.5580 ± 0.0002	0.719727 ± 0.000051
KB103.23 WR	(100.9)	165.2	44.4	10.8602 ± 0.0167	0.793269 ± 0.000061
KB103.23 WR rep.	(110.4)	165.2	44.1	10.9348 ± 0.0337	0.793328 ± 0.000032
KB103.24 WR	(104.3)	35.9	214.7	0.4837 ± 0.0001	0.719245 ± 0.000030
KB103.25 WR	(104.4)	177.0	27.1	19.1778 ± 0.0213	0.850638 ± 0.000026
KB103.26 WR	(100.3)	44.0	200.0	0.6378 ± 0.0004	0.720567 ± 0.000062
KB103.27 WR	(100.6)	146.3	59.9	7.1028 ± 0.0065	0.766219 ± 0.000050
KB103.28 WR	(101.6)	164.0	76.0	6.2780 ± 0.0024	0.761252 ± 0.000065
KB103.29 WR	(115.3)	174.2	64.1	7.9112 ± 0.0061	0.772696 ± 0.000032
KB103.30 WR	(108.4)	141.8	92.6	4.4504 ± 0.0086	0.748368 ± 0.000057
KB103.31 WR	(101.8)	156.8	91.1	5.0024 ± 0.0053	0.752374 ± 0.000041
KB103.32 WR	(104.5)	174.2	64.9	7.8155 ± 0.0174	0.772615 ± 0.000045
KB103.33 WR	(102.0)	144.5	273.6	1.5305 ± 0.0024	0.728565 ± 0.000037
KB103.34 WR	(100.9)	335.3	6.6	162.5677 ± 0.0946	1.865351 ± 0.000402
KB103.13 Ga 125-250 μm	(67.2)	1.2	0.1	48.5229 ± 2.6122	1.035932 ± 0.019083
KB103.13 Ga 250-500 μm	(82.1)	0.9	0.1	47.7689 ± 2.1877	1.042799 ± 0.015080
KB103.09 Bi 125-250 μm	(76.6)	501.4	1.9	1617.7427 ± 3.6398	12.200357 ± 0.002966
KB103.09 Bi 250-500 μm	(18.2)	513.3	2.0	1521.9628 ± 6.7868	11.422283 ± 0.012058
KB103.13 Bi 125-250 μm	(70.4)	471.1	2.6	792.3161 ± 7.5174	6.197282 ± 0.000192
KB103.13 Bi 250-500 μm	(68.4)	495.9	2.3	1049.2983 ± 1.3966	7.971628 ± 0.004810
KB103.23 Bi 125-250 μm	(75.8)	500.7	2.0	1480.9349 ± 3.5429	11.234219 ± 0.001835
KB103.23 Bi 250-500 μm	(64.5)	520.4	2.0	1502.7222 ± 1.4770	11.132308 ± 0.003439
KB103.28 Bi 125-250 μm	(60.3)	497.3	1.9	1615.5188 ± 2.7744	12.098673 ± 0.003387
KB103.28 Bi 250-500 μm	(27.9)	502.7	1.9	1550.3201 ± 3.4411	11.589730 ± 0.008141

**Table A.14: Rb-Sr analytical data for sample CO343,  
Donkerhuk Granite (farm Nomatsaus 28)**

Sample	(mg)	Conc. Rb (ppm)	Conc. Sr (ppm)	$^{87}\text{Rb}/^{86}\text{Sr}$	$^{87}\text{Sr}/^{86}\text{Sr}$
CO343 WR	(104.9)	119.0	243.6	1.4151 ± 0.0022	0.718775 ± 0.000056
CO343 Ap <250 μm	(26.5)	0.3	171.8	0.0048 ± 0.0000	0.718111 ± 0.000035
CO343 Mu 125-250 μm	(79.3)	335.2	25.7	8.8187 ± 0.0971	0.989886 ± 0.000056
CO343 Mu 250-500 μm	(79.1)	336.6	19.5	51.8665 ± 0.0703	1.080919 ± 0.000043
CO343 Bi 160-250 μm	(41.9)	700.9	9.2	259.7665 ± 0.2561	2.529552 ± 0.000095

Table A.15: Apparent age data calculated from the Rb-Sr whole-rock and mineral analyses

Samples	Age (Ma) $\pm 2 \sigma$	MSWD	$R_i \pm 2 \sigma$
<b>Microprofile KB167</b>			
KB167, slabs A-K: WR	488 $\pm$ 13	1.7	0.71841 $\pm$ 0.00049
KB167, slab B: WR - biotite (80-160 $\mu$ m)	491 $\pm$ 10	-	-
KB167, slab C: WR - biotite (80-160 $\mu$ m)	483 $\pm$ 10	-	-
<b>Microprofile KB117 and sample C0117</b>			
KB117, slabs B-M: WR	449 $\pm$ 20	0.5	0.71905 $\pm$ 0.00083
KB117, slab B: WR - biotite (60-180 $\mu$ m)	472 $\pm$ 10	-	-
KB117, slab B: WR - plagioclase (< 60 $\mu$ m)	491 $\pm$ 15	-	-
C0117: WR - biotite (60-180 $\mu$ m)	485 $\pm$ 10	-	-
C0117: WR - muscovite (60-100 $\mu$ m)	546 $\pm$ 17	-	-
C0117: WR - apatite (60-100 $\mu$ m)	500 $\pm$ 22	-	-
<b>Microprofile KB307</b>			
KB307, slabs A-M: WR	509 $\pm$ 17	1.2	0.71833 $\pm$ 0.00128
KB307, slab D: WR - biotite (60-180 $\mu$ m)	488 $\pm$ 11	-	-
<b>Microprofile KB421</b>			
KB421, slabs 1-16, 31, 33: WR	500 $\pm$ 14	1.4	0.71438 $\pm$ 0.00015
KB421, slab 33: WR - biotite (60-180 $\mu$ m)	489 $\pm$ 10	-	-
KB421, slab 33: WR - hornblende (60-180 $\mu$ m)	506 $\pm$ 57	-	-
<b>Microprofile KB115</b>			
KB115, slabs A-K: WR	479 $\pm$ 11	0.8	0.71963 $\pm$ 0.00066
KB115, slab D: WR - plagioclase (< 60 $\mu$ m)	486 $\pm$ 13	-	-
KB115, slab E: WR - biotite (80-160 $\mu$ m; 160-250 $\mu$ m)	491 $\pm$ 7	0.4	-
KB115, slab E: WR - plagioclase (< 40 $\mu$ m)	492 $\pm$ 16	-	-
KB115, slab F: WR - plagioclase (< 60 $\mu$ m)	497 $\pm$ 14	-	-
KB115, slab J: WR - biotite (60-180 $\mu$ m)	496 $\pm$ 10	-	-
KB115, slab J: WR - plagioclase (< 40 $\mu$ m; < 60 $\mu$ m)	476 $\pm$ 15	0.3	-
<b>Microprofile KB103</b>			
KB103, slabs 4-34: WR	504 $\pm$ 8	3.2	0.71587 $\pm$ 0.00018
KB103, slabs 5-8: WR	501 $\pm$ 17	0.5	0.71635 $\pm$ 0.00094
KB103, slabs 11-14: WR	498 $\pm$ 11	0.5	0.71592 $\pm$ 0.00031
KB103, slabs 20-24: WR	499 $\pm$ 7	0.5	0.71581 $\pm$ 0.00007
KB103, slabs 28-32: WR	498 $\pm$ 20	0.5	0.71678 $\pm$ 0.00164
KB103, slab 9: WR - biotite (125-250 $\mu$ m; 250-500 $\mu$ m)	496 $\pm$ 7	0.6	-
KB103, slab 13: WR - biotite (125-250 $\mu$ m; 250-500 $\mu$ m)	485 $\pm$ 7	0.03	-
KB103, slab 23: WR - biotite (125-250 $\mu$ m)	498 $\pm$ 10	-	-
KB103, slab 23: WR - biotite (250-500 $\mu$ m)	486 $\pm$ 10	-	-
KB103, slab 28: WR - biotite (125-250 $\mu$ m; 250-500 $\mu$ m)	493 $\pm$ 7	0.3	-

## U-Pb data

Table A.16: U-Pb data for zircon fractions of sample CO 117

Zircon population	Sieve fraction ( $\mu\text{m}$ )	weight of sample (mg)	conc. U (ppm)	conc. Pb (ppm)	conc. $\text{Pb}_{\text{rad}}$ (ppm)	
1) rounded	40-60	2.0	661	75.7	71.7	
2) rounded	80-100	3.5	413	57.2	55.2	
3) subhedral	60-80	2.9	467	51.2	48.5	
4) euhedral	40-60	2.1	801	66.5	61.9	
5) euhedral	60-80	3.0	743	61.1	56.6	
6) euhedral	80-100	3.9	582	60.9	48.3	
Measured Ratios			Isotopic Ratios			
$\frac{^{206}\text{Pb}}{^{204}\text{Pb}}$	$\frac{^{207}\text{Pb}}{^{206}\text{Pb}}$	$\frac{^{208}\text{Pb}}{^{206}\text{Pb}}$	$\frac{^{206}\text{Pb}}{^{238}\text{U}}$	$\frac{^{207}\text{Pb}}{^{235}\text{U}}$	$\frac{^{207}\text{Pb}}{^{206}\text{Pb}}$	
1)	984.4	0.110992	0.175552	625	872	1567
2)	1384.7	0.108354	0.171505	757	1005	1594
3)	1005.8	0.095805	0.166139	611	764	1242
4)	799.0	0.086832	0.163695	470	550	895
5)	734.1	0.086109	0.168435	463	529	823
6)	245.7	0.125655	0.263603	503	569	843

Table A.17: U-Pb monazite data

Sample	Locality	Coordinates	Sieve fraction ( $\mu\text{m}$ )	Weight of sample (mg)								
KB103	Migmatite (composite), (1)	Davetsaub 29	60-125	1.65								
KB103	Migmatite (composite), (2)	Davetsaub 29	125-180	2.10								
KB103	Migmatite (composite), (3)	Davetsaub 29	60-125	1.48								
KB103	Migmatite (Neosome), (4)	Davetsaub 29	60-180	3.06								
CO437	Migmatite (Neosome)	Davetsaub 29	125-180	4.04								
CO429	Kuiseb Formation Pelite	Keises 312	< 80	1.02								
CO343	Donkerhuk Granite (white)	Nomatsaus 28	60-180	0.61								
CO444	Granitic Vein (foliated)	Davetsaub 29	60-180	2.21								
CO453	Granodiorite (foliated)	Otjimbingwe 104	60-180	1.49								
Sample	Conc. U (ppm)	Conc. Pb (ppm)	Conc. Pbrad (ppm)	Measured $^{206}\text{Pb}/^{204}\text{Pb}$	Ratios $^{208}\text{Pb}/^{206}\text{Pb}$	Isotopic Ratios $^{206}\text{Pb}/^{238}\text{U}$	Isotopic Ratios $^{207}\text{Pb}/^{235}\text{U}$	Isotopic Ratios $^{207}\text{Pb}/^{206}\text{Pb}$	Apparent Ages $^{206}\text{Pb}/^{238}\text{U}$	Apparent Ages $^{207}\text{Pb}/^{235}\text{U}$	Apparent Ages $^{207}\text{Pb}/^{206}\text{Pb}$	
KB103	10141	1693	1690	15065	0.058633	1.231930	0.084333	0.670547	0.057668	522	521	517
KB103	10441	1718	1715	17139	0.058528	1.184251	0.084869	0.674666	0.057655	525	524	518
KB103	13417	2257	2252	14964	0.058645	1.225468	0.085182	0.677360	0.057673	527	525	517
KB103	10310	1713	1711	17557	0.058244	1.213468	0.084669	0.669982	0.057390	524	521	508
CO437	7731	1874	1870	9867	0.059033	2.274386	0.083942	0.666174	0.057558	520	518	513
CO429	10701	1039	1036	18616	0.058465	0.300119	0.082890	0.659252	0.057683	513	514	518
CO343	7027	1374	1369	4739	0.060449	1.709206	0.081518	0.644947	0.057381	505	505	506
CO444	5965	1303	1296	4378	0.060806	2.016868	0.081767	0.648063	0.057483	507	507	510
CO453	12839	2456	2445	5856	0.059708	1.636539	0.081855	0.645818	0.057222	507	506	500

\* after correction

---

## APPENDIX V: K-Ar AND $^{40}\text{Ar}$ - $^{39}\text{Ar}$ ISOTOPE ANALYSES

### Analytical techniques

K-Ar and  $^{40}\text{Ar}$ - $^{39}\text{Ar}$  analyses were carried out by Dr H. Kreuzer and his coworkers at the Bundesanstalt für Geowissenschaften und Rohstoffe, Hannover.

Samples used for K-Ar analyses are splits of mineral fractions which were investigated with the Rb-Sr method. Potassium and argon were analysed in separate, representative aliquots, the former by flame photometry, and the latter by mass spectrometric isotope dilution analysis. For  $^{40}\text{Ar}$ - $^{39}\text{Ar}$  analyses the pure mineral concentrates were sealed under vacuum in quartz vials and irradiated in the FRG reactor of the Forschungszentrum Geesthacht G.m.b.H. For corrections for interferences a mean value for different nuclear piles was used (Rittmann, 1984; Brereton, 1970). Argon was extracted by means of the incremental heating technique (Lanphere and Dalrymple, 1971; Dalrymple and Lanphere, 1971; 1974).

Errors are quoted as internal errors on a  $2\delta$  level (95% confidence) in the Tables A.18-A.20, based on the run-internal errors enlarged by an additional term of 0.5%. Error calculation for plateau/average dates is based on the uncertainty of analyses of monitor samples inserted for calibration. A standard deviation ranging from 0.3 to 0.6% was obtained from measurement of 8 standard biotites. For error calculation, a factor of twice the standard deviation of the calibration factor was used, i.e. 1.2%. For further details of analytical techniques and age calculation refer to Bröcker *et al.* (in prep).

## Analytical data

Table A.18: Rock profile KB 167, slab B, biotite (0.0251 g)

	Temperature °C	<sup>40</sup> Ar <sub>rad</sub> %	<sup>39</sup> Ar/ $\Sigma$ <sup>39</sup> Ar %	Age Ma
0	500	70.10	0.51	253.5 ± 16.4
1	550	86.43	0.79	304.0 ± 7.3
2	580	92.39	2.40	444.8 ± 3.8
3	600	96.95	2.64	488.2 ± 3.6
4	620	98.14	3.95	486.8 ± 4.0
5	650	99.15	6.14	485.9 ± 3.0
6	680	99.62	7.65	490.4 ± 3.8
7	720	99.46	6.29	488.5 ± 2.7
8	780	99.66	5.92	488.5 ± 3.0
9	830	99.49	4.74	489.5 ± 3.0
10	870	99.39	3.98	489.7 ± 5.0
11	910	99.45	5.12	490.0 ± 4.4
12	940	99.80	7.33	494.2 ± 2.9
13	970	99.39	12.84	492.8 ± 3.1
14	1000	99.96	9.91	492.6 ± 3.2
15	1040	99.74	8.14	489.1 ± 5.5
16	1100	99.51	10.73	487.2 ± 2.9
17	1550	98.45	0.80	482.9 ± 10.1
18	1550	96.12	0.14	462.9 ± 40.4
Total		99.09	100.00	486.2 ± 1.0

Table A.19: Rock profile KB115, slab J, biotite 60-180  $\mu$ m (0.0234 g)

	Temperature °C	<sup>40</sup> Ar <sub>rad</sub> %	<sup>39</sup> Ar/ $\Sigma$ <sup>39</sup> Ar %	Age Ma
0	500	71.42	0.56	2,924 ± 9.8
1	550	90.96	0.87	404.6 ± 11.1
2	580	95.08	3.19	461.2 ± 3.5
3	600	97.64	3.18	480.0 ± 3.4
4	620	98.68	4.08	480.5 ± 4.2
5	650	99.26	6.47	484.2 ± 2.7
6	680	99.57	6.62	485.1 ± 3.1
7	720	99.60	5.24	480.9 ± 2.8
8	780	99.48	5.52	481.9 ± 6.1
9	830	99.85	6.05	487.1 ± 2.8
10	870	99.81	5.98	488.9 ± 3.3
11	910	99.76	8.35	488.0 ± 2.5
12	940	99.70	9.76	486.2 ± 2.5
13	970	99.84	12.58	488.7 ± 2.6
14	1000	99.71	9.13	483.9 ± 3.0
15	1040	99.49	6.34	483.7 ± 3.1
16	1100	99.73	4.20	484.4 ± 3.4
17	1550	98.78	1.86	485.8 ± 4.2
Total		99.21	100.00	482.8 ± 0.9

Table A.20: Rock profile KB115, slab J, muscovite 60-180  $\mu\text{m}$  (0.0198 g)

	Temperature $^{\circ}\text{C}$	$^{40}\text{Ar}_{\text{rad}}$ %	$^{39}\text{Ar}/\Sigma^{39}\text{Ar}$ %	Age Ma	
0	500	86.25	0.94	286.5	$\pm 7.2$
1	600	97.42	1.53	446.6	$\pm 6.6$
2	700	98.79	5.94	485.8	$\pm 2.9$
3	715	98.92	4.21	487.8	$\pm 4.0$
4	730	98.96	5.45	489.5	$\pm 3.0$
5	745	98.80	6.46	490.3	$\pm 3.1$
6	760	99.14	6.89	490.6	$\pm 2.9$
7	775	99.52	6.85	493.9	$\pm 3.2$
8	800	99.30	7.46	491.5	$\pm 3.3$
9	825	99.59	8.24	492.8	$\pm 2.9$
10	860	99.65	8.75	482.7	$\pm 12.8$
11	900	99.43	7.61	492.7	$\pm 4.2$
12	1000	99.29	10.50	491.8	$\pm 4.2$
13	1050	98.87	7.96	492.6	$\pm 3.0$
14	1450	99.47	8.44	497.2	$\pm 2.7$
15	1550	98.19	2.78	495.1	$\pm 5.1$
<b>Total</b>		99.11	100.00	488.6	$\pm 1.5$